UNIVERSITY OF BIRMINGHAM

Microstructure and Mechanical Properties of Mg-Zn-(Y/Gd) alloys

JING WU

A thesis submitted to the University of Birmingham

for the degree of

DOCTOR OF PHILOSOPHY

2016

School of Metallurgy and Materials

University of Birmingham

Edgbaston

Birmingham

United Kingdom

B15 2TT

Preface

This research was carried out by Jing Wu in School of Metallurgy and Materials, University of Birmingham (from September 2012 to August 2016), under the supervision of Dr. Y.L. Chiu and Prof. I.P. Jones.

The present work is original and no part of the work has been submitted for another degree at any other university. Wherever other researchers' work has been drawn from or cited, it is acknowledged in the text and the references are listed.

Parts of the work have been published as follows:

[1] **J. Wu**, Q. Shi, H.C. Ma, Y.L. Chiu, *Microstructure and mechanical behaviour of a $Mg_{94}Zn_2Y_4$ alloy processed by equal channel angular pressing.* Materials Science and Engineering: A, 2016. **669**: 417-427.

[2] **J. Wu**, Y.L. Chiu, and I.P. Jones, *Effect of Gd on the microstructure of as-cast Mg-4.2Zn-0.8Y (at.%) alloys.* Journal of Alloys and Compounds, 2016. **661**: 455-460.

[3] **J. Wu**, Y.L. Chiu, and I.P. Jones, *Microstructure of as-cast Mg-4.2Zn-0.8Y (at.%) alloys containing Gd.* Journal of Physics: Conference Series, 2014. **522**(1): 012033.

Acknowledgements

I would like to thank Dr YuLung Chiu and Professor Ian P. Jones for their guidance through the PhD. Dr YuLung Chiu is passionate and he encourages my ideas and tries his best to help me with both work and life. Professor Ian P. Jones is knowledgeful and he guides me out of the woods with his wisdom.

I am grateful for Dr Rengen Ding's help with the experiments and the discussions, Professor Mike Loretto for the advice for my writing, Dr Ken-ichi Ikeda for the help with dislocation analysis of LPSO phase, Dr Q. Shi for the assistance for ECAP processing and Dr Dan Reed for the help with XRD. Special thanks go to Dr Tianxiang Zhen for the help of sample preparations.

I would like to give thanks to Paul Stanley and Theresa Morris for the technical support of the electron microscopes. I am thankful for David Price, Andy Bradshaw, Geff Sutton for the help with other instruments.

I would like also thank my colleagues: Dr Y. Lu, H.C. Ma, M.S. Wang, G. Douglas, S. Rai, X.Y. Lu, Z.R. Liu, J.S. Tian, R. Ameen, D. Higgins, S.S. Si, Dr R.L. Zeng, Dr B. Pang.

And thank my friends and all the people who helped me.

My financial acknowledgements go to Li Siguang Scholarship, which is jointly funded by University of Birmingham and China Scholarship Council. Their financial support allows me to carry out the research in UK.

Last but not least, I want to thank my parents and my brother for their support and understanding. My parents raised me to be a strong and happy girl, which helps go through the hard times.

Abstract

As-cast $Mg_{94}Zn_2Y_4$ alloy has been subjected to compression and equal channel angular pressing (ECAP) separately; the microstructure was characterised using optical microscopy (OM), scanning electron microscopy (SEM) and transmission electron microscopy (TEM). Electron backscattered diffraction (EBSD) and transmission Kikuchi diffraction (TKD) are also used.

The as-cast $Mg_{94}Zn_2Y_4$ alloy contains mainly a long-period stacking ordered (LPSO) phase and a $Mg_{24}Y_5$ phase as secondary phases. During compression, kinking occurs in the LPSO phase. Most kink boundaries are composed of straight basal <a> type dislocations. The dislocation arrangement in the kink boundaries of the LPSO/Mg mixture (alternate thin layers of LPSO and Mg) is similar to that in the LPSO. The rotation axes of the kink boundaries in LPSO/Mg are preferentially located in the (0001) plane; the [0001] rotation axis has occasionally been observed. Double kinking has also been observed in the LPSO/Mg region. Non-basal slip in the LPSO/Mg mixture can accommodate a strain similar to kinking.

ECAP processing develops a bimodal microstructure consisting of large deformed grains (Mg and LPSO) and sub-micron sized dynamically recrystallised (DRXed) grains, which are decorated with a large number of nano-sized $Mg_{24}Y_5$ precipitates. The DRXed grains are mainly located in the interior along the original grain boundaries. DRXed grains are also observed in the kink boundaries of the LPSO/Mg structure, preferentially in the kink boundaries with high misorientation angles. The kink boundary acts as a DRX nucleation site due to the high energy stored.

Small punch test (SPT) results show that the ECAP processing increased significantly the strength of the alloy. Under the biaxial tensile stress induced by SPT, the sample started to crack along the ECAP shear direction shortly after the linear elastic region on the load-displacement curve; the DRXed grains are potential crack sources. These phenomena may be explained by different deformation behaviours of the fibre textured coarse grains and the random oriented DRXed grains, and the distribution of the DRXed grains.

A fragmentation mechanism has been proposed for eutectic $Mg_{24}Y_5$ intermetallic particles during ECAP. Initially cracks are formed in $Mg_{24}Y_5$ particles; DRX of these intermetallics occurred in the heavily deformed area. The agglomeration of DRXed $Mg_{24}Y_5$ grains gives rise to necking and thus to a dispersion of small $Mg_{24}Y_5$ particles.

In the as-cast Mg-Zn-Y alloys, the main secondary phase changes when different ratios of Zn/Y are applied: LPSO (Zn/Y ratio is 0.5) → LPSO+W (Zn/Y ratio is 1, W is $Mg_3Zn_3Y_2$) → W (Zn/Y ratio is 2.33). When Y is half replaced by Gd, the types of secondary phases are similar. When Y is replaced fully by Gd, W phase becomes the mai

n secondary phase. The structure of the LPSO phase also changes. The results indicate that Gd stabilises the 14H LPSO while Y stabilises the 18R LPSO in the as-cast condition; 14H LPSO is more likely to form with larger Zn to Y+Gd ratio. The hardness of the alloys is most affected by the presence of the secondary phases. In general, alloys with W phase have higher hardness than these with LPSO phase if similar area fractions of secondary phases are compared.

Contents

1 Introduction

Mg is the lightest of all commonly used structural materials; it has a density of about 1.7g/cm^3, which is 2/3 that of Al and ¼ that of steels. Thus it has the potential to replace Al in the automotive and aerospace industries. However, compared to Al, Mg has relatively low strength and ductility, and its poor fire resistance limits its use. Recently, a Mg-Zn-Y alloy system has been developed and its good mechanical properties have attracted lots of attention.

Many ternary phases are observed in Mg-Zn-Y alloys and they are related to the Zn to Y ratios in the system. With increasing Zn/Y ratio, the following precipitates form in a sequence, viz. $Mg_{24}Y_5$ → LPSO (long-period stacking ordered) phase→ W ($Mg_3Zn_3Y_2$)→ I-phase (icosahedral quasicrystalline phase, $Mg_3Zn_6Y_1$) [1-4]. Mg-Zn-Y alloys with LPSO phase are the most heavily studied. Kawamura et al. [5] reported that a $Mg_{97}Zn_1Y_2$ alloy prepared by rapid solidification and powder metallurgy (RS/PM) has a yield strength about 600 MPa and ductility of about 5%. The excellent properties are mainly due to two reasons: the nano-sized grain size and the dispersed LPSO phase. The LPSO phase deforms mainly via basal slip and kinking, and it strengthens the alloys by introducing kink boundaries into the alloys which result in grain refinement.

Lots of issues exist in this alloy system and need to be clarified:

1. The kink is commonly believed to form via generating dislocation pairs and rearrangement of the dislocations. However, no detailed dislocation analysis of kink boundaries in LPSO has been reported in the literature.

2. The excellent strength is due partly to the nano-sized grains, which themselves are due to the RS/PM process. However, RS/PM is expensive and time consuming, so alternant effective grain refinement methods suitable for as-cast alloys need to be developed. And the effect of the secondary phases on the microstructural evolution needs to be clarified.

3. The secondary phases determine the mechanical properties at some level. Mg-Zn-Y alloys contain lots of ternary phases and it is important to study effect of the Zn/Y ratio on the formation of the secondary phases. Gd is another widely used RE element; it is interesting to find out the microstructure and mechanical properties change when Y is (partially) replaced by Gd

This thesis aims to clarify these issues.

The outline for the thesis is therefore as follows:

Chapter 2 presents an introduction to Mg alloys and alloying, especially with RE (Rare Earth) elements. Literature on the secondary phases, strengthening mechanisms and mechanical processing of Mg-Zn-RE alloys is also reviewed.

Chapter 3 summarises the experimental procedures used in the current study.

Chapter 4 studies the dislocations in the kink boundaries of the LPSO phase and the LPSO/Mg mixture (alternate thin LPSO and Mg lamellae) in deformed $Mg_{94}Zn_2Y_4$ alloys.

Chapter 5 investigates the bimodal grain structure and corresponding mechanical properties of $Mg_{94}Zn_2Y_4$ alloys modified by equal channel angular pressing (ECAP). The deformation

behaviours of LPSO, $Mg_{24}Y_5$ and the Mg matrix and their effects on the dynamic recrystallisation and microstructural evolution during the ECAP process are discussed.

Chapter 6 studies the secondary phases in as-cast Mg-Zn-(Y)-(Gd) alloys. The effect of Zn to RE ratio on the secondary phases and the effect of Gd additions on the formation of the LPSO are investigated. The effect of alloying elements on the lattice parameters of the secondary phases and Mg matrix are also discussed.

2 Literature review

2.1 Introduction to Mg

As the lightest of all structural metals, Mg has a density of 1.738 g/cm^3. It is also remarkably abundant; it constitutes about two percent of the Earth's crust and is the third most plentiful element dissolved in seawater. Due to a relatively low melting point and high specific heat, Mg has good castability, especially suitable for high pressure die-casting. Its alloys have higher specific strength than aluminium and steel, whereby the principal applications are found in the automotive and aerospace industries because of environmental performance gains. Figure 2.1 shows some automotive components where Mg is used [6].

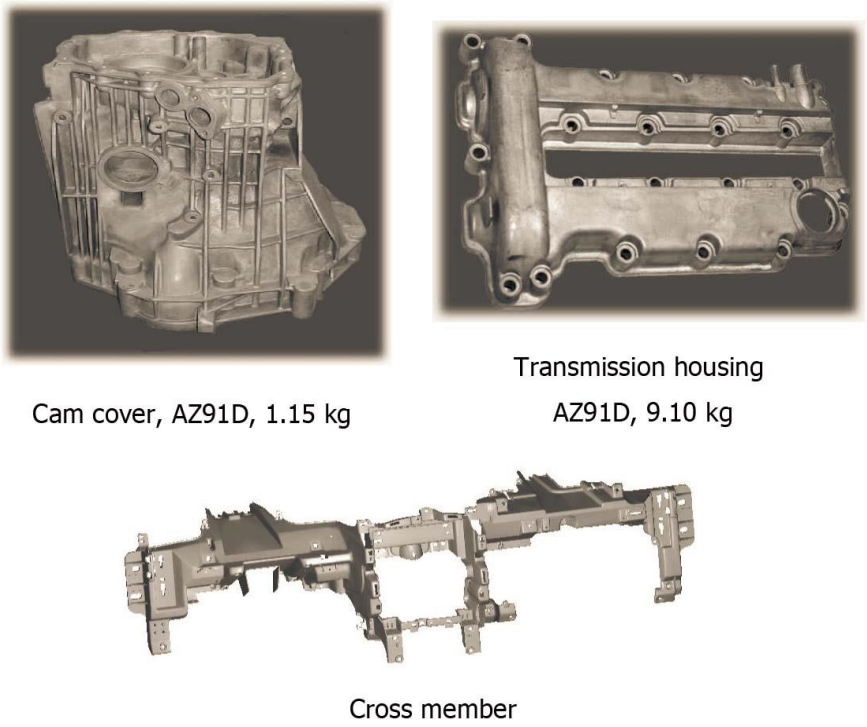

Figure 2.1 Some automotive components made of Mg alloys [6].

Figure 2.2 shows some Mg applications in the aerospace industry [7]. By reducing the total vehicle weight, Mg parts lead to improved fuel economy and significantly lower emissions, in addition to the increased recyclability. There are other applications for Mg parts ranging from power tools, sporting goods, computer and electronic products.

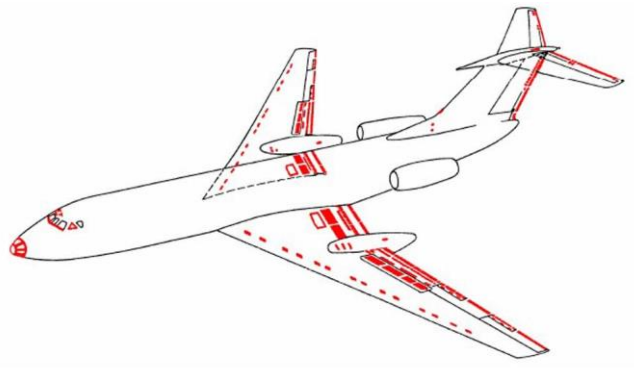

Location of magnesium components (in red) in TU-134

Magnesium (AM50) die-cast helicopter components (IAI, Israel)

Back panel of aircraft door pretreated by Gardobond® X4729 and painted (AZ31B, Israel)

Figure 2.2 Some Mg applications in the aerospace industry [7].

2.2 The deformation of Mg

The crystal structure of Mg is hexagonal close packed (h.c.p), with lattice parameters a = 3.2092 Å and c = 5.2105 Å at room temperature. The c/a ratio of the unit cell is 1.623, which is very close to the ideal ratio 1.633. Figure 2.3 illustrates the lattice structure, slip systems and twins in h.c.p alloys. There are some especially important planes and directions. (0001) is the basal plane.

$\{1\bar{1}00\}$ are known as the prism planes of type I; the $\{1\bar{2}10\}$ planes are prism planes of type II. $\{10\bar{1}1\}$ and $\{11\bar{2}2\}$ are the 1st and 2nd order pyramidal planes respectively. The independent slip systems of Mg are displayed in Table 2.3. Von Mises [8] proposed that at least five independent slip systems are required to enable a crystal to undergo a general homogeneous strain. Taylor [9] then suggested that the actual five systems that became active were those requiring the least amount of work. At room temperature, only basal ⟨a⟩ slip is easily activated during deformation, which indicates that the ductility of Mg at lower temperature is poor. When the temperature increases, non-basal slip systems will be activated, e.g. prismatic ⟨a⟩ slip and pyramidal ⟨c+a⟩ slip. Noted that the slip plane for pyramidal ⟨c+a⟩ slip direction is the 2nd order pyramidal plane $\{11\bar{2}2\}$.

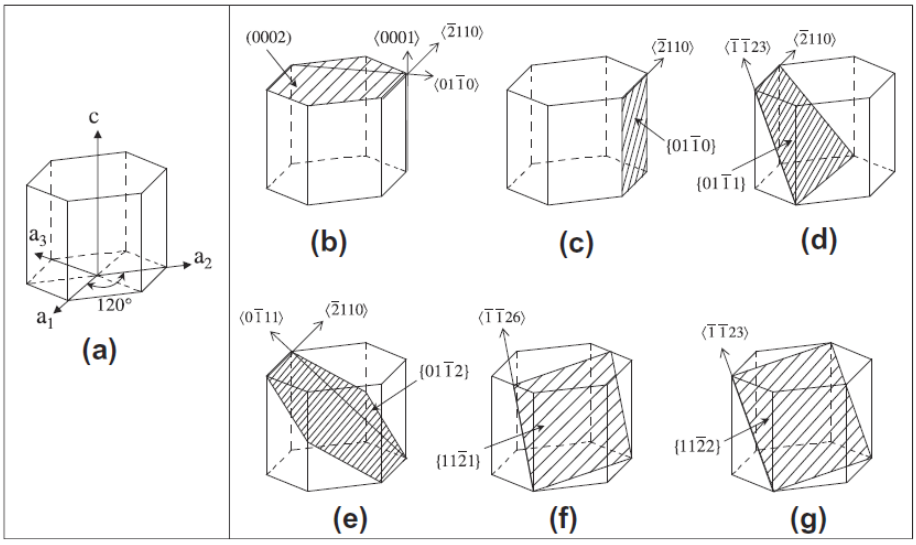

Figure 2.3 (a) h.c.p. lattice and axes; (b) planes and directions for deformation by basal ⟨a⟩ slip; (c) prism ⟨a⟩ slip; (d) pyramidal ⟨c+a⟩ slip; (e and f) tension twin; (g) compression twin [10].

Another deformation mode, twinning, is also illustrated in Figure 2.3(e-g). Because the threshold stress for twinning is lower than that for ⟨c+a⟩ slip, the former is usually activated to

accommodate c-axis stress below 200℃ [11]. Two types of twins are frequently reported in Mg alloys when the loading direction is along the c-axis: $\{10\bar{1}2\}\langle 10\bar{1}1\rangle$ tension twin (tensile along the c-axis) and $\{10\bar{1}1\}\langle 10\bar{1}2\rangle$ compression twin (compression along the c-axis) [12]. In addition, secondary twinning can form after primary twins, which is known as double twinning.

Table 2.1 Slip systems of Mg alloys [10].

Slip system	Burgers vector type	Slip direction	Slip plane	No. of slip system	
				Total	Independent
1	a	$\langle 11\bar{2}0\rangle$	Basal plane (0001)	3	2
2	a	$\langle 11\bar{2}0\rangle$	1st order prism plane $\{10\bar{1}0\}$	3	2
3	a	$\langle 11\bar{2}0\rangle$	1st order pyramidal plane $\{10\bar{1}1\}$	6	4
4	c+a	$\langle 11\bar{2}3\rangle$	2nd order pyramidal plane $\{11\bar{2}2\}$	3	2
5	c	$\langle 0001\rangle$	1st order prism plane $\{10\bar{1}0\}$	3	2
6	c	$\langle 0001\rangle$	2nd order prism plane $\{11\bar{2}0\}$	3	2

2.3 Strengthening mechanisms in Mg alloys

2.3.1 Grain refinement strengthening

The grain refinement strengthening is based on the fact that grain boundaries act as barriers to dislocation movement. It is commonly expressed via the Hall-Petch relationship. The yield strength $\boldsymbol{\sigma_y}$ has an inverse square root relation with grain size d:

$$\sigma_y = \sigma_0 + kd^{-1/2} \qquad \text{Equation 2.1}$$

where σ_0 is the intrinsic yield strength of the alloy. So, the finer the grain, the higher the yield strength. Grain refinement also improves the toughness.

For Mg alloys, the grain size can be reduced by the following methods. 1) Superheating [13]. The melt is held above the melting temperature for a short time before cooling it back to pouring temperature. 2) Introduction of additives. For example, the Elfinal process, which consists of adding anhydrous ferric chloride ($FeCl_3$) into the molten alloy at about 750 ℃ [14]. Carbon inoculation [15], which involves introduction of carbon (includes but not limited to graphite, paraffin wax, lampblack and some organic compounds) into molten alloy. Other additives include AlN, MgO, TiB2, and TiC. 3) Agitation method. This involves the stirring the molten alloy vigorously before casting and is relatively successful when conducted at relatively high temperature. 4) Addition of solute elements. Zr, Al, Sr, Ca et al. can effectively reduce the grain size, especially Zr, which shows a great grain refinement effect on Al free Mg alloys [15], [13]. 5) Increasing the cooling rate during solidification. Rapid solidification like melt-spinning [16] and gas-atomization [5] provide a novel method for obtaining ultrafine Mg grains. 6) Plastic deformation, especially severe plastic deformation like ECAP [17], ball milling [18] and friction stir processing [19]. An average grain size of 100–300 nm of Mg-Al-Zn has been obtained by friction stir processing [19].

2.3.2 Solution strengthening

The strengthening effect of solute atoms in metallic alloys was reported by Fleischer [20] and Labusch [21], and the relation between yield strength σ_y and the concentration of the solute atoms $\boldsymbol{c}$ can be determined by the following equation:

$$\sigma_y = \sigma_{yo} + kc^n \qquad \text{Equation 2.2}$$

where σ_{yo} is the yield strength of pure Mg, *n* is 1/2 or 2/3, and *k* is a constant which indicates the strengthening rate of the solute atoms. Y and Gd in pure Mg were studied by Gao et al. [22], and the results suggests better strengthening by Y and Gd than Zn and Y. The strengthening rates of Y, Gd, Zn and Al atoms in Mg are summarised in Table 2.2 together with the misfits of the solute atoms in Mg. Fleischer [20] suggested that the degree of solid solution strengthening could be correlated with an interaction parameter (ε) defined as a combined effect of atomic size (δ) and shear modulus (η).

Table 2.2 Solid solution strengthening parameters for Y, Gd, Zn and Al atoms in Mg [22].

Solute	misfits			Strengthening rate, k	
	δ	η	ε	n=1/2	n=2/3
Y	+11%	0.404	1.81	737	1249
Gd	+11%	0.247	1.78	683	1168
Zn	-17%	0.867	2.85	578	905
Al	-14%	0.419	2.28	118	196

2.3.3 Precipitation hardening

Most cast and wrought Mg alloys are age-hardenable. Normally Mg alloys are heated to a relatively high temperature to obtain an α-Mg single phase region, which is called solution treatment. Then a supersaturated solid solution (SSSS) is achieved during water quenching and eventually subsequent aging is used to obtain a controlled decomposition of the supersaturated solid solution into a fine distribution of precipitates in the Mg matrix. A series of metastable and equilibrium precipitate phases is formed during the aging process. Table 2.3 lists the precipitation sequences in some typical Mg alloy systems [23]. In age-hardenable Mg alloys, precipitates play

an important role in hindering dislocations or propagating twins. So the crystal structure, morphology, volume fraction of precipitates and orientation relationships between precipitates and the Mg matrix make a decisive contribution to mechanical strength. For example, precipitates which form on the prismatic planes of the Mg matrix like β (Mg_5Gd) in Mg-Gd-Y alloys are more effective barriers to dislocations and twins than particles which form on basal planes like β ($Mg_{17}Al_{12}$) in Mg-Al alloys.

Table 2.3 Precipitation sequences in some Mg alloy systems [23].

Alloys	Precipitation sequences					
Mg-Al	SSSS →	β ($Mg_{17}Al_{12}$) bcc ($I\bar{4}3m$, a=10.6 Å); $(0001)_\alpha$ plate/lath				
Mg-Zn(-Al)	SSSS →	G.P. zones →	i-phase → icosahedral or approximant diamond	Φ and/or T Φ: orthorhombic, Pbcn a = 9.0 Å b = 17.0 Å c = 19.7 Å $(0001)_\alpha$ lath	T: bcc, a = 14.0 Å	
Mg-Gd(-Y)	SSSS →	ordered G.P. zones → zig-zag shape d=3.7 Å *	β″ (Mg_3Gd) → hcp a = 6.4 Å c = 5.2 Å hexagonal prism	β′ (Mg_7Gd) → orthorhombic, a = 6.5 Å b = 22.7 Å c = 5.2 Å lenticular shape	β_1 (Mg_3Gd) → fcc, a = 7.3 Å $\{10\bar{1}0\}_\alpha$ plate	β (Mg_5Gd) fcc, a = 22.3 Å $\{10\bar{1}0\}_\alpha$ plate
Mg-Y-Zn	SSSS →	I_2 stacking fault → $(0001)_\alpha$ plate	γ′ (MgYZn) → hcp, $P\bar{3}m1$ a = 3.2 Å c = 7.8 Å $(0001)_\alpha$ plate	γ′ ($Mg_{12}YZn$) → ordered hcp, 14H a = 11.1 Å c = 36.5 Å $(0001)_\alpha$ plate		

*d is separation distance of columns of RE atoms, SSSS represents supersaturated solid solution.

For shear-resistant particles in Mg alloys, the increment of critical resolved shear stress (CRSS) $\Delta\tau_p$, which produced by the need for basal slip dislocations to bypass the particles, is described by the following equation [24].

$$\Delta\tau_p = \frac{Gb}{2\pi\lambda\sqrt{1-\nu}} ln \frac{d_p}{r_0}$$ Equation 2.3

where G is the shear modulus of Mg matrix, b is the magnitude of the Burgers vector of the gliding dislocations in Mg, ν is Poisson's ratio, λ is the effective planar interparticle spacing which varies with the shape and orientation of the particles, d_p is the mean planar diameter of the particles, and r_0 is the core radius of the dislocations.

For shearable particles in Mg alloy, the contribution from the shearable particles to the CRSS can be described by the following equation [24].

$$\Delta\tau_p = \frac{2}{L_p b\sqrt{\Gamma}} \cdot \left(\frac{F}{2}\right)^{3/2}$$ Equation 2.4

Where Γ is the dislocation line tension in the Mg matrix, force F is a measure of the resistance of the particle to dislocation shearing and L_p is the mean planar centre-to-centre distance between particles.

2.3.4 Work hardening

Strain hardening, which represents the change in the flow stress with strain, depends on the dislocation structure formed via plastic deformation. Dislocation storage will lead to an increase in the flow stress and dislocation annihilation will lead to a decrease in the flow stress. It is widely accepted that the internal stress τ_i can be expressed by the following equation [25].

$$\tau_i = \alpha_1 Gb{\rho_t}^{1/2}$$ Equation 2.5

where ρ_t is the total dislocation density, G is the shear modulus, b is the magnitude of the Burgers vector and α_1 is a constant.

For Mg single crystals, the hardening effect is strongly dependent on the crystal orientation [26]. The work hardening is highest when the basal plane is oriented either parallel or perpendicular to the tensile axis. For polycrystalline Mg alloys, the main interaction causing hardening is the intersections of gliding basal dislocations with forest dislocations.

2.4 Mg alloy development and rare earth (RE) additions

2.4.1 Alloy development

Like for most other metals, pure Mg is rarely used for engineering applications. Alloying is applied to improve virtually all the properties of Mg for both cast and wrought products. Thus an alloy designation has been developed by the American Society for Testing and Materials to describe the alloying elements and the corresponding contents. The method typically consists of two letters followed by two numbers (In some occasion, three letters followed by three numbers are also used). The two letters represent the two most principal alloying elements and the numbers represent the weight percentage of these alloy elements rounded to the nearest whole number. The letter abbreviations for most commonly used alloying elements are listed below: A – Aluminium; C – Copper; E – Rare earth element; H – Thorium; J – Strontium; K – Zirconium; L – Lithium; M – Manganese; Q – Silver; S – Silicon; V – Gadolinium; W – Yttrium; X – Calcium; Z – Zinc. After years of research, plenty of Mg alloy systems have been developed. They can be classified into three categories depending on the increasing demand for specific properties like specific strength, ductility and creep resistance in the automotive industry, as shown in Figure 2.4 [27].

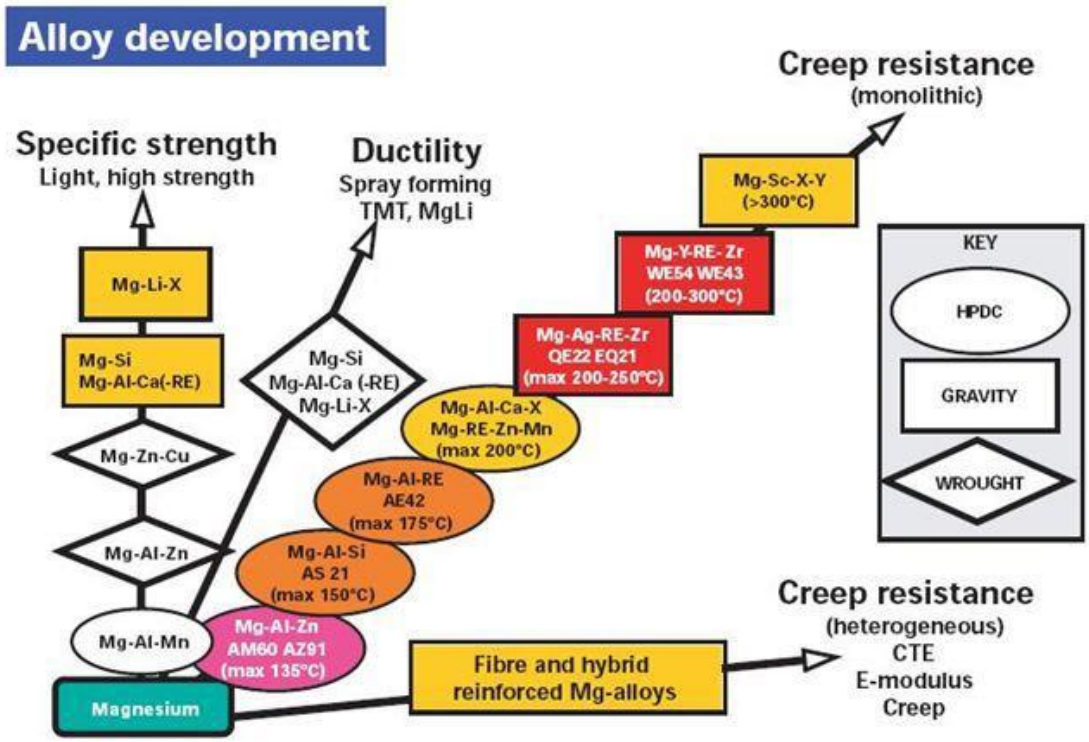

Figure 2.4 Directions of alloy development to improve the performance of Mg components [27].

Mg-Al-Zn alloys including AZ91 are the most popular Mg alloys. AZ91 has reasonable mechanical properties and exhibits excellent castability at room temperature, along with Mg-Zn-Cu and Mg-Li-X. However, at temperatures above 130 ℃, its mechanical properties deteriorate significantly. In order to improve the creep resistance, Mg-Al-Ca, Mg-Al-RE, Mg-Y-RE-Zr alloys have been developed for application above 150 ℃. Some typical tensile properties of Mg alloys at room temperature are listed in Table 2.4. Compared to AZ91, Mg alloys with rare earth (RE) additions, e.g. WZ75 and VWZ1062, exhibit better yield strength and elongation.

Table 2.4 Typical tensile properties of Mg alloys at room temperature

Alloy	Composition, wt. %	Testing condition	Tensile properties		
			UTS, MPa	YS, MPa	ε, %
AZ91	Mg-8.7Al-0.7Zn-0.1Mn	As-cast, T6	200	120	2
ZC63	Mg-6Zn-2.7Cu-0.3Mn	As-cast, T6	210	125	4
WE54	Mg-5.2Y-3RE-0.7Zr	As-cast, T6	280	205	4
WZ75 [28]	Mg-6.7Y-4.9Zn	Extrusion	425	390	5
VWZ1062 [29]	Mg-10Gd-5.7Y-1.6Zn-0.7Zr	Extrusion	461	419	4
ZW153 [30]	Mg-14.6Zn-3.3Y	Chill-cast, extrusion	416	386	16

2.4.2 RE elements

Rare earth elements are very effective in improving the creep resistance, strength, ductility and toughness and in refining the grain size of Mg-based alloys [31]. Rare earth elements can be divided into two groups: light rare earths (La, Ce, Nd, Pr, Pm, Sm, Eu), and heavy rare earths (Gd, Tb, Dy, Ho, Er, Tm, Yb, Lu, Y). The rare earths are common transition metals with similar constitutions for their outer electronic shells. Each of them has two electrons in the outermost *s* shell and some elements have one electron in the second outer *d* shell. This fact causes the similarity of the chemical properties of the rare earths via the proximity of the energy levels of the 4f and 5d shells in atoms. Eu and Yb are divalent (the 4f shell is half-filled or completely filled) and others are trivalent. The anomalous behaviour of Eu and Yb is connected with their ability to show a valence of two, as compared with a valence of three for other rare earth metals.

In general, the atomic radius decreases with increasing atomic number of the RE elements. Because the 4f electrons are so well embedded within the core orbitals the valence electrons are those in the $5d^16s^2$ states. In salts these electrons are readily transferred to other ions, while in metals they form a conduction band. Hence in most practical circumstances the rare earth ions are

tri-positive, in which case all the electrons are in closed shells, and therefore inactive, except for the 4f electrons. Greater charge density is predicted at larger radius. As the nuclear charge Z increases throughout the rare earth series the potential seen by the 4f electrons deepens and their orbitals show a systematic contraction in radius. The 'Lanthanide Contraction' is the result of poor shielding by the 4f electrons. The shielding is the phenomenon whereby the inner-shell electrons shield the outer-shell electrons so that they are not affected by the nuclear charge. So when the shielding is not as good, the positively charged nucleus has a greater attraction for the electrons, thus decreasing the atomic radius as the atomic number increases.

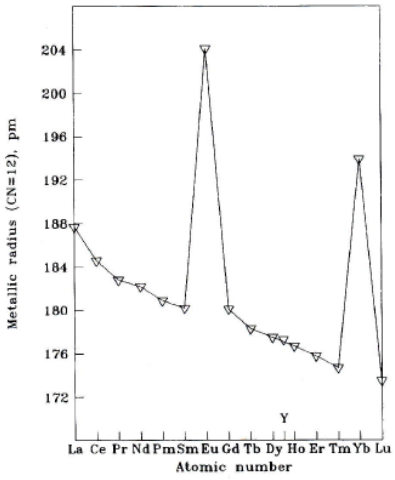

Figure 2.5 The metallic radius (coordination 12) of the lanthanides plotted against their atomic number [31].

Unlike other elements which lose three electrons to form a hybridized s-d contraction band in the pure metals, Eu and Yb are divalent in the metallic state. Consequently their ionic diameters are greater than those of their neighbours in the series. The size of the rare earth atoms controls, to a great extent, the ability of rare earths to form solid solutions and compounds with other elements.

The electronegativities of the lanthanum series, except for Eu and Yb, but also for Y are very close to each other and are within the limits 1.17-1.22. These values are also close to the electronegativity of Mg of 1.2 calculated in the same way [32].

2.4.3 RE additions and Mg-Zn-RE alloys

2.4.3.1 Effect of RE additions on the mechanical properties of Mg

The RE additions change effectively the mechanical properties of the Mg alloys. Firstly, the solid solution hardening caused by RE addition contributes to the improvement of the strength. The solid solubility increases gradually from the light to heavy rare earth elements. This may be related to the progressive decrease of the rare earth metallic radius, which becomes nearer to that of Mg. The solubility of heavy rare earths is relatively high, so it can result in solid solution hardening.

Solid solution strengthening by Gd and Y are much larger than that of Zn and Al. In addition to the size and/or modulus misfits between solute and solvent atoms, the valency effect is suggested to be possibly responsible [22]. It was suggested that the bond energy between Mg and Y is much stronger than that between Mg and Al.

Secondly, the precipitation hardening introduced by RE addition also contributes to the strength improvement. The solubility drops intensely as the temperature drops (Figure 2.6). This enables remarkable precipitation hardening during the decomposition of the supersaturated solid solution. During the aging process, intermetallics with high melting point and thermal stability form and improve the strength.

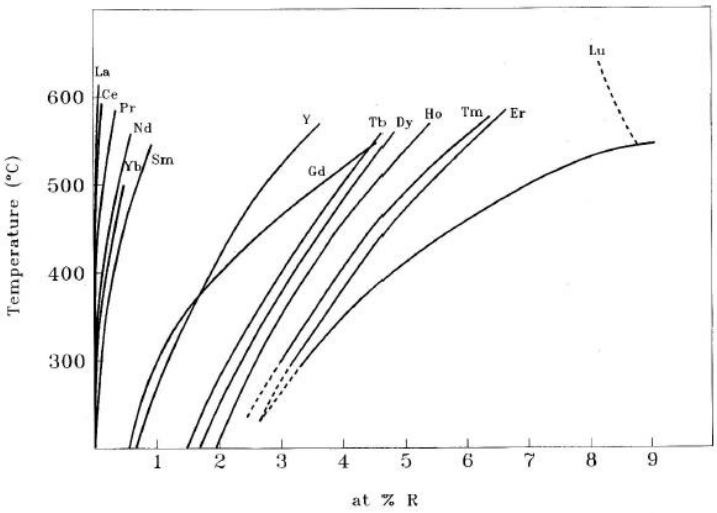

Figure 2.6 Trends of solid solubility limits versus temperature of several rare earths in Mg [31].

With RE additions, an important alloy system has been developed: Mg-Zn-RE alloys. This alloy system has been heavily studied due to the presence of peculiar secondary phases, e.g. icosahedral quasicrystalline phase (i-phase) and long period stacking ordered (LPSO) phase, which result in excellent mechanical performance at room and elevated temperatures. The LPSO phase has a long period ordered stacking sequence in the c direction of Mg and segregated Zn and Y was found in certain stacking layers [3], [4], [33]. The structure of the LPSO is presented in Section 2.5.1.

2.4.3.2 Mg-Zn-RE alloys

Mg-Zn-Y ternary phase diagram system was studied by [34] [35] [36]. A calculated isothermal section of the Mg-Zn-Y ternary phase diagram at 500 ℃ is shown in Figure 2.7 [36]. An LPSO phase (including 18R and 14H) has been found in the Mg-rich corner. The ternary phases and some binary phases are listed in Table 2.5.

Table 2.5 Phases in Mg-Zn-Y ternary system.

Phase name	Structure	Lattice parameter	reference
LPSO (18R, 14H)*			
I-phase (Mg_3Zn_6Y)	Quasicrystalline icosahedral $Fm\bar{3}\bar{5}$	a_R=5.19 Å	[34]
W ($Mg_3Zn_3Y_2$)	Cubic $Fm\bar{3}m$	a=6.83 Å	[34]
H (Zn_3MgY)	hP36 $P6_3/mmc$	a=9.08 Å, c=9.415 Å	[37]
$Mg_{24}Y_5$	bcc	a=11.26 Å	[38]
$MgZn_2$	$P6_3/mmm$	a=5.253 Å, c=8.568 Å	[39]

* The structure of LPSO phase is present in Section 2.5.1

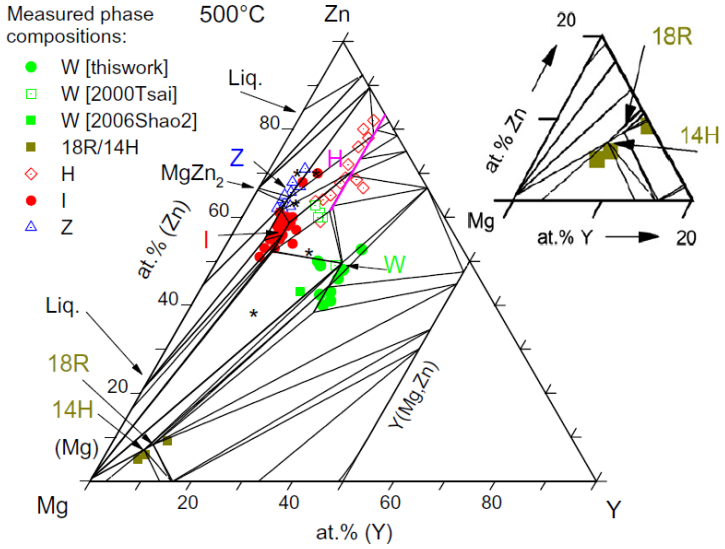

Figure 2.7 Calculated isothermal section at 500 ℃ including all measured compositions of ternary Mg-Zn-Y phases. Inset shows enlarged Mg-rich part including 18R and 14H type LPSO.

Studies [1-3] have shown that the Zn to Y ratio plays a key role in the secondary phase stability of Mg-Zn-Y ternary alloys. With increasing Zn/Y ratio, the following precipitates form in a sequence, viz. $Mg_{24}Y_5$ → LPSO → W→ I-phase [1-4]. In general, the trend is consistent with the calculated results in Figure 2.7. However, it is very difficult to determine the boundary values of the Zn/Y ratio for formation of secondary phases in as-cast conditions. Wang et al. [40] reported

that W phase and LPSO phase co-exist when the Zn/Y ratio is 1.23, but the LPSO phase disappears when the ratio is greater than 1.9. Lee et al. [1] reported that i-phase and W phase are the secondary phases when the Zn/Y ratio is between 1.8 and 6 in Mg-Zn-Y alloys. When two or more secondary phases co-exist, the distributions of the alloying elements are very important because they will affect the types and the area fractions of the secondary phases. As shown in Figure 2.7, the chemical compositions of the secondary phases obtained from the experimental results have a large range of compositions. A systematic study of the Zn and Y distributions in the secondary phases and Mg matrix has not been carried out in as-cast Mg-Zn-Y alloys, and how the alloying elements will affect the secondary phases is unclear. As the secondary phases determine the strengths observed [5, 41, 42], it is very important to investigate the effect of the Zn/Y ratio on the formation of the secondary phases.

Although the RE elements are quite similar, they have different roles in forming LPSO phase. For example, LPSO forms in as-cast $Mg_{97}Zn_1Y_2$, but not in as-cast $Mg_{97}Zn_1Gd_2$ [2]. Based on the formation of LPSO, Mg-Zn-RE alloys are divided into two categories [2]: I. Mg-Zn-RE alloys including Y, Dy, Ho, Er and Tm elements, normally develop 18R type LPSO phase during solidification. The 18R type LPSO can transform into 14H type after heat treatment; II. In Mg-Zn-Gd and Mg-Zn-Tb, 14H type LPSO phases normally precipitate from supersaturated solid solution or transforms from other secondary phases during annealing at high temperatures. No LPSO phase is observed in as-cast ingots.

Kawamura et al. [2] proposed general criteria for RE which forms LPSO phase in Mg-Zn-RE systems (include type I and type II alloys). The RE elements must have negative mixing enthalpy for the pairs Mg-RE and Zn-RE, exhibit hcp structure at room temperature, have large solubility

limits (above approximately 3.75 at%) in Mg and have larger atomic size than Mg by 8.4 to 11.9% [2]. However, why the various RE performs differently in forming LPSO phase is still unknown. And what will happen if type I and type II RE elements, e.g. Y and Gd, are both present in an Mg-Zn-RE alloy? As Y and Gd are the most common RE elements used in the Mg alloys, it is of great interest to investigate the effect of Gd addition in the Mg-Zn-Y alloys with different Zn/Y ratios.

2.5 Mg-Zn-Y alloys with long-period stacking ordered (LPSO) phase

In 2001, a $Mg_{97}Zn_1Y_2$ at.% alloy was first reported by Kawamura et al. [5]. It soon became a focus of interest due to its excellent tensile yield strength of 610 MPa and ductility of 5%. Besides the nano-sized grains obtained by rapid solidification and powder metallurgy process, the finely dispersed LPSO phase is considered to supply important strengthening to the novel mechanical properties of $Mg_{97}Zn_1Y_2$. Due to the limited knowledge concerning the LPSO phase, much research has been carried out on this particular phase during the past 15 years, including its structure, formation mechanism, deformation mechanisms, strengthening mechanism, thermal stability et al. Figure 2.8 shows that the LPSO-type Mg-Zn-Y alloy (the Mg-Zn-Y alloy containing LPSO phase) has specific yield strength competitive with the commercial Mg and commercial Al alloys.

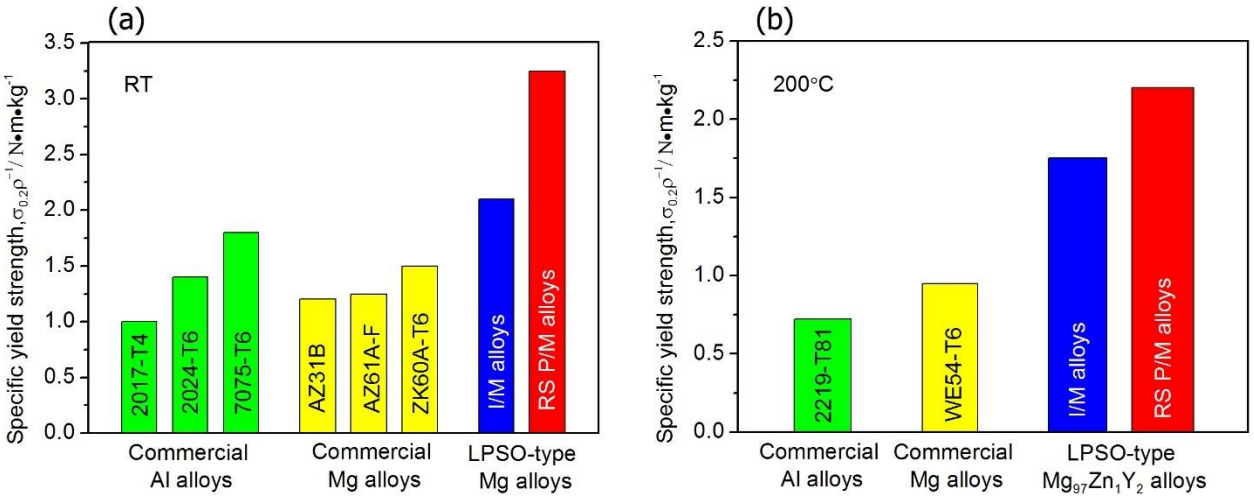

Figure 2.8 Specific yield strengths of LPSO-type Mg-Zn-Y alloys in comparison to commercial Al and Mg alloys at room temperature and 200 ℃ [43].

The typical morphology of the LPSO phase is illustrated in Figure 2.9 and Figure 2.10. At low magnification, the LPSO normally forms honeycomb-like network in as-cast $Mg_{97}Zn_1Y_2$ alloy. At higher magnification, the grains show a straight interface with the Mg matrix. The TEM image also shows that the LPSO lamellae share the same basal plane with Mg matrix.

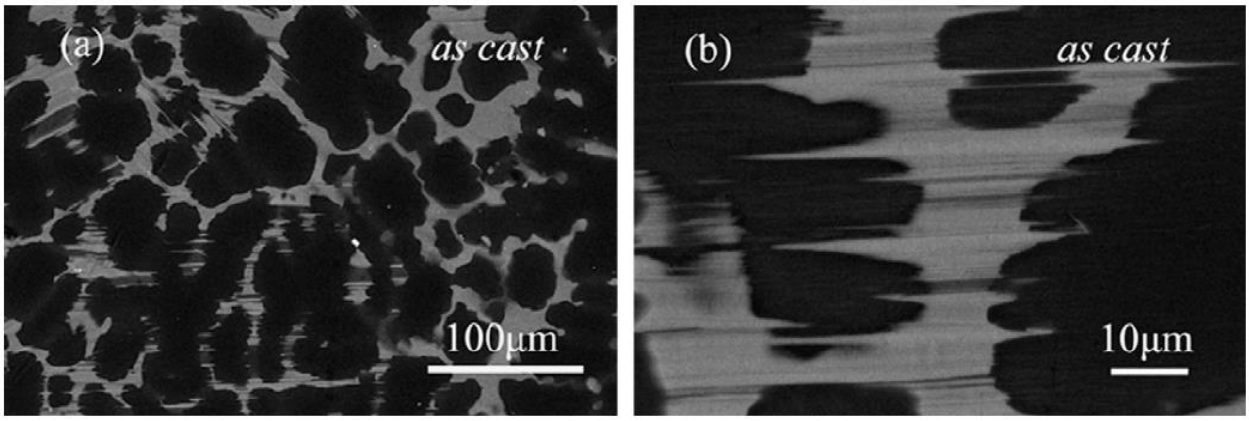

Figure 2.9 Typical morphology of LPSO phase in $Mg_{97}Zn_1Y_2$ alloy [44].

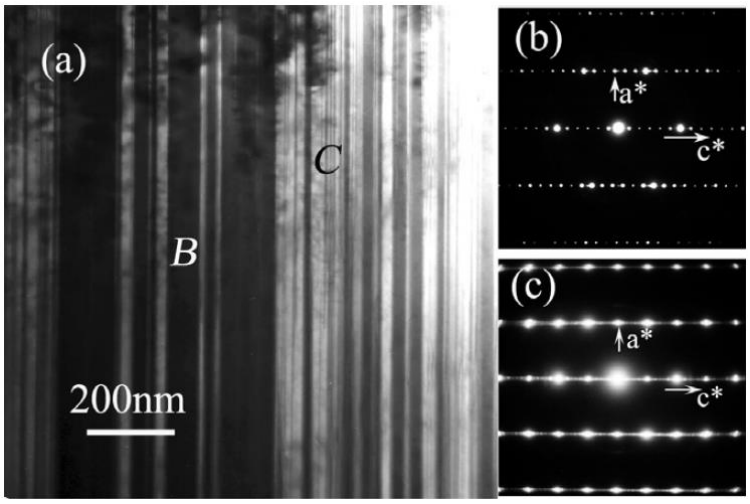

Figure 2.10 (a) TEM image of the LPSO phase in the $Mg_{97}Zn_1Y_2$ cast alloy; (b) and (c) selected area diffraction patterns obtained along $[11\bar{2}0]$ direction for the areas marked B and C.

It is clear that the morphology of the LPSO phase is different from that of typical small and densely distributed precipitates. Typical precipitate hardening employs the precipitates as obstacles for dislocation movement and results in strengthening. LPSO phase has weak effect in stopping basal <a> slip because they share the same basal plane. However, LPSO phase is anisotropic, it can inhibit deformation in the c direction, and actually deforms via kinking. It is generally believed that the LPSO strengthening is actually by effective grain refinement as lots of kink boundaries are introduced.

2.5.1 The cell structure of LPSO phase

LPSO phase exhibits a range of long-period stacking ordered structures and it exists widely in the Mg-TM (transition metal)-RE alloys. The long period stacking ordered phase is not unique to Mg alloys, it has also been observed in Ni-Mn-Ga [45], Al-Cu-Ni [46], Fe-Mn-Al-C [47], Ti-Al [48] Cu-Pd [49] and many other alloys. To date, various types of LPSO phases have been reported in Mg-TM-RE alloys: e.g. 18R, 14H, 10H, 24R, 15R, 12H, and 21R, which are formed by stacking

structural blocks composed of 6, 7, 5, 8, 5, 6, and 7 close packed atomic layers [50] [51]. The structure of the LPSO phase is commonly regarded as periodic stacking faults in 2H Mg with the enrichment of the TM and RE elements in two or four consecutive layers [3] [4] [33]. Figure 2.11 shows the stacking sequence of LPSO polytype structures in Mg-Zn-Y alloys. 18R and 14H are the most common types of LPSO phase in Mg-Zn-Y alloys. The stacking sequence of the close packed planes of 18R is ABABABCACACABCBCBC, while stacking sequence of 14H is ABABCACACACBAB [4] [50] [52].

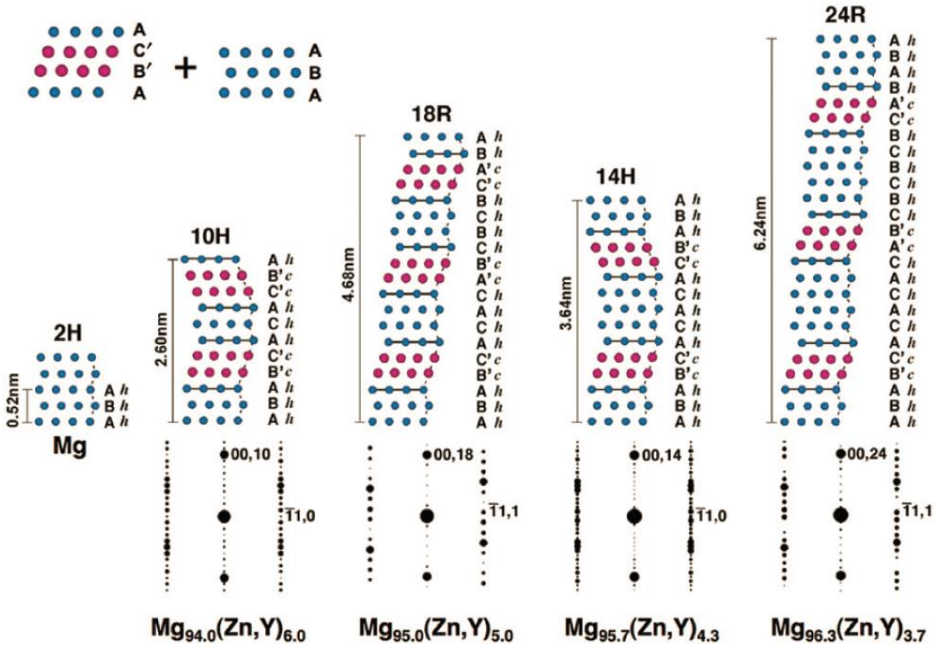

Figure 2.11 Structural models of some Mg-Zn-Y LPSO polytype structures. Blue and red circles represent the Mg and Zn/Y sites, respectively [50].

Whether 18R or 14H depends on the Zn/Y concentration and arrangement [53]. Early studies [4] showed that Zn/Y atoms are enriched in two consecutive layers (see red atoms in Figure 2.11). 18R is ordered base-centred monoclinic structure (a = 11.12 Å, b= 19.26 Å, c = 46.89 Å, β =

85.25°; space group C2/m) with chemical composition of $Mg_{10}Zn_1Y_1$. 14H is hexagonal (a= 11.1 Å and c = 36.5 Å) with a chemical composition of $Mg_{12}Zn_1Y_1$.

However, LPSO does not have stoichiometrical compositions. Egusa and Abe [53] summarised the measured chemical compositions of LPSO which had been reported elsewhere (Figure 2.12). The values change but appeared to have a fixed Zn/Y ratio of around 3/4. When the alloy contains less Zn and Y, the LPSO also contains less Zn and Y.

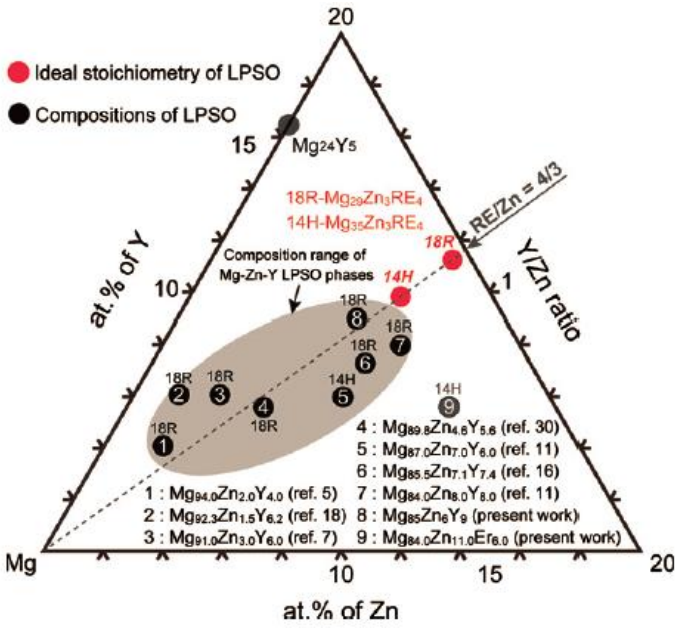

Figure 2.12 Schematic quasi-isothermal section of the Mg-Zn-Y ternary phase diagram. The experimentally measured compositions of LPSO in Mg-Zn-Y alloys and the ideal stoichiometric compositions of LPSO are plotted [53].

Egusa and Abe [53] proposed that Zn_6Y_8 clusters exist. This was later confirmed by Kishida et al. [33] using atomic resolution STEM, as shown in Figure 2.13a. A schematic drawing of a Zn_6Y_8 cluster appears in Figure 2.13b [54]. Kishida et al. [33] used ultra-high resolution Cs-corrected

STEM to analyse the clusters and the results indicate the central sites of the clusters are occupied partially by Zn, Y and Mg (Figure 2.13c). Based on the existence of Zn_6Y_8 clusters (without the central site atom), Egusa [53] and Kishida [33] both concluded the ideal stoichiometries of 18R-LPSO and 14H-LPSO in Mg-Zn-Y alloys are $Mg_{29}Zn_3Y_4$ and $Mg_{35}Zn_3Y_4$ respectively.

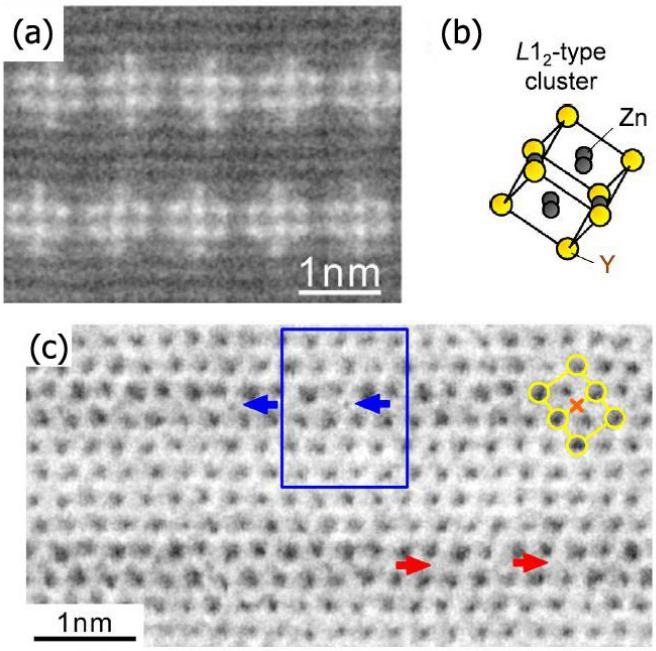

Figure 2.13 (a) HAADF-STEM image of 18R LPSO in $Mg_{76.7}Zn_{10}Y_{13.3}$ heat-treated at 500°C for 72 h [33]; (b) schematic illustration of a Zn_6Y_8 cluster [54]; (c) ultra-high resolution Cs-corrected STEM image of 18R Mg-Zn-Y LPSO phase. Blue and red arrows indicate the central site with and without the appearance of dark spots [33].

2.5.2 Formation, growth and transformation of LPSO phase

The formation mechanism of LPSO phase has been studied. Horiuchi et al. [55] reported that LPSO phase in the Mg-Y-Zn ternary system is not formed via a eutectic reaction but via a peritectic reaction during the solidification. Abe et al. [3] suggested that in a $Mg_{97}Zn_1Y_2$ alloy

prepared by rapid solidification and extrusion, the LPSO phase is formed by precipitation during warm extrusion. The transformation process involves introducing stacking faults into hcp-Mg and supplying the solute Zn and Y atoms to the faulted layers. The formation of LPSO by enrichment of solute atoms at stacking faults in the solid solution is also suggested by Yosuke et al. [56] through energetic assessments by first principles calculations. Pan et al. [57] also used first-principles calculations to calculate the stacking fault energy (SFE) of Mg-Zn-Y-Zr alloy, which shows that the addition of Y can sharply decrease the SFE while Zn slightly increases the SFE of the alloy. Iikubo et al. [58] suggested that the dominant factors in the formation of LPSO phase include spinodal decomposition and a structural transformation from 2H to other structures with periodic stacking faults; this was predicted using first-principles calculations combined with the cluster variation method. Okuda et al. [59] suggested the LPSO forms through a novel hierarchical phase transformation during the heating of an amorphous sample; in this transformation, clustering occurs first and then the nano-clusters rearrange with the introduction of stacking faults, which eventually results in a two dimensional nanoscopic ordering of segregated layers. Although different opinions exist, LPSO structures including the stacking faults, solute elements of Zn and Y, and the Zn_6Y_8 cluster, are considered to be central to LPSO formation.

Zhu et al. [60] investigated the further growth of 18R and 14H type LPSO in solid Mg matrix and found that it proceeded through generation and propagation of growth ledges. In order to propagate ABCA stacking, the formation of a growth ledge requires a Shockley partial dislocation with Burgers vector of $a/3\langle\bar{1}010\rangle$ to generate lateral glide and the diffusion of Y and Zn atoms into the B and C layers. The 18R type LPSO can transform to 14H after an appropriate

heat treatment, e.g. Itoi et al. [61] reported a transformation was observed in Mg-Zn-Y alloy after heating at 500 ℃ for 5h. Gr**ö**bner et al. [36] provided a calculated vertical section through the Mg-Zn-Y phase diagram (Figure 2.14) showing that the transformation from 18R to 14H occurred at 537 ℃, which was partially confirmed by DSC measurements.

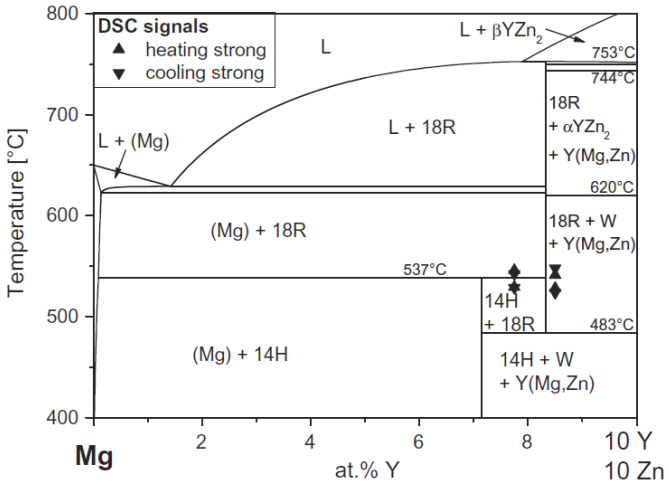

Figure 2.14 Calculated vertical section from Mg-rich corner to $Mg_{80}Y_{10}Zn_{10}$ through the phases 14H and 18R, including DSC measurements [36].

A possible structural transformation mechanism of LPSO from 18R to 14H is described by Zhu et al. [60] and it involves the formation of stacking faults in 18R and cooperative gliding of Shockley dislocations. Figure 2.15 shows the proposed transformation model, the gliding of two Shockley partials on two neighbouring planes can shift an 18R building block upwards by one atomic layer and change the stacking sequence from ABCA to ACBA. The transformation rate is controlled by the diffusion of Zn and Y into the segregated layer. The work carried out by

Kiguchi et al. [62] agrees with the above transformation model, but added that an irregular stacking sequence as a part of 24R acts as a catalyst for the transformation.

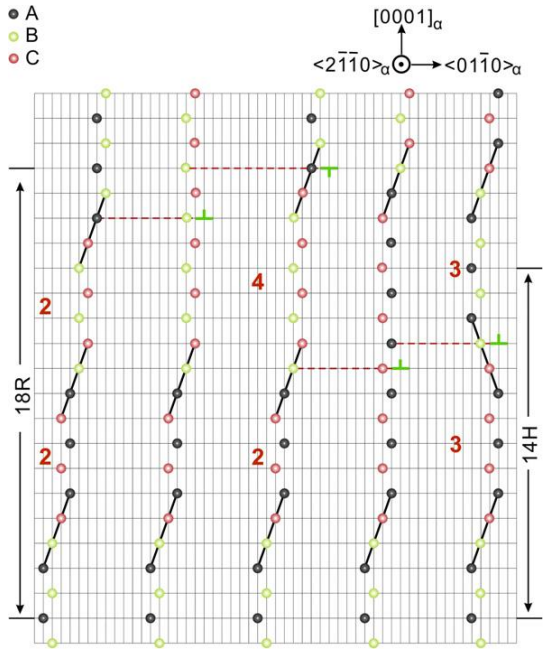

Figure 2.15 A proposed model by Zhu et al [60] showing the transformation from perfect 18R to 14H. A pair of Shockley partial dislocations shift the top ABCA block of 18R upwards two layers and another pair of Shockley partials shift the middle ABCA block of 18R upwards one layer and shear in the opposite direction forming 14H.

2.5.3 The deformation of LPSO phase and the α-Mg matrix

2.5.3.1 Slip and twinning in LPSO

Deformation of the LPSO phase is anisotropic. The c/a ratios of 14H and 18R type LPSO are about 11.4 and 14.6, which favours basal slip. Many studies confirm that $(0001)\langle 11\bar{2}0\rangle$ basal slip is the dominant operative slip system in LPSO phase at room and elevated temperature [63] [64]. The Zn and Y segregation has a weak influence on the plastic deformation of the basal slip.

The critical resolved shear stress (CRSS) for basal slip in the 18R LPSO phase is about 7 MPa, which is measured by micro-pillar compression using a single crystal [64]. Hagihara et al. [63] estimated the CRSS of basal slip for 18R type LPSO to be about 10-30 MPa using the compression of directionally solidified polycrystalline LPSO. By comparison, the CRSS of basal slip for a Mg-1.0Y single crystal is about 9.5 MPa [65].

Non-basal slip, e.g. prismatic and pyramidal slip of LPSO phase has not been observed at room temperature. This is due to the large c/a ratio and Zn and Y segregation inhibit non-basal slip. At high temperature, non-basal slip traces have been observed [63]. <a> type dislocations on prismatic planes are confirmed to exist in both 14H and 18R type LPSO during hot extrusion at 400 ℃ [66]. However, compared to basal slip, non-basal slip is less common and only occurs at high temperature.

In hcp alloys, twinning frequently occurs as an alternative deformation mode when independent slip systems are limited. However, there is no evidence for twinning in bulk LPSO phase. Only in thin LPSO phase in a Mg matrix does twinning occasionally exist [67].

So, in the LPSO phase, the dominant basal slip provides two independent slip systems only and deformation along the c direction cannot be accommodated. Instead, kinking of LPSO is frequently observed. Figure 2.16a shows band-like features on a polished surface through LPSO phase during compression [64]. Figure 2.16b shows the typical zigzag morphology of a kink band in the LPSO phase [68].

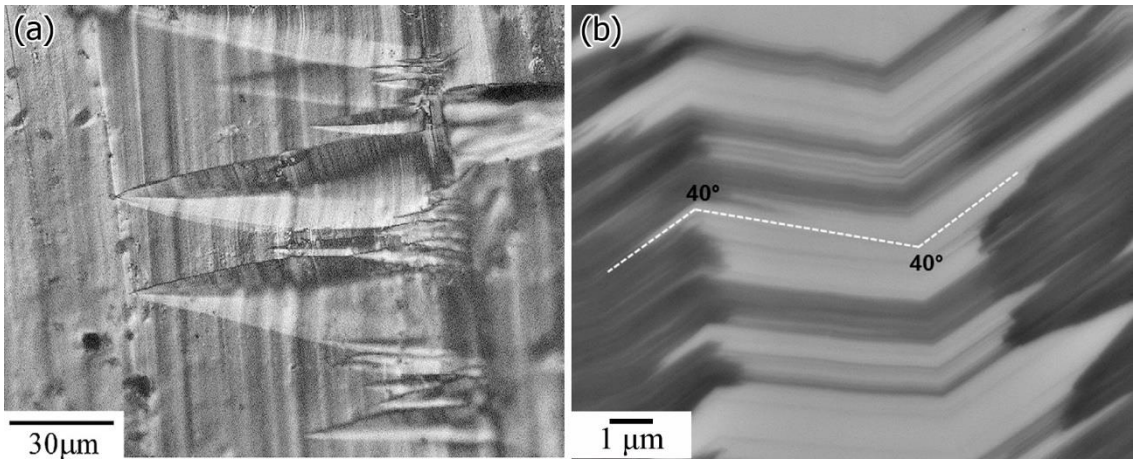

Figure 2.16 (a) Band-like kinking of LPSO observed on a polished surface after compression at room temperature of $Mg_{88}Zn_5Y_7$ alloy [64]; (b) typical zig-zag morphology of kink band in LPSO phase in $Mg_{97}Zn_1Y_2$ after re-polishing of the sample [68].

2.5.3.2 Introduction to kinking

Kinking was first reported by Orowan in a Cd alloy as shown in Figure 2.17a [69]. When Cd cylindrical wire is axially compressed along the c direction, it suddenly collapsed by forming peculiar kinks with sharp ridges and a regular curvature. Figure 2.17b shows the structure of the kink where the k and k' are the mirror plane of the glide planes before and after deformation. However, unlike twinning, the lattice in the kink is not a mirror image of the undeformed lattice. A comparison of glide, twinning and kinking is shown in Table 2.6.

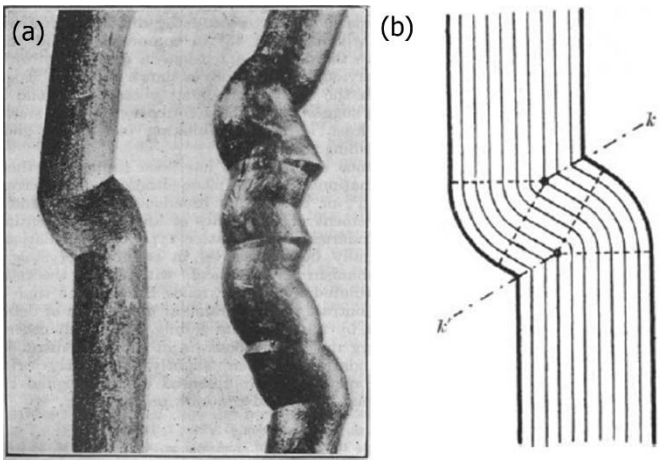

Figure 2.17 (a) Kinks in originally cylindrical cadmium single crystal wires; (b) structure of the kinks [69], thin parallel lines represent glide planes, dashed lines represent the wedge-shaped region of the flexural glide and dash-dotted lines represent the planes of kinking.

Table 2.6 Comparison of glide, twinning and kinking.

	Glide	**Twinning**	**Kinking**
Atomic movement	Atoms move a whole number of atomic spacings on a single plane.	Planes of atoms move by a fractional atomic spacing. Distributed over entire volume.	The amount of atom movement is flexible, depending on the stress condition
Microscopic appearance	Thin lines	Wide bands or broad lines	Wide bands, sharp ridges or regular curvatures
Lattice orientation	No change in lattice orientation. The steps are only visible on the surface of the crystal and can be removed by polishing. Have specific slip planes	Lattice orientation changes. Surface polishing will not destroy the evidence of twinning. Certain crystallographic planes. Deformed lattice is mirror image of undeformed lattice.	Lattice orientation changes. Surface polishing will not destroy the evidence of kinking. No crystallographic planes. Deformed lattice is not a mirror image of the undeformed lattice.
schematic drawing of the deformation mode	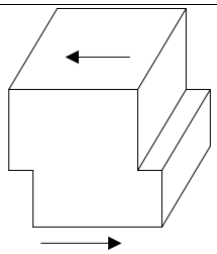	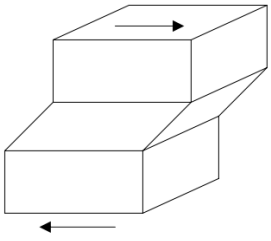	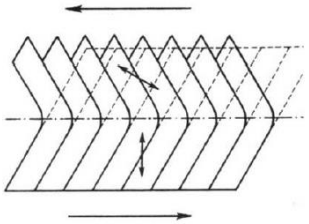

Kinking has been found in many anisotropic materials, such as mica, graphite, polymers, wood and metals like Zn (c/a=1.856) [70] [71] [72] [73]. The mechanism of kinking was extensively studied soon after kinking was reported. It is generally considered that the kink band is composed of dislocation pairs on many parallel planes, spaced regularly a small number of atomic distances apart [74] [72]. Hess and Barrett [72] proposed a dislocation model for the formation of kinks, as shown in Figure 2.18. Hagihara et al. [63] also used this model to explain the formation of kinks in LPSO phase. When the loading direction is parallel to the basal plane such that the Schmid factor for the basal slip is negligible, elastic buckling of the planes occurs and the crystal become unstable. Then basal dislocation pairs of opposite signs generate and move in opposite directions. They will be stopped by some agency and form permanent boundaries to the kink bands, as shown in Figure 2.18a. When further stress is applied, the rotation of the plane increases and the Schmid factor of the basal plane increases which causes more dislocations to generate within the band. As successive pairs are generated, the bend angle at the groove will increase (Figure 2.18B and C).

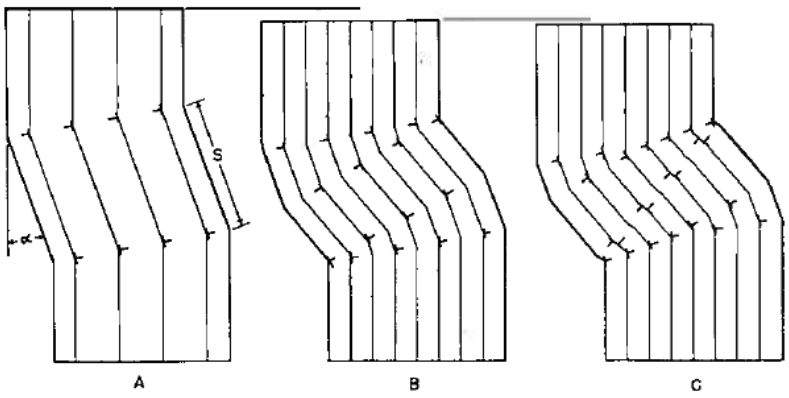

Figure 2.18 Formation of a kink by dislocations [72].

2.5.3.3 Kinking in LPSO phase

Based on the Hess and Barrett model, the dislocations generated in the kink bands should be <a> type dislocations when the loading stress is parallel to (0001) plane. This type of kink boundary has been directly observed in extruded $Mg_{97}Zn_1Y_2$ alloy where basal edge dislocations with Burgers vector $b = 1/3\langle 11\bar{2}0\rangle_{LPSO}$ are found in the kink boundary. As a result, the basal plane rotates around the $[1\bar{1}00]$ zone axis [44]. The rotation axis is normally used to describe the kink type.

The kink bands in LPSO exhibit different crystal orientation relationships with respect to the matrix, e.g. not a fixed rotation axis and with different rotational angles [75]. If 18R LPSO is described as trigonal rhombohedral, $\langle 1\bar{1}00\rangle/\langle 0\bar{1}10\rangle$ ($solely\ \langle 1\bar{1}00\rangle$ in the case of the hexagonal structure), $\langle 0001\rangle$ and $\langle 1\bar{2}10\rangle$ type rotation axes have all been confirmed by EBSD (Figure 2.19 [76]). Yamasaki et al. [76] suggested that the rotation axes are composed of geometrically necessary dislocations (GND). The $\langle 1\bar{1}00\rangle/\langle 0\bar{1}10\rangle$ rotation type kink band is composed of basal <a> slip. The $\langle 0001\rangle$ rotation type kink band is composed of prismatic <a> dislocations. The $\langle 1\bar{2}10\rangle$ type rotation type kink band is more likely produced through a combination of $\langle 1\bar{1}00\rangle$ and $\langle 0\bar{1}10\rangle$ rotational kinks.

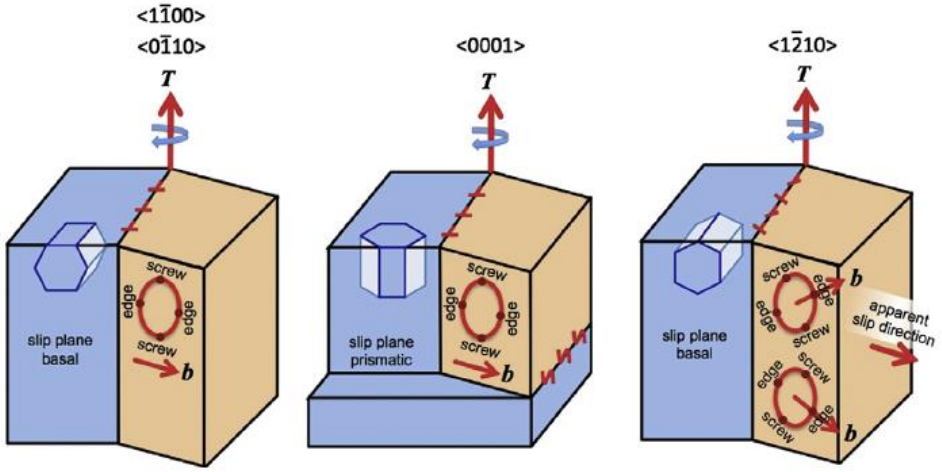

Figure 2.19 Crystallographic nature of the kink bands possessing (a) $\langle 1\bar{1}00\rangle/\langle 0\bar{1}10\rangle$, (b) $\langle 0001\rangle$ and (c) $\langle 1\bar{2}10\rangle$ rotation axes in extruded $Mg_{89}Zn_4Y_7$ [76].

However, the dislocation configurations of different rotation type kinks are based on EBSD results. No direct dislocation analysis is in the literature. In order to understand the origin of the kink deformation, TEM analysis of the dislocations in the kink bands is required. So Chapter 4 of this thesis investigates the dislocations in the kink boundaries of the LPSO phase in a $Mg_{94}Zn_2Y_4$ alloy after compression.

2.5.3.4 The strengthening mechanism of LPSO phase in Mg-Zn-Y alloys

The strengthening mechanism of LPSO phase has always been the focus of attention due to its impressive magnitude. Shao et al. [44] investigated a $Mg_{97}Zn_1Y_2$ alloy after hot compression. The microstructure revealed that the hard LPSO phase as well as a coherent interface between the LPSO phase and the Mg matrix contribute to the ability to resist fracture. Deformation kinking

during compression introduced lots of kink boundaries which are believed to be beneficial to the strength and ductility. Hagihara et al. [77] also studied the effect of LPSO phase on the mechanical properties of extruded $Mg_{97}Zn_1Y_2$. He pointed out the LPSO phase strongly accelerated the refinement of Mg recrystallized grains due to a stress concentration frequently occurs at the vicinity of the LPSO and Mg interface. Meanwhile, the LPSO phase aligned along the (0001) plane strengthened the extruded alloy via the short-fibre reinforcement mechanism.

Matsuda et al. [67] studied the interaction between LPSO phase and deformation twins in rapidly solidified $Mg_{97}Zn_1Y_2$. The twins traverse straightforwardly the region with a low density of LPSO phase, but are deflected in the region with a high density of LPSO phase. This indicates that a high density of LPSO phase with can resist twinning.

2.5.3.5 Kink deformation of the Mg matrix

Previous studies [44] [68] have shown that Mg matrix in the interior of the LPSO phase also deforms via similar manner to the kinking of the surrounding LPSO. Shao et al. [44] suggested the thin Mg deformed via ½[0001] prismatic dislocations when the surrounding LPSO has kinked. However, previous studies hardly observe <c> type dislocations in the Mg matrix.

For example, Matsuda et al. [78] investigated the dislocation structure in rapid solidified $Mg_{97}Zn_1Y_2$ ribbon with LPSO phase. In grains with LPSO phase, ⟨c+a⟩ dislocations are observed instead of ⟨a⟩ dislocations. In grains without LPSO phase, many ⟨a⟩ dislocations are observed, therefore the critical resolved shear stress (CRSS) for basal slip is increased by the formation of LPSO phase. Kim et al. [68] suggest that the α-Mg matrix deforms by basal <a> slip and

pyramidal <c+a> slip and the elastic modulus mismatch between the Mg matrix and the LPSO phase promotes the activation of non-basal slips.

As kinking is an important deformation mode in the Mg/LPSO structure (thin LPSO with alternate Mg thin slices) in Mg-Zn-Y, the origin of the kinks in the Mg needs to be clarified.

2.6 Thermomechanical processing of Mg-Zn-Y alloys

Conventional as-cast Mg alloys often have large-scale dendritic microstructures, which are detrimental to their mechanical properties. As shown in Figure 2.20, as-cast $Mg_{97}Zn_1Y_2$ alloys have a low yield strength of about 100 MPa. Although the best mechanical properties are obtained after rapid solidification and power metallurgy (RS/PM), the RS/PM route is very expensive and complex. Thermomechanical processing is often used to refine the grain sizes of the as-cast alloys, distribute the secondary phases and finally improve the strength. Conventional processing like hot extrusion [42], hot rolling [79] and hot forging [80] have been applied to Mg-Zn-Y alloys, and the mechanical properties of Mg-Zn-Y alloys are somewhat improved (Figure 2.20). However, it is very difficult to obtain ultra-fine grain size by conventional thermomechanical techniques.

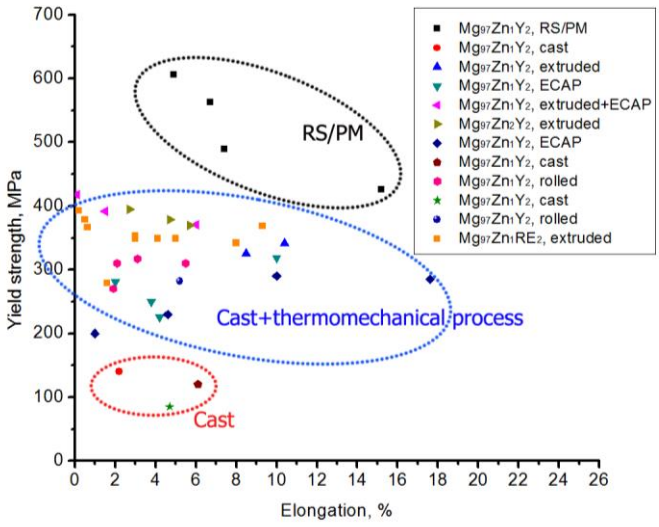

Figure 2.20 Yield strength and elongation data of Mg-Zn-Y alloys containing LPSO phase taken from the literature [5] [81] [82] [83] [84] [85] [2]. Extruded $Mg_{97}Zn_1RE_2$ alloys are also included.

2.6.1 Equal channel angular pressing (ECAP)

ECAP is a type of severe plastic deformation which involves very high strains through simple shear without introducing significant changes in the shape of specimen. Figure 2.21a shows the principle of ECAP [86]. The die contains two intersecting channels which are equal in cross-section. The specimen is machined to fit these channels and well-lubricated before pressing through them. The material passing through the channel suffers a simple shear, as shown in Figure 2.21b. The shear is imposed at the shear plane between two adjacent elements labelled 1 and 2. The total strain ε_N imposed by the ECAP process can be expressed by the equation [86]:

$$\varepsilon_N = \frac{N}{\sqrt{3}}\left[2\cot\left(\frac{\Phi}{2}+\frac{\Psi}{2}\right)+\Phi cosec\left(\frac{\Phi}{2}+\frac{\Psi}{2}\right)\right] \qquad \text{Equation 2.6}$$

where N is the total number of passes through the die. Φ and Ψ are the channel angle and the outer arc angle of the ECAP die, as shown in Figure 2.21c. The resultant microstructure after ECAP depends on the angle between the two channels and the rotation of the samples between successive passes.

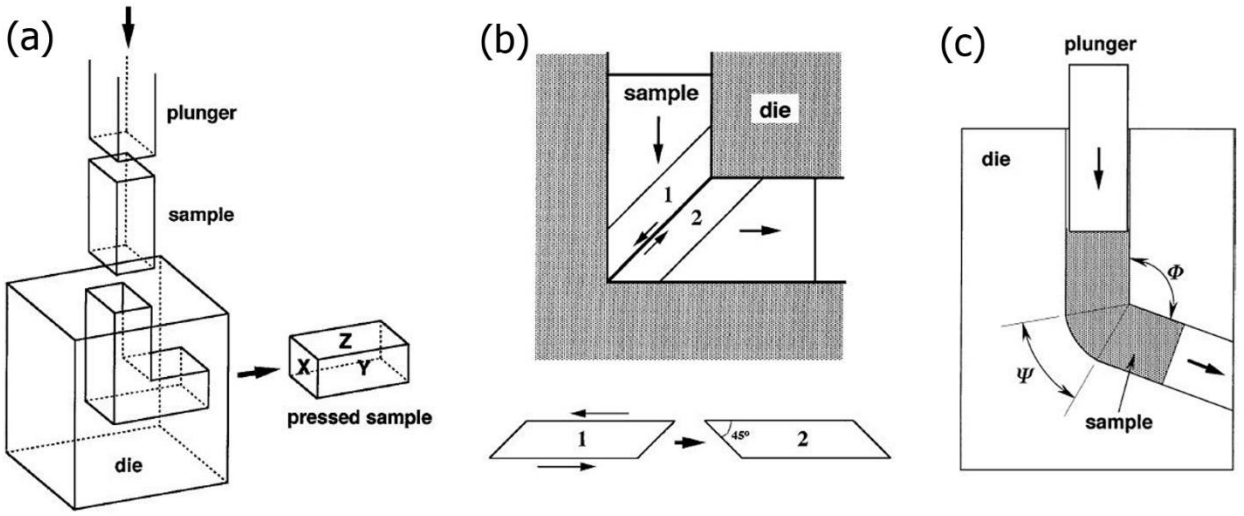

Figure 2.21 (a) Schematic drawing of a typical ECAP process; (b) Schematic drawing showing the simple shear between elements 1 and 2 at the bend of the die; (c) Schematic drawing showing the channel angle Φ and the outer arc angle Ψ of the ECAP die [86].

ECAP is especially attractive for grain refinement. It has been successfully employed in various Mg alloys and nano-sized grains or ultra-refined grains have been obtained [87] [88] [89]. For example, Reberto et al. [88] reported a ECAP processed ZK60 alloy with a grain size of about 0.8 μm and an optimum ductility of about 1310%. However, compared to conventional thermomechanical processes, limited studies of the ECAP process have been carried out on Mg-Zn-Y alloys[81] [83]. So, in order to improve further the strength of the Mg-Zn-Y alloy, ECAP will be used to process the Mg-Zn-Y alloys.

2.6.2 Deformed microstructure of Mg-Zn-Y alloys: bimodal grain size distribution

Thermo-mechanical processing of Mg-Zn-Y alloys often results in a bimodal microstructure, containing coarse grains (including deformed Mg grains and bulk LPSO phases) and fine dynamically recrystallised (DRXed) Mg grains [90] [81] [91]. Bimodal grain size distributions are especially important for nano-structural materials to maintain both high strength and ductility. For example, Wang et al. [92] reported on a pure copper that contains micro-sized grains embedded in nano-sized (less than 300 nm) grains. The bi-modal structure Cu has comparable strength with only nano-sized grain Cu, but has much higher ductility.

To obtain a bimodal structure, different methods are employed. First, larger grains form by abnormal grain growth, e.g. the annealing of cryo-rolled Cu [92] and annealing of an eletrodeposited nanocrystalline Ni [93]. Second, consolidation of different grain size powders. Witkin et al. [94] mixed different amounts of the cryo-milled powders with unmilled powders and achieved bi-modal grain sizes after extrusion. Third, dynamic recrystallisation (DRX) or static recrystallisation of the deformed alloys. The Mg-Zn-Y alloys formed a bimodal structure during deformation. It is quite clear that the smaller grains are formed by dynamic recrystallisation, but how the DRXed grains form in Mg-Zn-Y alloys and how the LPSO phase affects the bimodal structure are still unclear.

2.6.3 Dynamic recrystallisation (DRX) of Mg alloys

DRX is the elimination of dense dislocation tangles by the nucleation and growth of new, strain-free grains [95] during deformation. It occurs frequently in Mg alloys during deformation.

Dynamic recrystallisation normally takes place in regions in the microstructure with high local misorientations [96]. Nucleation of the dynamic recrystallisation in Mg alloys is commonly observed at the following sites: high angle grain boundaries, twins, shear bands and the deformation zones around large particles.

2.6.3.1 High angle grain boundaries

Recrystallisation at pre-existing high angle grain boundaries commonly results in a necklace microstructure: DRXed small grains are found around the original grain boundaries. Two dominant nucleation mechanisms for DRX are found at the grain boundaries: strain induced boundary migration and rotational recrystallisation.

Strain induced boundary migration happens when a slip band interacts with a grain boundary. The dislocations build up on one side of the boundary which results in a difference in stored energy. The stress caused by the dislocations is relieved by a bulging of the boundary into a neighbouring grain [97]. The region left behind the bulging has a lower dislocation density and the rearrangement of the substructure within the bulge forms a low angle grain boundary and then a recrystallised grains [98]. Because the bulge formation requires high grain boundary mobility, strain induced boundary migration only occurs at high temperature (T>300℃) [99] [100] [101] .

Besides strain induced boundary migration, rotational recrystallisation is often observed in Mg alloys [102]. Ion et al. [102] reported that in a Mg-8%Al alloy the limited operation of the non-basal slip systems leads to a high density of dislocations close to the grain boundary, which results in lattice rotation. As the lattice rotation proceeds, dynamic recovery results in the geometrically necessary dislocations forming well defined subgrains in the old grain boundaries.

With strain increasing continuously, the high locally stored energy drives the subgrain boundaries to migrate and leads to the coalescence of boundaries and the formation of high angle grain boundaries. The rotational recrystallisation only operates at moderate to high temperatures (typically 200-350℃) when non-basal slip and cross slip are active [102] [100] [101] .

2.6.3.2 Twinning and shear bands

In Mg alloys, compression twins and double twins often act as nucleation sites for recrystallisation [103]. The generation of the contraction and double twins provides a soft direction for generating the basal dislocations which will be further hindered by the twin boundary. The building up of the dislocations provides the stored energy for recrystallisation. Twinning-induced dynamic recrystallisation in Mg alloys is typically observed at low deformation temperatures (lower than 200 ℃) where the non-basal slip systems are limited and the twinning is active [100] [101] [102]. In addition, the dynamiclly recrystallised grains are likely to have a texture where the basal plane is parallel to that of the parent twin.

Shear bands are also observed in various Mg alloys [104] [105] [106]. These shear bands contain highly localised strains, which are not surprisingly ideal sites for recrystallisation. The recrystallised grains in the shear bands are likely to have similar orientations to the Mg matrix in the shear band [107] [108].

2.6.3.3 Secondary phases

Secondary phases exist in most structural Mg alloys. These particles have a strong influence on the recrystallisation kinetics, microstructure and texture, and it is possible to control the

distribution of the particles by a combination of alloying and materials processing [96]. The role of the secondary phases in DRX are complex.

Non-deformable large particles (e.g. larger than 1 μm) normally introduce a region with a high density of dislocations and large orientation gradient during deformation. This is caused by the strain difference between the particle and the matrix. So, the vicinity region is a preferential site for DRX. Humphreys et al. [109] described nucleation of recrystallised grains from a deformation zone in an Al alloy. During annealing, recovery forms sub-grain boundaries by eliminating the statistically stored dislocations and arranging the geometrically necessary dislocations. The coarsening of a sub-grain is likely to happen during further annealing and to become a nucleation sites for the recrystallisation. This process is normally referred to particle stimulated nucleation (PSN).

The PSN nuclei are widely considered as randomly oriented due to the high level of misorientations in the deformation zone [99]. So, it is expected to be able to control the Mg texture by controlling the amount of PSN recrystallisation. However, as Griffiths [99] reviewed for Mg alloys, DRX by PSN is not dominant compared to other DRX mechanisms. The significant strain localisation caused by grain boundaries, twins and shear bands is more effective than that of the particles. The DRXed grains by PSN make a relatively small contribution to the overall texture.

2.6.3.4 DRX in Mg-Zn-Y alloys

Yamasaki et al. [90] suggested that the refined grains in the bimodal microstructure of Mg-Zn-Y extruded alloys are caused by rotational recrystallisation. The central region of the grain remains relatively undeformed while grain rotation occurs in the region close to the grain boundaries by

basal slip and kinking. This accelerates dynamic recrystallisation of the regions adjacent to the grain boundaries. The DRXed grains around the LPSO phase are also formed in a similar manner. The close linkage between DRX and the LPSO region has also been reported elsewhere [110]. Tong et al. [110] suggested that the LPSO phase can accelerate DRX through particle-stimulated recrystallisation. These mechanism do not consider the peculiar kink deformation mechanism of the LPSO phase. Due to the presence of large amounts of LPSO phase, it is necessary to clarify the effect of the kinking in the LPSO phase on the DRX of Mg-Zn-Y alloys.

2.6.4 Small punch tests

Yamasaki et al. [90] studied as-extruded $Mg_{97}Zn_1Y_2$ alloys and suggested that the small, randomly orientated DRXed grains increased ductility, while the textured, coarse grains contribute to the strength. Their results [90] were based on uniaxial tensile/compression tests performed in the direction of extrusion. Since the bimodal structure shows distinct differences between the extrusion and transverse directions of the processed sample, it is interesting and important to study the deformation and cracking behaviour when stress is also applied to other directions.

Small punch test (SPT) is a disc bending technique, which was originally designed for testing radiated samples with limited size in the nuclear power industry. It can also be used to analyse the elastic-plastic properties, the ductile fracture toughness J_{IC} and the brittle fracture toughness K_{IC} [111] [112]. SPT involves applying a force with a spherical indenter to a thin round disc with the edge clamped by a fixture, as shown in Figure 2.22. The displacement of the indenter and the force are recorded [113]. As the stress on the disc caused by the spherical indenter along radial

directions is axially symmetrical along radial directions, it provides a good method to compare the mechanical behaviour and fracture of the bimodal structure in all directions.

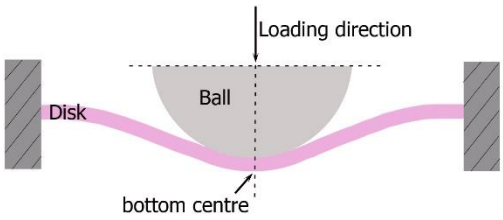

Figure 2.22 *Schematic drawing of the Small Punch Test.*

2.7 Aims and objectives

This project aims to improve and understand the mechanical properties of Mg-Zn-RE alloys by:

- Understanding the deformation behaviour of some advanced Mg alloys, including LPSO containing alloys, and the importance of kink formation.
- Employing ECAP processing and investigating the effect of LPSO on microstructural evolution and the importance of dynamic recrystallisation induced by kinking
- Studying the effect of Gd additions on Mg-Zn-Y alloys

3 Experimental details

3.1 Preparation of as-cast samples

The as-cast Mg-Zn-(Y)-(Gd) alloys were prepared by induction furnace under an argon environment using pure Mg, pure Zn, Mg-30Y wt. % and Mg-30Gd wt. % master alloys. Two induction furnaces which are shown in Figure 3.1, were used.

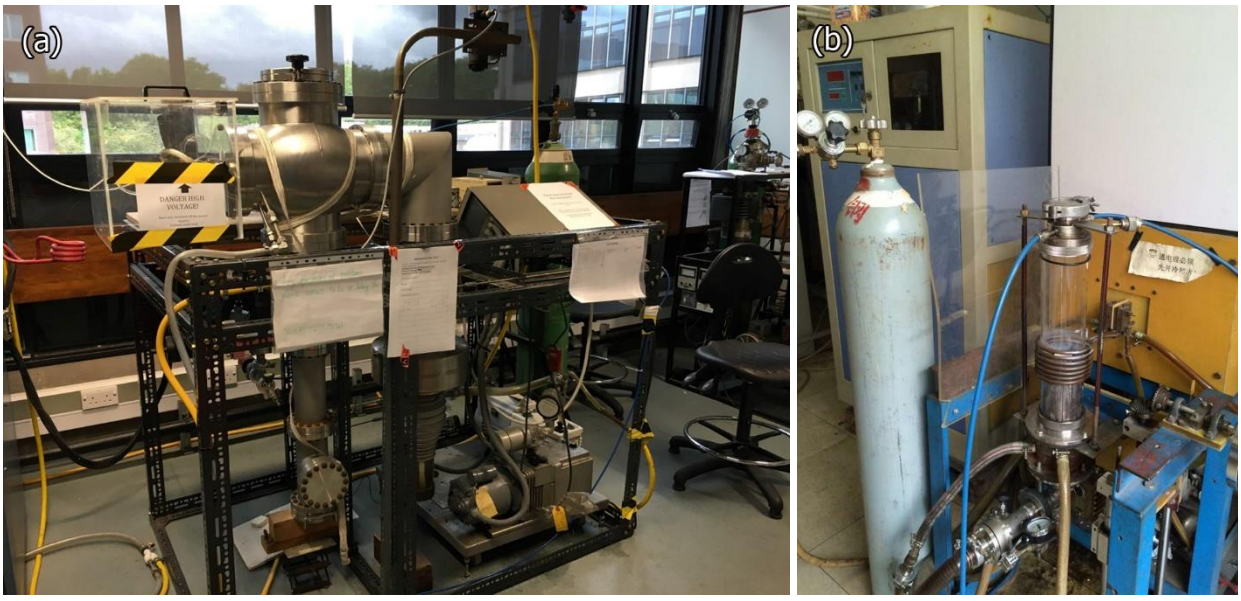

Figure 3.1 (a) Induction furnace 1; (b) Induction furnace 2

The $Mg_{94}Zn_2Y_4$ (Chapter 4 and 5), $Mg_{94}Zn_{4.2}Y_{0.8}Gd_1$ (Alloy 9 in Chapter 6) and $Mg_{94.5}Zn_{4.2}Y_{0.8}Gd_{0.5}$ (Alloy 10 in Chapter 6) were melted and cast in vacuum induction furnace 1. Before the melting, the furnace chamber was pumped down to 4×10^{-1} Torr using a rotary pump and then back filled with Ar gas to 400 Torr. This pumping and re-filling was repeated 3 times. The alloys were then melted in a steel crucible under 400 Torr Ar protection. The melt was held for 10 min and then cast into a 5 mm thick steel mould of 100 mm (length) × 67 mm (width) × 34

mm (height). The mould was located on top of a steel cylinder, also accommodated in the same chamber. The cast alloys were allowed to cool down in the chamber under Ar protection.

The rest of the as-cast alloys were prepared using induction furnace 2. Before melting, the chamber was pumped down to about 6.0 $\times 10^{-2}$ MPa, and then back filled with Ar gas to 1 atmosphere. The pumping and refilling were repeated 4 times. The alloys were melted in a cylinder graphite crucible with dimensions of 50 mm (outside diameter) × 40 mm (inside diameter) × 50 mm (height) using a heating power of about 5 kW. The melt was held for 10 to 15 mins with mechanical stirring. The samples were cooled in the crucible.

The chemical compositions of the as-cast samples may differ using different furnaces. So the compositions of the alloys were then measured by SEM EDS based on 5 measurements at a magnification of ×200.

3.2 Compression of $Mg_{94}Zn_2Y_4$ alloys

The compression sample was cut from an as-cast $Mg_{94}Zn_2Y_4$ ingot using a CUT 20 High Precision Wirecut EDM machine. The sample size was 6 × 6 × 12 mm. The compression tests were performed at room temperature in a Zwick 1484 twin screw driven universal test machine with 200kN load cell and utilising Zwick TestXpert2 software (Figure 3.2). The initial strain rate is about $5\times10^{-4}s^{-1}$. The first sample was tested until failure (about 20% percent) and the others subjected to specific strains of 2%, 5%, 10% and 15%.

Before the compression test, a surface of the sample was polished and marked with 11 spots 1 mm apart in straight line using an automated Struers DuraScan-50 micro-hardness machine with

0.2 kg load. SEM images were taken in the same areas of interest before and after the compression test for direct comparison.

Figure 3.2 Zwick 1484 twin screw driven universal test machine with 200kN load cell.

3.3 ECAP processing of the $Mg_{94}Zn_2Y_4$ alloys

The $Mg_{94}Zn_2Y_4$ specimens of 10 mm (width) × 10 mm (height) × 20 mm (length) were cut from the as-cast ingot using a CUT 20 High Precision Wire cut EDM machine. The specimens were ECAP processed for 1, 2 and 3 passes at 300 °C with back pressure. The channel angle Φ and the outer arc angle Ψ of the ECAP die are 90° and 36°, respectively. The specimens were rotated 90 degrees about the same direction between two consecutive passes. The forward pressure and backward pressure during ECAP were maintained at about 700 MPa and 50 MPa, respectively. After the ECAP processing, the three orthogonal planes x, y and z of the sample are defined as perpendicular to the extrusion direction (ED), the transverse direction (TD) and the longitudinal direction (LD) respectively after ref [114].

Figure 3.3 Macro-scale morphologies of four as-ECAPed samples

3.4 Microstructural characterisation techniques

3.4.1 X-ray diffraction (XRD)

X-ray diffraction (XRD) was performed on the as-cast Mg-Zn-(Y)-(Gd) specimens (Chapter 6) using a Bruker D8 Advanced diffractometer with Cu Kα radiation with a scanning speed of 4°/min and a scanning angle ranging from 5° to 120°. The XRD data was then simulated by Topas software via Rietveld method. The phases used for indexing of the XRD peaks are listed in Table 3.1. Examples of the Topas fitted curves are shown in Figure 3.4. Figure 3.4a indicates that the simulated spectrum (red) fitted well with the original spectrum (blue). Figure 3.4b indicates that small partially overlapped peaks can be identified by the fitted curve. The simulated results provided more accurate indexing of the phases and the positions of the X-ray peaks, which can be used to measure the lattice parameters of the phases.

Table 3.1 Crystallographic information used for indexing the XRD peaks.

	Structure formula	**Structure**	**Space group**	**Lattice parameter**	**Reference**
Mg	Mg	Hexagonal	P63/mmc	a=3.2085Å, c= 5.2106Å	ICSD
W phase	$Mg_{2.88}Y_2Zn_{3.12}$	cubic	$Fm\bar{3}m$	a=6.848 Å	ICSD [115]
18R-LPSO	$Mg_{80.6}Zn_{8.3}RE_{11.1}$	Monoclinic	C/2c	a=11.67 Å, b=13.79 Å, c=31.32 Å, β=93.53°	[33]
14H-LPSO	$Mg_{83.3}Zn_{7.2}RE_{9.5}$	Rhombohedral	$P6_3/mcm$	a=11.1 Å, c=36.2 Å	[53]
i-phase	Mg_3Zn_6Y	Icosahedral quasicrystal			[115]

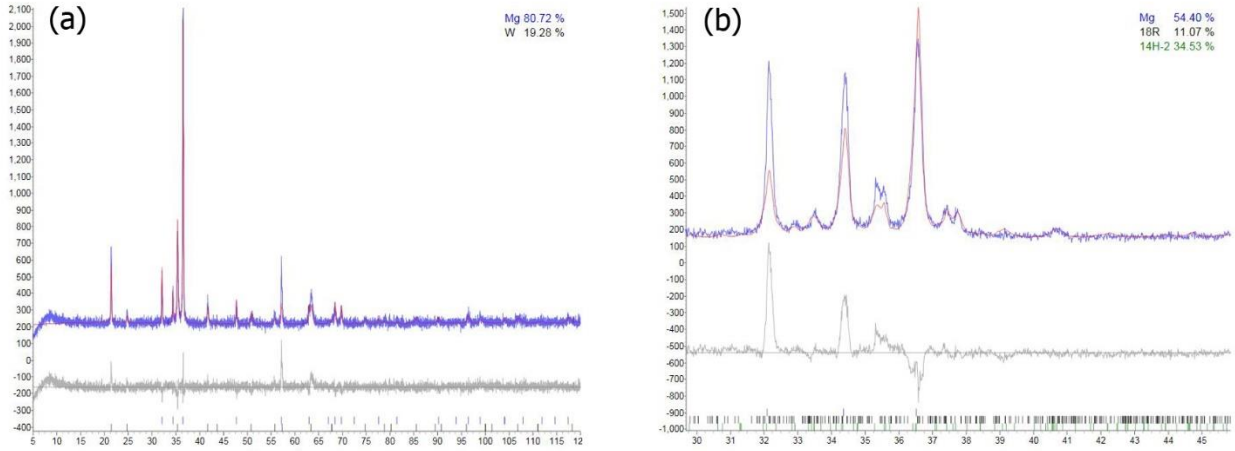

Figure 3.4 Examples of comparison of fitted XRD spectra (red) with original XRD spectra. The grey spectra are the difference between the fitted and original spectrums: (a) XRD spectrum obtained from $Mg_{94}Zn_2Gd_4$ alloy; (b) XRD spectrum obtained from $Mg_{94}Zn_2Y_2Gd_2$ alloy.

3.4.2 Optical microscopy (OM)

OM provides a comprehensive microstructural overview of grain boundaries, phases and twins of the alloys at low magnification (normally <1000x). The as-cast samples and as-ECAPed samples were characterized using a ZEISS Axioskop 2 (Figure 3.5). The samples for OM were gently polished mechanically and etched in a solution containing 4 mL nitric acid and 96 mL ethanol.

Figure 3.5 Optical microscopy: ZEISS Axioskop 2

3.4.3 Scanning Electron Microscopy (SEM)

Two SEMs were used in this project, a Jeol 7000F with Oxford Inca EDS (Figure 3.6a) and a Tescan Mira-3 with Oxford X-Max SDD EDS detector and Nordlys EBSD detector (Figure 3.6b). SEM was used mostly for microstructural characterization and chemical analysis.

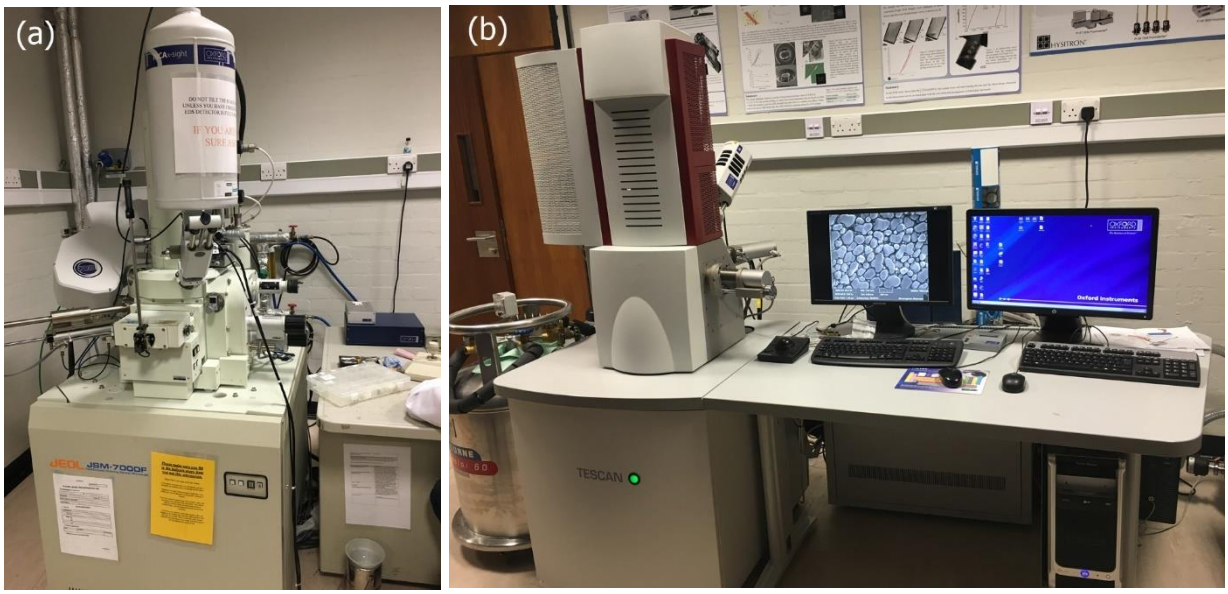

Figure 3.6 (a) JEOL 7000F SEM; (b) Tescan Mira-3 SEM

3.4.4 Transmission Electron Microscopy (TEM) and Scanning TEM (STEM)

TEM was used for high resolution chemical analysis and microstructure characterization of the Mg-Zn-(Y)-(Gd) samples. Dislocation distributions in the ECAP processed samples and compressed samples were also studied by TEM. Two TEMs were used: a JEOL 2100 with Oxford Instruments Si(Li) Detector (Figure 3.7a) and an FEI TALOS with Super-X EDS system (Figure 3.7b).

TEM foils from bulk samples, e.g. as-cast alloys and as-ECAPed samples, were prepared using twin-jet eletropolishing. The 3 mm diameter discs were cut using the EDM machine and mechanically ground from 1mm thickness down to 150 μm. They were then twin-jet polished using a solution containing 8.8 g lithium chloride, 19.3 g Mg perchlorate, 833 mL methanol, and

167 mL butoxyethanol at -30 °C and 70 V, cleaned repeatedly using ethanol and stored in a drying vessel.

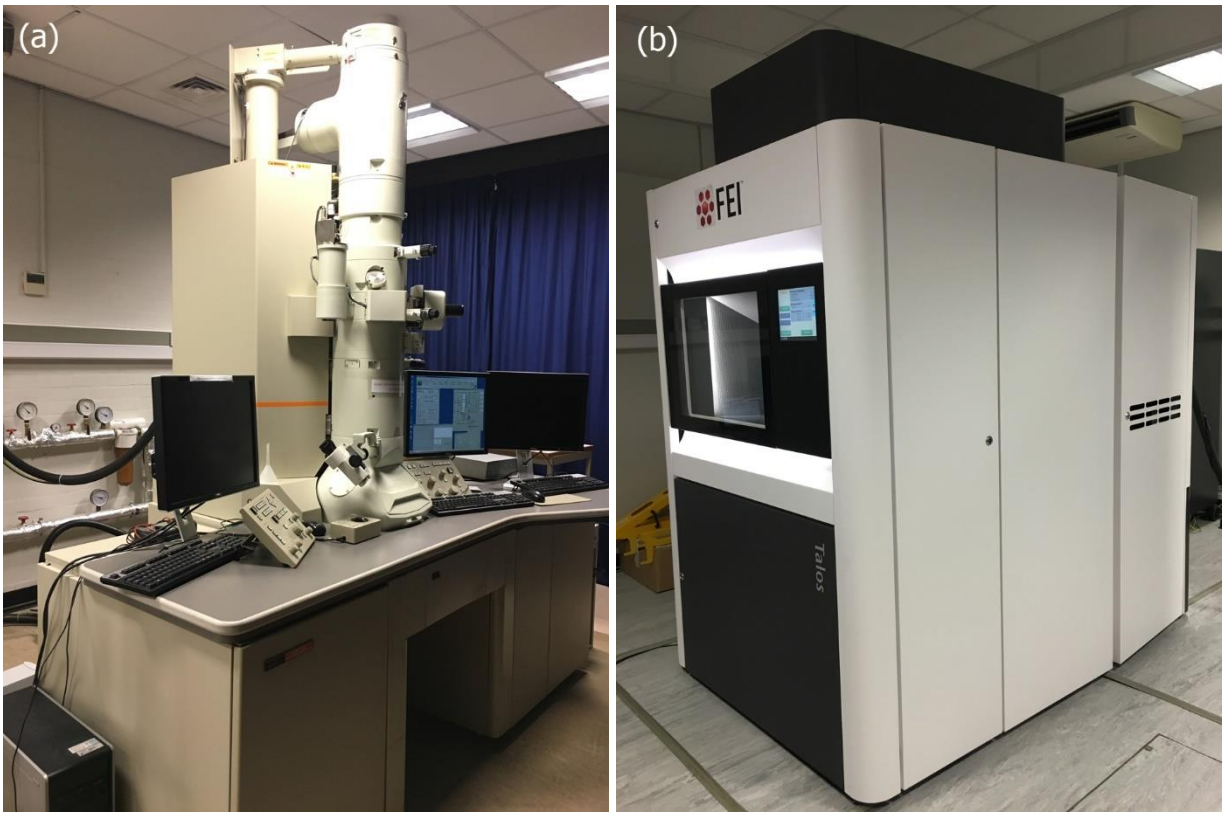

Figure 3.7 (a) Jeol 2100 TEM; (b) FEI Talos TEM

3.4.5 Electron Back-Scattered Diffraction (EBSD) and Transmission Kikuchi Diffraction (TKD)

EBSD is a powerful technique that provides quantitative microstructural information about the crystallographic nature of metals, minerals, semiconductors and ceramics, and it delivers grain sizes, grain boundary characters, grain orientations, textures, and phase identities of the samples. Conventional EBSD is performed when a flat, highly polished sample is tilted to 70° from

horizontal, as shown in Figure 3.8a [116]. When an incident electron beam interacts with sample, incoherent backscattering is followed by electron diffraction and an EBSD pattern emanates from this point, later to be recorded by the EBSD camera and analysed by the attached software [116].

In recent years, Transmission Kikuchi Diffraction (TKD) has been introduced. It is a new SEM-based electron diffraction technique that provides a significant improvement in spatial resolution over conventional EBSD for crystallographic analysis of materials [117] [118]. The specimen-detector configuration of TKD is shown in Figure 3.8b. The sample is tilted to 10~20° from horizontal. The electron-specimen interaction volume associated with TKD is much smaller than that of conventional EBSD because the sample is thin.

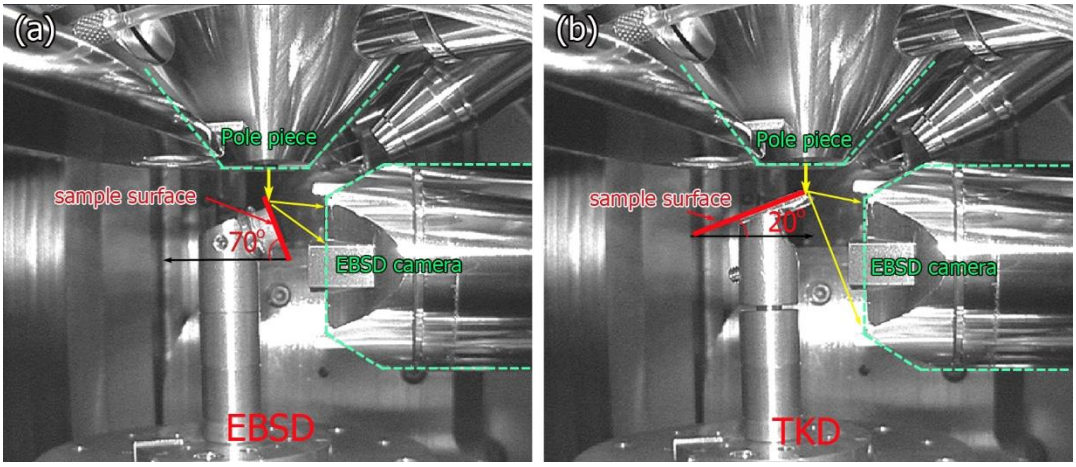

Figure 3.8 (a) Conventional EBSD specimen-detector configuration, showing a sample is tilted to 70° from horizontal; (b) TKD specimen-detector configuration. A simple specimen holder is used to hold a sample at 10° to 20° from horizontal. [116]

Figure 3.9 shows an example of Monte-Carlo simulations of scattering trajectories in a Ni/Ta/Si_3N_4 sample showing a significant difference in the interaction volume of a sample in conventional EBSD and in TKD. The typical surface interaction range for conventional EBSD

and TKD are about 150 nm and 12 nm respectively. The true physical resolution of conventional EBSD is typically in the order of several tens to hundreds of nanometres for bulk materials and TKD technique successfully improved the resolution up to 10 nm [117] [118].

In this thesis, conventional EBSD is used to analyse the texture after ECAP, and TKD was used to investigate the deformation mechanisms of the secondary phases (including LPSO and $Mg_{24}Y_5$) in the deformed Mg-Zn-Y alloys. The thin foil samples for EBSD and TKD were prepared using twin-jet eletropolishing. The specimens of the ECAPed $Mg_{94}Zn_2Y_4$ samples for microstructural characterisation were sectioned close to the central region parallel to the y plane.

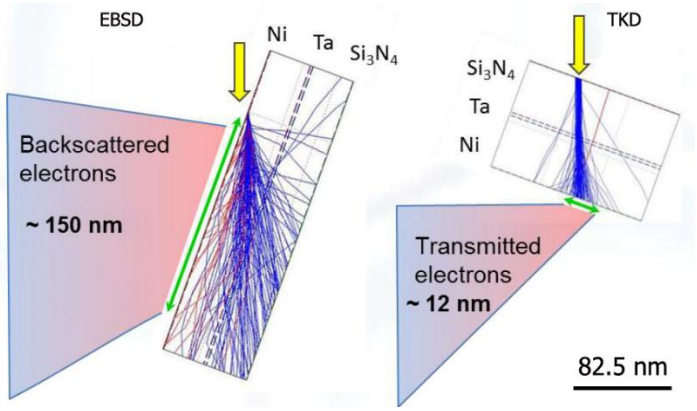

Figure 3.9 Monte-Carlo simulations of scattering trajectories for Ni/Ta/Si_3N_4 with beam energy 28 keV showing a significant difference in interaction volumes between conventional EBSD (left hand side) and TKD (right hand side) [117].

3.5 Evaluation of mechanical properties

3.5.1 Micro-hardness test

The Vickers hardness test was performed using an automated Struers DuraScan-50 micro-hardness machine (Figure 3.10). The hardness of the as-cast Mg-Zn-(Y)-(Gd) alloys (Alloys 1-8 in Chapter 6) were measured with 2.5 kg load; 5 measurements were taken in each alloy. The

remaining hardness tests on the as-cast and ECAP processed alloys were performed with 0.2 kg applied load; 10 measurements were taken under each condition.

Figure 3.10 Struers DuraScan-50 micro-hardness machine

3.5.2 Small punch test

SPT was performed on a ESH 200 kN Servo-hydraulic analogue controlled test machine (Figure 3.11a) with a SPT mould (Figure 3.11a) sitting in the middle of the load cell. A compression force was applied to the SPT mould. The specimens for SPT are disc-shaped and their size is about Φ8×0.5 mm. The foil sample was placed between the top and bottom mould with the loading ball on top of the disc. The cylinder is on top of the loading ball and in contact with the top punch. The diameters of the loading ball and the lower die for the SPT were 2.4 mm and 4.5 mm respectively. A constant displacement rate of 0.1 mm/min was imposed during the SPTs and the tests were stopped when a 50 % load drop was reached. Thin discs of the ECAPed samples were sectioned parallel to the y plane (transverse plane). Three tests were carried out under each condition.

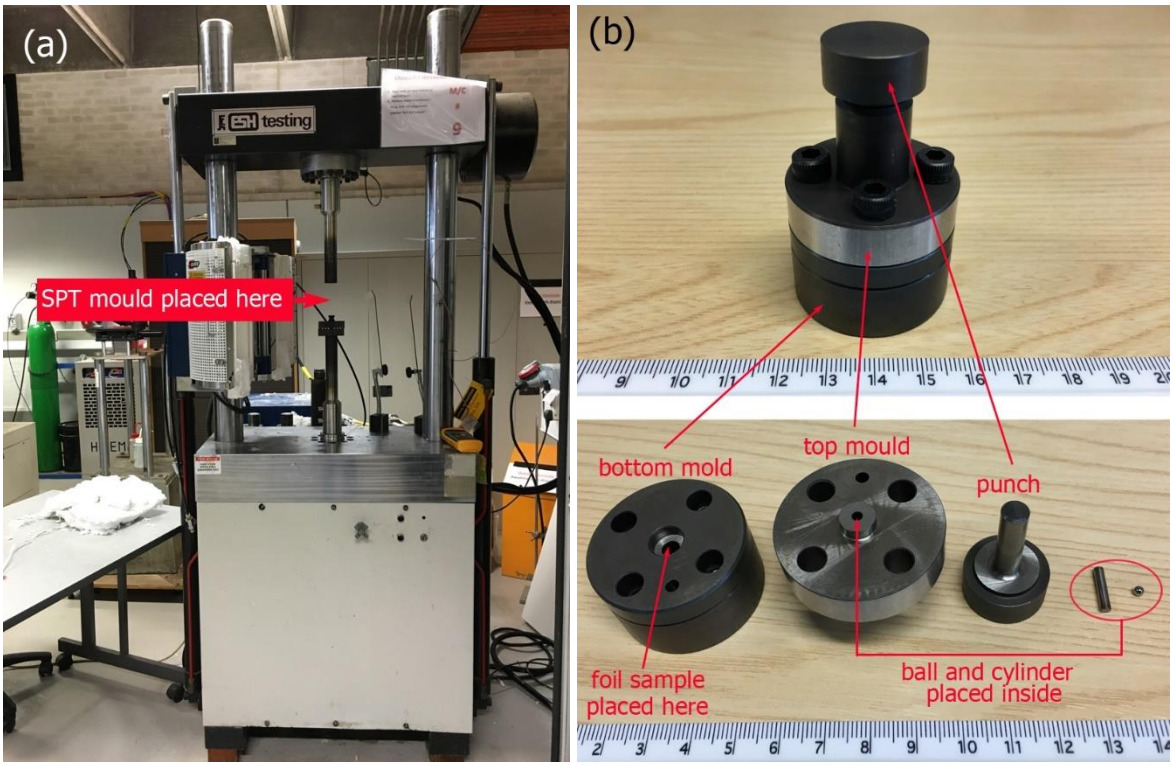

Figure 3.11 (a) ESH 200 kN Servo-Hydraulic analogue controlled test machine used for small punch test; (b) Small punch test mould with separate parts.

4 Dislocation analysis of kink in LPSO phase and LPSO/Mg structure

In the work reported in this chapter, a $Mg_{94}Zn_2Y_4$ alloy was compressed and the dislocation organisation in the alloy analysed, focusing on the kink boundaries within the LPSO phase. In addition, the kink deformation of the LPSO/Mg structure (alternate thin layers of LPSO and Mg) after a 3-pass ECAP process was studied by TKD and TEM. The difference between the kink mechanisms of the LPSO phase and LPSO/Mg structure are discussed.

4.1 Microstructure of as-cast $Mg_{94}Zn_2Y_4$ at. % alloy

The as-cast $Mg_{94}Zn_2Y_4$ samples used for compression and ECAP were prepared using an induction furnace. The designed and actual compositions measured using EDS are shown in Table 4.1.

Table 4.1 The designed and measured chemical compositions of the $Mg_{94}Zn_2Y_4$ specimen.

	Atom percentage, %		
	Mg	Zn	Y
Designed composition	94.00	2.00	4.00
Measured composition	94.25±0.32	1.48±0.11	4.27±0.23

Figure 4.1 shows optical images of the as-cast $Mg_{94}Zn_2Y_4$ alloy. The secondary phases are obvious after etching using nitric acid with ethanol, but the grain boundaries are not revealed.

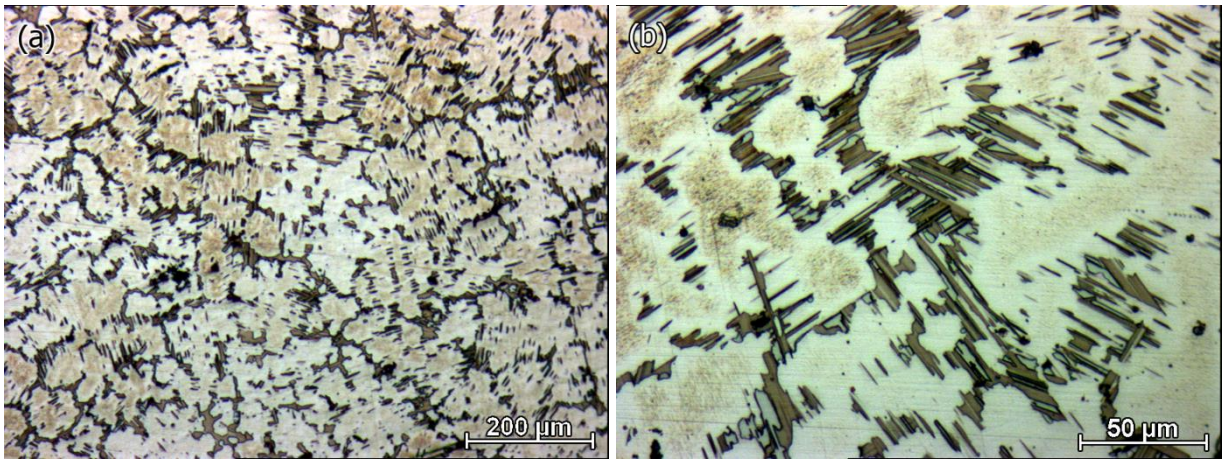

Figure 4.1 Optical images of the as-cast $Mg_{94}Zn_2Y_4$ alloy.

Figure 4.2a-b show backscattered electron images of the as-cast $Mg_{94}Zn_2Y_4$ alloy. A dense distribution of secondary phases forming a network is observed in the Mg matrix. The Mg phase has a dendritic morphology with the secondary phases inside the dendritic arms. A magnified image is shown in Figure 4.2c and the corresponding EDS maps are presented in Figure 4.2d-f. Two types of precipitates can be distinguished easily by the grey scale in the BSE image or the Y and Zn concentration in the EDS maps. The phase indicated by the yellow arrow is the main precipitate LPSO, which is plate shaped and is enriched with Zn and Y compared with the Mg matrix. The average chemical composition of the LPSO is $Mg_{87.48+0.33}Zn_{4.91+0.13}Y_{7.61\pm0.20}$ at. % (listed in Table 4.2). The phase indicated by a white arrow contains slightly more Y but less Zn than the LPSO phase is $Mg_{24}Y_5$, which has an average composition of $Mg_{86.43\pm0.70}Zn_{0.83\pm0.23}Y_{12.74\pm0.78}$ at. %. $Mg_{24}Y_5$ has usually been found to be attached to LPSO or inside two LPSO slices forming a sandwich structure. Besides the bulk LPSO and $Mg_{24}Y_5$ phases, a brighter zone in the matrix (the dashed rectangular box in Figure 4.2c) was found in the region between the precipitates, which seems like a bridge connecting the secondary phases to form a network. An EDS line scan carried out to analyse this brighter zone is displayed in Figure 4.3.

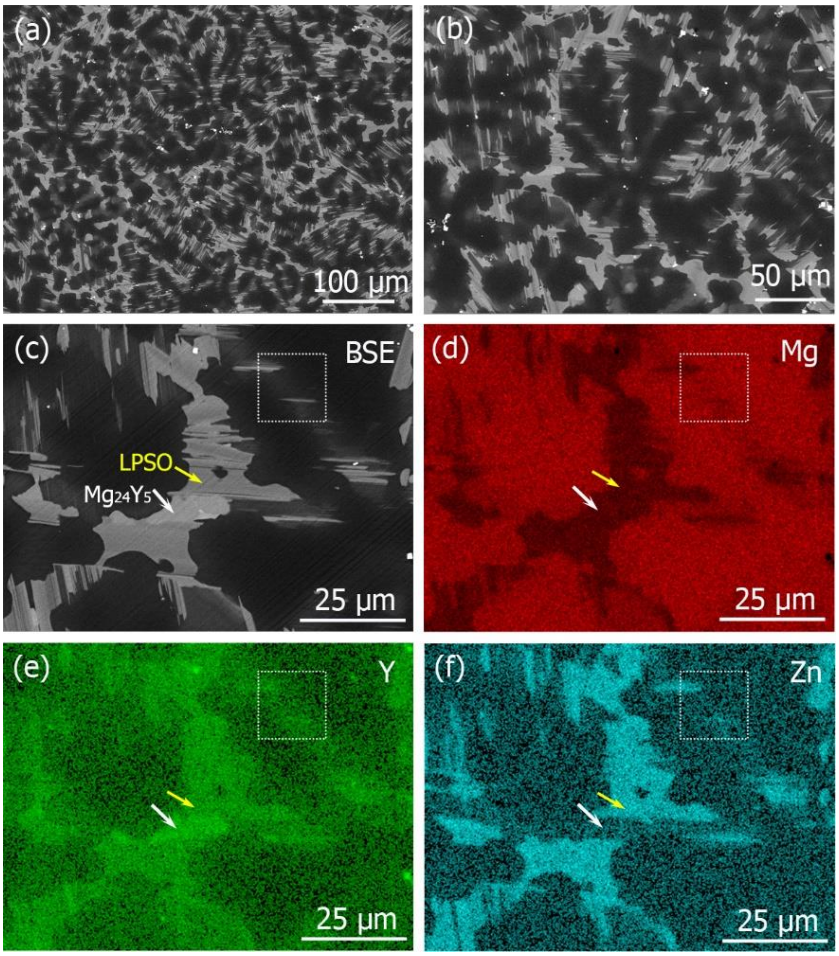

Figure 4.2(a, b) Backscattered electron images of the as-cast $Mg_{94}Zn_2Y_4$ alloy showing prolific secondary phases; (c) higher magnification image showing two secondary phases (indicated by arrows) and corresponding EDS mapping (d-f) showing high Zn and Y in LPSO phase and high Y $Mg_{24}Y_5$ phase.

Figure 4.3a shows a BSE image indicating that the EDS line scan starts from the matrix, crosses the brighter zone and ends in the matrix. The line scan in Figure 4.3b shows both Zn and Y are rich in the area between the precipitates. More EDS point analyses were carried out in the matrix and in the brighter zone, and the average compositions are listed in Table 4.2. Figure 4.3c shows that the bright zone has a serious of parallel thin lines with brighter contrast, indicated by the dashed line, which is probably LPSO lamellae inside the matrix. The EDS results in Table 4.2

shows that Zn is concentrated in the LPSO phase, while in $Mg_{24}Y_5$ phase about 0.83 at.% Zn was found.

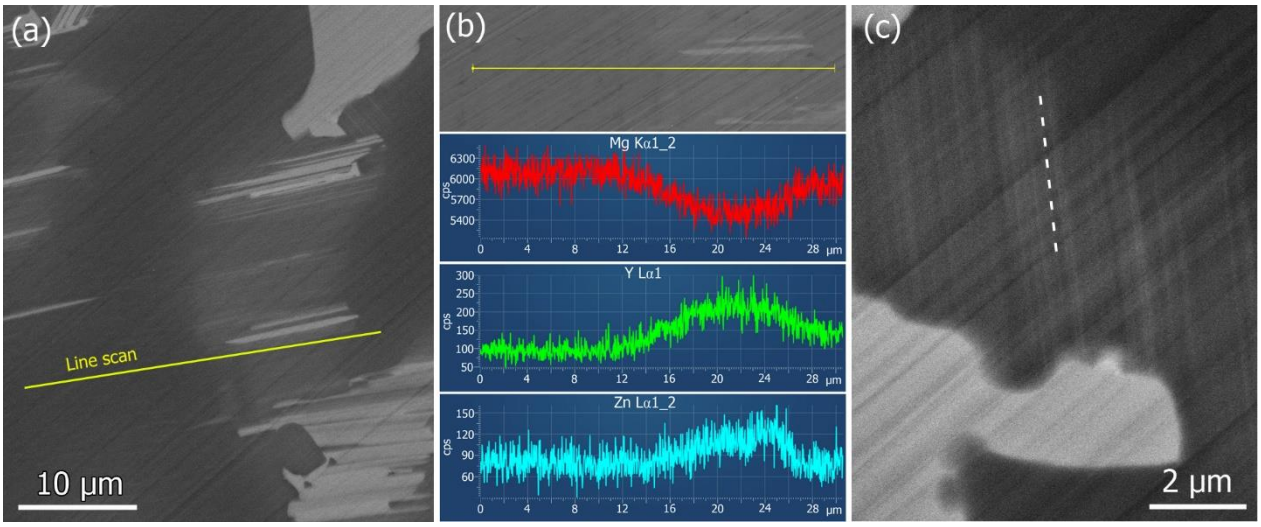

Figure 4.3 (a) BSE image showing an EDS line scan carried out to analyse the composition difference between the matrix and the area with brighter contrast; (b) EDS line scan result corresponding to Figure 4.3a showing Zn and Y are rich in the brighter area; (c) A higher magnification image shows that the bright area contains thin LPSO lamellae.

Table 4.2 EDS results of the as-cast $Mg_{94}Zn_2Y_4$ alloy showing the chemical compositions of the secondary phases and matrix, based on 10 measurements for each phase.

	Mg, at. %	**Zn, at.%**	**Y, at. %**
Matrix	98.30±0.28	0.10±0.05	1.60±0.29
LPSO/Mg structure (bright region)	95.59±0.62	0.56±0.18	3.85±0.47
LPSO	87.48+0.33	4.91+0.13	7.61±0.20
$Mg_{24}Y_5$	86.43±0.70	0.83±0.23	12.74±0.78

TEM was used to confirm the structures of the precipitates. Figure 4.4 shows a bright field image of the bulky shaped LPSO phase and the corresponding diffraction patterns taken from it along

three zone axes. The LPSO phase shows a 18R structure, which has 5 extra reflections between (0000)hcp and (0002)hcp reflections. As introduced in Chapter 2, 18R-LPSO is monoclinic, but it can be simplified by ignoring the Zn and Y segregation to certain layers and it becomes $R\bar{3}m$. It is useful when using EBSD to index the LPSO phase and easy to compare to Mg. So the indices of the LPSO phase are based on the $R\bar{3}m$ structure. The DPs of 18R-LPSO are taken from $[1\bar{2}10]$, $[0\bar{1}10]$ and $[0\bar{9}91]$ zone axes, which correspond to $[1\bar{2}10]$, $[0\bar{1}10]$, and $[0\bar{1}11]$ for the Mg hcp indices.

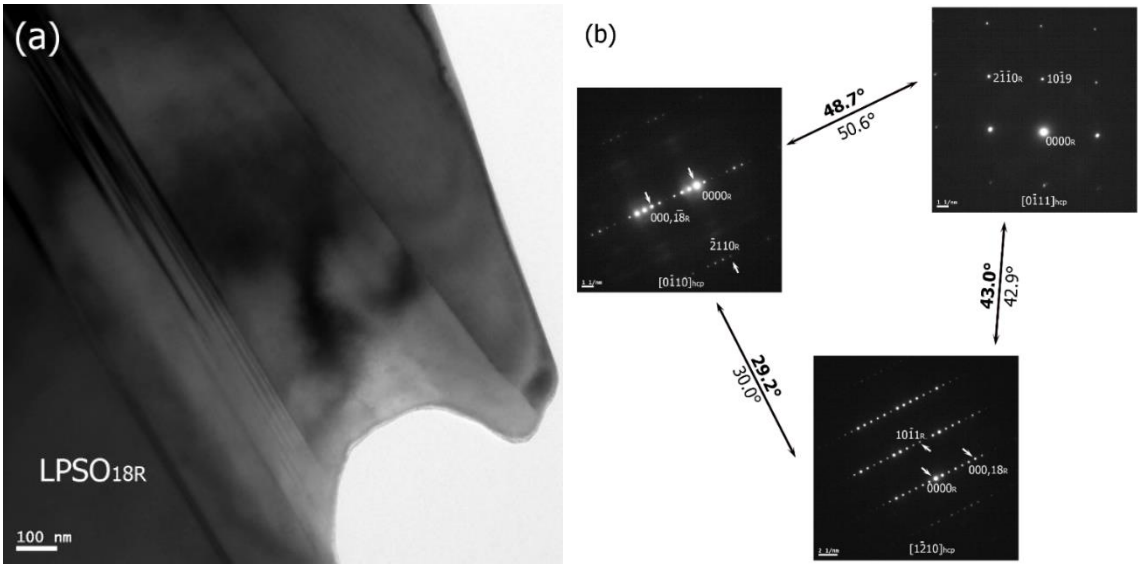

Figure 4.4 (a) TEM bright field image of the as-cast $Mg_{94}Zn_2Y_4$ showing LPSO phase; (b) Selected area diffraction patterns obtained along three zone axes of the LPSO phase, the **bold** angles are measured total tilt angles while the unbold are the calculated angles.

Figure 4.5 shows the LPSO phase inside the Mg grain has different thicknesses, and they generally have the same specific orientation relationship with the Mg matrix, i.e. $(0001)_{LPSO}//(0001)_{Mg}$, consistent with the fact that the LPSO phases appear in the same direction

in one grain (Figure 4.3a). The EDS linescan in Figure 4.5c shows the difference of Zn and Y concentrations in different phases. Zn is enriched in the matrix close to the LPSO phase.

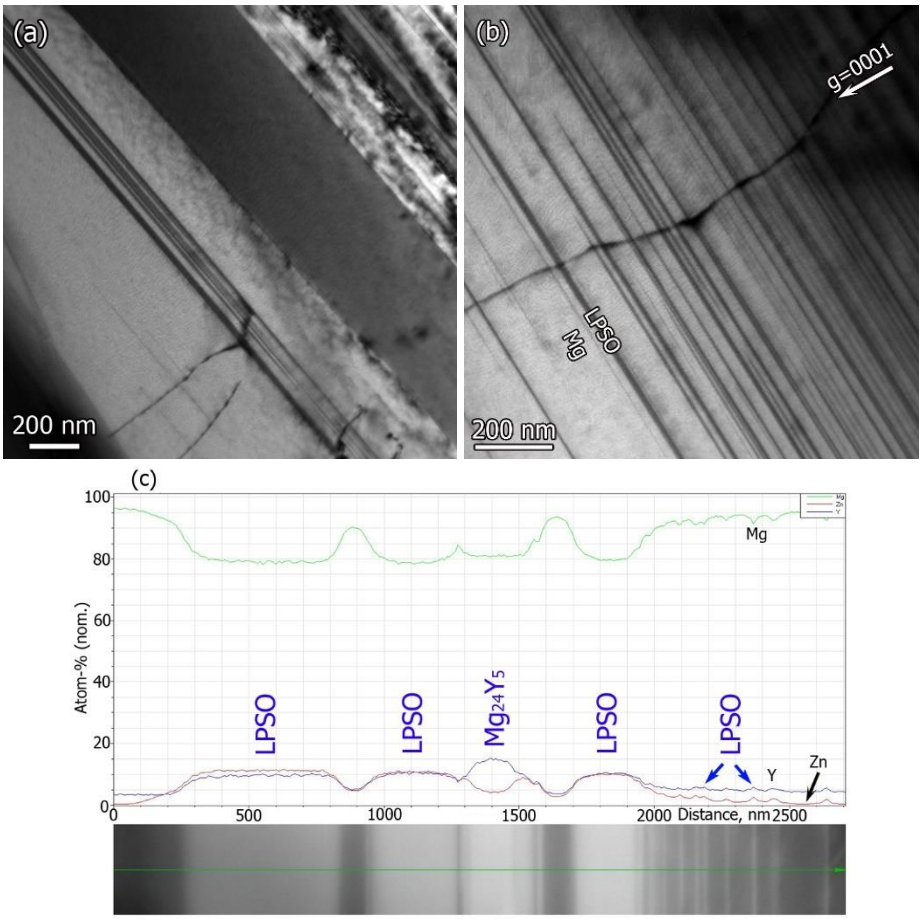

Figure 4.5 (a) (b) TEM bright field images of the as-cast $Mg_{94}Zn_2Y_4$ alloy showing the LPSO phase with different thicknesses. (c) EDS line scan taken from a different area cross LPSO lamellae with different thicknesses. The dark area in the above image is the Mg matrix.

Figure 4.6 shows the $Mg_{24}Y_5$ phase and diffraction patterns taken along three zone axes, which confirms the cubic structure. According to the Mg-Zn-Y ternary phase diagram [36] and the Mg-Y binary phase diagram [32], the 18R structure starts to form at around 720 ℃ and $Mg_{24}Y_5$ starts to form at around 605 ℃. It is therefore possible that during the solidification process, LPSO

phase will form first which leads to the Zn being removed rapidly from the surrounding liquid metal. The overall Y in the liquid metal is still much higher than its solubility limit in magnesium. When the liquid metal is further cooled, $Mg_{24}Y_5$ formed directly from the liquid metal.

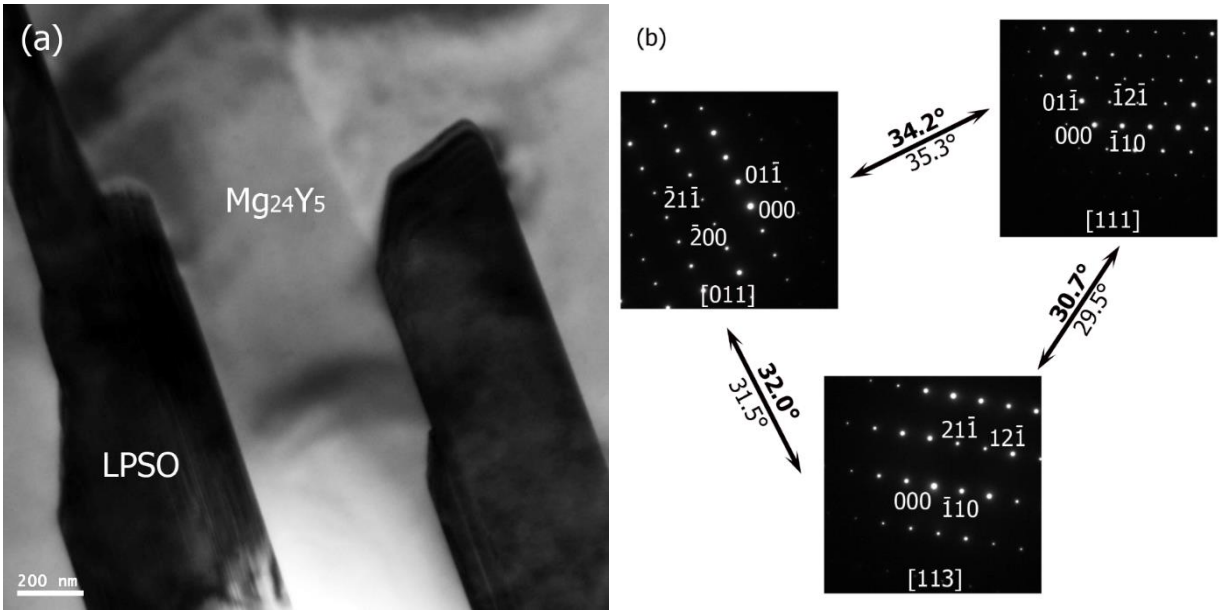

Figure 4.6 (a) TEM bright field image of as-cast $Mg_{94}Zn_2Y_4$ showing $Mg_{24}Y_5$ phase with adjacent LPSO phase; (b) Selected area diffraction patterns obtained from the $Mg_{24}Y_5$ phase along three zone axes, the **bold** angles are measured total tilt angles while the unbold are the calculated angles.

In brief, the as-cast $Mg_{94}Zn_2Y_4$, with a measured composition of $Mg_{94.25}Zn_{1.48}Y_{4.27}$, has a dense distribution of secondary phases LPSO and $Mg_{24}Y_5$. The main secondary phase is LPSO, which mostly have large thinkness (in comparison to thin LPSO lamellae). Thin LPSO lamellae are also observed as alternating structures with thin Mg lamellae, which conglomerate is called 'LPSO/Mg structure'.

4.2 Kink deformation of LPSO in compressed $Mg_{94}Zn_2Y_4$ alloy

4.2.1 Compression tests

The as-cast $Mg_{94}Zn_2Y_4$ samples were compressed to different stains, and the engineering strain-nominal stress curves are shown in Figure 4.7. The compression tests were performed at room temperature with an initial strain rate of about $5\times10^{-4}s^{-1}$. The dimensions of the samples were measured before and after the compression tests to calculate the actual strains, which are listed in Table 4.3. The samples are named after the designed strain, e.g. $Mg_{94}Zn_2Y_4$ with 2% strain. The sample with 20% strain was compressed until fracture and the stress suddenly dropped. The 0.2 % proof stress of the alloy is about 195 MPa. This is higher than the yield stress of the as-cast $Mg_{97}Zn_1Y_2$ alloys (see Figure 2.20) due to the more densely presence of the secondary phases. The measured Young's modulus of the $Mg_{94}Zn_2Y_4$ alloy is about 9 GPa, which is smaller than $Mg_{97}Zn_1Y_2$ alloy prepared by the RS/PM (45 GPa) [5]. This is probably because the measurement of the displacement is not accurate without using extensometer.

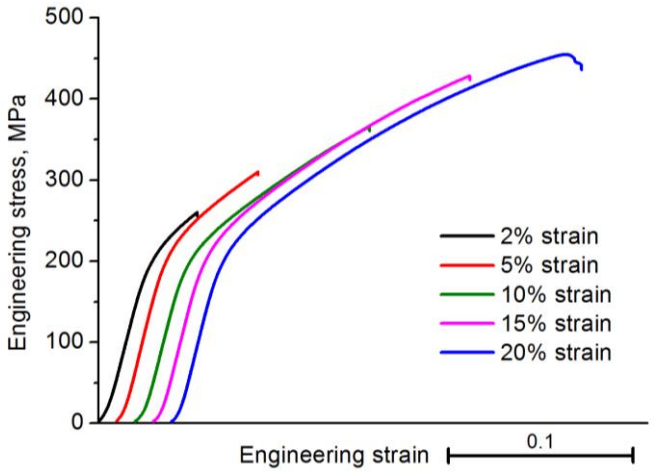

Figure 4.7 The compression engineering stress-strain curves of as-cast $Mg_{94}Zn_2Y_4$. The curves for samples with 5-20% strains are shifted.

Table 4.3 Compression properties of as-cast $Mg_{94}Zn_2Y_4$.

Sample No	Designed strain	Measured strain	E modulus, GPa	0.2% proof strength, MPa
1	0.02	0.025	8.88	190
2	0.05	0.046	9.33	195
3	0.1	0.091	8.91	188
4	0.15	0.135	8.97	195
5	0.2	0.186	9.11	192

4.2.2 SEM observation of the microstructure before and after compression

The samples were polished before compression and indented by microhardness test so that a direct comparison of the same area can be made before and after the compression. Figure 4.8 shows backscattered SEM images of the as-cast and as-compressed samples. No obvious change can be observed in the sample with only 2% strain using the SEM analysis. However, kink bands were observed in the TEM, which will be described later. When the strain increased to 10%, slip traces can be observed as indicated by the red arrows in Figure 4.8e. After 20% strain, there are obvious deformation kinks indicated by the red arrows in Figure 4.8f. The two kink bands show a beak-like shape which lie in the direction almost perpendicular to the basal plane of LPSO phase.

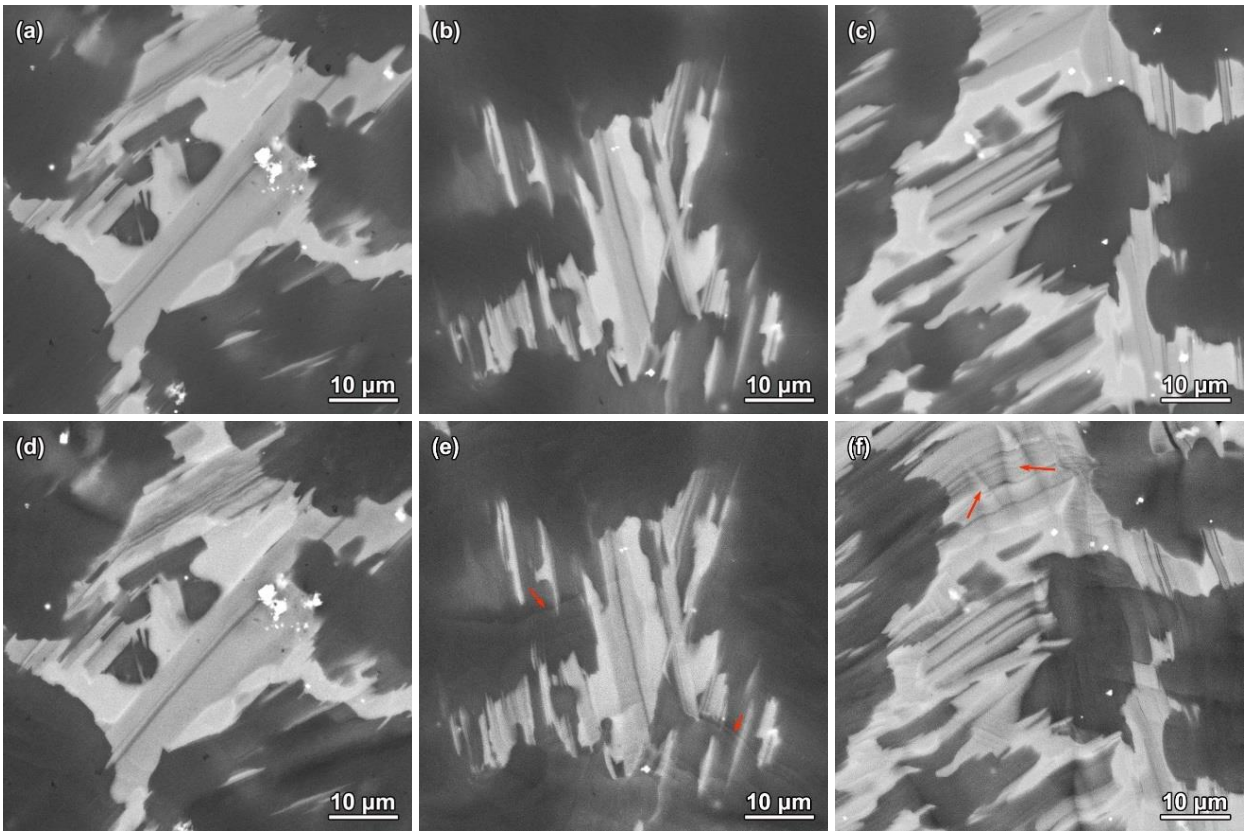

Figure 4.8 Comparision of LPSO phase before and after compression to different strains: (a-c) as cast samples before compression; (d-f) as-compressed samples corresponding to (a-c) with strains of 2%, 10% and 20% respectively.

4.2.3 TEM analysis of small angle kink boundaries in the 2% strained sample

Figure 4.9a shows a bright-field TEM image of $Mg_{94}Zn_2Y_4$ after 2% strain; the TEM foil is sectioned from long side of the cuboid sample which is parallel to the compression axis. A kink band (indicated by yellow arrow) was found to cross through three separate LPSO lamellae, which induced a similar strain in all three. Both sides of the kink band are called kink boundaries. As shown in the higher magnification image in Figure 4.9b, the LPSO appears very dark, because it is close to the Bragg condition along the $[1\bar{2}10]$ zone axis. The kink band in the middle

appears in brighter contrast and is obviously off the zone axis. The boundaries of the kink band (indicated as 4 and 5) are essentially dislocation walls, which are more obvious in Figure 4.9e. It is interesting to notice that not only are two dislocation walls found in this LPSO: other dislocation walls (1, 2 and 3) are observed in the dark region. They all lie in a direction almost perpendicular to the LPSO basal plane and can be regarded as kink boundaries. The dislocation walls caused low angle grain boundaries which correspond to strain along the c direction. A closer look of dislocation walls 2 and 3 is shown in Figure 4.9c, where very straight dislocations are found lying on the basal plane. Different interspacings in different dislocation walls correspond to different misorientation angles. After tilting the sample to the $[1\bar{5}40]$ zone axis, the dislocations in kink boundary 5 are end on, but the dislocations in kink boundary 4 still have a certain length (Figure 4.9d). This is particularly obvious when the dislocations are observed under the two-beam condition in Figure 4.9e, where the dislocations in kink boundary 5 now show very short length (tilted a little) and the dislocations in kink boundary 4 are longer. It is interesting to notice that the dislocation spacing may vary within one kink boundary and that a large kink boundary may contain two or more small boundaries, e.g. kink boundary 5 consists two smaller boundaries with larger dislocation spacings. Figure 4.9f confirms that the crystal rotates around the $[1\bar{5}40]$ zone axis; the misorientations caused by the kink boundary can be measured directly from the diffraction patterns.

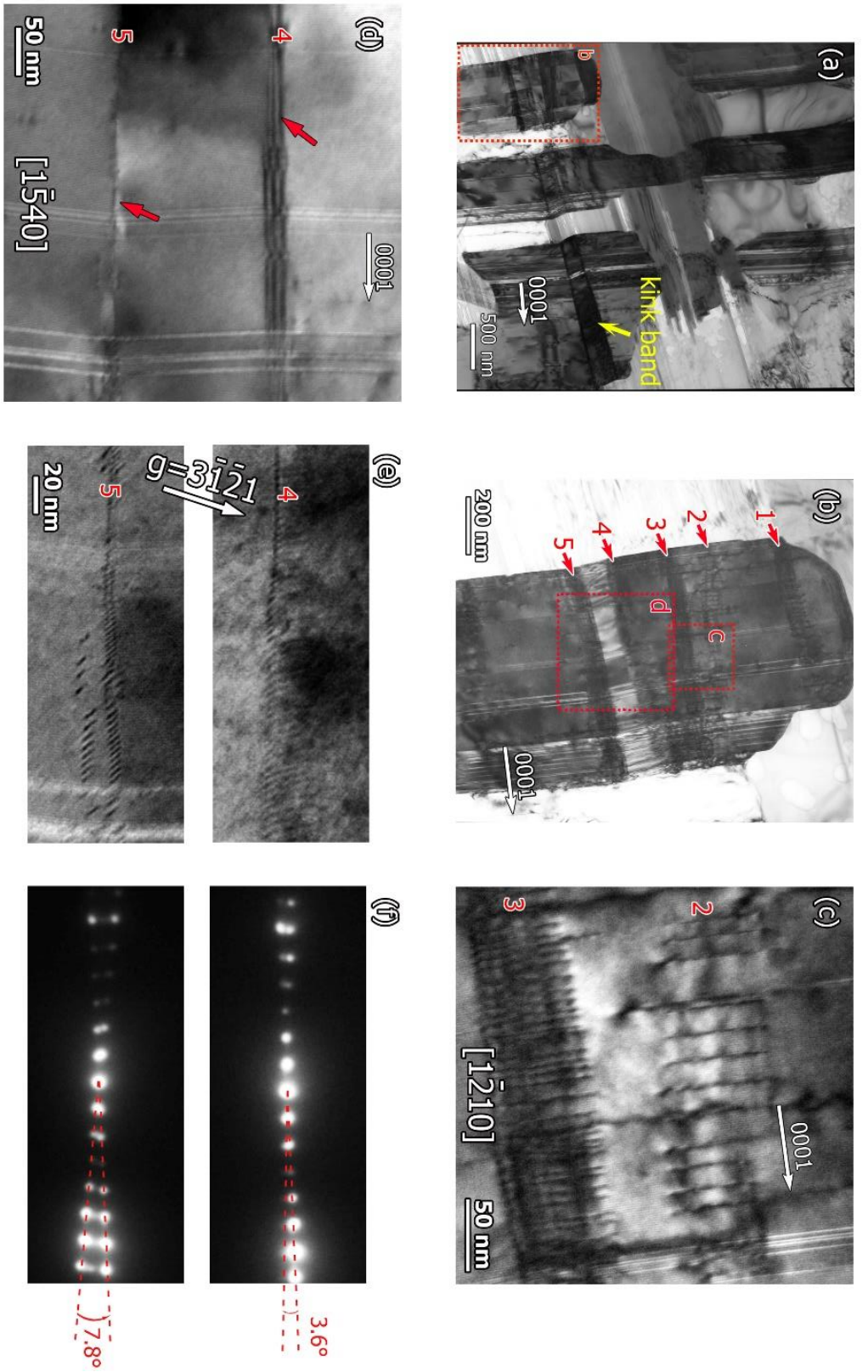
(a)
kink band
b
0001
500 nm
(b)
1
2
3
4
5
c
d
200 nm
0001
(c)
2
3
0001
[1$\bar{2}$10]
50 nm
(d)
4
5
50 nm
[15$\bar{4}$0]
0001
(e)
g=3$\bar{1}\bar{2}$1
4
5
20 nm
(f)
3.6°
7.8°

Figure 4.9 (a) TEM bright-field image of the 2% compressed $Mg_{94}Zn_2Y_4$ alloy showing a kink band; (b) a magnified image from Region *b* in Figure 4.9a showing five dislocation walls in the LPSO phase. The electron beam direction is parallel to Mg $[1\bar{2}10]$; (c) a magnified image of LPSO phase from Region *c* showing the kink boundaries contain straight and parallel dislocations on the basal plane. The electron beam direction is parallel to Mg $[1\bar{2}10]$; (d) a magnified image of Region *d* in Figure 4.9b observed along Mg $[1\bar{5}40]$; the dislocations in kink boundary #5 are end on; (e) Dislocations taken under the two-beam condition with g = $3\bar{1}\bar{2}1$ and BD~ $[1\bar{5}40]$ showing dislocation morphology. The top image corresponds to the region indicated by red arrow in kink boundary 4 in Figure 4.9d and the bottom image corresponds to the region indicated by red arrow in kink boundary 5; (f) SAD patterns taken from regions including kink boundaries in the Figure 4.9d showing different misorientation angles. Top SAD pattern correspond to kink boundary 4 and bottom SAD pattern corresponds to kink boundary 5.

Figure 4.10a shows the lattice fringes suggesting that the basal plane rotation caused by kink boundary #5 is about 7.6°, which is close to the 7.8° measured from the diffraction pattern in Figure 4.9f. Figure 4.10b shows the dislocations in kink boundary 5 when the electron beam direction is close to the $[1\bar{2}10]$ zone axis. Closer look of the region using diffraction contract indicates that there are two groups of dislocations as shown by the yellow arrows in Figure 4.10b.

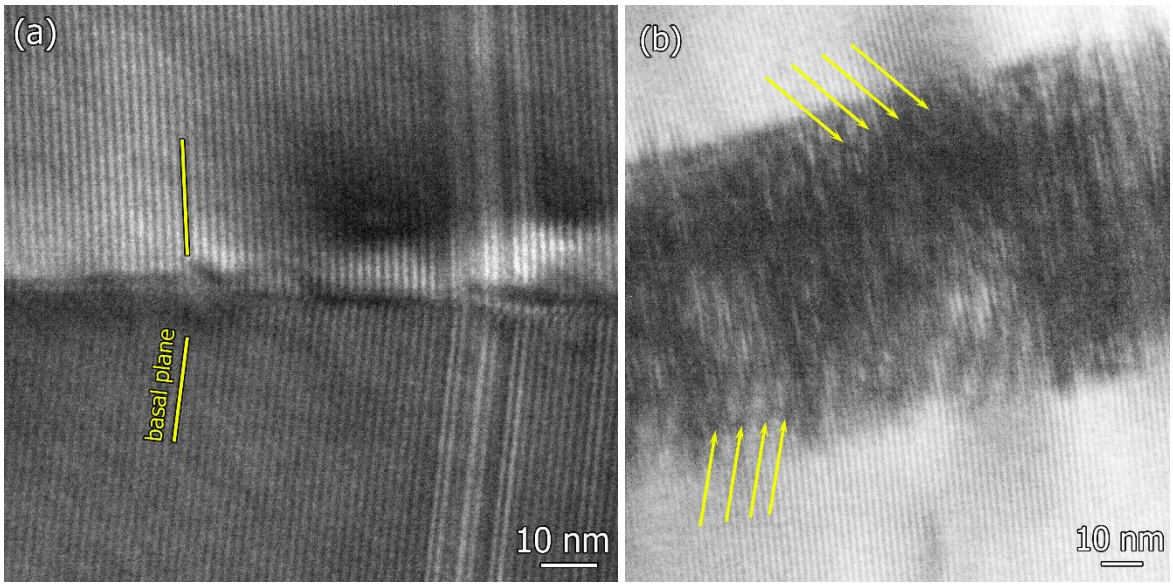

Figure 4.10 (a) High resolution TEM image of kink boundary 5 shows the basal plane rotating around the $[1\bar{5}40]$ zone axis; (b) Two groups of dislocations are found in the kink boundary, indicating different dislocation line directions, the electron beam direction is close to $[1\bar{2}10]$.

Figure 4.11 shows the dislocations inside a different kink boundary taken using different **g** vectors. The dislocations in the kink boundary are very straight and lies in the same direction, as indicated by the yellow arrow. Other dislocations in the LPSO phase, indicated by the red arrow, are curly and lie in other directions. All these dislocations lose contrast under two beam conditions when g is $0\bar{1}12$ and 0002, which indicates the dislocations have a Burgers vector of $\frac{1}{3}[2\bar{1}\bar{1}0]$.

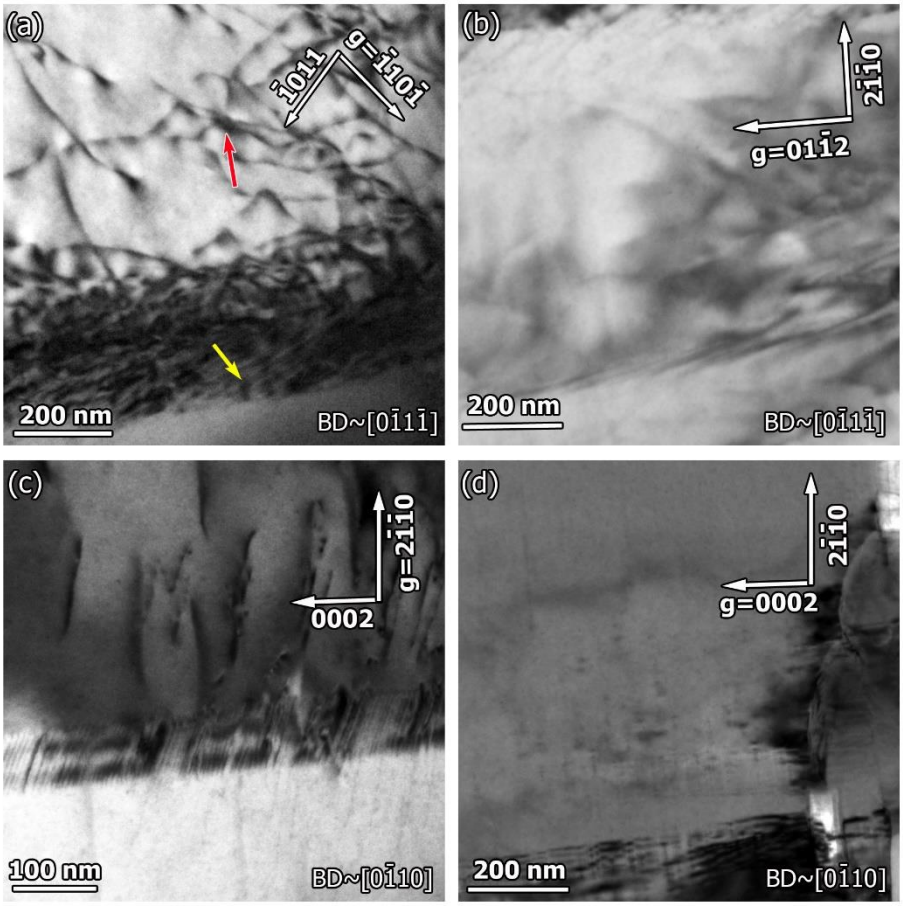

Figure 4.11 Dislocations in a kink boundary viewed under two beam conditions in different reflection **g** vectors

The kink boundaries with low misorientation angles are essentially the low angle grain boundaries constructed from <a> type basal dislocations. The misorientation angles of the kink boundaries in Figure 4.9 can be measured directly by the rotation of the diffraction patterns or of the basal planes themselves (Figure 4.10a). According to the dislocation model for low angle boundaries, the edge dislocation spacing D in a low angle boundary should be given by

$$D = \frac{b}{2\sin\theta/2} \qquad \text{Equation 4.1 [119]}$$

where **b** is the magnitude of the Burgers vector (0.3211 nm) and θ is the misorientation angle.

Table 4.4 shows the misorientation angles of the kink boundaries 1-5 in Figure 4.9b measured directly from the rotation of the diffraction patterns and the basal planes. In addition, the misorientation angles resulting from the low angle grain boundaries are also calculated from the dislocation spacing D using Equation 4.1. The calculated results are also shown in Table 4.4 with the average dislocation spacing D measured directly from the TEM images. The calculated angles are in good agreement with the measured angles.

Table 4.4 Misorientation angles of kink boundaries in Figure 4.9b

Kink boundary	1	2	3	4	5
Directly measured angle, °		0.79	1.57	3.6	7.8
Average dislocation spacing D, nm	14.7	14.4	7.39	4.18	2.1*
Angles calculated from dislocation spacing, °	1.30	1.28	2.32	3.592	7.1

*The average dislocation spacing of kink boundary 5 is measured using dislocations in the left part of the kink boundary 5 (see Figure 4.9e); Figure 4.9e shows kink boundary 5 contains one dislocation wall in the left part, which is divided into 2 dislocation walls in the right part. In addition, the average dislocation spacings of the two small dislocation walls on the right are about 3.74 nm and 4.79 nm and the misorientation angles are calculated as 3.16 ° and 4.01 ° respectively. And the sum of the two small kink boundaries is thus also about 7.2 °.

Figure 4.12 shows some examples of dislocations in the LPSO phase and the Mg matrix in the 2% strained sample. Figure 4.12a shows a small step is observed in the kink boundary, as indicated by the yellow dashed line. The dislocations in the kink boundary are straight and well aligned, which agree with previous observations. However, the arrangement of the dislocations in the dislocation wall varies, which can form small steps and this indicates that the kink boundaries are not always straight. Figure 4.12b shows stacking faults are also observed in the LPSO phase. The

stacking fault fringes are parallel to each other. An open rectangular parallelepiped shape was observed and indicated by the white dashed box. As shown in the schematic drawing, two parallel red surface are stacking fault fringes and the top yellow surface are the kink boundary where the dislocation walls in the kink boundary are also labelled in the figure.

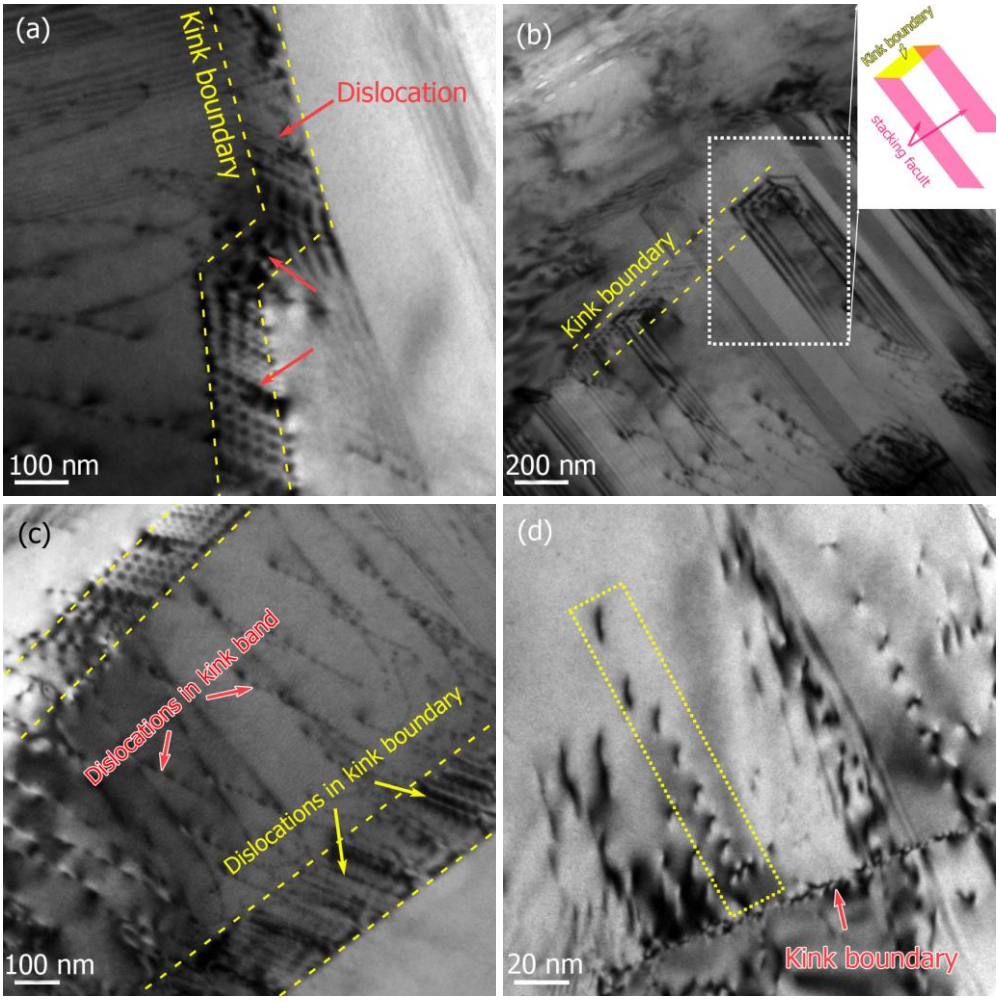

Figure 4.12 (a) TEM bright field image showing a kink boundary with a small step; (b) TEM bright field image showing stacking faults; (c) discrete dislocations in the kink band; (d) dislocations pile up on the kink boundary.

Figure 4.12c shows that inside a kink band, between two kink boundaries, discrete dislocations are observed. Compared to the dislocations in the kink boundaries, which have similar dislocation

line directions and a very ordered arrangement, these dislocations within the kink band have different lengths and line directions. This indicates other types of dislocations also generate during the deformation, but in a smaller portion comparing to the ones forming kink boundaries which accommodates most strains. Figure 4.12d shows the interaction between dislocations in the kink boundary and outside the kink boundary. Some dislocations (in the yellow dashed box) piled up around a kinking boundary (indicated by red arrow) and forming dislocation walls perpendicular to the kink boundary. The spacing between the dislocations are smaller when close to kink boundary and are larger when away from the kink boundary. This suggests further dislocation movement are hindered by the kink boundaries.

4.3 The kink deformation of LPSO/Mg in an ECAPed alloy

In the ECAP processed sample, many kink boundaries are found in the LPSO phase. Figure 4.13 shows the kink deformation of LPSO phase in the sample ECAP processed for 3 passes. The LPSO phase formed zig-zag shapes, and the kink boundaries exhibit as straight dark lines composed of black etch pits in Figure 4.13a. A higher magnification picture of a kink boundary is shown in Figure 4.13b. It is worth noting that the long $Mg_{24}Y_5$ phase (as indicated by an arrow) in the middle of the LPSO phase shows a similar morphology of kink band. When a kink forms in the lamellar structured LPSO phase, the surrounding thin matrix layers deform in a similar manner.

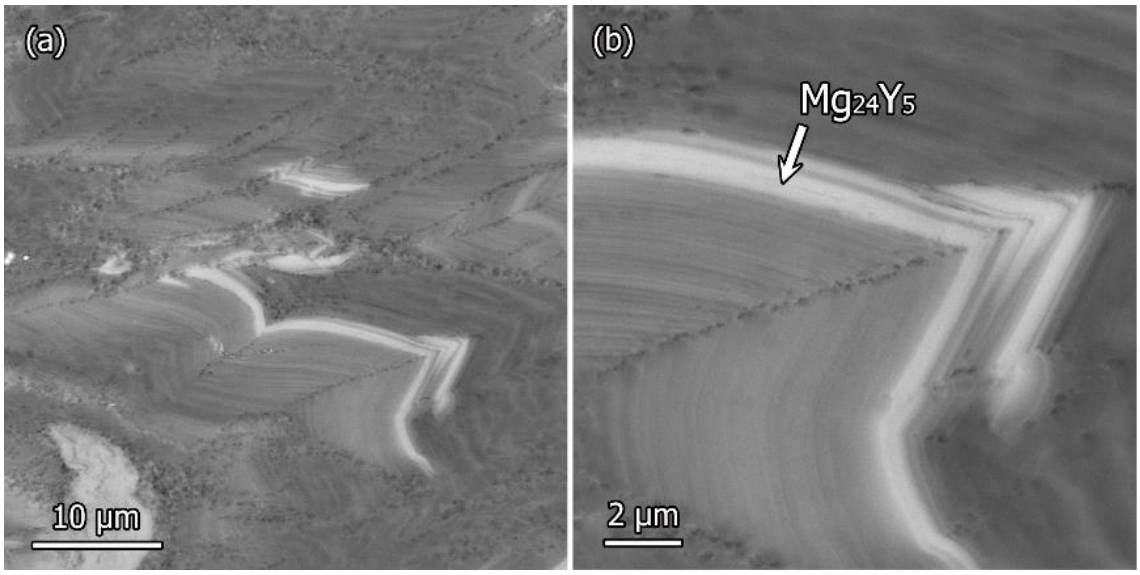

Figure 4.13 (a) Backscattered electron image showing the kink microstructure of LPSO phase after 3 ECAP passes (the sample was slightly etched); (b) SEM image of a kink boundary at higher magnification.

4.3.1 Kink band analysis by EBSD/TKD

Figure 4.14 shows an area of Mg matrix containing a small amount of LPSO phase in a 2-pass ECAPed sample. The LPSO phase is slightly bent. The orientation map in Figure 4.14b shows large strain in the bent area, which is similar to a kink boundary. Area I represents a low angle boundary with a misorientation angle of about 4 degrees: the cell structures are shown in the map. LPSO phase appears as a long line inside the Mg matrix, and the low angle boundary is almost parallel to the LPSO phase. The rotation axes of the boundary in Figure 4.14c indicate that the crystal rotates around the [0001] zone axis of Mg. Similar to area I, area III also shows the [0001] orientation axis. Area II has a larger misorientation angle than areas I and III, and the rotation axis in crystal coordinates is $[01\bar{1}0]$.

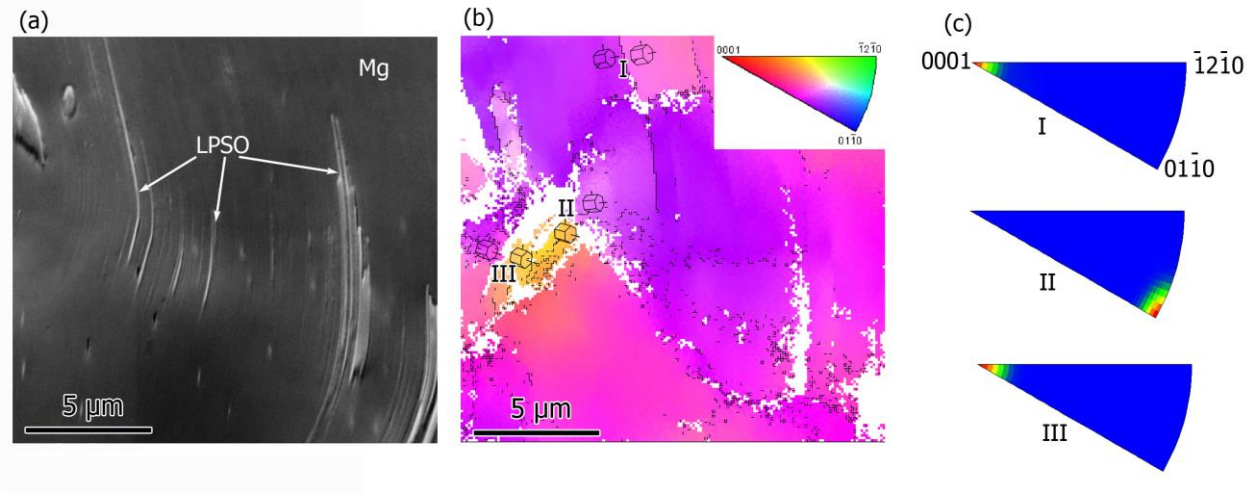

Figure 4.14 (a) SEM image of an area of Mg matrix containing a small amount of LPSO phase; (b) orientation map of Mg; the white regions are not indexed; (c) Rotation zone axis of areas I, II and III in crystal coordinates.

Figure 4.15a shows a TKD orientation map of the LPSO/Mg structure in a 3-pass ECAPed sample where the corresponding forward scattered image is shown in Figure 4.15b. The Y map in Figure 4.15c confirms the thin bright phase as LPSO, which contains more Y than Mg matrix and less Y than the $Mg_{24}Y_5$ particles in the lower-right corner. The LPSO phase is very thin and the Kikuchi pattern is similar to Mg, so the orientation map only shows Mg.

The deformed Mg phase contains sharp boundaries and a zigzag shape, which is similar to the kinking of the LPSO phase. Some kink boundaries end inside the Mg alloy (black arrow) and some high angle kink boundaries are divided into low angle kink boundaries (white arrow). The rotational axis contour map of the kinking boundaries in crystal coordinates shows that the kink boundaries are mainly rotated around the $[\bar{1}2\bar{1}0]$ zone axis. A relatively high density of rotational axes is distributed in a ring connecting the $[\bar{1}2\bar{1}0]$ and $[01\bar{1}0]$ zone axes. The rotational axes

observed can be regarded as a combination of $\langle 1\bar{1}00\rangle$ and $\langle 0\bar{1}10\rangle$ rotational type kink bands as proposed in [76].

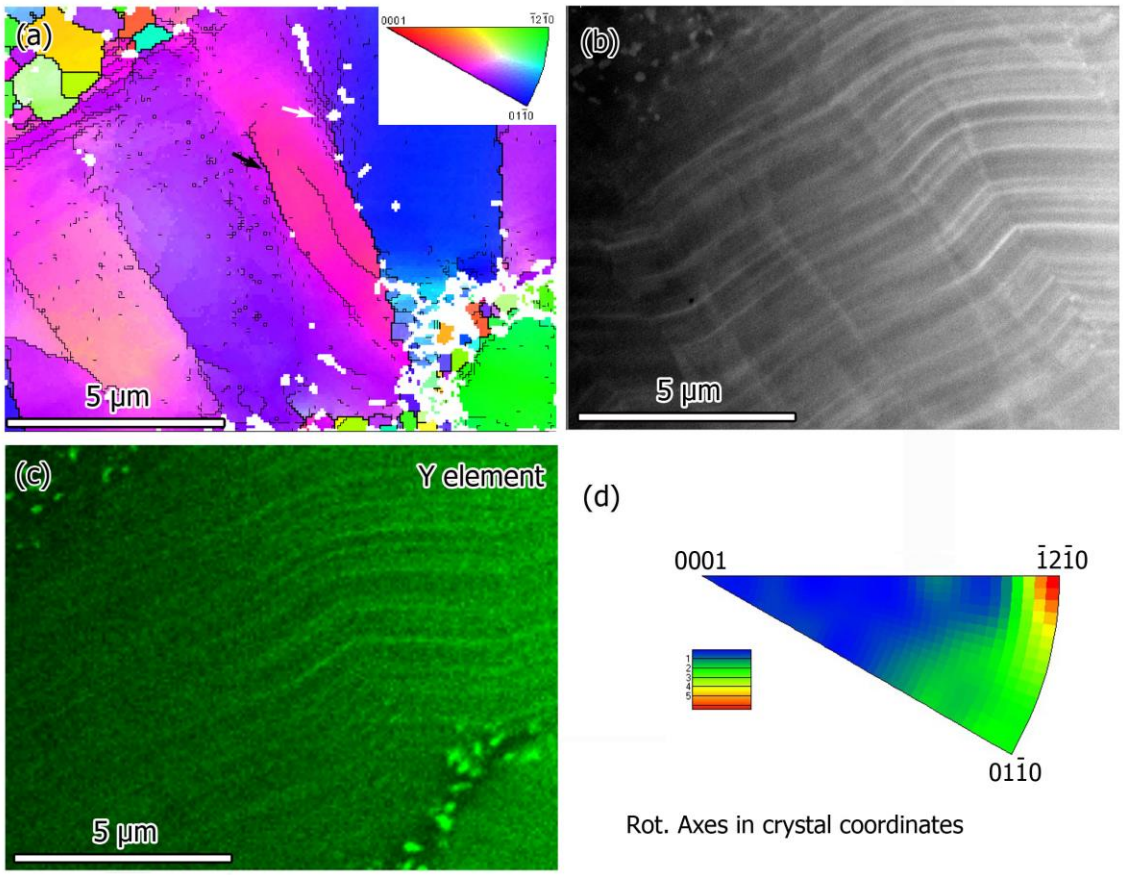

Figure 4.15 (a) Orientation map of Mg phase in the 3-pass ECAPed sample. Low angle boundary (2°~10°) is indicated by thin black line, high angle boundaries (>10°) by thick black line, (b) forward scattered image; (c) EDS Y mapping; (d) rotational axis of the kink boundaries in crystal coordinates.

Figure 4.16 shows a forward scattered image and its corresponding TKD orientation map of a LPSO/Mg region in a 3-pass ECAP sample. The forward scattered image shows the LPSO exhibit as white lamellae in the Mg matrix, as indicated by the yellow arrow. The dashed line

indicates the trace of the LPSO lamellae and the zigzag shape indicates kinking occurred during the deformation. The kink boundaries are obvious in the Figure 4.16b and labelled as I, II and III; they have a large misorientation angle and the rotation axes are scattered around the edge of the stereogram connecting the $[01\bar{1}0]$ to the $[\bar{1}2\bar{1}0]$ zone axis, all in the (0001) plane; as shown in Figure 4.16c. The low angle boundaries IV and V are found inside the kink bands and parallel to the LPSO lamellae, and they are rotated around [0001].

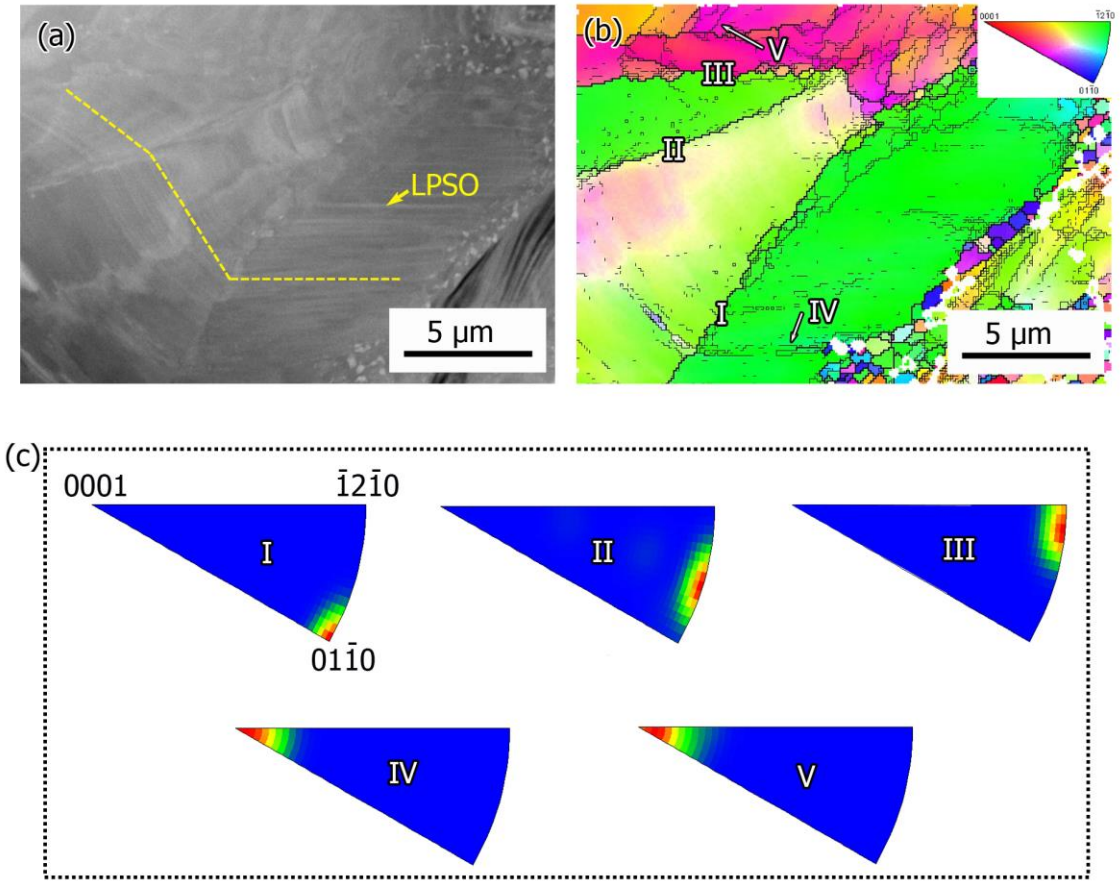

Figure 4.16 (a) Forward scattered electron image of a LPSO/Mg region shows the thin LPSO slices in the Mg matrix. The trace of the LPSO phase are indicated by dashed lines, which show the zigzag shape of the kink bands; (b) orientation map of LPSO/Mg structure with several kink boundaries and (c) its corresponding rotation axes.

Figure 4.17a shows a TEM bright field image of deformed LPSO/Mg in a 3-pass ECAP processed sample. It shows that a clear kink boundary exists in the right hand part of the image with a misorentation angle about 68º measured directly by the basal planes. The low angle kink boundaries, on the other hand, are difficult to identify by the morphology in the TEM image, e.g. as arrowed in Figure 4.17a. Figure 4.17b shows that the low angle kink boundary (corresponding to the arrowed area) contains lots of dislocations. In order to understand the crystallographic nature of the kink boundaries, the same area was characterised by TKD. The orientation map is shown in Figure 4.17c, where low angle boundaries (misorientation angles 2~10°) are indicated by thin black lines and high angle boundaries (misorientation angle >10°) are indicated by thick black lines. It is interesting to notice that kink boundaries I and II are almost parallel to each other, and have similar misorientaion angles of about 16°. The areas outside the kink boundaries I and II have similar orientations. The rotational zone axis contour maps of kink boundaries I and II in Figure 2d show that the maxima were both found close to the $[04\bar{4}1]$ zone axis. So the kink boundaries I and II belong to the same type with opposite rotation directions. A similar morphology was found in boundaries III and IV, which have smaller misorientation angles of about 4° and a rotation zone axis of [0001]. It is worth mentioning that kink boundaries III and IV are located inside the kink boundaries I and II to form a morphology which is similar to double twinning. This phenomenon has not been reported elsewhere for the LPSO phase.

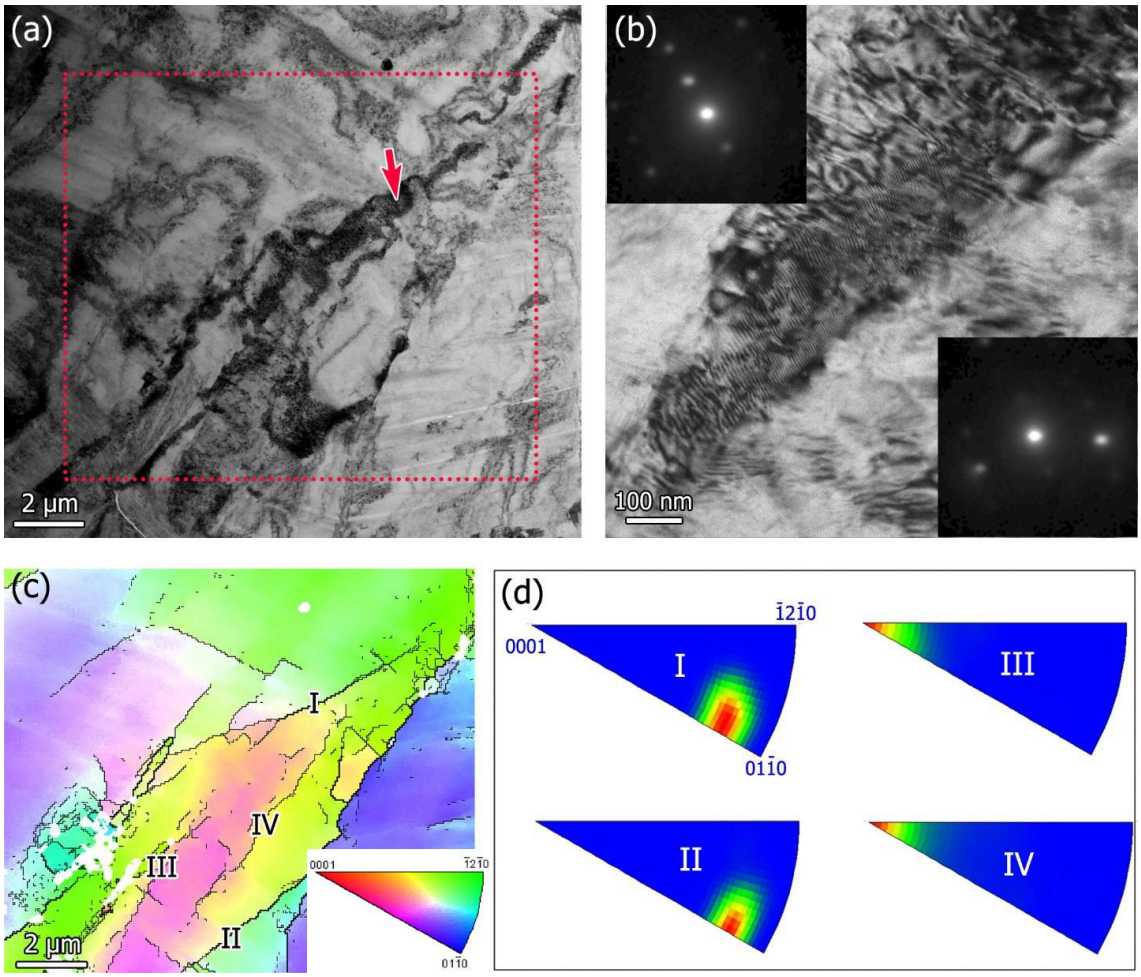

Figure 4.17 (a) TEM bright field image of the LPSO/Mg; (b) higher magnification image corresponding to the arrowed area in Figure 4.17a; (c) orientation map showing paired kink boundaries in Mg/LPSO; (d) rotation axes of kink boundaries.

4.3.2 Dislocation analysis of kink band using TEM

Figure 4.18a shows some kink boundaries, indicated by red arrows, dividing the LPSO/Mg into small domains. The LPSO lamellae are thin black lines in the Mg matrix as indicated by yellow arrow. The kink boundaries show a rotational morphology, which has been described in ref. [120]. The LPSO lamellae shows a circular shape instead of a zigzag shape and allows a continuous

strain accommodated by the kink boundaries. In general, a large rotational angle can be obtained through serious of low angle kink boundaries in the LPSO/Mg structure. The diffraction pattern was obtained from the region containing the kink boundaries; it shows the elongated reflections.

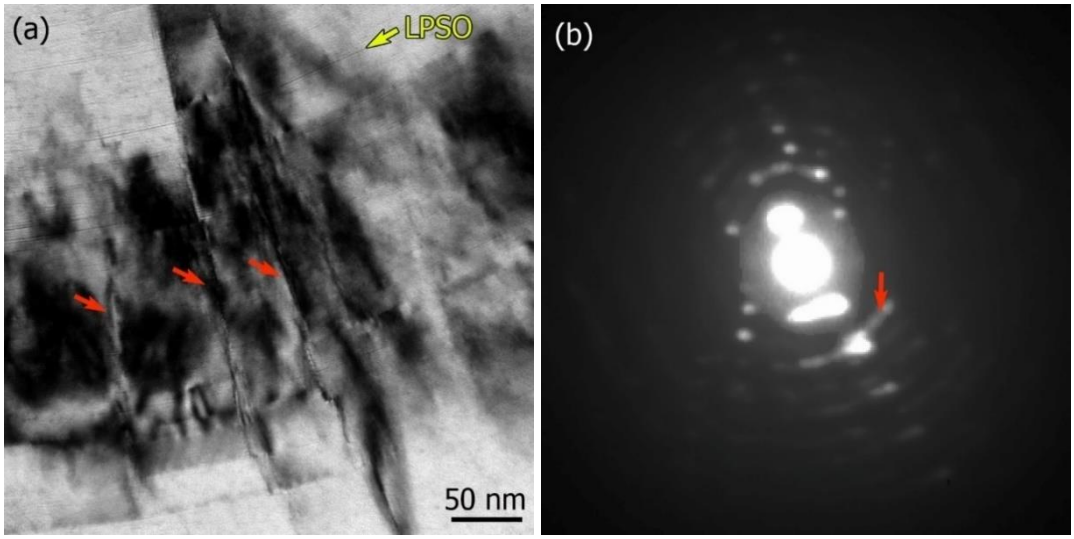

Figure 4.18 (a) TEM bright field image showing kink boundaries (indicated by red arrows) arranged in a rotational morphology inside LPSO/Mg; (b) selected area diffraction pattern obtained from a region covering the kink boundaries in Figure 4.18a.

Figure 4.19a shows a bright field image of a kink boundary in a LPSO/Mg region. The magnified image in Figure 4.19b shows that the kink boundary is essentially a dislocation wall: the morphology is similar to a kink boundary in the LPSO phase. The misorientation angle of about 14.4° between the original and kinked areas, measured using basal planes, is caused by a dislocation wall. Figure 4.19c shows a bright field image in the same area with the incident beam close to $[1\bar{2}10]$. Besides the dislocations described in Figure 4.19b, other dislocations have also been observed close to kink boundary.

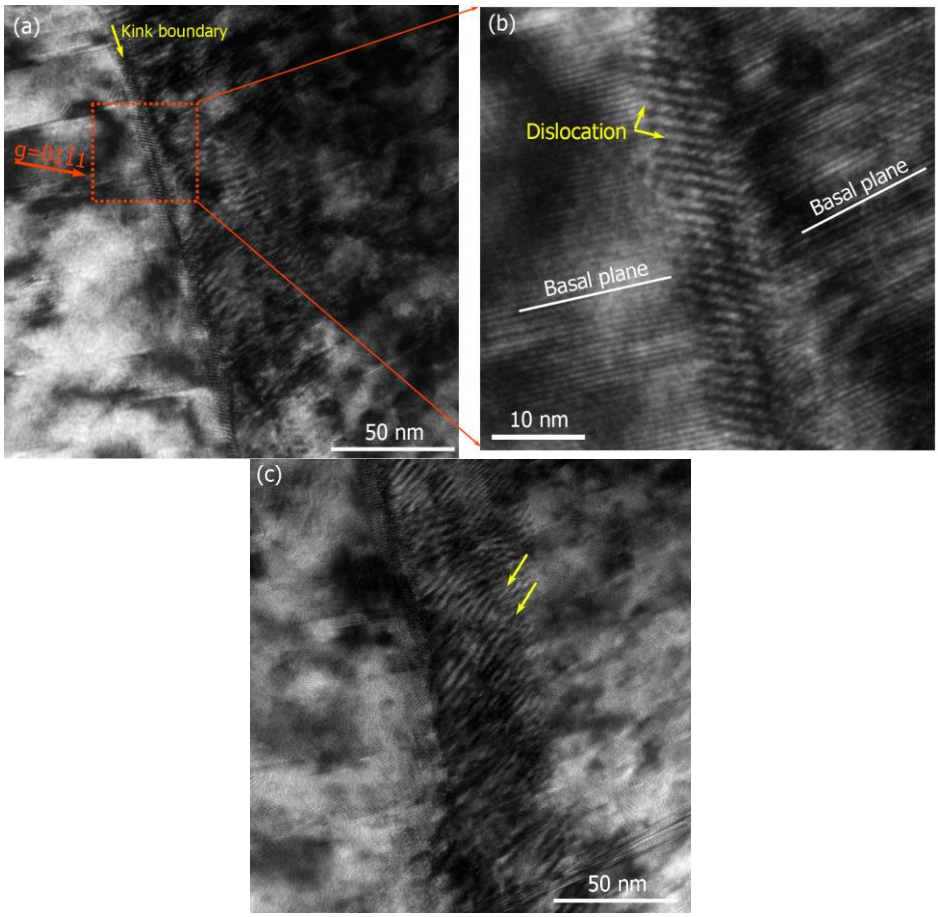

Figure 4.19 (a) Bright field image of a kink boundary in a LPSO/Mg region; the g vector indicated is to the left hand side of the kink boundary only; (b) a magnified image of dislocations in the kink boundary; (c) a bright field image showing other dislocations (indicated by yellow arrows) close to the kink boundary; beam direction close to $[1\bar{2}10]$.

Figure 4.20a shows another example of a kink boundary in a LPSO/Mg region. The kink boundary contains a straight part, whose magnified image in Figure 4.20b shows a dislocation wall. Besides the straight kink boundary, a less straight area is also indicated by arrows. This is probably because different types of dislocations can be generated and used to form the kink

boundary; and also the arrangement of the dislocations in the kink boundary can vary and form the less straight kink boundary (c.f. Figure 4.12a).

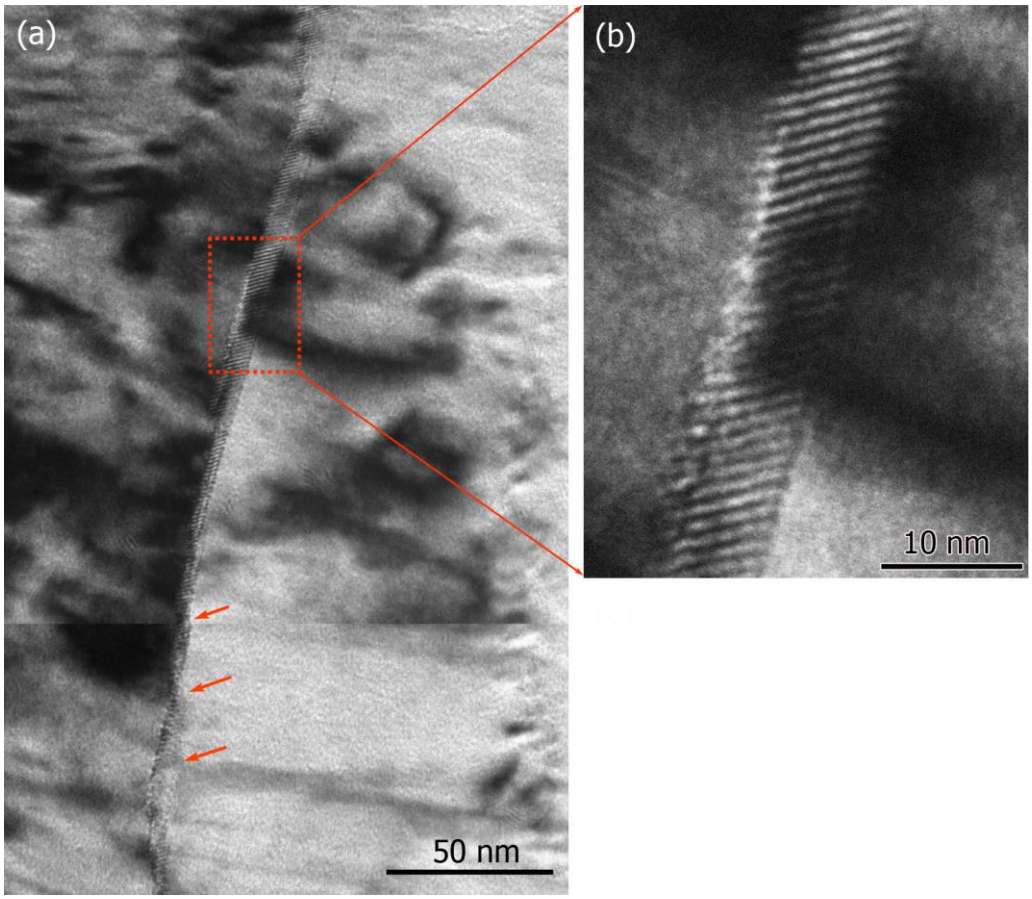

Figure 4.20 (a) Bright field image of a kink boundary in the LPSO/Mg region; (b) the magnified image showing the dislocation wall.

Figure 4.21a shows an LPSO/Mg region with a rotational morphology (c.f. Figure 4.18a). Some rotational kink boundaries are found in the top right corner of the image. A similar morphology is found in the left bottom corner where the LPSO lamellae show curvature. However, no kink boundaries were found in this area. A magnified image is shown in Figure 4.21b. The dark area is close to the Bragg condition for the (0001) reflection and is bounded by LPSO lamellae. This indicates that sudden orientation changes can be found in the LPSO/Mg interface. The red arrows

point at two misaligned LPSO lamella, which probably originate from the same LPSO lamella before deformation. This indicates that a movement of the LPSO lamellae has occurred in the c direction relative to the original LPSO lamellae. After tilting a few degrees for better imaging, dislocations with <c> component, indicated by the yellow arrows, were observed in this area.

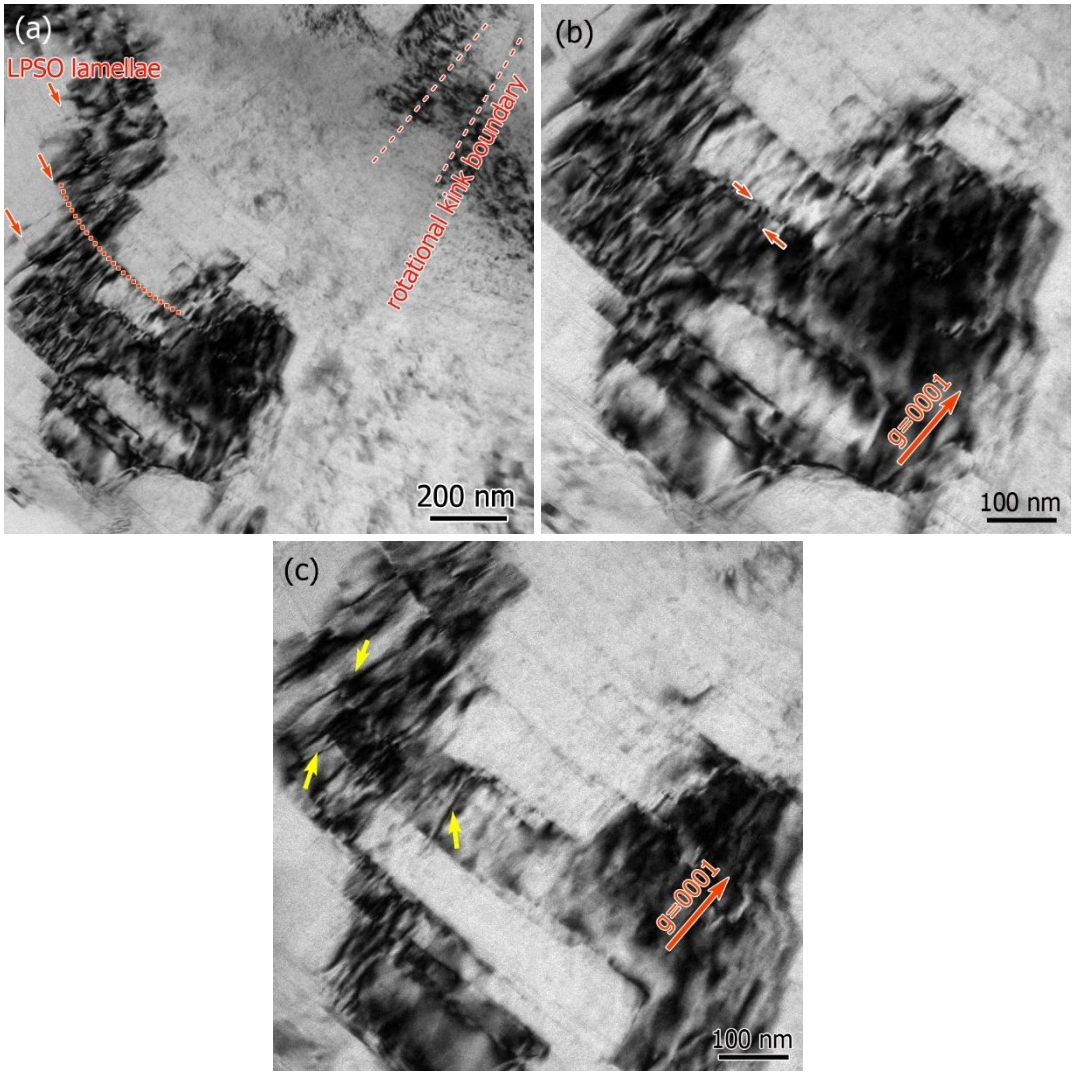

Figure 4.21 (a) Bright field image of a LPSO/Mg region showing rotational morphology; (b) a magnified image of the bottom left corner of Figure 4.21a; (c) same area as in Figure 4.21b after tilting a few degrees. The yellow arrows indicate the dislocations with <c> component.

4.4 Discussion

4.4.1 Kink deformation of LPSO phase

After compression, kinking occurs in the LPSO phase in Mg-Zn-Y alloys. In general, the kinking of LPSO tends to have larger misorientation angles when more strain is applied. Dislocations analysis in some kink boundaries in a 2% strained sample was carried out by TEM. The results show that the dislocations in the low angle kink boundaries of the LPSO phase generally are <a> type. This also applies to the dislocations in the regions other than the kink boundaries. The dislocations in the low angle kink boundaries are normally very straight and well aligned, while dislocations in the other regions are curly and not well aligned.

The misorientation angles of the low angle kink boundaries can be measured directly by diffraction patterns and the rotational angles of the basal plane and these values agree with the misorientation angles calculated by the dislocation spacing of the dislocations based on Equation 4.1. One low angle kink boundary has been confirmed rotating the basal plane around $[1\bar{5}40]$ zone axis by basal dislocations and the dislocation line directions appear to in the two directions.

It is well known that <a> type basal slip is the main slip system in the LPSO phase [63] [64]. This particular phase is highly anisotropic due to its unique crystallographic structure and is hard to deform except for by <a> type basal slip, i.e. no <c+a> or <c> dislocations or twinning can be activated. This agrees with the current findings. At higher temperatures, e.g. after hot extrusion at 400 ℃, limited activities of <a> type dislocations on prismatic planes has also been observed [66]. Consequently, kinking is common when the LPSO phase is subjected to plastic deformation where there is a sudden basal dislocation avalanche within a localized deformation zone.

Applying Hess and Barrett's dislocation model [72] to the LPSO phase, when only one type of <a> dislocations is generated, the rotation axis is $\langle 1\bar{1}00\rangle$ type. An example was shown in Shao. et al. [44], where a kink boundary with $[1\bar{1}00]$ rotational axis was composed of $\frac{1}{3}[11\bar{2}0]$ dislocations. However, the Mg-Zn-Y alloys are polycrystalline and the actual stress environment is more complicated. So more than one type of dislocation can be generated. This explains the current finding that a $[1\bar{5}40]$ rotational axis was found with two groups of dislocations. $[1\bar{5}40]$ is found between the $[1\bar{1}00]$ and $[0\bar{1}10]$ zone axes, which are probably composed of $\frac{1}{3}[11\bar{2}0]$ and $\frac{1}{3}[2\bar{1}\bar{1}0]$ dislocations by considering that the kink boundary is formed of geometrically necessary dislocations (GNDs). As reviewed earlier, the CRSS for $\frac{1}{3}\langle 11\bar{2}0\rangle$ type in LPSO phase is about 7 MPa [64], and it is the only dislocation system that is operative in LPSO phase under room temperature. So when the stress is close to c direction or perpendicular to the c direction, the simple $\frac{1}{3}\langle 11\bar{2}0\rangle$ type slips are unable to accommodate the stains. This is when kinking occurs. Due to different types of kinking can be generated in LPSO phase, it can accommodate the strains in various deformation directions. The typical kinking with $\langle 1\bar{1}00\rangle$ rotation axis can cause the titling of the basal plane, which leads to the movement of the material along c direction. Also the kinking angle can be very high, e.g. 130º observed in [44], which indicates large amount of strains can be accomodated by kinking.

4.4.2 Kink deformation of Mg/LPSO phase

In the area with LPSO phase, the Mg tends to deform like the LPSO phase. This can be divided into two cases: 1. Mg matrix around bulk LPSO; 2. LPSO/Mg structure, where the thin LPSO and Mg alternately arranged. The former has been reported by Shao. et al. [44] who reported that

a Mg nano-slice between bulk LPSO phases sheared along the kink directions by prismatic slip of $\frac{1}{2}[0001]$. However, this has not been reported elsewhere in the works on the Mg-Zn-Y alloys and cannot explain the massive kinks in the LPSO/Mg structure.

Yamasaki [76] divided the lattice rotation zone axis of LPSO kinking band into 3 main types by EBSD analysis: $\langle 1\bar{1}00\rangle/\langle 0\bar{1}10\rangle$, $\langle 0001\rangle$ and $\langle 1\bar{2}10\rangle$. The kinking with $\langle 1\bar{1}00\rangle/\langle 0\bar{1}10\rangle$ rotation axes form from basal $\langle a\rangle$ dislocations with Burgers vectors along close-packed directions, while $\langle 0001\rangle$ axes are considered to be an array of prismatic $\langle a\rangle$ type geometrically necessary edge dislocations and geometrically necessary screw dislocations. The $\langle 1\bar{2}10\rangle$ rotation axes is likely to be the combination of $\langle 1\bar{1}00\rangle$ and $\langle 0\bar{1}10\rangle$ axes.

The current finding by TKD indicates that the rotation axis of kinking (Figure 4.15) is distributed over a wide annulus including $\langle 1\bar{2}10\rangle$ and $\langle 0\bar{1}10\rangle$ zone axes. This is quite similar to the rotation axes proposed by Yamasaki [76]. However, the rotation zone axes are not restricted to specific crystallographic zone axes: they can be positioned in the annular area, which is likely to lie in the (0001) plane. This is due to the dislocation nature of the kink boundary. In a complicated stress environment, the basal <a> slip consists three individal Burgers vectors: $\frac{1}{3}[11\bar{2}0]$, $\frac{1}{3}[1\bar{2}10]$ and $\frac{1}{3}[\bar{2}110]$, and the combination of different dislocations can result in various rotational axes in the (0001) plane. This kind of kinking normally results in an accommodation of c direction strain.

A [0001] rotational axis of low angle grain boundaries is also observed in Figure 5.14 and Figure 5.16. These boundaries lie in the basal plane and cause a rotation of the crystal along the c-axis. So no strain was accommodated along c direction. It can not be called a kink boundary dut to the boundary is parallel to the slip plane. According to the definition of a kink band, it is a thin plate

of sheared material in a crystal, transverse to the slip direction, bounded by opposite ‘tilt walls’ of edge dislocations [76]. Nevertheless, basal low angle grain boundaries with [0001] rotational axis are frequently observed in the alloy. The GND for this type boundary is an array of screw dislocations [76].

The [0001] rotational axis type of kink boundary in a LPSO/Mg region is shown in Figure 4.17. These kink boundaries are in pairs with opposite rotation directions. It is reasonable to believe that the paired kink boundaries are formed by dislocation pairs with opposite Burgers vectors, as proposed by Hess and Barrett [72]. The double kinking morphology (paired kink boundaries located inside another pair of kink boundaries) has been reported for the first time. It is likely that the outside paired kink boundaries form first due to the deformation and when further stress is applied to the sample, the inside paired kinks occur.

The kink boundaries in a LPSO/Mg region are essentially composed of dislocations just like in the LPSO phase. Although the Burgers vectors of the dislocations in the kink boundaries of the LPSO/Mg have not been confirmed using TEM, it is reasonable to believe that the dislocations might be <a> type dislocations in most cases. This is based on the TKD results that <a> basal dislocations are the geometrically necessary dislocations for the most common rotation axes of the kink boundaries in LPSO/Mg. In addition, the morphology of the kink boundaries in the LPSO/Mg region is similar to that in the LPSO phase.

Differently from the LPSO phase, dislocations with <c> components also frequently exist in the Mg (Figure 4.21c). Kim et al. [68] reported that <c+a> type dislocations are observed in the Mg matrix in the presence of thin LPSO lamellae. The non-basal dislocations provide an alternative deformation mode in comparison to the LPSO phase. As indicated in Figure 4.21, the adjacent

area outside a rotational kinked LPSO/Mg region is deformed by non-basal dislocations; the non-basal dislocations accommodated similar strains along the c direction as in the kinked area.

4.5 Highlights

The main highlights of this chapter are summarised:

1. The dislocations in the low angle kink boundaries of the LPSO phase were clearly imaged under two beam condition in the TEM; this provides direct insight into the dislocation nature of the kink boundaries. The kink boundaries, essentially, are dislocation walls, composed of mainly basal <a> type dislocations.

2. The kink boundaries in the LPSO/Mg studied by TKD show that the rotation axes of the kink boundaries are located mainly in the (0001) plane. The rotation axes do not necessarily be a crystallographic zone axis; this is related to the dislocations.

3. The morphology of the dislocation walls in the kink boundaries of the LPSO/Mg region is similar to those in the LPSO phase. A double kinking morphology has been observed for the first time.

4.6 Conclusions

An as-cast $Mg_{94}Zn_2Y_4$ alloy containing LPSO and $Mg_{24}Y_5$ was compressed and ECAP processed separately. The deformed microstructure is investigated focusing on the dislocations in the kink boundaries of the LPSO phase and LPSO/Mg region. The following conclusions are drawn:

1. Deformation kinks have been observed after compressing at room temperature to 2%. The low angle kink boundaries in the LPSO phase are essentially dislocation walls, which are

composed of <a> type (Burgers vector of $\frac{a}{3}\langle\bar{2}110\rangle$) basal dislocations. One example shows a dislocation wall caused crystal lattice rotation around the $[1\bar{5}40]$ zone axis; two dislocation line directions have been observed in this kink boundary. The misorientation angles calculated using dislocation spacings are consistent with those measured by TEM.

2. The TKD results shows that the kink boundaries in the LPSO/Mg region have rotation axes mainly distributed around the edge of a stereogram with 0001 at the centre, from $\langle 1\bar{2}10\rangle$ to $\langle 0\bar{1}10\rangle$. The rotation zone axes are not restricted to specific crystallographic zone axes: they can be positioned in the annular area, which is likely to lie in the (0001) plane. An [0001] rotational axis has also been observed.

3. Paired kink boundaries rotating in two opposite directions with a resulting total kink angle of about zero have been observed in the LPSO/Mg region; this may be explained by the generation of dipole-pair dislocations as proposed by Hess and Barrett. The double kinking, one pair of kink boundaries located inside another pair of kink boundaries (c.f. double twinning), has also been observed.

4. The dislocation morphology of the kink boundaries in LPSO/Mg is similar to that in the LPSO phase. However, non-basal slip in the Mg can accommodate strains comparable to those in the kinked area.

5 The effect of ECAP on the microstructure and mechanical properties of $Mg_{94}Zn_2Y_4$ alloy

In this chapter, $Mg_{94}Zn_2Y_4$ alloys were modified by equal channel angular pressing (ECAP) with the aim of obtaining a bimodal structure and of improving the mechanical properties. The microstructure of the ECAPed alloys was investigated by a combination of SEM, TEM, EBSD and TKD. The deformation behaviours of LPSO, $Mg_{24}Y_5$ and the Mg matrix and their effects on the dynamic recrystallisation and microstructural evolution during the ECAP were discussed. The mechanical behaviour and fracture of the ECAP processed $Mg_{94}Zn_2Y_4$ alloys were studied using the small punch test (SPT). The role of coarse grains and DRXed grains in the fracture will be discussed.

5.1 Microstructure of ECAPed $Mg_{94}Zn_2Y_4$ alloys

Figure 5.1 shows the microstructures obtained from a transverse section (y plane) through a $Mg_{94}Zn_2Y_4$ ingot after different numbers of ECAP passes. The ED and the LD are indicated by the arrows. In contrast to the as-cast condition (Figure 5.1a), it can be seen that after 1 ECAP pass (Figure 5.1b) the grains are elongated and obvious flow lines can be observed. However, no obvious refining of the grains or of the LPSO phase was observed. The LPSO phase in the 1-pass sample tends to lie in the direction inclined to the shear direction (45° from ED towards LD). Some black regions, which were identified as $Mg_{24}Y_5$ particles and DRXed Mg grains, can be

observed along grain boundaries and large LPSO grain boundaries. After 2 ECAP passes, the Mg grains were fragmented, and the fraction of the DRXed Mg region increased. This trend continued in the 3 ECAP passes sample. The microstructure after 3 ECAP passes remained heterogeneous.

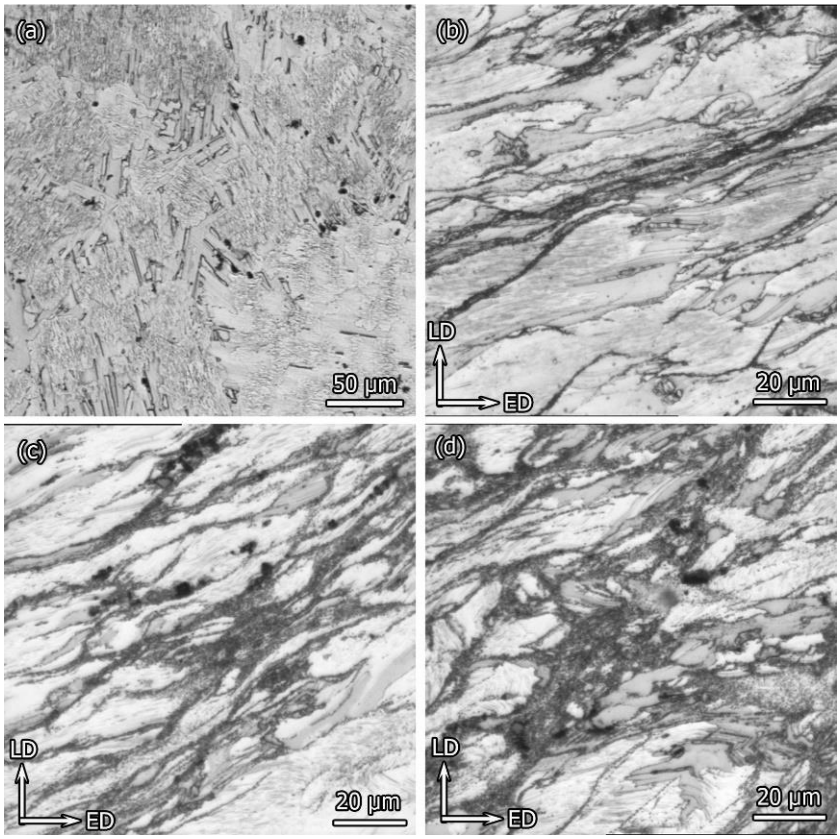

Figure 5.1 Optical images obtained from the $Mg_{94}Zn_2Y_4$ alloy (a) as-cast and ECAP processed for (b)1-pass, (c) 2-passes and (d) 3-passes, respectively.

The 2-pass ECAPed sample was analysed using SEM for better imaging of the DRXed grains (the dark areas in Figure 5.1c). Figure 5.2a and b show backscattered electron images obtained from the 2 ECAP passes sample. As indicated by the arrows, the DRXed grains are dark and the $Mg_{24}Y_5$ particles are white. The DRXed grains are mainly located around the deformed grains and secondary phases and formed a bimodal structure. The coarse deformed grains are elongated,

with a width of about 10-20 μm and a length less than 100 μm. The grain size of the DRXed grains, less than 1 μm, was measured from the TEM bright field images obtained from the 3 ECAP passes sample (Figure 5.2c). A high density of $Mg_{24}Y_5$ particles, typically 200 nm or smaller, appears in the grain boundaries of the DRXed grains. The diffraction patterns (e.g. inset to Figure 5.2c) obtained from the particles are consistent with those expected from the bcc $Mg_{24}Y_5$. Figure 5.2d shows some LPSO lamellae which are occasionally observed in the DRXed grains. The LPSO phase, however, is not frequently observed in the DRXed grains.

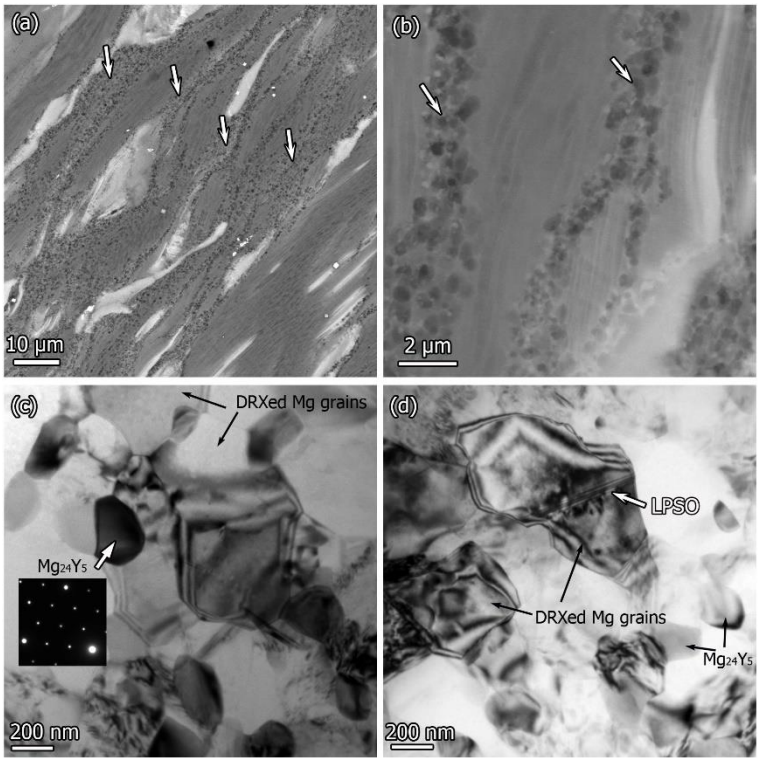

Figure 5.2 Backscattered electron image showing (a) at low magnification and (b) high magnification a region of DRXed grains in the 2-pass ECAP processed $Mg_{94}Zn_2Y_4$ sample; (c) TEM bright field image showing DRXed grains together with some $Mg_{24}Y_5$ particles in a 3-pass ECAP processed sample; a diffraction pattern along [111] obtained from the arrowed $Mg_{24}Y_5$ particle is inset; (d) TEM bright field image showing the occasionally observed LPSO phase in a DRXed grain in the 3-pass ECAPed sample.

5.2 Microhardness and small punch test (SPT)

The micro-hardness results from the ECAP processed samples are shown in Figure 5.3. The hardness of the as-cast sample is about 90 Hv, and an improvement of about 30% has been obtained after 1 ECAP pass, reaching 120 Hv. The hardness value increased but only slightly with further ECAP processing at about 5 Hv per pass.

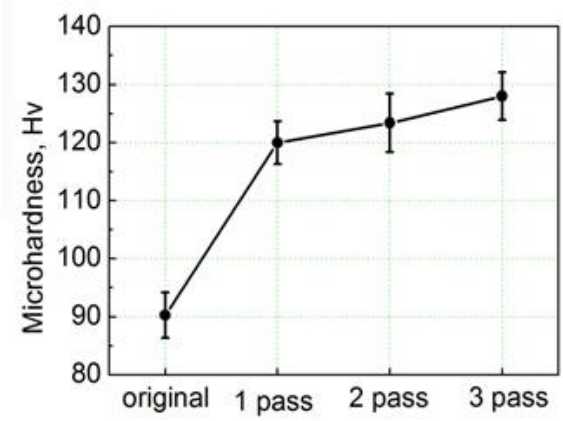

Figure 5.3 Micro-hardness of as-cast and ECAPed $Mg_{94}Zn_2Y_4$ samples.

The load versus displacement curves obtained from the SPTs are shown in Figure 5.4. The SPT load-displacement curves display (I) elastic bending, (II) plastic bending, (III) membrane stretching and (IV) plastic instability as described in [121]. After 1 ECAP pass, the maximum load before failure increased significantly compared to that of the as-cast sample. With more ECAP passes, the maximum load increased further by small amounts. Although the yield strength cannot be obtained directly from the SPT load-displacement curve, it can be linked to the load at breakaway, which is the value measured at the end of the elastic domain I [122]. Cheon and Kim [122] tested a SA508 pressure vessel steel and concluded that the yield stress is proportional to

the load at breakaway with a coefficient which varies with the material and the thickness of the sample. After 1 ECAP pass, the load at breakaway increased from about 60 N to about 100 N. After 2 passes and 3 passes the load at breakaway increased slightly further. This indicates that the strength of the sample increased with each ECAP pass.

In the ECAP processed samples, a distinct load deflection, as illustrated by the arrow in Figure 5.4, can be observed after the linear elastic region. The load continues to increase after the load deflection, and then starts to drop when the displacement reaches about 0.5 mm. In order to understand the origins of the load deflection, a 2-pass ECAPed sample was tested using SPT and stopped right after the load deflection (Figure 5.5).

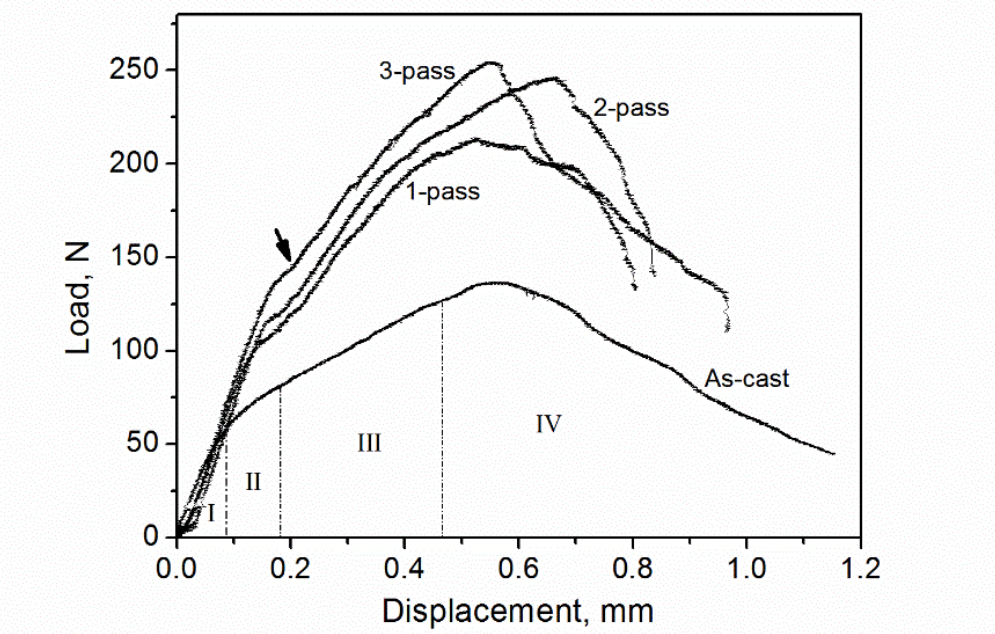

Figure 5.4 Load vs displacement curves obtained from the SPTs of the as-cast and ECAP processed samples.

5.3 Crack morphology of the SPT samples

Figure 5.5a and b show that a long crack had appeared in the 2-ECAP pass sample after the load deflected and the test was stopped. The corresponding SPT load-displacement curve is shown in Figure 5.5c. The back-scattered electron image (Figure 5.5b) shows that the crack is parallel to the shear direction of the ECAP process (i.e. 45° from ED to LD). Figure 5.5d shows that near the centre of the crack there is a region decorated with a large number of white small particles (see the magnified image) corresponding to the DRXed region associated with small $Mg_{24}Y_5$ particles. Figure 5.5e indicates some inclusions near the end of the crack. According to the EDS results (Figure 5.5f), the inclusions have high contents of Y, O and Mg, and probably came from the as-cast alloy.

Figure 5.6 shows the fractures after SPT tests were stopped until 50% load drop was reached; the fully developed cracks form a rosette pattern in both the as-cast and the ECAP processed samples. This indicates that the crack was initiated at the centre of the specimen. The crack pattern on the as-cast sample is more symmetrical than in the ECAP processed samples which have large cracks in the centre linked to secondary cracks father away. The higher magnification image obtained from the as-cast SPT sample (Figure 5.7a) shows a cleavage fracture with numerous facets. After the ECAP processing, the fracture surface (Figure 5.7b) contains cleavage features as well as micro-voids. Figure 5.7c and d show higher magnification images of the DRXed region in the crack surface.

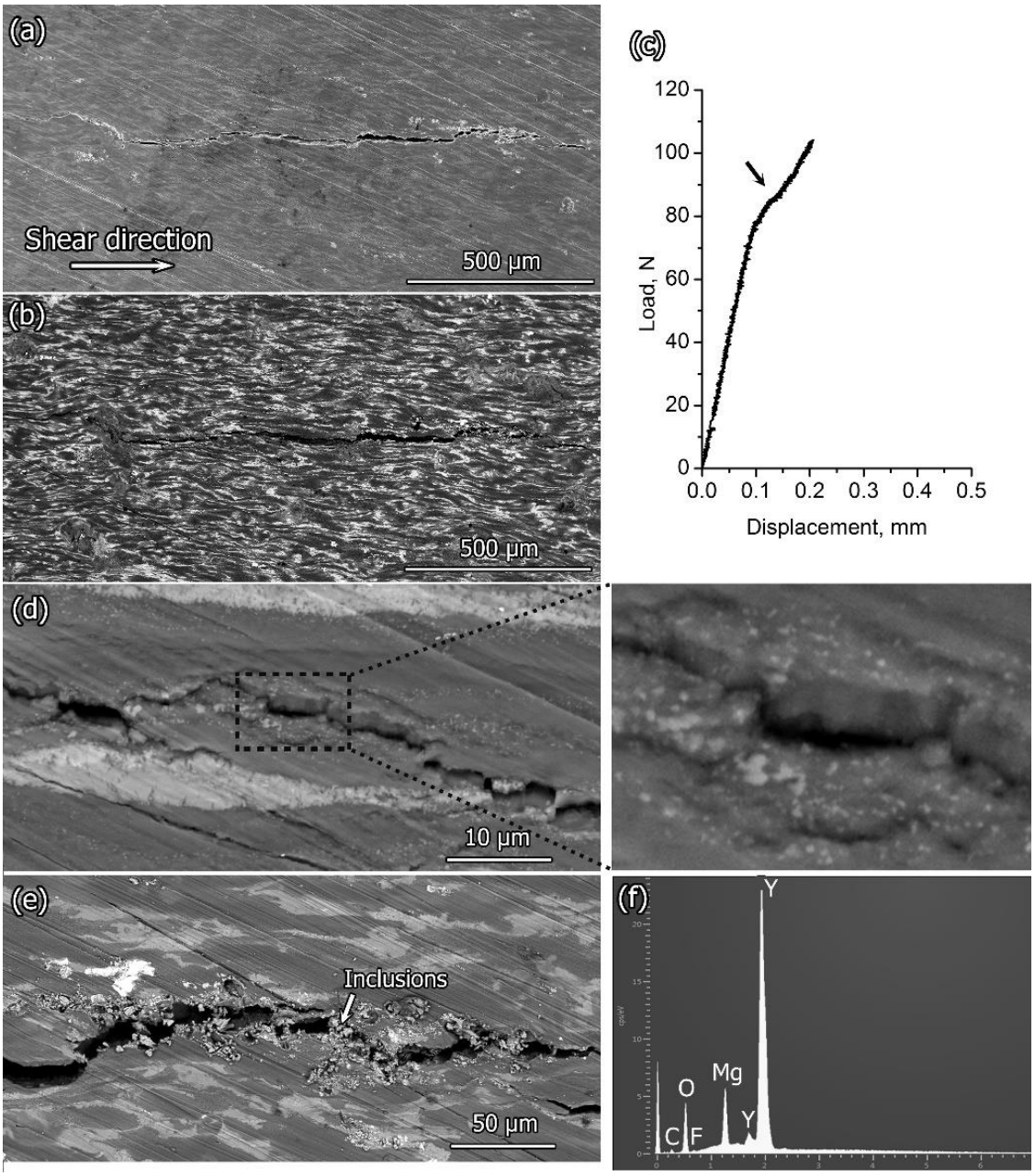

Figure 5.5 (a) Secondary electron image and (b) Backscattered electron image of 2-pass sample showing crack initiated during SPT; (c) Corresponding SPT load-displacement curve showing how the test was stopped when a load deflection was observed after elastic deformation (see arrow); (d) Magnified images showing that the crack goes through the DRXed region; (e) Inclusions in the crack; (f) EDS spectrum of the inclusions which have a high content of Y, O and Mg.

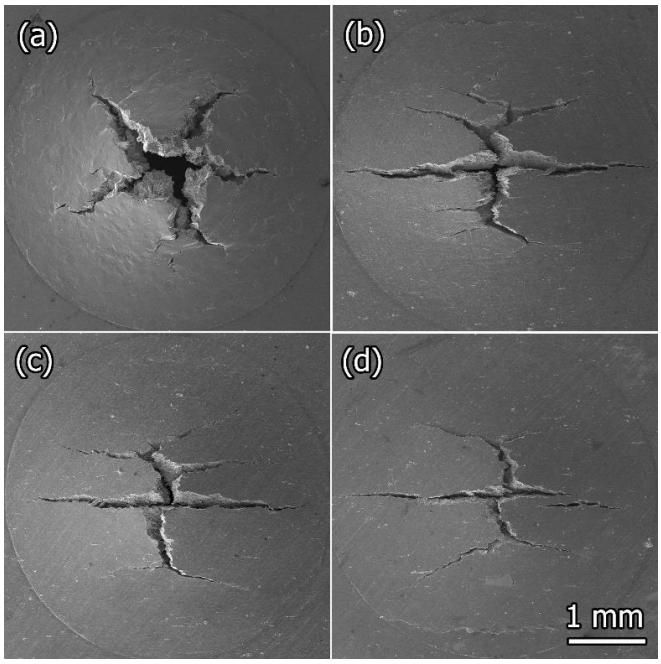

Figure 5.6 Low magnification SEM images showing cracks after SPT tests which stopped after 50% load drop has been observed: (a) as-cast sample; (b) 1 ECAP pass sample; (c) 2 ECAP passes sample; (d) 3 ECAP passes sample.

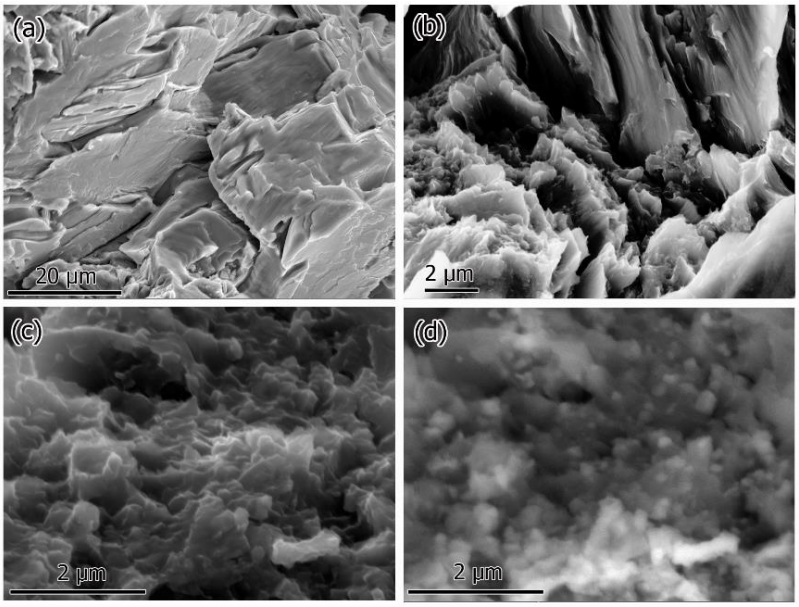

Figure 5.7 Images of fracture morphology in Mg-Zn-Y alloy after SPT: secondary electron images of (a) as-cast condition; (b) 2-pass sample; (c, d) secondary and backscattered electron images of the same area in the 2-pass sample.

In addition, fracture information from the sample processed by 1-pass ECAP at 200 ℃ is also provided in Figure 5.8. The SEM image shows some cavities at low magnification and some straight traces (as indicated by the dashed lines) along the shear direction. At higher magnification, lots of voids and particles of about 100 nm in size are observed as shown in Figure 5.8b. A large number of voids on the fracture surface is often linked to ductile failure. The morphology and size of the particles observed on the fracture surface and the $Mg_{24}Y_5$ particles shown in Figure 5.2 are very alike.

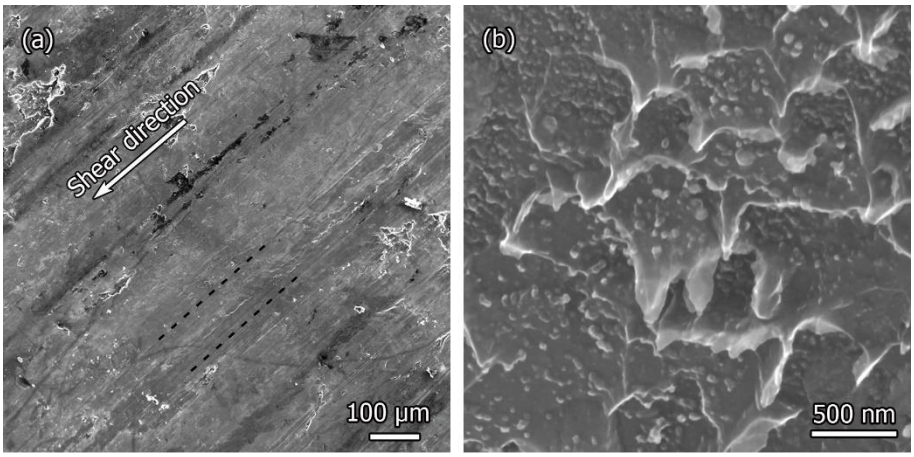

Figure 5.8 SEM images of fracture surface of the sample processed by 1-pass ECAP at 200 ℃: (a) lower magnification image shows a relatively flat surface; (b) higher magnification image shows a large density of voids and $Mg_{24}Y_5$ particles.

5.4 Texture evolution during ECAP

EBSD results mainly obtained from the coarse deformed Mg grains from y sections are shown in Figure 5.9. which indicates that strong textures have formed after ECAP. The orientation map of the as-cast alloy is given in Figure 5.9a, which suggests that the grains in the as-cast condition have random orientations. After 1 ECAP pass, the texture intensity peak in the (0001) pole figure is found at 60° from ED towards LD. After 2 passes two peaks are found (at 77° and at 41°).

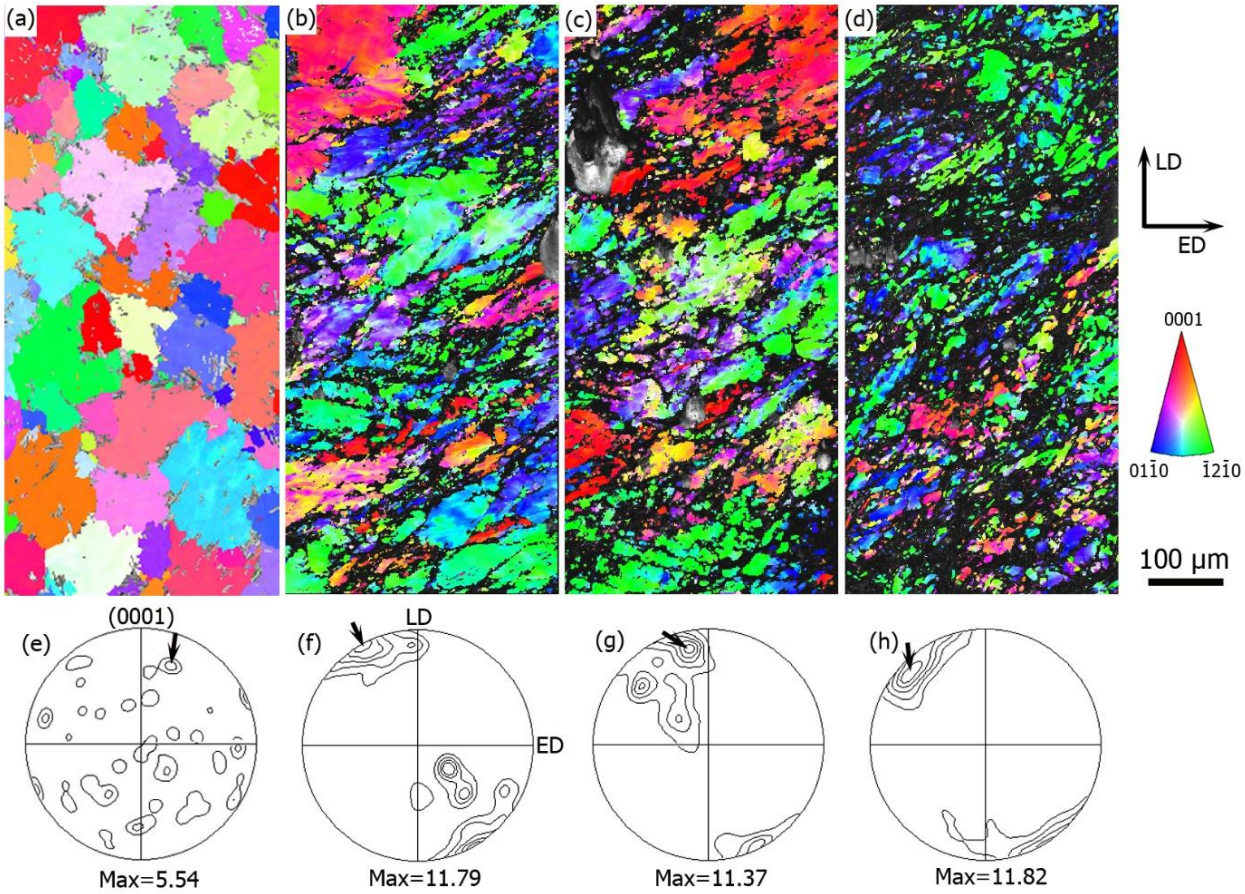

Figure 5.9 *EBSD results obtained from the as-cast and ECAP processed samples: (a-d) IPF colour images of as-cast, 1-pass, 2-pass and 3-pass ECAP samples respectively; (e-h) Mg (0001) pole figures of the as-cast, 1-pass, 2-pass and 3-pass ECAP samples. The interval of the contour lines is 2, and the maximum intensity is indicated by an arrow.*

After 3 passes, the basal plane is inclined at 45° to the ED. In principle, the texture of hexagonal crystals after the first pass of ECAP should be a simple shear fibre at 45° from ED to LD; after 2 passes with the sample rotated by 90°, the symmetry of the (0001) texture component formed after the first pass of ECAP is lost [123]. Valle et al [124] reported that an AM60 alloy, after 2 ECAP passes, showed a simple shear fibre texture. In the current experiment, the (0001) pole figures show that the key texture components after 1 – 3 passes of ECAP are all close to 45° from ED to LD.

The DRXed Mg grains are difficult to analyse using conventional EBSD due to their limited size and the presence of adjacent small $Mg_{24}Y_5$ particles. In order to characterise the texture of the DRXed grains, a thin foil of the 3-pass ECAP sample was studied using TKD. Figure 5.10a is a secondary electron image showing a deformed Mg grain surrounded by DRXed grains. The corresponding EDS maps (Figure 5.9b and c) show that Y is highly concentrated in some particles, and a slightly higher content of Zn element is also observed within the particles.

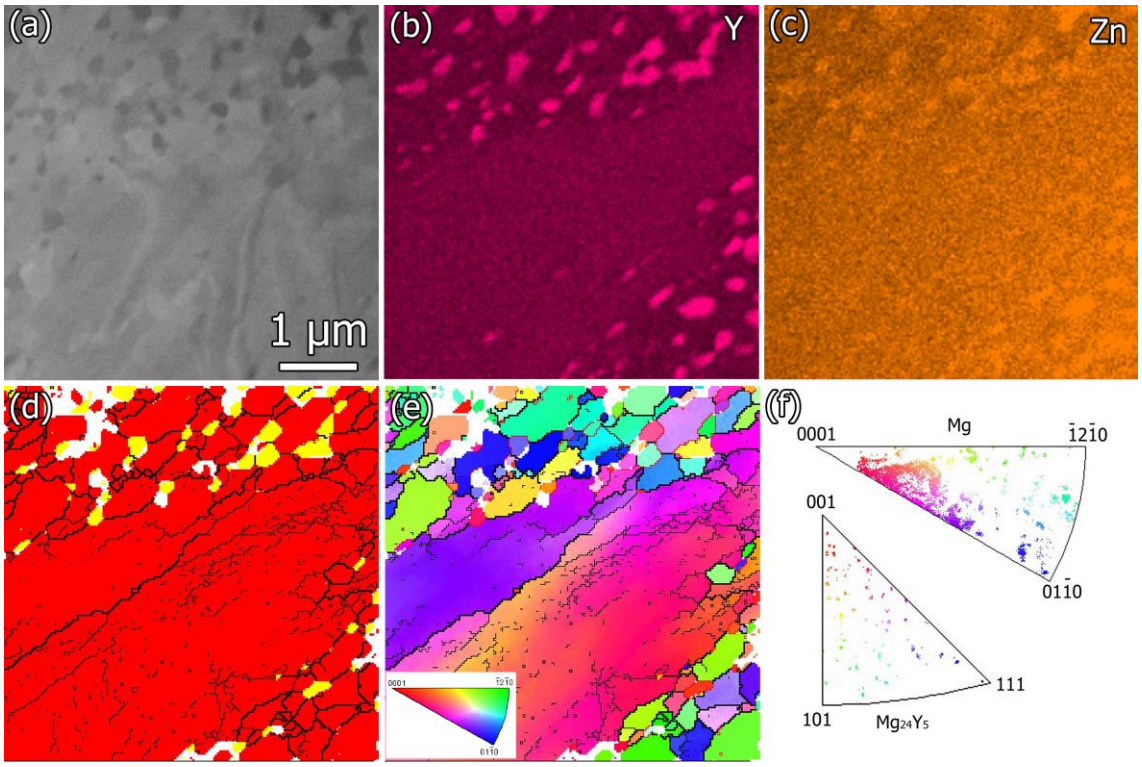

Figure 5.10 TKD results from 3-pass ECAP sample: a) Secondary electron image of a typical area; b) EDS map for Y; c) EDS map for Zn; d) TKD phase map, with Mg as red, $Mg_{24}Y_5$ as yellow and zero solution spots as white; (e) Orientation map; (f) inverse pole figures of Mg and $Mg_{24}Y_5$.

These particles are indexed as $Mg_{24}Y_5$ in the phase map (yellow phase in Figure 5.9d). Using also the orientation map (Figure 5.9e), the $Mg_{24}Y_5$ particles lie on the grain boundaries of small Mg grains (upper-left and lower-right area), and are absent from the large deformed Mg grains (centre area where two large deformed Mg grains are found) which contain lots of subboundaries. The inverse pole figures of both phases are shown in Figure 5.9f. Besides the heavily deformed magnsium, the recrystallized Mg grains and $Mg_{24}Y_5$ particles are scattered across the whole area, and there is no obvious texture in the recrystallised region.

5.5 Dynamic recrystallisation of Mg induced by kinking

Figure 5.11 shows backscattered electron images of the 3-pass ECAPed sample. Strings of small $Mg_{24}Y_5$ particles are commonly found in the kink boundaries of the LPSO phase or LPSO/Mg phase, as indicated by the red arrows. Strings of small $Mg_{24}Y_5$ particles are also frequently observed in the boundaries between the Mg matrix and the LPSO/Mg phase, as indicated by yellow arrows.

Figure 5.12a shows the forward scattered image of an LPSO/Mg area with DRXed grains. The brighter LPSO lamellae are in a Mg matrix and zig-sag shaped kinking is observed. Lots of $Mg_{24}Y_5$ particles are shown in the lower right part. The corresponding TKD orientation map (Figure 5.12b) indicates the orientation difference in LPSO/Mg caused by the kink boundaries. The kink boundary areas exhibit different morphologies which relate to the misorientation angles. For example, the kink boundary c with a misorientation angle of about 26° is relatively straight locally, which is also confirmed in the TEM image in Figure 5.12c. The kink boundary d, on the

other hand, has a misorientation angle of about 50°. Lots of grains, containing low misorientation angle grain boundaries, are located in the curly kink boundary. Figure 5.12d shows that the small grains exhibit a capsule shape with the long side along the kink boundary d. They contain the original lamellar LPSO which suggests that the boundaries moved via dislocation movement without any nucleation of new grains. The long side is actually a small KB. Some small $Mg_{24}Y_5$ particles are observed in the boundaries of the low angle grains as indicated by the arrow.

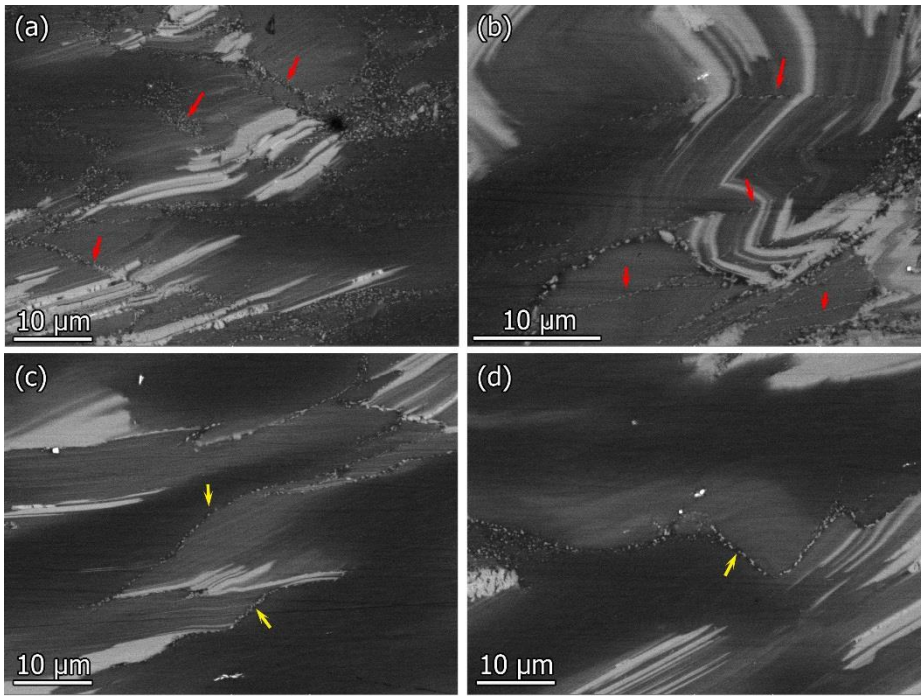

Figure 5.11 Backscattered electron image of 3-pass ECAP processed $Mg_{94}Zn_2Y_4$ alloy: (a, b) shows the small $Mg_{24}Y_5$ particles on the kink boundaries; (c, d) shows the small $Mg_{24}Y_5$ particles on the boundary between the LPSO and LPSO/Mg phase.

In the area e (Figure 5.12b), some recrystallised grains are observed. Judging from the surrounding area, it is reasonable to believe this area was originally a kink boundary. The misorientation angle measured from the left and right surrounding areas is about 110°, which is

larger than kink boundaries c and d. The DRXed grains shown in Figure 5.12e have a polygon shape and have grown into the deformed area. $Mg_{24}Y_5$ particles are also observed.

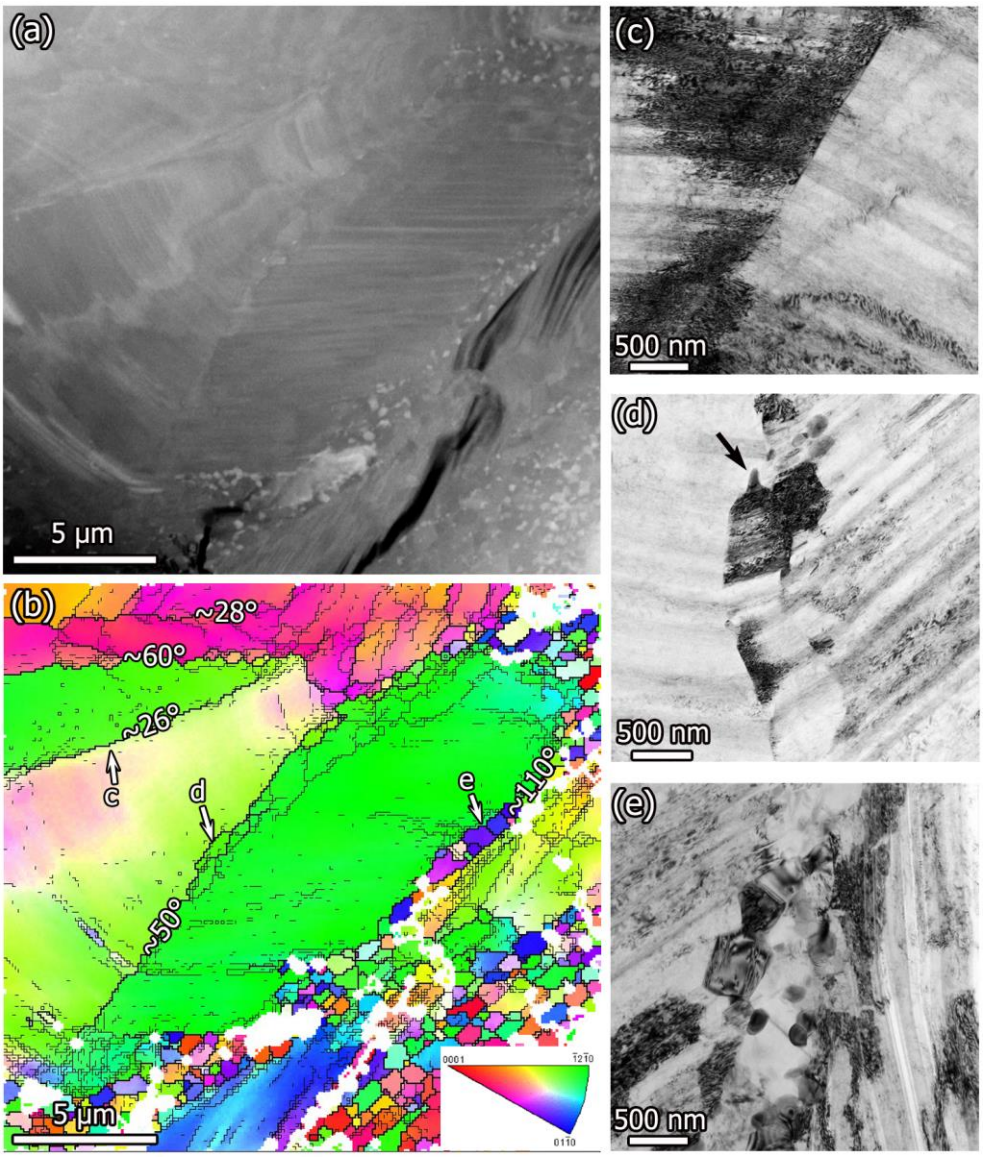

Figure 5.12 (a) Forward scattered image of 3-pass ECAPed sample; (b) orientation map of Mg; the values inserted in the grain boundaries represent the misorientation angles; (c-e) TEM bright field images corresponding to the area in Figure 5.12b, the image is rotated anticlockwise about 30-40° in the TEM.

5.6 Microstructural evolution of pre-existing $Mg_{24}Y_5$ particles

Figure 5.13 shows the typical morphology of the $Mg_{24}Y_5$ particles after 3 ECAP passes. Figure 5.13a shows a long particle which has cracked and also become thin in some areas. In the higher magnification image (Figure 5.13b), fragmented particles (indicated by the arrows) are found in the thin area. The morphology of the thin $Mg_{24}Y_5$ particle area resembles the necking morphologies reported in the literature [125] [126]. Figure 5.13c shows an area with $Mg_{24}Y_5$ particles of irregular shape detaching from a large $Mg_{24}Y_5$ particle. The higher magnification image (Figure 5.13d) shows some sawtoothed shaped particles (like the micro-sized necking), as indicated by the white arrows. The black arrow indicates a piece of $Mg_{24}Y_5$ particle being torn off from the large particle to its right. This detaching particle has an irregular shape and sharp facets.

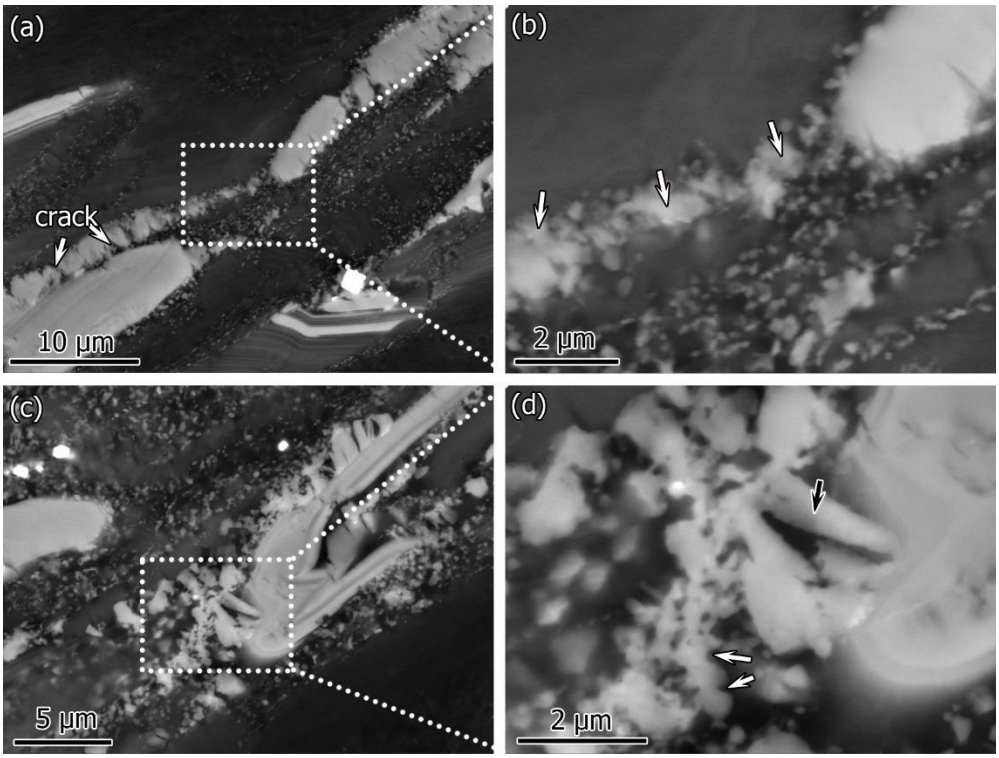

Figure 5.13 Backscattered electron images obtained from a 3-pass ECAPed sample showing the morphology of the $Mg_{24}Y_5$ phase.

Figure 5.14a shows an SEM image of a 2-pass ECAPed alloy. This area contains lath shaped $Mg_{24}Y_5$ surrounded by LPSO and Mg. The corresponding phase map is shown in Figure 5.14b. The $Mg_{24}Y_5$ lath has a few locations which failed in the EBSD indexing, presumably due to the localised deformation at these locations. The orientation map in Figure 5.14c shows that the lower half of the $Mg_{24}Y_5$ lath has an orientation very different from the top half. Unlike $Mg_{24}Y_5$, no sudden orientation change can be observed in LPSO and Mg as a result of deformation.

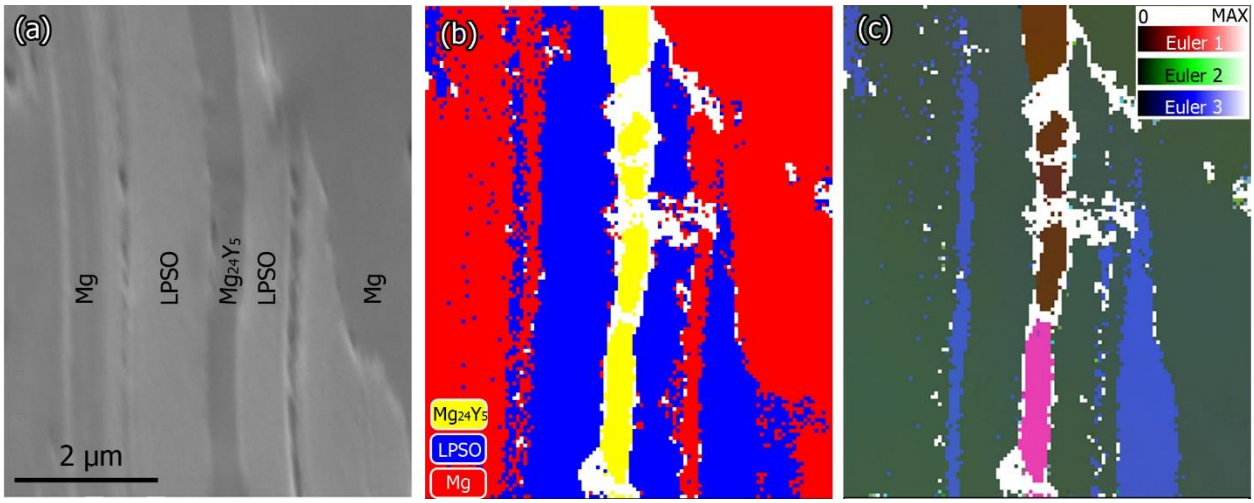

Figure 5.14 (a) Secondary electron image of 2-pass ECAPed Mg-Zn-Y alloy; (b) conventional EBSD phase map; (c) orientation map of the same area.

Figure 5.15a shows a forward scattered electron image of a deformed $Mg_{24}Y_5$ particle in a 2-pass ECAPed sample. Micro-cracks can be observed in the $Mg_{24}Y_5$ particle, but not in the surrounding Mg. Figure 5.15b and c show the TKD orientation maps from the Mg and $Mg_{24}Y_5$ respectively. As indicated by the arrows, small Mg grains are found inside the cracks in the $Mg_{24}Y_5$ particle. The orientations of the small Mg grains are quite different from each other, indicating that these are probably DRXed grains. The crystal orientation of $Mg_{24}Y_5$ changes gradually inside each part of the $Mg_{24}Y_5$ particle. Between different parts of the particle, the orientation variations are

obviously larger than that inside the individual part. The misorientation angle profile along the line AB in Figure 5.15c is plotted in Figure 5.15d, which confirms that the misorientation changes are normally smaller than 2° within each individual piece and less than 10° between neighbouring pieces.

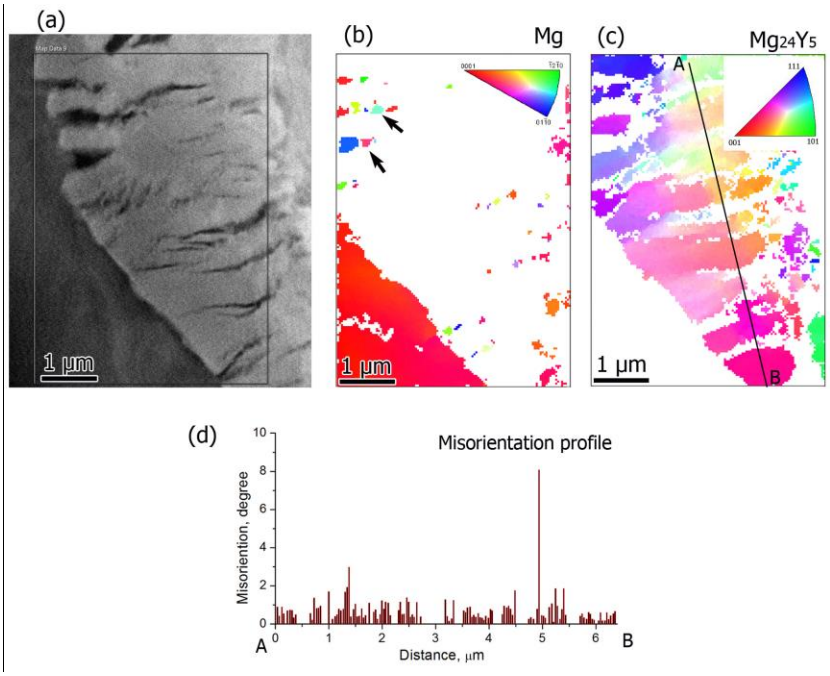

Figure 5.15 (a) forward scattered electron image of a 2-pass ECAPed Mg-Zn-Y alloy showing many cracks in large $Mg_{24}Y_5$ particle; (b) orientation map of Mg only; (c) orientation map of $Mg_{24}Y_5$ only; (d) relative misorientation angle profile along AB line in Figure 5.15c. Note that after 3 hours of TKD scanning, the orientation maps (b) and (c) drifted relative to the electron image in (a) which was taken at the beginning of the scan.

Figure 5.16a shows an area containing irregularly shaped bright particles in the 2-pass ECAPed sample. The EDS map of Y (Figure 5.16b) indicates that Y is rich in the bright particles and the phase map (Figure 5.16b) confirms that the bright particles are $Mg_{24}Y_5$. The orientation map (Figure 5.16d) show that the $Mg_{24}Y_5$ particle in the centre of the image has gradually changing orientation and contains a few low angle grain boundaries with misorientations of less than 10°.

The surrounding $Mg_{24}Y_5$ particles are composed of small grains a few hundred nanometres across and with random orientations. Compared with the original $Mg_{24}Y_5$ particles which were around 20 μm across and assuming one orientation within each particle in the cast alloy, it is likely that these small $Mg_{24}Y_5$ particles with random orientations are formed during the ECAP, and so were the low angle grain boundaries in the central $Mg_{24}Y_5$ particle. Some 'necking'-like features in the $Mg_{24}Y_5$ particles are observed in Figure 5.16a, indicated by the arrows. According to Figure 5.16b and c, these necking-like features correspond to small newly formed $Mg_{24}Y_5$ particles joining together.

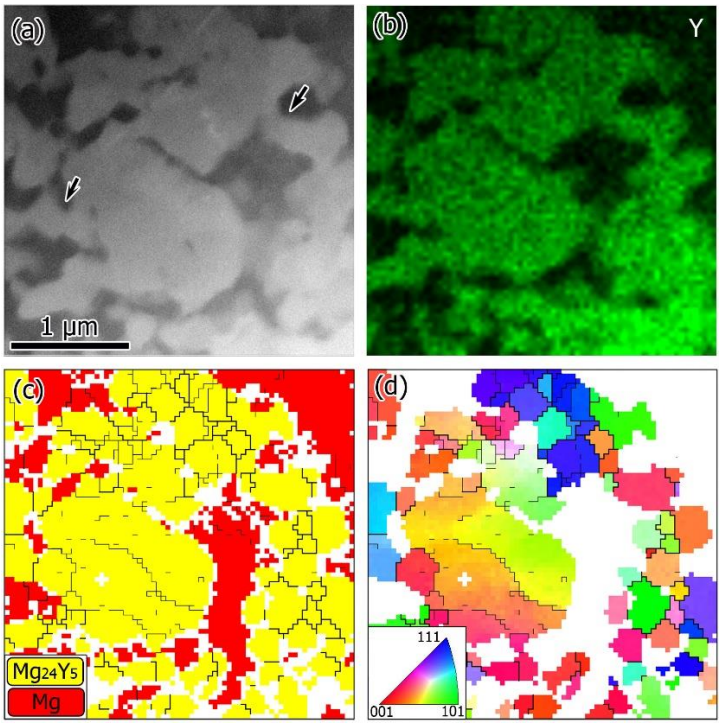

Figure 5.16 (a) FSE image of 2-pass ECAPed sample; (b) EDS map of Y; (c) phase map with magnesium in red, $Mg_{24}Y_5$ in yellow and unindexed spots in white. The unindexed spots are mainly due to the fact that Mg and $Mg_{24}Y_5$ may overlap in the TEM foil thickness direction, which causes difficulty indexing the Kikuchi patterns. The thick black lines are grain boundaries with a misorientation larger than 10°; the thin black lines are boundaries where the misorientaion lies between 2° and 10°; (d) $Mg_{24}Y_5$ orientation map.

Figure 5.17a shows a TEM bright field image of a deformed $Mg_{24}Y_5$ particle. A crack can be seen in the centre of the image, as indicated by the dashed line. Within the crack, a string of small $Mg_{24}Y_5$ particles are surrounded by Mg.

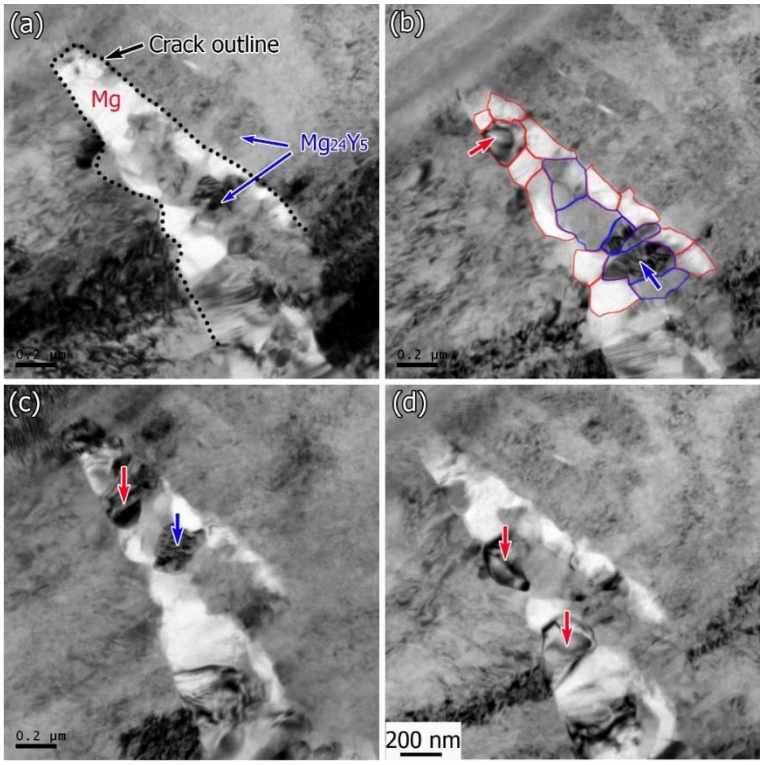

Figure 5.17 TEM bright field images taken using many beam imaging conditions showing a deformed $Mg_{24}Y_5$ particle with a crack in the centre in a 2-pass ECAPed sample. (a-d) images after tilting showing small grains of Mg and $Mg_{24}Y_5$ inside the crack. The dashed line in Figure 5.17 (a) indicates the outline of the crack. The red and blue grains/arrows indicate the DRXed Mg and $Mg_{24}Y_5$ grains respectively.

To further characterise the microstructure, the specimen was tilted to obtain changes in the diffraction contrast of the grains (Figure 5.17b-d). The grains highlighted in red and blue (in Figure 5.17b) are Mg and $Mg_{24}Y_5$ respectively. Both Mg and $Mg_{24}Y_5$ grains within the crack have different orientations, indicating these are recrystallised grains. This observation agrees with

the SEM results shown in Figure 5.15 where newly formed Mg grains were found in the cracks of a large $Mg_{24}Y_5$ particle.

5.7 Discussion

5.7.1 Dynamic recrystallization (DRX) of Mg

The grain size and texture of the Mg-Zn-Y alloys changed significantly after ECAP. The microstructure resulting from ECAP exhibits a bimodal grain size: coarse deformed grains (including Mg and LPSO) and fine DXRed Mg grains associated with small $Mg_{24}Y_5$ particles.

In the ECAPed Mg-Zn-Y alloys, the DRXed grains are found in the following areas: 1. around deformed Mg grains mainly; 2. around LPSO and LPSO/Mg regions; 3. in the kink boundaries of LPSO/Mg; 4. near $Mg_{24}Y_5$ phase

5.7.1.1 Rotational DRX induced by grain boundaries

The DRXed grains in the ECAPed alloys are found mainly around the deformed Mg large grains. This is consistent with the microstrucuture observed in extruded Mg-Zn-Y alloys [90]. Ion et al. [102] suggested that in LPSO-free alloys, e.g. Mg-0.8%Al solid solution, DRXed grains formed from the severely rotated regions adjacent to the original grain boundaries and that the original grain centre remain unchanged. The current morphology of the DRX agrees with rotational recrystallisation.

5.7.1.2 DRX around the LPSO and LPSO/Mg

The DRXed Mg grains are also found around large LPSO grains and LPSO/Mg regions, although the largest number of DRXed grains is found around deformed Mg grains. The close linkage between DRX and LPSO phase has also been reported elsewhere [90] [110]. It was suggested that the LPSO phase can accelerate DRX through particle-stimulated recrystallisation [110]. Humphreys [109] proposed that if the particle is non-deformable then local plastic deformation must maintain the particle in its original shape, leaving the matrix sheared, and that DRX occurs in the deformed zone near the particles.

However, the LPSO phase is deformable and is only a little harder than the Mg matrix [127]. The critical resolved shear stress (CRSS) of basal slip for a Mg-1.0Y single crystal is about 9.5 MPa [65], which is slightly higher than that of the LPSO phase (about 7 MPa) estimated using single phase LPSO pillar compression [64], and lower than the 10-30 MPa estimated by compression of directionally solidified polycrystalline LPSO [63]. This is different from typical particle stimulated recrystallisation where the particles are typically non-deformable. However, although the LPSO phase is deformable, the fact that its plasticity is confined to basal slip suggests that it would not be possible to transfer any non-basal slip activity in the Mg matrix into the LPSO phase. Strain localisation in the vicinity of the LPSO is therefore expected and would also promote the DRX.

5.7.1.3 DRX of Mg induced by kinking

When the misorientation angle of the kink band in LPSO/Mg increases, low angle grains tend to form at the kink boundaries and eventually DRXed Mg grains are observed. This indicates the nucleation of DRXed grains in the original KBs, especially the ones with high misorientation

angles. This phenomenon has not been reported for Mg-Zn-Y alloys in the literature. The DRX of Mg induced by kinking can be explained by the following reasons.

Firstly, the nucleation of DRXed grains is driven by the stored dislocations built up during the deformation. The kink boundary is formed by the rearrangement of the dislocations, which is essentially composed by dislocation walls regardless of dislocation type. According to the dislocation model of a low angle grain boundary, described in Equation 4.1, the edge dislocation spacing D can be calculated from the misorientation angle. The Burgers vector <a> in Mg is $\frac{1}{3}\langle 1\bar{2}10\rangle$ and the magnitude is 0.3209 nm. If θ is 15°, then the distance between adjacent dislocations is about 1.23 nm. When θ increases, the distance decreases. The high angle KB contains higher density of dislocation.

Secondly, the kink boundary is an efficient barrier to dislocation movement during further deformation. In the highly anisotropic LPSO/Mg structure, the dislocations tend to have similar types as the initial dislocation forming the kink boundary, so it is on unfavourable geometry for dislocations to pass. The higher the misorientation, the more difficult for the dislocation to go through. So the DRXed grains tend to form first in the high misorientation angle kink boundaries.

5.7.1.4 Absence of DRX in LPSO

The kinking is more dominant in the LPSO phase than in the LPSO/Mg, but DRX grains are absent from LPSO according to the literature and in the current work. This indicates that the activation energy for DRX of LPSO is much higher than that of the Mg matrix. This will be discussed in two parts.

Firstly, DRX is more favoured in materials with low stacking fault energy (SFE), such as Cu and Ni [96]. Dynamic recovery is limited and a large density of dislocations provides sufficient energy for DRX. Fan et al. [128] calculated the SFE energy for multi-stacking fault structures of Mg, which is similar to LPSO, but with no Zn and Y alloying elements. The results show the SFE for 18R structure ($3I_2$) is about 94.02 mJ/m^2, which is much higher than the SFE of 2H Mg of about 33.84 mJ/m^2. The effect of alloying elements on the SFEs of the LPSO are not reported. Datta et al. [129] reported that a Mg with ABACAB stacking has an intrinsic SFE of about 80.6 mJ/m^2, which is higher than that of 2H Mg with AB stacking of about 29.2 mJ/m^2. Datta et al. [129] also reported that the addition of 2% Zn into the Mg with ABACAB stacking leads to a decrease in the SFE to 18.9 mJ/m^2, while addition of 2% Y lead to an increase in the SFE to 113.2 mJ/m^2. The SFEs of the LPSO is probably higher than Mg, so DRX is unfavourable to occur in LPSO.

Secondly, the growth of DRXed grains requires movement of high angle boundaries. In Mg matrix, Zn and Y are present. The mobility of grain boundary can be inhibited by the solute elements. This is especially significant in metals with low solute levels, e.g. 0.01 wt.% Fe was added into a ultra-high purity Al and the recrystallisation temperature increased from room temperature to 250 ℃[130] [131]. The activation energy for the DRX with the presence of moderate purity level solute elements are expected for the bulk diffusion, which is higher than the grain boundary diffusion in the high purity metals.

In LPSO phase, the DRX requires the formation of the large cell and rearrangement of the Zn and Y elements at long range. So diffusion of the Zn and Y in LPSO phase are essential. However, these values have not been reported. Based on the LPSO structure, Zn and Y are segregated into

two or four layers in the LPSO and even form Zn_6Y_8 clusters when the Zn and Yconcentration are sufficient. This special configuration lowers the energy of the LPSO phase and accommodates the strain caused by size differences of Zn and Y during its formation [132]. Thus, the LPSO is quite stable at room temperature and the diffusion rates of Zn and Y in the LPSO phase are expected to be quite low. Although Zn and Y diffusion in LPSO occurs at relatively high temperature (for example, the 18R transforms into 14H during heat treatment at about 500℃), but the diffusion only cross short distance. Kim et al. [133] suggested only one close-packed atomic layer needed to move for 18R to 14H transformation. The resultant 14H shares the same basal plane with the original 18R. However, in order to form DRX grains, long-range diffusion of Zn and Y is necessary. The difficulty of Zn and Y movement may lead to the absence of DRXed grains in LPSO phase.

5.7.1.5 DRX grain growth controlled by $Mg_{24}Y_5$ particles

Accompanying the DRXed grains, small $Mg_{24}Y_5$ particles have formed. The concentration of Y in the Mg matrix is high, so the precipitation of $Mg_{24}Y_5$ particles might be assisted by the large shear strain imposed and therefore the high dislocation density caused by the ECAP process. For instance, the sub-grain boundaries in the deformed microstructures may act as heterogeneous nucleation sites for $Mg_{24}Y_5$ particles. This is also consistent with the observation that the $Mg_{24}Y_5$ particles observed always lie along the grain boundaries of the DRXed grains. The $Mg_{24}Y_5$ particles could effectively restrain grain growth by inhibiting boundary migration. Such an effect could be estimated following the Zener-Smith equation $d_{crit} \approx 4r/3f$ [134], where d_{crit} is the critical grain diameter, r is the radius of the particle and f is the volume fraction of the particles. The critical grain size is about 1 μm, taking the volume fraction and radius of the $Mg_{24}Y_5$

particles to be about 16 % and 120 nm (estimated from TEM observations) in the DRXed regions. The measured average DRXed grain size is about 600 nm and the largest is around 1 μm. This agrees with the critical grain size. The SPT strength of the Mg-Zn-Y alloys increased significantly after ECAP, which comes as no surprise due to the reduced grain size.

5.7.2 Analysis of crack in SPT of bimodal structure

The SPT crack morphology of the bimodal structure is quite different along the ECAP shear direction and in the perpendicular direction. The initial crack, observed immediately after elastic deformation, lies in the direction parallel to the shear direction.

Figure 2.22 shows a schematic drawing of the ball and disc contact during SPT. The sample disc is round with its edge supported by the die and the loading is applied to the disc though the spherical ball. The stresses on the disc are symmetrical along the radial directions. As shown in Figure 5.5 and Figure 5.6, the crack starts in the central region of the bottom surface. Byun et al. [135] described the stress state at the centre of the bottom surface and indicated that the principal stress component along the z direction, σ_{zz}, is zero as the bottom surface is free of contact. The stress state is biaxial and the two perpendicular principal stress components along the x and y directions, σ_{xx} and σ_{yy}, are equal and always tensile. The 3D stress state at the bottom centre is also shown in Figure 5.18a. Figure 5.18b shows a schematic drawing of the bimodal structure of the ECAP processed alloy under tensile stress. The deformed coarse grains show a fibre texture according to the EBSD data, where the c direction is indicated in the figure. The DRXed Mg grains (coloured ones) show random orientations mainly located in the interior of the coarse deformed grains.

When the tensile stress applied to the bimodal structure increases, the large Mg grains, LPSO phase and DRXed grains start to deform at different stress levels. The deformation sequence of $Mg_{97}Zn_1Y_2$ alloy with a bimodal structure has been investigated by Garces et al. [91], who suggested that the coarse Mg grains deform when the stress is below the macroscopic yield stress, followed by the fine Mg grains above the macroscopic yield strength with the coarse LPSO grains remaining elastic. The Mg matrix deformation is dominated by twinning and basal slip. However, in the present study, no twinning has been observed during ECAP. In fact, kinking was frequently observed in the Mg matrix associated with the abundant LPSO phase.

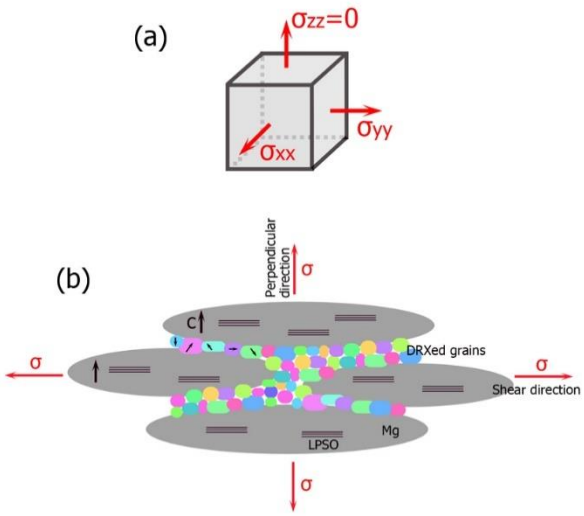

Figure 5.18 (a) The 3D stress state at the bottom centre of the disc; (b) The biaxial stress state of the bimodal structure at the bottom centre.

As indicated in Figure 5.18b, the deformed large grains show a preferential fibre texture, with the basal plane being parallel to the shear direction. The dominant basal slip of the deformed Mg and LPSO in the shear direction and its perpendicular direction is suppressed by the low Schmid factor, close to zero. Prismatic slip, pyramidal slip and twinning are limited by the small spacing between the LPSO lamellae in the Mg matrix. So, deformation of the large Mg grains is unlikely

in both directions. Compared with the large Mg grains, the macroscopic yield stress of the DRXed grains is normally higher due to the presence of the grain boundaries. In this case, the DRXed grains have random orientations and include many grains with high Schmid factors which started to deform plastically first. The DRXed grains can only accommodate limited strain. With increasing stress, the DRXed grains can not longer accommodate the imposed strain and cracks start to form. In the bimodal structure DRXed grains occupy thin layers between the deformed Mg grains, almost parallel to the shear plane and continuously across the whole sample. Once the crack has formed in the DRXed grain region, it will grow easily along the shear direction since there is a perpendicular tensile stress component. This leads to a less symmetrical morphology of the fully developed cracks in the ECAP processed alloys compared to that of the as-cast alloy. Yamasaki et al. [90] reported that the DRXed grains increased the ductility of the extruded $Mg_{97}Zn_1Y_2$ alloys, which seems contradictory to the current result that the DRXed grains act as potential crack sites during SPTs. It needs however to be clarified that Yamasaki et al. [90] studied the extruded samples which has different textures comparing to the ECAPed samples and focused on the ductility changes caused by different area fractions of DRXed grains in the extrusion direction, while this work focused on comparing the ductility differences of the bimodal structure in different directions and the direct evidence for ductility changes after ECAP is not provided. The DRXed grains accommodate the initial deformation in both directions and become potential crack sites during further deformation. When the tensile stress is applied to the shear direction, the crack can be hindered by the coarse Mg and LPSO grains. But when the tensile stress is applied to the perpendicular direction, the cracks can grow freely along these DRXed grains. This indicates that the effect of DRXed grains on the ductility may be different in the shear direction from the perpendicular direction.

During the ECAP process, large shear strains were introduced to the sample resulting in a bimodal microstructure containing large deformed Mg grains and DXRed grains associated with fine $Mg_{24}Y_5$ particles. In general, the grain size is reduced when more ECAP processing are performed. As discussed before, a significant grain size reduction is caused by the dynamic recrystallization. The deformed grains were refined by kink formation in the LPSO phase and LPSO/Mg region, where lots of kink boundaries were introduced to the specimen. There is no doubt both hardness and SPT strength are significantly increased after only 1 pass, although not much difference can be found between 1 pass, 2 passes and 3 passes. A crack is observed instantly after the elastic part of the SPT test, which indicates that the ductility of the bimodal structured alloys is poor.

5.7.3 Fragmentation of $Mg_{24}Y_5$ particles during ECAP

Unlike the LPSO phase, the pre-existing $Mg_{24}Y_5$ is a complex intermetallic compound, just like $Mg_{17}Al_{12}$, and shows extreme brittleness at room temperature [136]. The existence of large intermetallic particles is often undesirable due to their brittleness and the likelihood of crack initiation. On the other hand, fine and well dispersed intermetallic particles are very effective strengthers.

The present work confirms the fragmentation of the original large $Mg_{24}Y_5$ particles during ECAP and the generation of cracks of different sizes. Recrystallised $Mg_{24}Y_5$ and Mg grains have been identified within large cracks of the original large $Mg_{24}Y_5$ particles. The recrystallised $Mg_{24}Y_5$ particles exhibit irregular shapes or necks.

Intermetallic compounds are brittle in general with limited formability. The crystal symmetry of the intermetallics is lower than that of conventional alloys because of the increased atomic order and thus much larger energy is required to generate a perfect single dislocation. $Mg_{24}Y_5$ is extremely brittle, just like $Mg_{17}Al_{12}$, due to the tetrahedral packing and corrugated planes [136]. Pugh [137] introduced the modulus ratio G/B (G: shear modulus, B: bulk modulus) to predict the brittle or ductile behaviour of the material, where a high G/B ratio (larger than 0.57) is associated with brittleness, and vice versa. The G/B ratio of $Mg_{24}Y_5$ is about 0.57 based on the calculated results using density functional theory [138], while the G/B ratio of Mg is about 0.33 at room temperature [139]. This indicates that the ductility of $Mg_{24}Y_5$ is much lower than that of Mg at room temperature. The intermetallics generally have higher hardness and Young's modulus than Mg, e.g. $Mg_{17}Al_{12}$ [140] [141], so intermetallics are likely to concentrate stress during ECAP. It is not suprising that micro-cracks are formed inside the $Mg_{24}Y_5$ particles when their deformation is incompatiable with the surrounding Mg or LPSO phase. The micro-cracks efficiently reduce the size of the $Mg_{24}Y_5$ particles.

As shown in Figure 5.16 and Figure 5.17, small recrystallised $Mg_{24}Y_5$ particles are found frequently inside the cracks or around the large original $Mg_{24}Y_5$ particles. The $Mg_{24}Y_5$ particles show different morphologies in the SEM depending on the numbers of grains attached together. When two or more $Mg_{24}Y_5$ grains are joined they show a micro-necking-like shape. This is two round particles in contact where the contact region is smaller than the main diameter. The contact region is a weak site which is easily separated forming isolated $Mg_{24}Y_5$ particles. If the single $Mg_{24}Y_5$ grain is replaced by tens of intact grains, a macro-necking-like feature is observed. If a $Mg_{24}Y_5$ particle is composed of lots of DRXed grains, it exhibits a curved surface with some

bulges caused by the small particles. Dynamic recrystallisation of the $Mg_{24}Y_5$ occurs due to the severe shear strain induced in the ECAP process. Dynamic recrystallisation of intermetallic compounds, e.g. Nb_3Al and TiAl, has been reported in the literature [142] and is essentially the same as in other metals.

In the literature, necking of intermetallics has been associated with the fragmentation process instead of recrystallisation. Li et al. [125] claimed that the small $Mg_{17}Al_{12}$ particles observed were formed mostly by necking of the original large $Mg_{17}Al_{12}$ particles and that the necking process resulted in the irregular shape of the $Mg_{17}Al_{12}$ particle. In the current work, the irregular $Mg_{24}Y_5$ particles after deformation have a similar 'necking' morphology, but this is confirmed to be composed of small DRXed grains. Maghsoudi et al. [126] suggested that strain-induced dissolution caused the necking, thinning and separation of the $Mg_{17}Al_{12}$ particles and that small particles deformed at higher temperature and suffering more strain exhibit a more spherical shape. In the current work, the DRXed particles also exhibit a relatively round shape.

As indicated by Figure 5.15 and Figure 5.16, cracking and recrystallisation can occur independently. Both processes can break down the particles to a smaller size. However, the combination of both cracking and recrystallisation occurs widely and tends to be a more efficient fragmentation process.

It is worth noting that small DRXed Mg grains are found inside the crack while the surrounding Mg is still a deformed large grain (Figure 5.15). In some cases (Figure 5.17), the DRXed Mg is also accompanied by DRXed $Mg_{24}Y_5$ grains and therefore the fragmented $Mg_{24}Y_5$ particles are separated from the original $Mg_{24}Y_5$ particles. This is probably due to the better formability of Mg than that of $Mg_{24}Y_5$. During ECAP, the alloys are under very high compressive stress which

allows Mg to flow into the cracks. The Mg suffers extremely large strains, which results in small DRXed Mg grains. This indicates that the Mg matrix not only plays an important role in refining the eutectic $Mg_{24}Y_5$, but also fills the cracks and eliminates porosity. As the process continues, eventually $Mg_{24}Y_5$ will break into small separate parts and disperse in the Mg matrix.

5.8 Highlights

The main highlights in this chapter are:

1. Better strength has been obtained in the $Mg_{94}Zn_2Y_4$ alloys after ECAP; bimodal microstructure was obtained after ECAP.

2. The bimodal microstructure results in an asymmetrical fracture in the small punch tests. This fills the gap in the literature that only uniaxial tests (along the extrusion direction) have been performed on a bimodal structural Mg-Zn-Y alloys.

3. It is first reported that the dynamic recrystallisation of the Mg occurs at the kink boundaries of the LPSO/Mg, which indicates that the kink boundaries are nucleation sites for dynamic recrystallisation.

4. It has been confirmed that the $Mg_{24}Y_5$ particles crack and recrystallise during the ECAP process. This provide a new understanding of the fragmentation of other intermetallic particles in a metallic matrix during deformation.

5.9 Conclusions

Mg-Zn-Y alloys after ECAP develop a bimodal microstructure consisting of large deformed grains (Mg and LPSO) and sub-micron sized dynamically recrystallised (DRXed) grains. The DRXed Mg grains are mainly located in the original Mg grain boundaries. The DRXed grain boundaries are decorated with a large number of nano-sized $Mg_{24}Y_5$ precipitates, which limit grain growth.

LPSO phase and LPSO/Mg tend to kink to accommodate the strain, introducing many kink boundaries also into the surrounding matrix. The kink boundaries of LPSO/Mg are potential DRX nucleation sites for Mg grains. The DRXed Mg grains tend to form at kink boundaries with high misorientation angles. Although high angle kink boundaries also exist in the LPSO phase, DRX of LPSO phase doesn't occur. This may be due to the high stacking fault energy and the low diffusion rates of Zn and Y in the LPSO phase.

The SPT strength of the $Mg_{94}Zn_2Y_4$ alloy increased significantly after ECAP. The bimodal structure exhibits asymmetrically shaped cracks along the ECAP shear direction and the perpendicular direction after SPT. The cracks start shortly after the linear elastic region during SPT under a biaxial tensile stress. The initial crack lies in the shear direction and DRXed grains are potential crack sources. This may be due to the strong fibre texture of the large grains with the presence of LPSO phase inhibiting the dominant basal slip and leading to the deformation first of DRXed grains. These observations show that the bimodal structure exhibits better ductility when the tensile stress is applied along the shear direction than the perpendicular direction. If ECAP is to be used to refine the microstructure of Mg-Zn-Y alloys and allow them to be employed as

sheets it will be necessary to take into consideration the different deformation behaviours of the bimodal structure along different directions.

A fragmentation mechanism has been proposed for eutectic $Mg_{24}Y_5$ intermetallic particles during ECAP. Initially cracks are formed which lead to fragmentation and reduce significantly the size of the $Mg_{24}Y_5$ particles; secondly, dynamic recrystallisation of these intermetallics occurred in the heavily deformed areas, e.g. near the crack. The agglomeration of DRXed $Mg_{24}Y_5$ grains gives rises to necking and thus to a dispersion of small $Mg_{24}Y_5$ particles. Meanwhile, the Mg matrix exhibits better formability than the $Mg_{24}Y_5$, which makes it possible to separate the fragmented $Mg_{24}Y_5$ particles.

6 The effect of Gd additions on Mg-Zn-Y alloys

In this chapter, Mg-Zn-(Y)-(Gd) alloys with different Zn to RE ratios were prepared. The microstructure and hardness of the as-cast samples, instead of heat treated samples, were measured because of the potential employment of the alloys in the as-cast condition. The secondary phases were investigated using XRD, OM, SEM and TEM. The effect of Zn to RE ratio on the secondary phases and the effect of Gd additions on the formation of LPSO are investigated. The lattice parameters and the corresponding chemical compositions of the secondary phases and Mg matrix are studied and the effect of alloying elements on the lattice parameters of the Mg matrix and W phases are discussed.

6.1 The chemical compositions of the alloys

The chemical compositions of the as-cast samples are designed based on the Zn/RE ratio, e.g. 0.5, 1, 2.33, 3.23, as listed in Table 6.1. Ten samples were prepared and are numbered as 1-10. The chemical compositions were also measured by EDS.

Table 6.1 Designed and measured chemical compositions of the as-cast alloys 1-10.

Sample	Design compositions, at.%	Zn/(Y+Gd) ratio	Measured chemical compositions by EDS, at.%				Measured Zn/(Y+Gd) ratio
			Mg	Zn	Y	Gd	
1	$Mg_{94}Zn_2Y_4$	0.5	94.12±0.10	1.98±0.07	3.90±0.07		0.51
2	$Mg_{94}Zn_2Gd_4$	0.5	94.57±0.11	1.79±0.07		3.63±0.10	0.49
3	$Mg_{94}Zn_2Y_2Gd_2$	0.5	95.21±0.20	1.75±0.06	1.47±0.05	1.66±0.05	0.56
4	$Mg_{94}Zn_3Y_3$	1	94.6±0.16	2.87±0.11	2.53±0.07		1.13

5	$Mg_{94}Zn_3Gd_3$	1	94.00±0.12	3.07±0.10		2.94±0.05	1.04
6	$Mg_{94}Zn_3Y_{1.5}Gd_{1.5}$	1	94.90±0.19	2.56±0.12	1.32±0.05	1.22±0.06	1.01
7	$Mg_{94}Zn_{4.2}Y_{1.8}$	2.33	95.47±0.09	3.37±0.08	1.16±0.04		2.91
8	$Mg_{94}Zn_{4.2}Gd_{1.8}$	2.33	93.62±0.09	4.53±0.10		1.85±0.01	2.45
9	$Mg_{94}Zn_{4.2}Y_{0.8}Gd_1$	2.33	95.57±0.38	3.12±0.32	0.55±0.05	0.76±0.02	2.38
10	$Mg_{94.5}Zn_{4.2}Y_{0.8}Gd_{0.5}$	3.23	95.15±0.35	3.85±0.34	0.54±0.06	0.45±0.05	3.85

6.2 Phase identification by XRD

Figure 6.1 shows the XRD results from the as-cast samples with 2θ between 20-75°. The Mg phase is found in all the samples and the peaks are well aligned, which indicates the lattice parameters vary over a relatively small range. W phase is observed in almost all the alloys except alloy 1 and alloy 3. The positions of the XRD peaks for the W phase shift considerably, e.g. the W (111) peaks vary over a wide range as indicated by the black dashed lines. The W (022) peak (as arrowed) of the alloy 4 is found on the right side of the Mg (011) peak, while W (022) peak of the alloy 5 is found on the left side of the Mg (001) peak. This indicates that the lattice parameters of the W phase are quite different in each alloy. The lattice parameters of the phases were calculated and will be discussed later. The quasicrystalline i-phase is also observed in alloy 7-10, but the intensity of the i-phase peak is very low showing that small amount only of i-phase existed.

LPSO phases are observed in alloys 1, 3, 4 and 6. Figure 6.2 shows the magnified XRD spectra of these alloys with 2θ of 5-7° and 30-40° where relatively high intensity LPSO peaks are found. In alloy 1 and alloy 3, an obvious peak can be observed when 2θ is about 5.6°, which corresponds to (002) of an 18R type LPSO phase. The (002) peak of the 14H type LPSO should be at 4.8°, which is out of the current scanning range. In alloy 1, only peaks from 18R type LPSO are

observed. In alloy 2, when half the Y of alloy 1 is replaced by Gd, both 14H and 18R peaks are present with a similar intensity. In alloy 4, with a lower Y content than alloy 1, 14H type LPSO peaks have larger intensities than 18R type. In alloy 6, when half the Y of alloy 4 is replaced by Gd, only 14H type LPSO peaks are present.

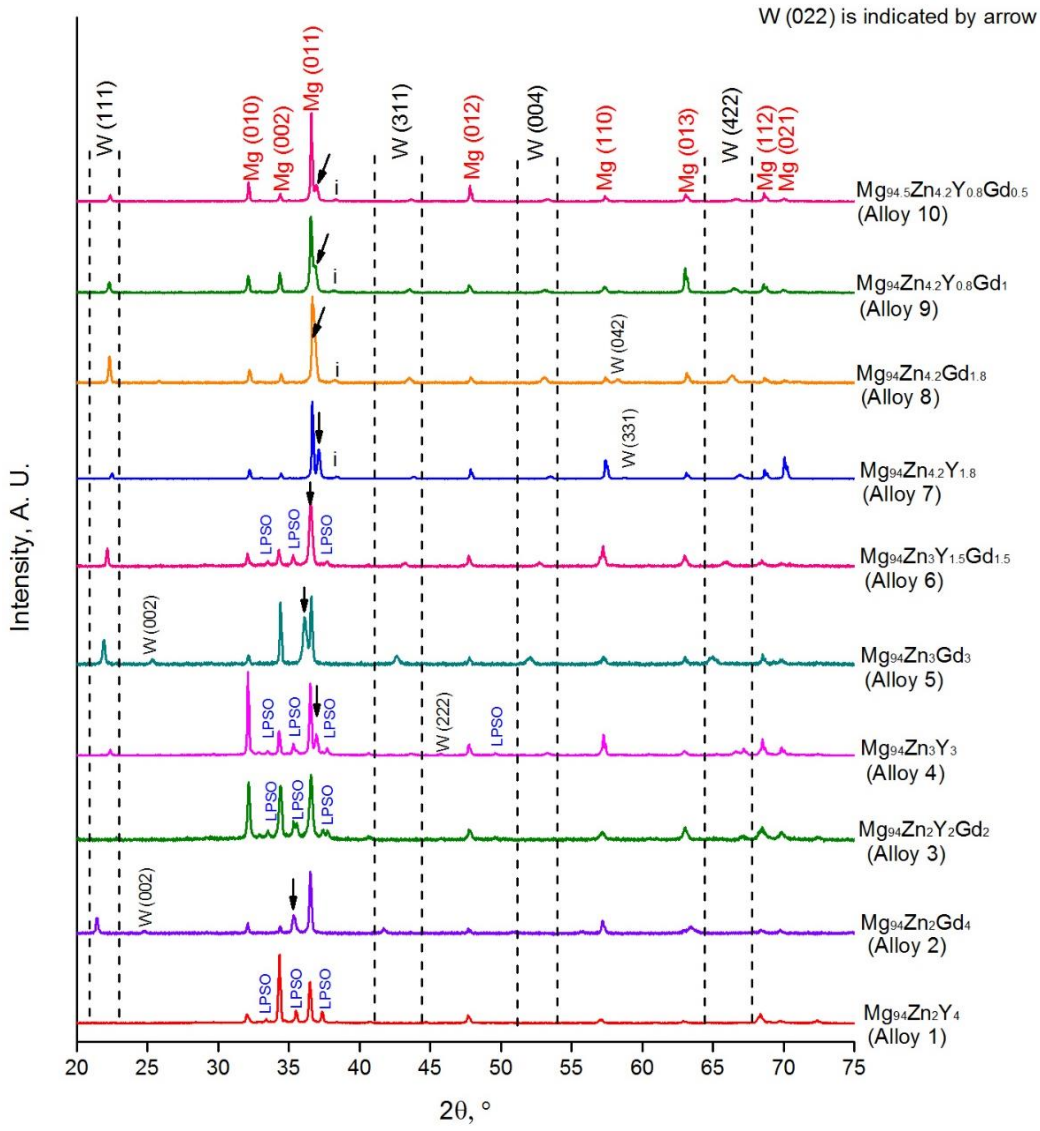

Figure 6.1 XRD spectra of as-cast alloys 1-10. The arrows indicate the (002) plane of the W phase.

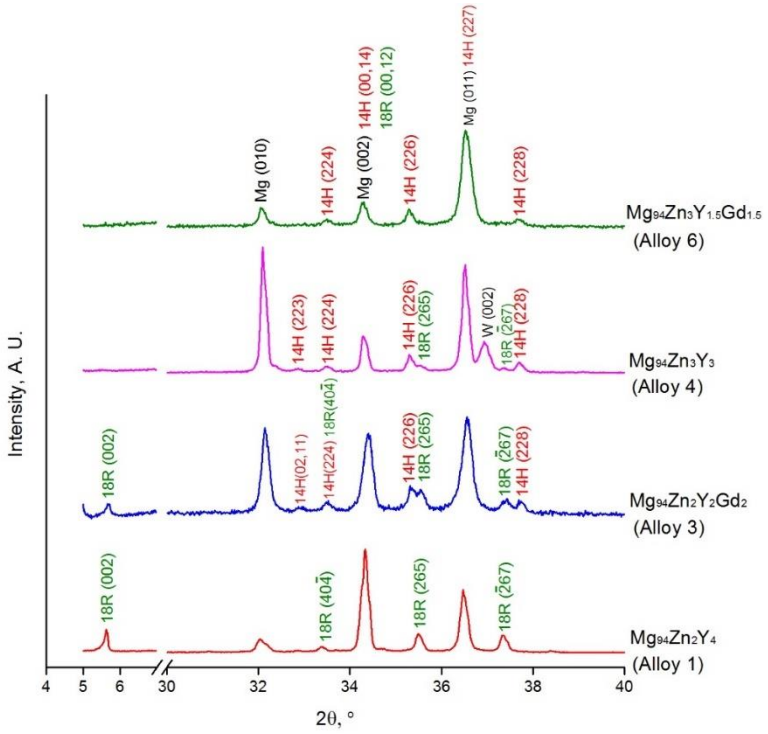

Figure 6.2 XRD spectra of alloy 1, 3, 4 and 6 containing LPSO phase.

6.3 Microstructure analysis by OM and SEM

Optical images of the as-cast alloys are shown in Figure 6.3. The lower magnification images show that the alloys exhibit distinct microstructural changes when different Zn/RE ratios are applied. Figure 6.3a shows that alloy 1 contains a large area fraction of the bulk shaped LPSO phases. Magnesium matrix appears in different contrasts: both dark and bright. In the higher magnification image, there were two matrix areas containing small precipitates which appear in different directions. Figure 6.3c shows that the alloy 2 has a dendritic structure with dark secondary phases between the dendrite arms. Figure 6.3d shows that the dark secondary phase appears is a eutectic product probably W phase based on XRD results. Small precipitates also

appear in the matrix. Figure 6.3e and f show that the alloy 3 is quite similar to alloy 1. Alloy 4 (Figure 6.3g and h) contains two types of secondary phases: LPSO shows a slightly darker contrast than the matrix; W phase is part of a eutectic and provide the dark contrast normally between the LPSO grains. Alloy 5 (Figure 6.3i and j) has a similar microstructure to alloy 2. Alloy 6 (Figure 6.3k and l) is similar to alloy 4.

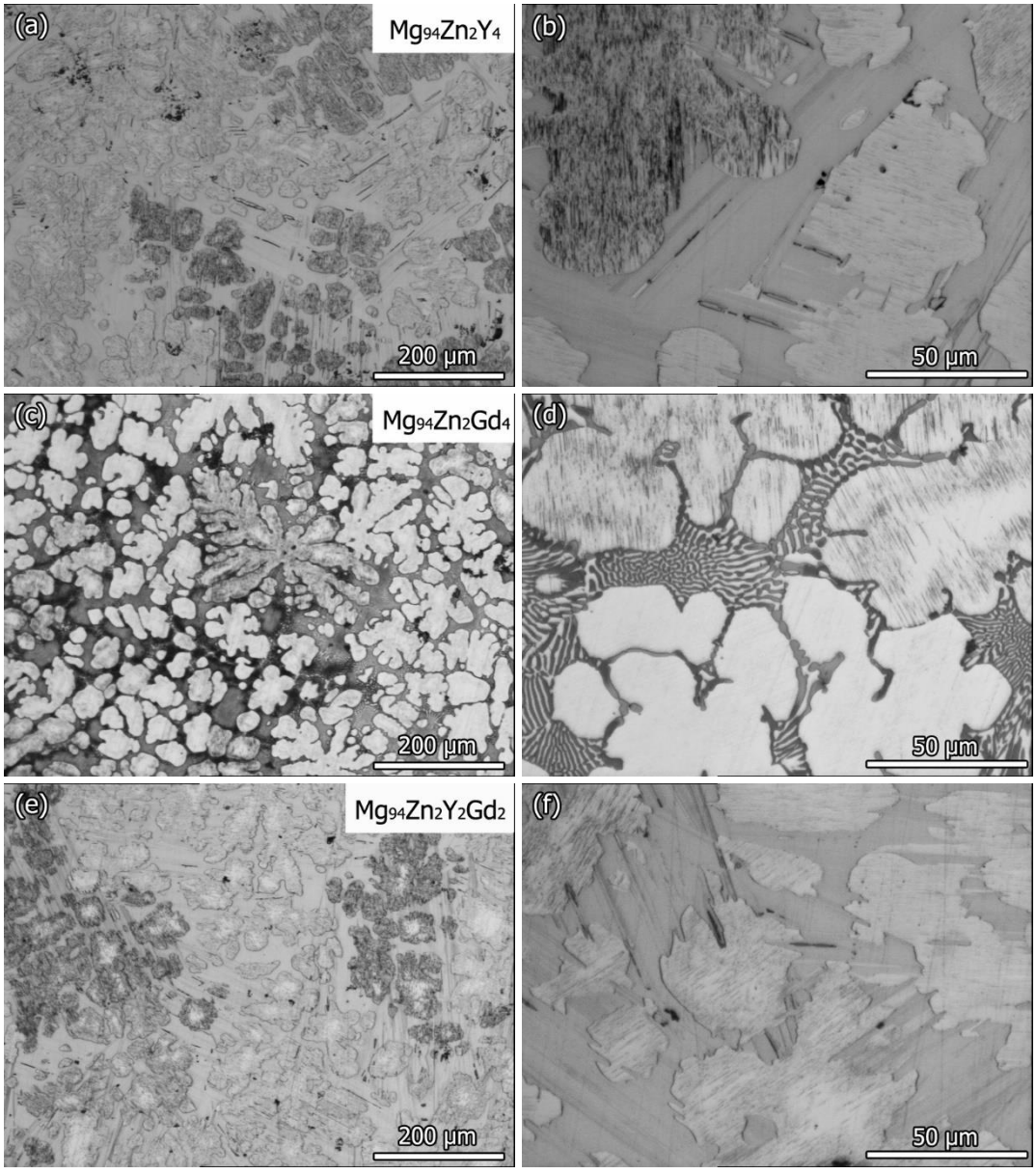

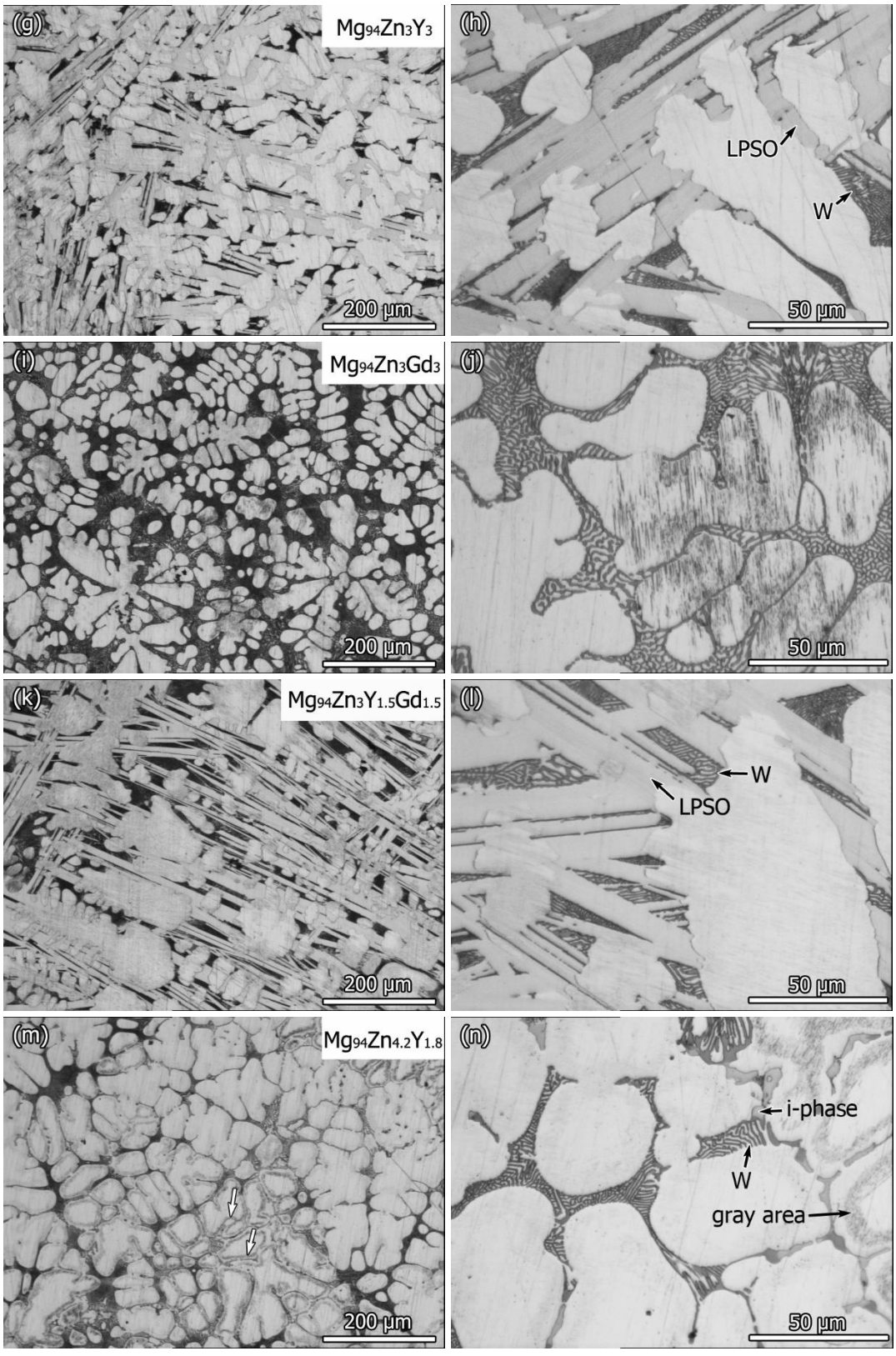
(g)
$Mg_{94}Zn_3Y_3$
200 μm
(h)
LPSO
W
50 μm
(i)
$Mg_{94}Zn_3Gd_3$
200 μm
(j)
50 μm
(k)
$Mg_{94}Zn_3Y_{1.5}Gd_{1.5}$
200 μm
(l)
W
LPSO
50 μm
(m)
$Mg_{94}Zn_{4.2}Y_{1.8}$
200 μm
(n)
i-phase
W
gray area
50 μm

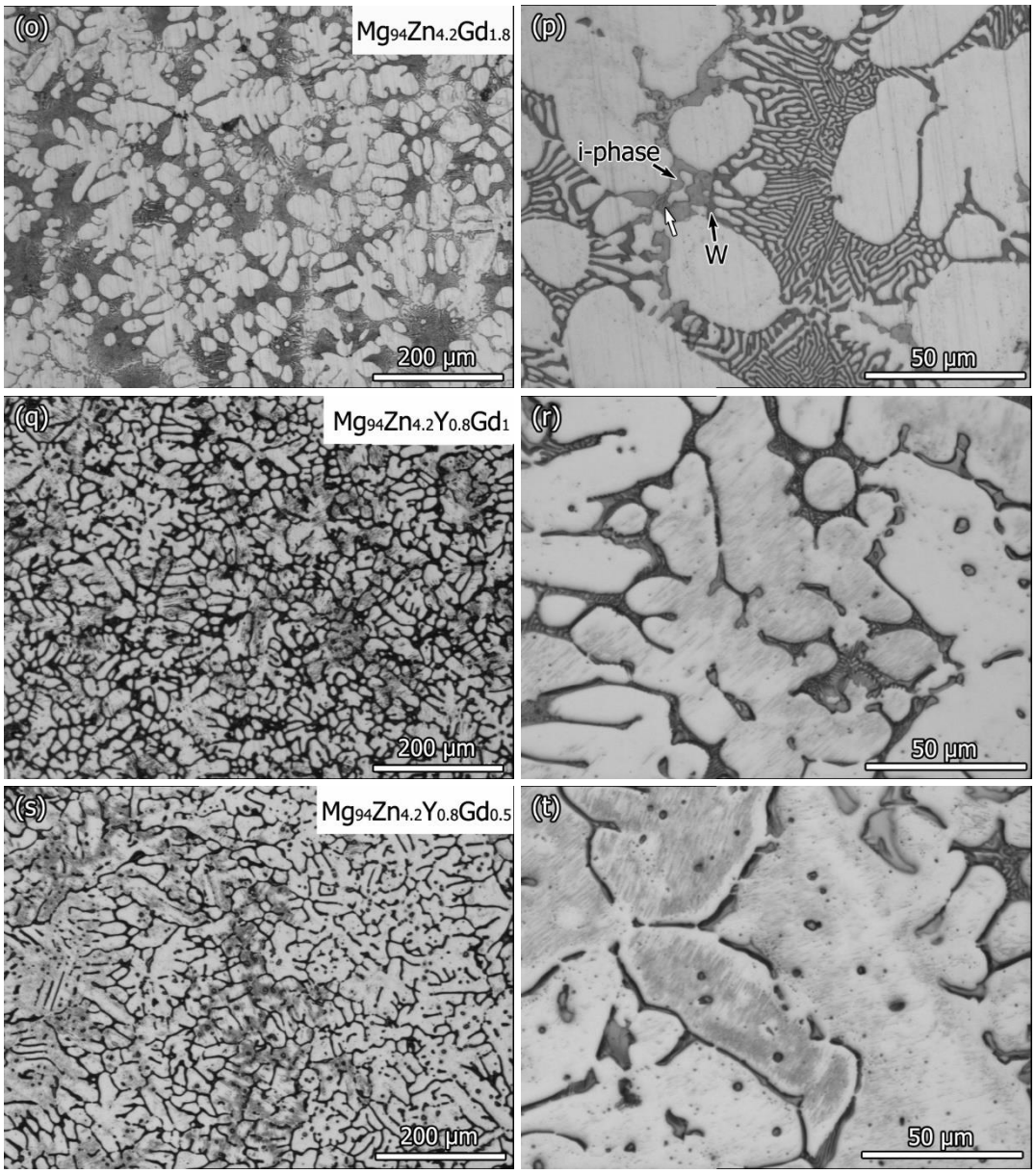

Figure 6.3 Low (left) and high (right) magnification optical images of the as-cast alloys: (a) (b) alloy 1; (c) (d) alloy 2; (e) (f) alloy 3; (g) (h) alloy 4; (i) (j) alloy 5; (k) (l) alloy 6; (m) (n) alloy 7; (o) (p) alloy 8; (q) (r) alloy 9; (s) (t) alloy 10.

Figure 6.3m shows that alloy 7 contains a dendritic structure with secondary phases between dendritic arms with some grey areas (arrowed) close to the secondary phases. From the higher

magnification image, two types of secondary phases can be distinguished: a eutectic with dark contrast, which is probably W phase and Mg; a thinner phase appears in brighter contrast than the W phase, probably i-phase. There are some areas showing W phase with i-phase attached. The grey areas are actually small precipitates which tend to be close to i-phase, but are also observed close to W phase. Figure 6.3o shows alloy 8 which also contains a network of secondary phases, but the area fraction of W phase is larger than in alloy 7. The higher magnification image shows the main secondary phases form part of a eutectic structure, probably W phase. In the region between the W phase, an irregularly shaped phase is observed, probably i-phase. There are small grains of another phase are normally found surrounded by i-phase, and are indicated by a white arrow. Figure 6.3q and s show that similar morphologies are observed in alloys 9 and 10.

Backscattered electron images of the as-cast alloys are shown in Figure 6.4. When the Zn/RE ratio is 0.5, alloy 1, which contains only Y, shows a similar morphology to alloy 3 which contains both Y and Gd. The LPSO phase shows bright contrast. However, alloy 2 which contains only Gd has a network of W phase.

When the Zn/RE ratio is 1, alloy 4 which contains only Y has a similar morphology to alloy 6 which contains both Y and Gd. There are two types of secondary phase: a W phase with the brightest contrast and a lath shaped LPSO with darker contrast. W phase is normally observed in the interiors of the LPSO grains. Alloy 5 with Gd only contains W phase as secondary phase.

With the Zn/RE ratio is 2.33, alloys 7-9 have very similar morphologies: W phase is the main secondary phase. In Figure 6.4g (alloy 7), the i-phase shows brighter contrast than theW phase.

When the Zn/RE ratio is 3.23 (alloy 10), the morphology is similar to that of alloy 9.

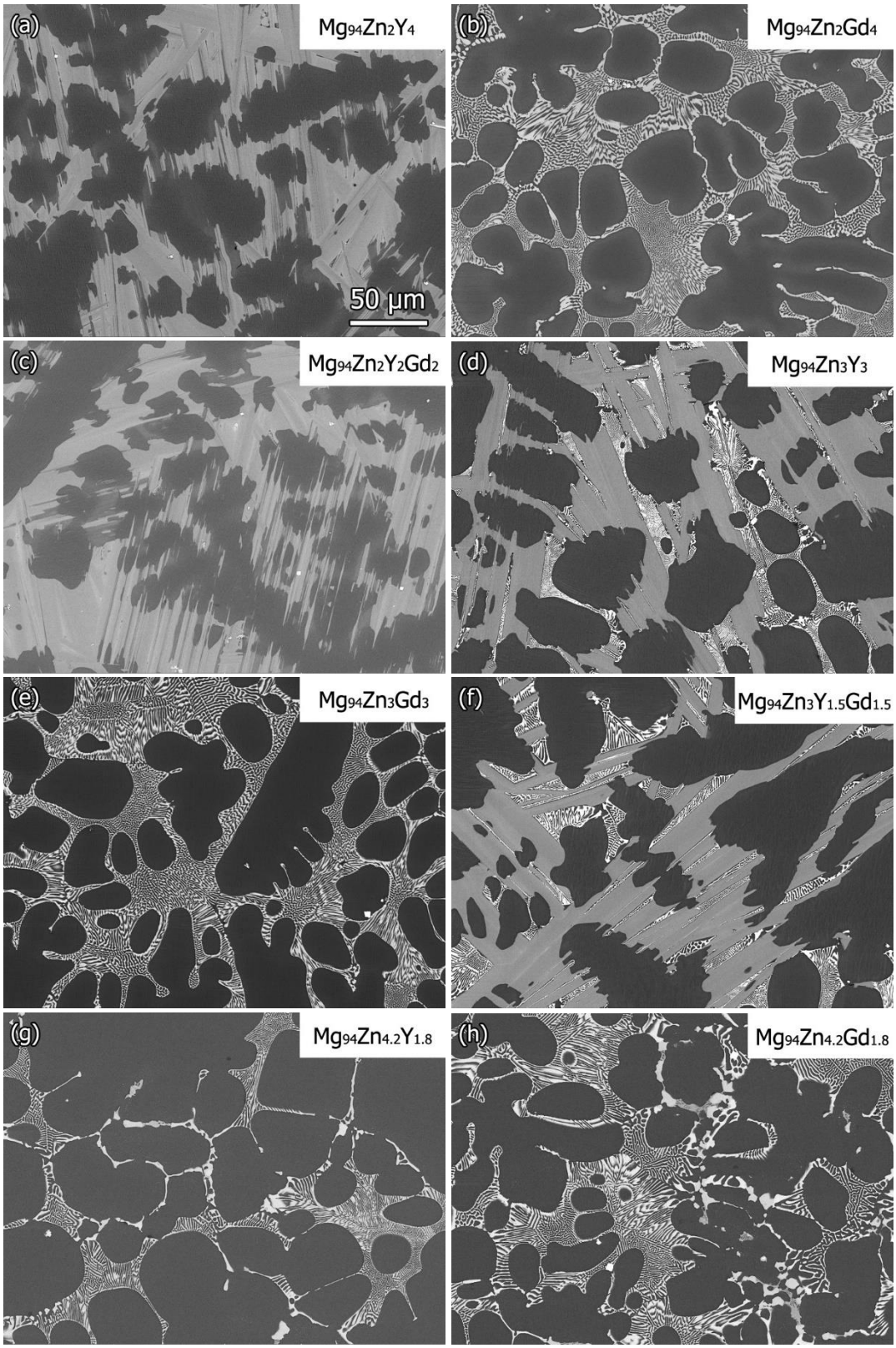
(a)
$Mg_{94}Zn_2Y_4$
50 μm
(b)
$Mg_{94}Zn_2Gd_4$
(c)
$Mg_{94}Zn_2Y_2Gd_2$
(d)
$Mg_{94}Zn_3Y_3$
(e)
$Mg_{94}Zn_3Gd_3$
(f)
$Mg_{94}Zn_3Y_{1.5}Gd_{1.5}$
(g)
$Mg_{94}Zn_{4.2}Y_{1.8}$
(h)
$Mg_{94}Zn_{4.2}Gd_{1.8}$

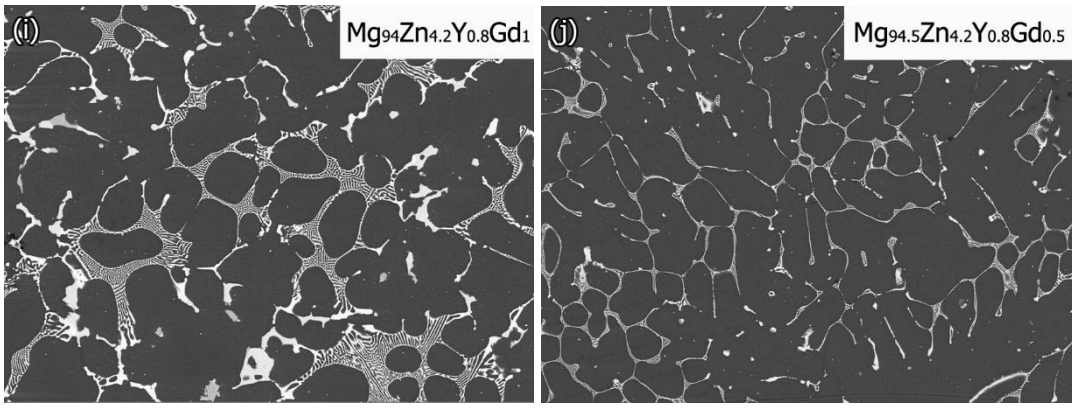

Figure 6.4 Backscattered electron images of the as-cast alloys. (a-j) correspond to alloys 1-10.

6.4 TEM results

6.4.1 Alloys with Zn/RE ratio of 0.5

Figure 6.5a and b show TEM bright field images of alloy 1 ($Mg_{94}Zn_2Y_4$). The dark phases are confirmed as 18R LPSO phase by diffraction pattern shown in Figure 6.5c. LPSO phases normally lie on the basal planes of the Mg matrix, where the LPSO laths appear parallel to each other, as indicated in Figure 6.5a. But in some areas, e.g. as arrowed in Figure 6.5b, some bulk shaped LPSO phases are not in the same orientation as the neighbouring ones. This has also been observed in the SEM images. The non-parallel phase normally appears in the grain boundaries or in the region contains large amounts of LPSO. Only 18R type LPSO has been observed in the alloy by TEM.

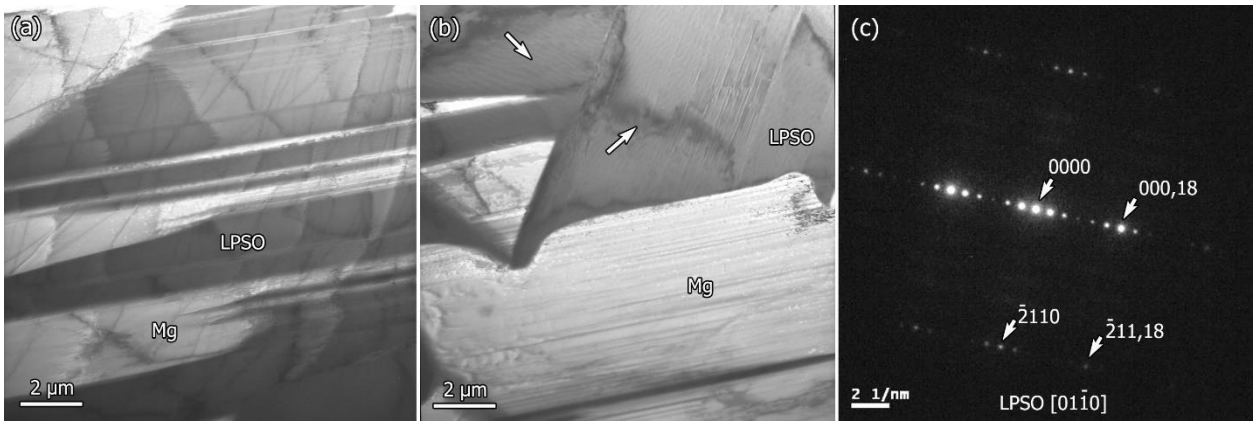

Figure 6.5 Bright field images (a, b) of alloy 1 and a diffraction pattern (c) from the LPSO phase. Arrows in Figure 6.5b shows the LPSO laths lie in different directions. The diffraction pattern shows that the LPSO is 18R type and that the beam direction is parallel to $[01\bar{1}0]$.

The TEM bright field image in Figure 6.6a shows the main secondary phase in alloy 2 ($Mg_{94}Zn_2Gd_4$). The diffraction patterns taken from three zone axes of the secondary phase suggest a fcc structure and the lattice parameter measured is consistent with W phase. Figure 6.6b shows that thin precipitates (arrowed) are also found in the matrix. A two beam image with g vector 0001 (Figure 6.6c), shows better contrast of the thin precipitates where thickness is a few nanometre. The selected area diffraction patterns taken from the matrix and the thin precipitates are shown in Figure 6.6 (e). Some bright spots are observed in the line connecting reflections (0001) and $(000\bar{1})$. The thin precipitates are probably LPSO phase.

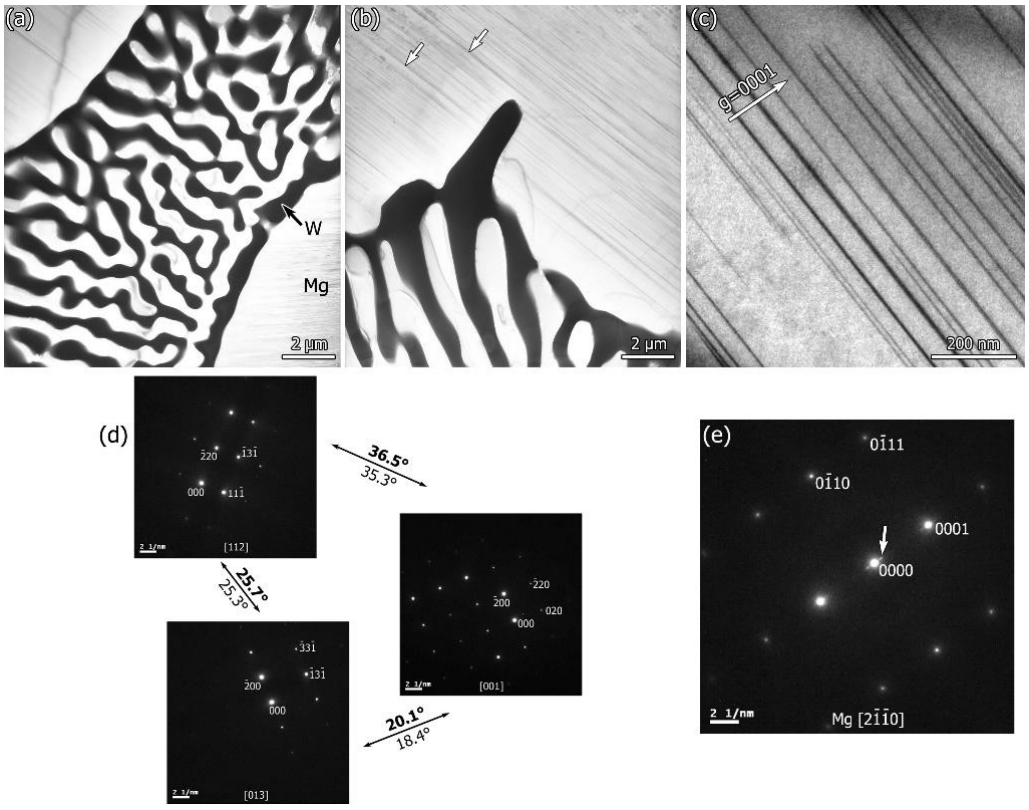

Figure 6.6 (a-c) TEM bright field images of alloy 2 showing W phase and thin LPSO lamellae; (d) diffraction patterns of W phase taken from three zone axes. The measured and calculated tilting angles between each zone axis are shown in bold and non-bold; (e) diffraction pattern obtained. from matrix and thin precipitates. The arrow indicates extra spot between 0000 and 0001 reflections of Mg.

The TEM bright field images of alloy 3 ($Mg_{94}Zn_2Y_2Gd_2$) in Figure 6.7 show similar morphologies of LPSO to that in alloy 1: both bulk and thin LPSO are observed. Figure 6.7c shows a diffraction pattern taken from the $[01\bar{1}0]$ zone axis of 18R LPSO, where 5 extra spots are found between (0000) and $(000, \overline{18})$ reflections. Figure 6.7d shows a diffraction pattern from the $[1\bar{2}10]$ zone axis of the 14H LPSO, where 13 extra spots are found between the (0000) and $(000, \overline{14})$ reflections.

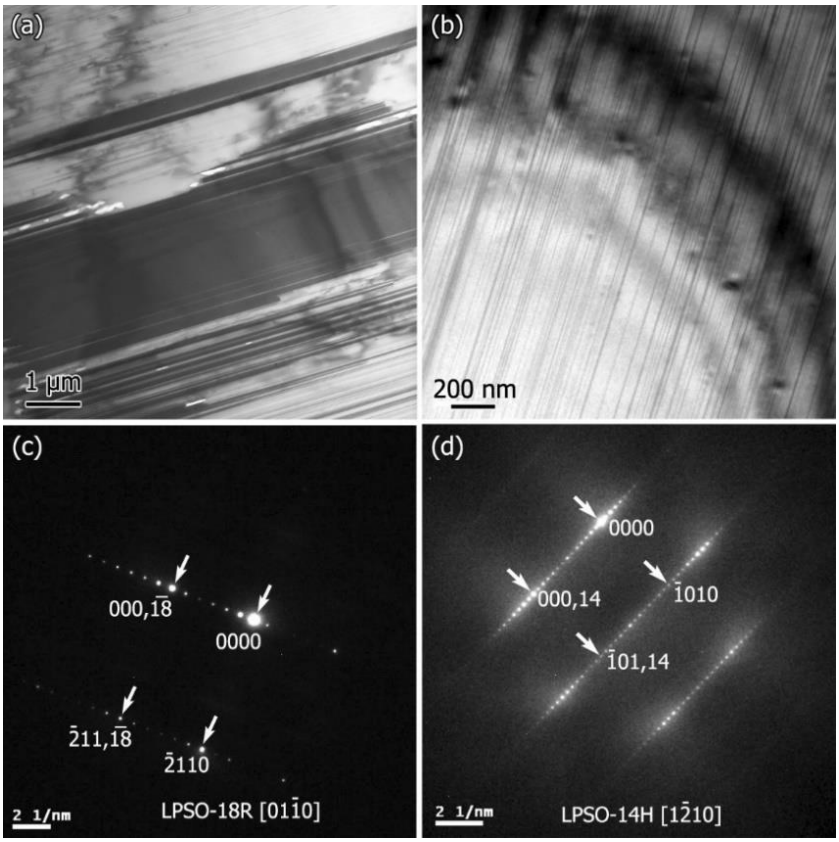

Figure 6.7 (a) (b) TEM bright field images showing morphology of LPSO phase; (c) (d) diffraction patterns taken from $[01\bar{1}0]$ and $[1\bar{2}10]$ zone axes from different LPSO phases showing 18R and 14H structures.

6.4.2 Alloys with Zn/RE ratio of 1

Two types of secondary phase are found in alloy 4 ($Mg_{94}Zn_3Y_3$, see Figure 6.8): the dark W phase and lath shaped LPSO phase. It is very difficult to identify the 18R and 14H LPSO phases from bright field images due to their similar morphologies. For example, the diffraction patterns in Figure 6.8d and e shows the neighbouring 18R and 14H phases have different structures. Three diffraction patterns taken from the three zone axes of the eutectic phase (Figure 6.8c) also confirm an fcc structure, which is consistent with W phase.

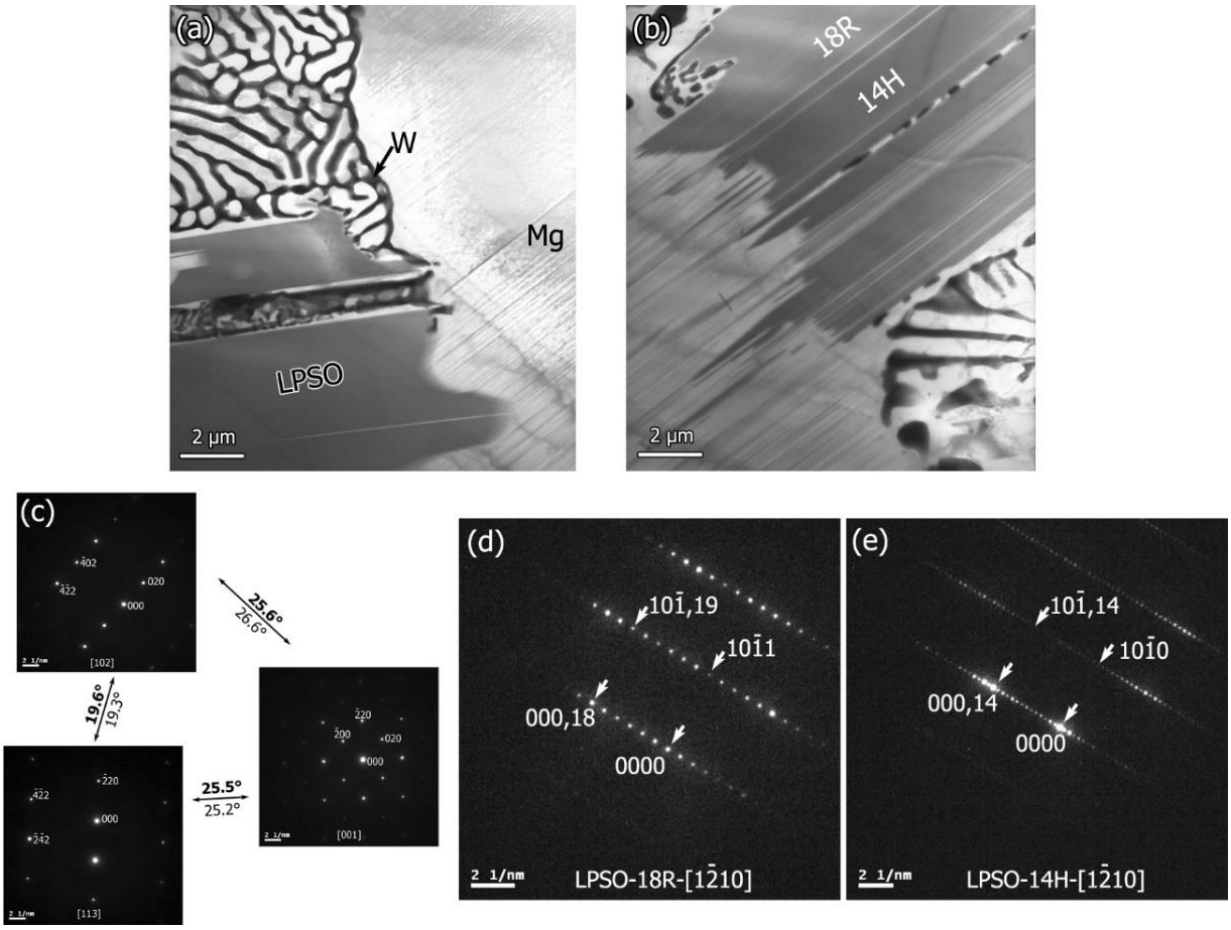

Figure 6.8 (a, b) TEM bright field images of alloy 4 showing the second phases; (c) diffraction patterns obtained from three zone axes of the W phase. The measured and calculated tilting angles between each zone axis are shown in bold and non-bold; (d) diffraction pattern obtained from $[1\bar{2}10]$ zone axis of 18R-type LPSO; (e) diffraction pattern obtained from $[1\bar{2}10]$ zone axis of 14H-type LPSO. (cf. Figure 6.7)

Alloy 5 ($Mg_{94}Zn_3Gd_3$) has a similar morphology to alloy 2, although containing less Gd. The main secondary phase is W phase. Thin LPSO lamellae are also observed in the matrix. The TEM images are not presented.

Alloy 6 ($Mg_{94}Zn_3Y_{1.5}Gd_{1.5}$) has a similar morphology to alloy 4. The main secondary phases are W phase and LPSO phase (both 14H and 18R are present). The TEM images are not presented.

6.4.3 Alloys with Zn/RE ratio of 2.33

Figure 6.9 shows EDS maps of the as-cast alloy 7 ($Mg_{94}Zn_{4.2}Y_{1.8}$). Two types of secondary phases have similar contrast in the secondary electron image. The skeleton phase is the main secondary phase, which is probably W phase based on the XRD results. The other phase is probably i-phase based on the EDS results. The EDS maps show that the W phase contains less Zn and more Y than the i-phase.

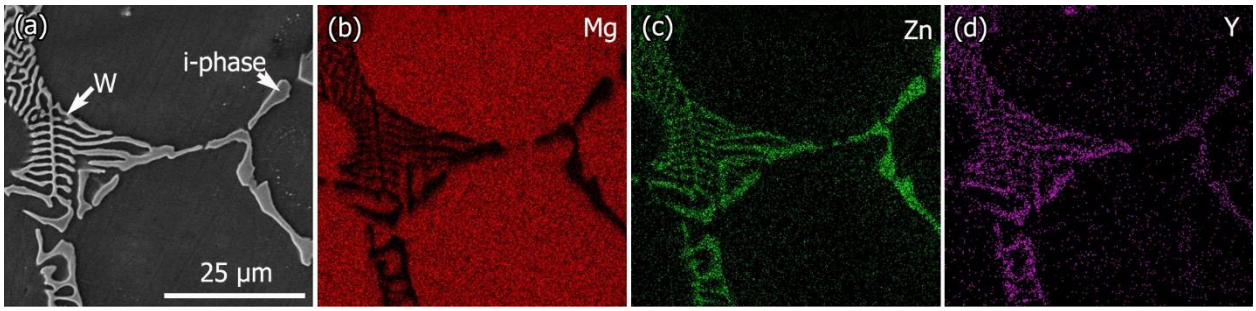

Figure 6.9 SEM EDS maps of alloy 7

Figure 6.10 shows a backscattered electron image and EDS maps of a typical area in alloy 8 ($Mg_{94}Zn_{4.2}Gd_{1.8}$). The magnesium matrix shows darkest contrast in the backscattered image. There are three types of secondary phase. The W phase shows the brightest contrast. The particle shaped phase shows a slightly darker contrast than the W phase. It has a higher Zn concentration than the W phase, and is possibly the i-phase. The small dark particles are darker than the i-phase. They have a similar concentration of Zn but lower concentration of Gd and shown below to be $MgZn_2$.

Figure 6.11a shows a bright field image of adjacent W phase and i-phase. The diffraction patterns from four zone axes of the i-phase confirms an icosahedral quasicrystalline structure, which is shown in Figure 6.11b. The angles between the zone axes are consistent.

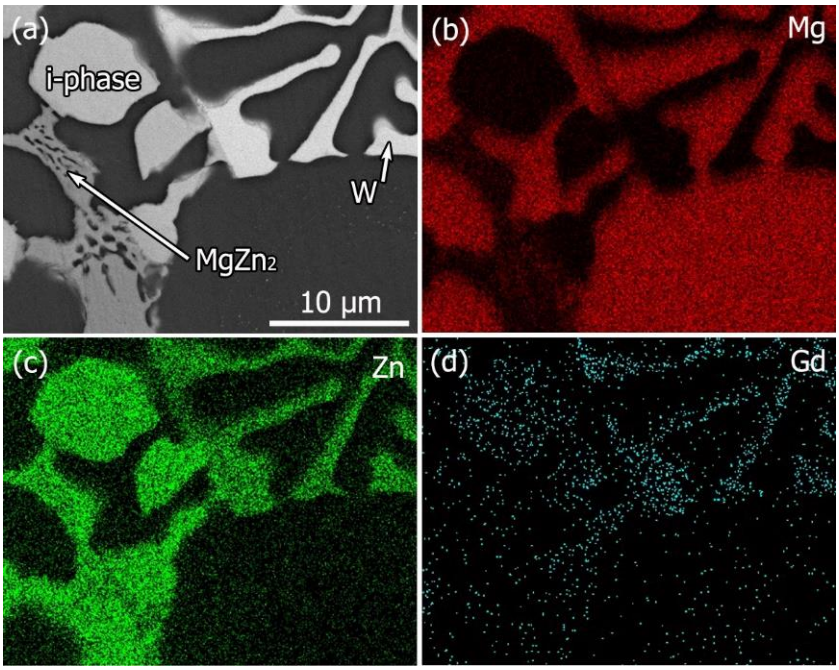

Figure 6.10 EDS maps of alloy 8: (a) BSE image; (b)-(d) showing Mg, Zn and Gd concentrations.

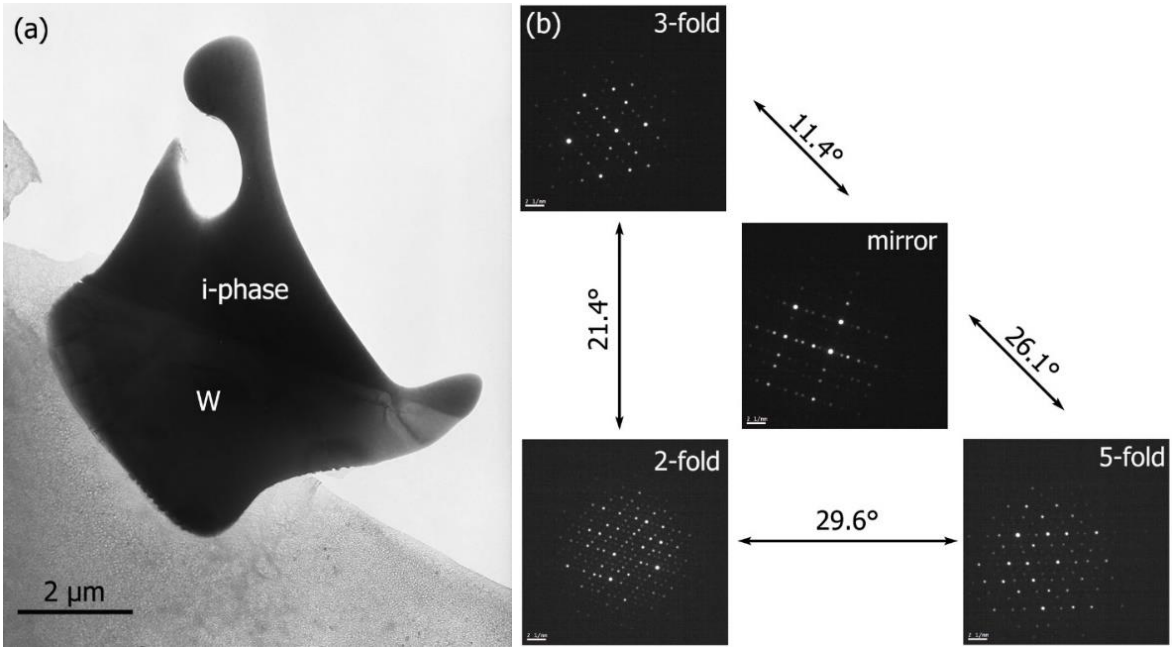

Figure 6.11 (a) Bright field image shows adjacent i-phase and W phase in alloy 8; (b) diffraction patterns taken from four zone axes of the i-phase; the tilt angles between each zone axis were measured and are shown in the figure.

Figure 6.12a shows a bright field image of the $MgZn_2$ phase. $MgZn_2$ phase has an irregular shape with spot-like Mg found inside. The EDS spectrum in Figure 6.12 shows a composition of about $Mg_{32.41}Zn_{67.33}Gd_{0.26}$, which is close to $MgZn_2$. The diffraction pattern in Figure 6.12b is consistent with a hcp structure with lattice parameters of a=5.32 Å, c=8.58 Å [143].

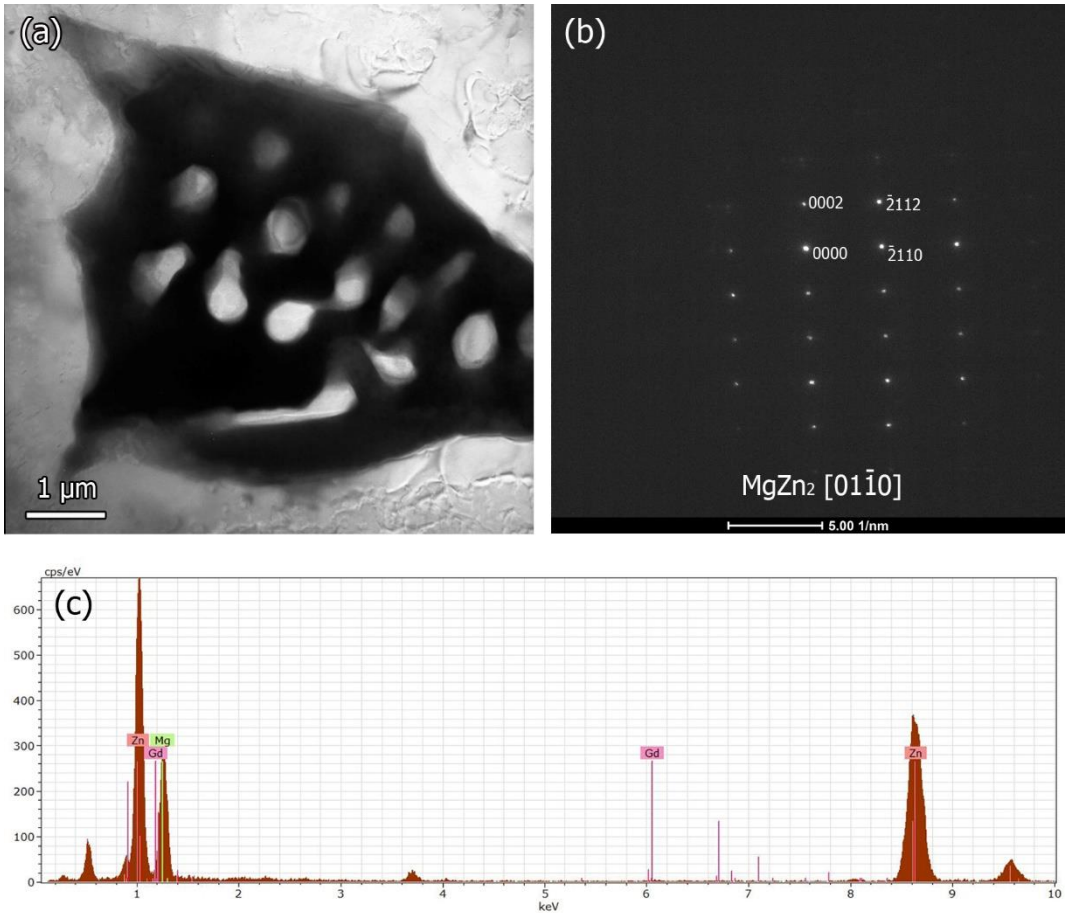

Figure 6.12 (a) Bright field image of $MgZn_2$ phase in alloy 8; (b) diffraction pattern taken from $MgZn_2$, beam direction parallel to $[01\bar{1}0]$ zone axis; (c) EDS spectrum taken from $MgZn_2$ phase.

Figure 6.13(a) shows a bright field image obtained from the as-cast alloy 9 ($Mg_{94}Zn_{4.2}Y_{0.8}Gd_1$). A W phase particle and an i-phase particle are attached together. The sample is tilted to different zone axes and the schematic drawing of the Kikuchi map is shown in Figure 6.13b, where red represents i-phase and blue W phase. Figure 6.13c was obtained from W phase with the electron beam close to an axis of [111], while Figure 6.13d was obtained from i-phase with electron beam close to an axis of 2-fold symmetry after tilting only 1.9°. The composite diffraction patterns obtained from both i-phase and W phase are shown in Figure 6.13e, which indicates the two zone axes are very close. The diffraction patterns obtained along the [101] (Figure 6.13f) and $[1\bar{1}1]$ (Figure 6.13i) zone axes of the W phase which are parallel to the neighbouring 5-fold (Figure 6.13g) and 3-fold symmetry (Figure 6.13j) axes of the i-phase. If the misorientation angle between, for example, the [111] zone axis of the W phase and the 2-fold rotation axis of the i-phase is described as $< [111]_W, \text{2-fold}_i >$, then $< [111]_W, \text{2-fold}_i >$, $< [101]_W, \text{5-fold}_i >$ and $<[1\bar{1}1]_W, \text{3-fold}_i >$ measured by TEM are 1.9°, 0° and 1.5° respectively. The diffraction patterns shown in Figure 6.13 c-k suggest a well defined orientation relationship. This orientation relationship observed between the i-phase and the W phase is consistent with that reported in the literature [144]. The LPSO phase has been occasionally observed in this alloy; an example is shown in Figure 6.14. The diffraction pattern shows 18R type.

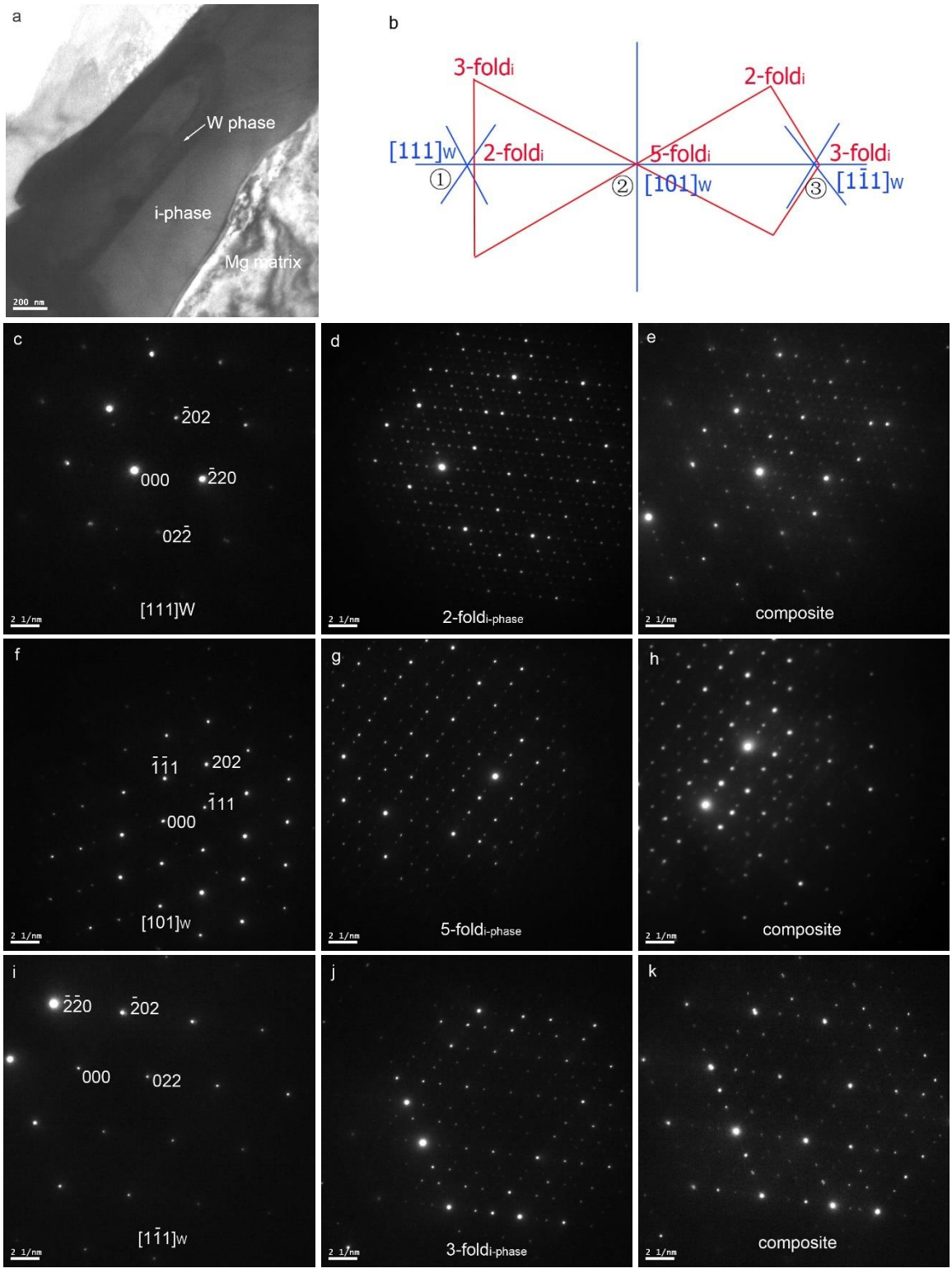

Figure 6.13(a) Bright field image obtained from the as-cast alloy 9 showing a W phase particle joined to an i-phase particle; (b) schematic drawing of Kikuchi lines of the i-phase (red) and the

W-phase (blue) establishing an OR; diffraction pattern from the W phase (c) and i-phase (d) and composite diffraction pattern (e) obtained from both phases; electron beam is parallel to $[111]_{W\ phase}$ and close to a 2-fold$_{i\text{-}phase}$ zone axis; diffraction pattern from the W phase (f) and i-phase (g) and composite diffraction pattern (h) obtained from both phases; electron beam is parallel to $[101]_{W\ phase}$ and a 5-fold$_{i\text{-}phase}$ zone axis; diffraction pattern from the W phase (i) and i-phase (j) and composite diffraction pattern (k) obtained from both phases; electron beam is parallel to $[1\bar{1}1]_{W\ phase}$ and close to a 3-fold$_{i\text{-}phase}$ zone axis.

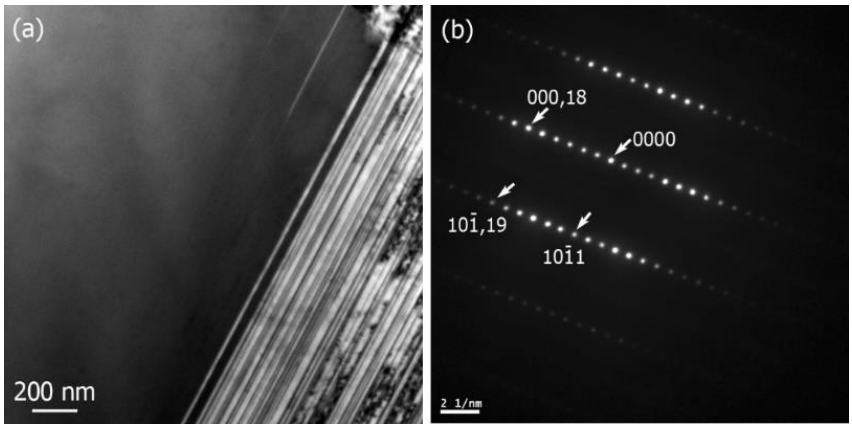

Figure 6.14 (a) Bright field image of LPSO phase in alloy 9; (b) diffraction pattern indicating 18R type.

6.4.4 Alloys with Zn/RE ratio is 3.22

Figure 6.15a shows a bright-field image of alloy 10 ($Mg_{94.5}Zn_{4.2}Y_{0.8}Gd_{0.5}$) with W phase lying preferentially along the grain boundaries. The image was taken with the electron beam direction parallel to the [011] zone axis of the W phase (as shown in the insert). Figure 6.15b is a bright-field image showing fine LPSO lamellae alternating with the Mg matrix. The LPSO phase is dark in the image and lies parallel to the basal plane of the Mg matrix, which is bright, as shown by the white arrow indicating the [0001] direction of the Mg matrix. The associated diffraction pattern of the LPSO phase is shown in Figure 6.15c and the electron beam direction is parallel to

the $[2\bar{1}\bar{1}0]$ zone axis of the Mg matrix. The diffraction pattern of the LPSO phase shows that there are 13 reflections at equal intervals between the transmitted beam and the 0002 reflection spot of pure Mg, consistent with the hexagonal 14H structure with lattice parameters a = 3.21 Å and c = 36.94 Å [61].

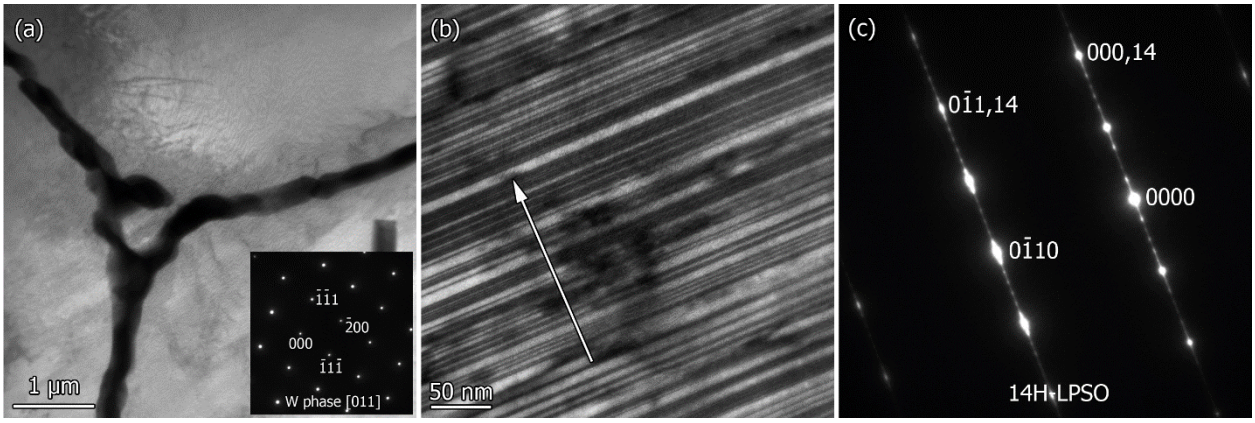

Figure 6.15 (a) Bright-field image and corresponding SAED pattern (inset) of W phase in as-cast alloy 10. The electron beam direction is parallel to the [011] zone axis of the W phase; (b) Bright-field image showing the lamellar LPSO phase. The basal plane of the LPSO phase is parallel to that of the magnesium matrix; (c) SAED pattern from centre of (b) confirming that the LPSO phase is of 14H type; the beam direction is parallel to $[2\bar{1}\bar{1}0]$ of the Mg matrix.

6.5 The chemical compositions of the phases

The chemical compositions of the phases in each of the as-cast alloys are shown in Table 6.2. The measurements were carried out using EDS in TEM to minimise the effect of the matrix on the compositions of the secondary phases. Each phase received five measurements. The lattice parameters of the phases based on the XRD results are also listed in Table 6.2.

Table 6.2 The chemical compositions and the corresponding lattice parameters of the phases in each as-cast alloy.

phase	No	Sample	Mg, at.%	Zn, at.%	Y, at.%	Gd, at.%	Lattice parameters
α-Mg	1	$Mg_{94}Zn_2Y_4$	98.11±0.20	0.25±0.04	1.63±0.19		a=3.224 Å, c=5.220 Å
α-Mg	2	$Mg_{94}Zn_2Gd_4$	97.73±0.27	0.41±0.04		1.85±0.24	a=3.221 Å, c=5.216 Å
α-Mg	3	$Mg_{94}Zn_2Y_2Gd_2$	97.81±1.23	0.63±0.55	0.79±0.33	0.77±0.35	a=3.219 Å, c=5.216 Å
α-Mg	4	$Mg_{94}Zn_3Y_3$	98.02±0.60	0.97±0.34	1.00±0.29		a=3.213 Å, c=5.213 Å
α-Mg	5	$Mg_{94}Zn_3Gd_3$	98.50±0.19	0.52±0.09		0.98±0.12	a=3.217 Å, c=5.215 Å
α-Mg	6	$Mg_{94}Zn_3Y_{1.5}Gd_{1.5}$	98.39±0.16	0.53±0.06	0.67±0.07	0.41±0.04	a=3.215 Å, c=5.213 Å
α-Mg	7	$Mg_{94}Zn_{4.2}Y_{1.8}$	98.02±0.40	1.48±0.27	0.49±0.13		a=3.208 Å, c=5.207 Å
α-Mg	8	$Mg_{94}Zn_{4.2}Gd_{1.8}$	98.55±0.11	1.11±0.07		0.34±0.04	a=3.207 Å, c=5.205 Å
α-Mg	9	$Mg_{94}Zn_{4.2}Y_{0.8}Gd_1$	97.73±0.84	1.33±0.63	0.42±0.11	0.53±0.13	a=3.209 Å, c=5.206 Å
α-Mg	10	$Mg_{94}Zn_{4.2}Y_{0.8}Gd_{0.5}$	97.48±0.43	2.32±0.42	0.14±0.04	0.06±0.02	a=3.208 Å, c=5.206 Å
W	2	$Mg_{94}Zn_2Gd_4$	62.95±3.81	15.96±2.14		21.21±1.94	a=7.178 Å
W	4	$Mg_{94}Zn_3Y_3$	31.12±2.21	43.15±1.16	25.73±1.14		a=6.866 Å
W	5	$Mg_{94}Zn_3Gd_3$	42.19±1.47	30.79±1.12		27.01±0.52	a=7.035 Å
W	6	$Mg_{94}Zn_3Y_{1.5}Gd_{1.5}$	47.25±6.34	30.82±3.82	9.94±1.09	11.99±1.46	a=6.934 Å
W	7	$Mg_{94}Zn_{4.2}Y_{1.8}$	29.9±2.16	44.54±1.49	25.58±0.67		a=6.852 Å
W	8	$Mg_{94}Zn_{4.2}Gd_{1.8}$	29.94±1.35	43.87±1.19		26.19±0.41	a=6.902 Å
W	9	$Mg_{94}Zn_{4.2}Y_{0.8}Gd_1$	39.79±3.91	34.96±1.50	9.09±1.10	16.16±1.62	a=6.883 Å
W	10	$Mg_{94}Zn_{4.2}Y_{0.8}Gd_{0.5}$	32.84±3.97	41.94±2.50	15.24±1.26	9.98±0.59	a=6.868 Å
18R	1	$Mg_{94}Zn_2Y_4$	87.06±1.06	5.19±0.46	7.76±0.63		a=11.201 Å, b=19.377 Å, c=31.456 Å, β=93.439 º
18R	3	$Mg_{94}Zn_2Y_2Gd_2$	86.69+0.86	5.35±0.86	3.83±0.39	4.14±0.41	a=11.206 Å, b=19.375 Å, c=31.389 Å, β=93.391 º
18R	4	$Mg_{94}Zn_3Y_3$	83.61±0.62	8.97±0.66	7.42±0.39		
18R	6	$Mg_{94}Zn_3Y_{1.5}Gd_{1.5}$	87.37±2.02	5.27±0.80	4.25±0.63	3.10±0.62	
14H	3	$Mg_{94}Zn_2Y_2Gd_2$	86.99±0.78	5.08±0.32	3.89±0.25	4.07±0.30	a=11.190 Å, c=36.532 Å
14H	4	$Mg_{94}Zn_3Y_3$	85.18±1.06	8.63±1.02	6.19±0.36		a=11.152 Å, c=36.571 Å
14H	6	$Mg_{94}Zn_3Y_{1.5}Gd_{1.5}$	86.88±0.69	5.49±0.26	4.38±0.32	3.24±0.13	a=11.168 Å, c=35.972 Å
LPSO	9	$Mg_{94}Zn_{4.2}Y_{0.8}Gd_1$	86.86±1.35	6.97±1.13	2.73±0.23	3.44±0.43	
i-phase	7	$Mg_{94}Zn_{4.2}Y_{1.8}$	28.66±1.52	59.49±1.40	11.85±0.16		
i-phase	8	$Mg_{94}Zn_{4.2}Gd_{1.8}$	30.75±5.18	57.87±4.40		11.23±0.70	
i-phase	10	$Mg_{94}Zn_{4.2}Y_{0.8}Gd_{0.5}$	26.23±0.98	62.67±0.86	5.79±0.19	5.32±0.07	
$MgZn_2$	8	$Mg_{94}Zn_{4.2}Gd_{1.8}$	32.05±2.99	67.69±2.91		0.26±0.09	

6.6 Discussion

6.6.1 The effect of alloying elements on the lattice parameters of the Mg matrix.

Table 6.2 indicates the lattice parameters of the Mg matrix are different in the different alloys, e.g. a from 3.2072 Å to 3.2242 Å and c from 5.2050 Å to 5.2196 Å. Figure 6.16 shows how the lattice parameters of Mg (red spots) change with the concentrations of alloying elements Zn, Y and Gd. Y and Gd have not been separated since the lattice parameters of Gd and Y are quite similar.

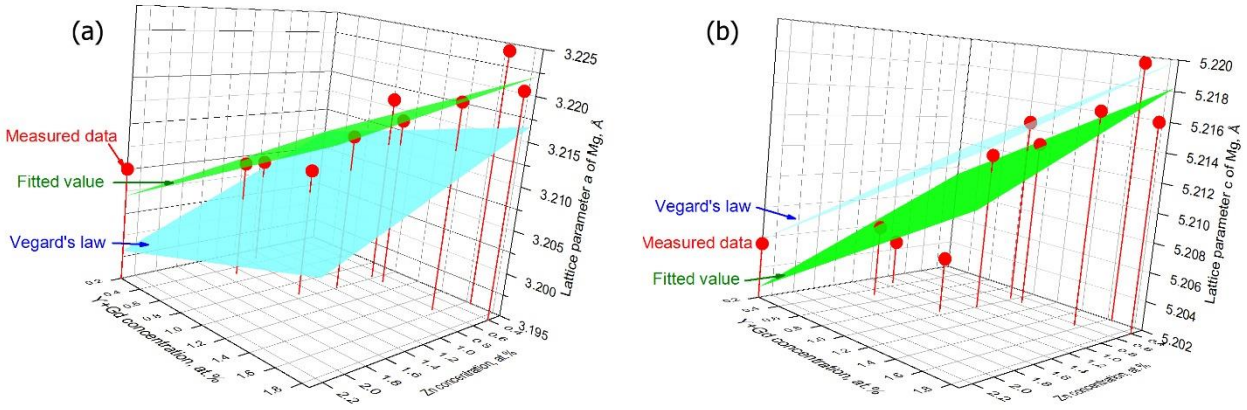

Figure 6.16 (a) lattice parameter a of Mg matrix; (b) lattice parameter c of Mg matrix.

Figure 6.16 shows that in general, a and c increase with increasing Y+Gd content and decreases with Zn content. This is due to the atomic radius of Mg being smaller than those of Y and Gd and larger than that of Zn, as shown in Table 6.3. Alloying elements Zn and Y are present in the Mg matrix as substitutional atoms. Vegard's law [145] states that when two salts form a continuous solid solution, the effective lattice parameter often varies almost linearly with the solute concentration, as a weighted mean of the lattice spacings of the solute and solvent. Although

Vegard's law is commonly used for binary systems, in this alloy, Zn, Y and Gd all form an hcp structure, which is same as that of Mg. Applying the Vegard's law to this alloy system:

$$a_s = a_{Mg} - 0.545 \times C_{Zn} + 0.437 \times C_{Y+Gd}$$
$$c_s = c_{Mg} - 0.264 \times C_{Zn} + 0.520 \times C_{Y+Gd}$$

where a_s and c_s are the lattice parameters (Å) for the solution and a_{Mg} and c_{Mg} are the lattice parameters (Å) for pure Mg. The lattice parameters for pure Mg are about a = 3.210 Å and c = 5.211 Å [146]. C_{Zn} (unit is 1) is the atomic concentration of Zn and $C_{(Y+Gd)}$ (unit is 1) is the combined concentration of Y and Gd. -0.545 Å is the difference between a_{Zn} and a_{Mg}. $+0.437$ Å is the difference between a_Y and a_{Mg}. The lattice parameters of the pure alloys are listed in Table 6.3.

Table 6.3 Lattice parameters of pure elements [147].

	a, Å	**c, Å**	**metallic radius, Å**
Mg	3.210	5.211	1.50
Zn	2.665	4.947	1.35
Y	3.647	5.731	1.77
Gd	3.636	5.783	1.80

The calculated lattice parameters based on Vegard's law have also been shown as a blue surface in Figure 6.16 in comparison with the measured data. For lattice parameter a, the calculated results from Vegard's law are normally smaller than the measured data but with the same trend with some scatterings. For c, the calculated results from Vegard's law are a little larger than the measured data, but also with a similar trend. It is commonly observed that the measured data can deviate from the theoretical data. By using multiple line regression to fit the measured data, the constants of the equation are obtained. The fitted values are shown in green plane, which is a

better fit than the Vegard's law. When there is no alloying element in the matrix, the fitted lattice parameters of a are very close to those of pure Mg.

$$a_s = 3.2086 - 0.242 \times C_{Zn} + 0.764 \times C_{Y+Gd}$$
$$c_s = 5.2092 - 0.326 \times C_{Zn} + 0.539 \times C_{Y+Gd}$$

6.6.2 Chemical compositions and lattice parameters of the W phase.

The W phase was first reported in the Mg-Zn-Y system by Padezhnova et al. [115] and the structure was given by Tsai et al. [34] as fcc with a lattice parameter of 6.83 Å. A formula was given as $Mg_2Zn_3Y_3$ at. % [34] although the measured data differ, e.g. a typical composition measured after anneals at 700K is $Mg_{25}Zn_{60}Y_{13}$. In Mg-Zn-Gd alloys, e.g. alloy 2, a fcc phase in the eutectic has been identified as W. It is worth pointing out that the W phase can also be identified as Mg_3Gd phase with a fcc structure and lattice parameter a of about 7.33 Å [148] when Mg is partially replaced by Zn. Zhang et al. [149] reported a $(Mg,Zn)_3(Gd,Y)_1$ phase with a composition of $Mg_{65\pm3}Gd_{21.5\pm2}Y_{3.5\pm1}Zn_{6\pm10}$. However, in Mg-Y binary alloys, Mg_3Y phase is not observed [32].

The current work shows W phase has a large range of compositions. The measured compositions for W phase in each alloy are presented in Figure 6.17. The data in the literature are summarised in Table 6.4 and some are also shown in Figure 6.17. The current data show the Y+Gd content in W phase is quite similar in each alloy, it lies close to 25% when the Mg content is less than 43%. When Mg is more than 43%, the Y+Gd content also decreases a little.

Table 6.4 The chemical compositions of W phase in the literature.

	Chemical compositions of W				Alloy conditions	Reference
	Mg	**Zn**	**Y**	**Gd**		
Mg-Zn-Y	20	60	18		Annealed at 873K for 20h	[34]
	24	61	15		Annealed at 773K for 20h	
	24	60	16			
	27	49	24			
	24	62	13		Annealed at 700K for 20h	
	25	60	13			
	37	43	20		As-cast	[150]
	26.3	49.5	24.2		Annealed at 723-793 K for several days	[151]
	26.9	48.5	24.6		Annealed at 693-813 K for several days	
Mg-Zn-Gd	42.5	35.17		22.32	Annealed at 473K for 720h	[152]
	32.65	44.52		22.83		
	32.52	47.72		19.76		
	37.52	38.63		23.95		
	26.20	48.68		25.11		
	26.05	49.06		24.89		
	25.52	49.17		25.31		
	43.01	37.47		19.51		
	27.21	48.30		24.49		
	31.21	43.05		25.74	After extrusion at 463K	[153]

The varying chemical compositions of the W phase are caused by substitutional Mg and Zn atoms and are related to the atomic positions. Shao et al [154] proposed a model of $(Mg, Zn)_{0.4}Y_{0.2}(Mg, Zn)_{0.4}$ which is based on a composition of $Mg_3Zn_3Y_2$, and then changed it to $Mg_{0.2}Y_{0.2}(Mg, Zn)_{0.6}$ based on $MgYZn_3$ in an erratum [155]. The possible compositions based on $Mg_{0.2}Y_{0.2}(Mg, Zn)_{0.6}$ are represented by black dashed line in Figure 6.17. Gröbner et al. [36] used $Y_{0.25}Mg_{0.25}(Mg, Zn)_{0.5}$ to calculate the Mg-Zn-Y ternary phase diagram. Two compositions of $Y_{0.25}Mg_{0.25}(Mg, Zn)_{0.5}$ are shown as red squares and the line connecting both spots shows the possible compositions. Although the chemical compositions of the W phase in this work are in non-equilibrium, the compositions observed is quite close to this model.

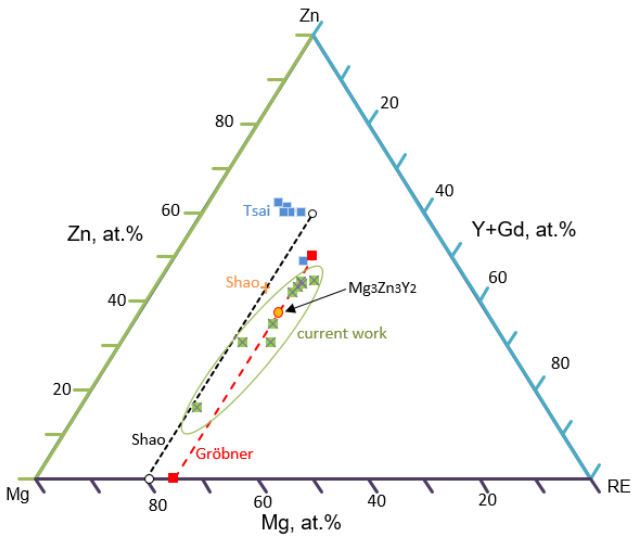

Figure 6.17 The chemical compositions of W phase in Mg-Zn-Y comparing to the literatures [34] [150] [36] [155].

The schematic drawing of the W phase (Figure 6.18) based on the model shows the larger Y/Gd atoms are in the 4a position (0, 0, 0) and the Mg atoms are in the 4b position (0.5, 0.5, 0.5). The smaller Zn atoms are in the 8c position (0.25, 0.25, 0.25) associated with Mg (ideally the Mg:Zn ratio is 1:3 in the Mg-Zn-Y system, indicated by the blue balls). In the models, the atoms in 8c position are more likely to be replaced by Mg or Zn.

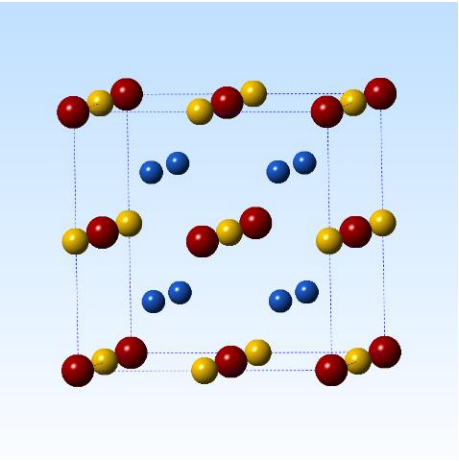

Figure 6.18 Cell structure of W phase, red ball is Y, yellow ball is Mg, blue ball is Mg or Y (Mg:Y=1:3)

This model provides a possible explanation that the total compositions of Zn and Mg are quite similar in all the alloys while Mg has a wide range from about 30-63%. However, the W phase in alloys 2, 5 and 6 (all containing Gd) has relatively higher Mg concentrations than these observed in W phase in Mg-Zn-Y alloys the literature. This is probably because the existence of Gd lead the phase to be close to Mg_3Gd, where a high concentration of Mg can exist.

The lattice parameters of the W phase also vary with the varying chemical compositions. The total compositions of Y and Gd are quite stable, so it is likely that the lattice parameters change with the Zn and Mg concentrations. The largest lattice parameter of W phase has been observed in alloy 2 with a very high concentration of Mg atoms (up to 63%) and the smallest lattice parameter was found in alloy 7 with the lowest Mg concentration of about 30%. This is due to the metallic size of Mg being larger than that of Zn. The measured data are shown in Figure 6.19. Although Vegard's law is not suitable for the W phase, the lattice parameter generally increased with greater Mg concentration. So, the lattice parameter was fitted using multiple linear regression, and the fitted results are very similar to the measured data except for alloys 7 and 8, which has a 0.4 and 0.7 Å offset. The fitted equation is

$$a_W = 6.9209 - 1.267 \times (C_{Zn} - 37.5\%) + 1.384 \times (C_{Y+Gd} - 25\%)$$

where a_W (Å) is the lattice parameter of W phase, C_{Zn} (unit is 1) is the chemical concentration of Zn and C_{Y+Gd} is the total chemical concentration of Y and Gd.

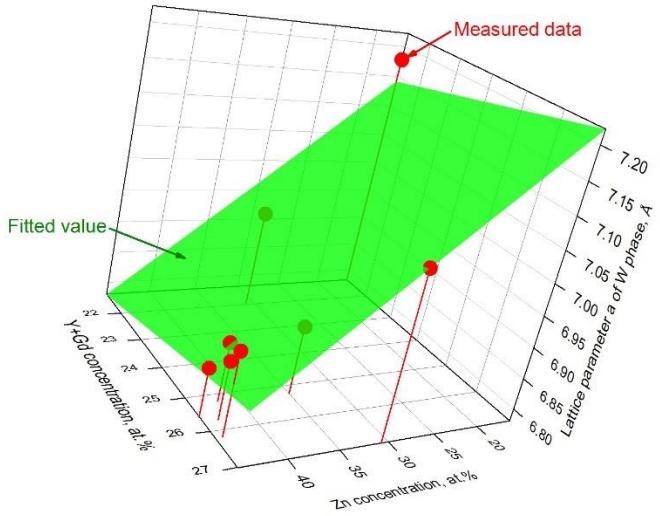

Figure 6.19 Lattice parameter a of W phase as a function of Zn and Y+Gd concentration.

6.6.3 The chemical composition of the LPSO phase.

As shown in Table 6.2 and Figure 6.20, there is no obvious difference in chemical composition between 14H and 18R type LPSO phases. The 18R type LPSO shows quite similar lattice parameters in different alloys due to the similar concentrations of Zn and Y. The 14H type LPSO phase shows slightly a larger difference between the lattice parameter of each phase than the 18R type LPSO. The smallest lattice parameter is found in alloy 4 where the highest Zn concentration of about 8.6% is found. A slightly larger lattice parameter for 14H type LPSO is found in alloy 3 where there is less Zn and more Y+Gd compared with alloy 6. This is also caused by the smaller atomic size of Zn compared with that of Gd and Y.

The chemical compositions of the LPSO phase differ depending on the concentrations of alloying elements in the system [53]. For example, in the dilute $Mg_{97}Zn_1Y_2$ system, the composition of LPSO phase measured by TEM-EDS is about $Mg_{94}Zn_2Y_4$ [53]. In $Mg_{88}Zn_5Y_7$ alloy, the

composition of the 18R LPSO phase measured by SEM-EDS is about $Mg_{85.5}Zn_{7.1}Y_{7.4}$ [63]. The composition based on the ideal model is $Mg_{80.6}Zn_{8.3}RE_{11.1}$ for 18R type LPSO and $Mg_{83.3}Zn_{7.2}RE_{9.5}$ for 14H type LPSO phase [53] [33].

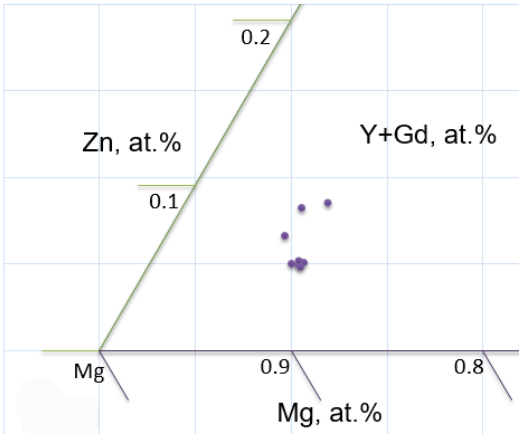

Figure 6.20 The chemical compositions of LPSO phase

6.6.4 The effect of Zn/RE ratio and Y/Gd on secondary phase formation.

A summary of the secondary phases and the hardnesses of the alloys is presented in Table 6.5. Besides the bulk W and LPSO phases, very thin LPSO phase, i-phase and $MgZn_2$ have also been observed in several alloys in a minor role. The area fractions of the bulk shaped secondary phases were measured using Image J based on 5 SEM images. The area fractions of minor secondary phases are not given.

In the Mg-Zn-Y alloys (Alloy 1, 4, 7), the main secondary phase changes when different ratios of Zn/Y are applied: LPSO (Zn/Y ratio is 0.5) → LPSO+W (Zn/Y ratio is 1) → W (Zn/Y ratio is 2.33). In the Mg-Zn-Y-Gd alloys (alloy 3, 6, 9, 10), the secondary phases are similar to those when only Y is present: LPSO (Zn/(Y+Gd) ratio is 0.5) → LPSO+W (Zn/(Y+Gd) ratio is 1) →

W (Zn/(Y+Gd) ratio is 2.33, 3.23). In the Mg-Zn-Gd alloys (alloy 2, 5 and 8), W phase is the main secondary phase. Very thin LPSO also exists in alloy 2 and 5.

Table 6.5 summaries of secondary phases and their area fractions and hardness of the alloys.

No	Chemical compositions	Hardness, HV	Secondary phases	Area fraction, %
1	$Mg_{94}Zn_2Y_4$	82±1	LPSO (18R)	41.2±3.1
2	$Mg_{94}Zn_2Gd_4$	113±5	W	21.3±0.3
			thin LPSO (minor)	
3	$Mg_{94}Zn_2Y_2Gd_2$	72±6	LPSO (18R, 14H)	40.0±1.6
4	$Mg_{94}Zn_3Y_3$	77±3	W	5.3±0.1
			LPSO (14H>18R)	30.0±1.7
5	$Mg_{94}Zn_3Gd_3$	108±5	W	20.4±0.9
			thin LPSO (minor)	
6	$Mg_{94}Zn_3Y_{1.5}Gd_{1.5}$	84±2	W	7.2±0.6
			LPSO (mainly 14H)	27.7±2.0
7	$Mg_{94}Zn_{4.2}Y_{1.8}$	75±2	W	10.0±0.9
			i-phase (minor)	
8	$Mg_{94}Zn_{4.2}Gd_{1.8}$	91±4	W	17.0±0.7
			i-phase (minor)	
			$MgZn_2$ (minor)	
9	$Mg_{94}Zn_{4.2}Y_{0.8}Gd_1$	85±5	W phase	18.0±2.0
			thin LPSO (minor)	
			i-phase (minor)	
10	$Mg_{94.5}Zn_{4.2}Y_{0.8}Gd_{0.5}$	76±6	W phase	12.0±1.0
			thin LPSO (minor)	
			i-phase (minor)	

Previous studies [1] [4] [33] [36] [156] [151] [157] have shown that the Zn to Y ratio plays a key role in the secondary phase stability in Mg-Zn-Y ternary alloys. With increasing Zn/Y ratio, the stability of the secondary phase increases in the sequence: $Mg_{24}Y_5$ → LPSO → W → i-phase → Mg_7Zn_3. The results from the current work agree with this. From the EDS results, LPSO normally contains more Y than Zn, so if a two phase alloy (Mg and LPSO) is designed, more Y

than Zn should be added to the alloy. This has been confirmed by alloy 1 and alloy 4. When the Zn to Y ratio is 0.5, only LPSO is observed. When the Zn to Y ratio is 1, W phase is also observed along with LPSO phase.

In Mg-Zn-Gd alloys, LPSO phase does not form in the as-cast condition [158]. Normally, it forms after solution treatment or aging at high temperature [159] [160]. The current results show that the main precipitate in the Mg-Zn-Gd is W phase regardless of the Zn to Gd ratio changing from 0.5 to 2.33. It results in different chemical compositions of the W phase in alloys 2, 5 and 8. The Zn content of the W phase increases when the Zn content in the alloys increases. For example, W phase in alloy 2 ($Mg_{94}Zn_2Y_4$) and alloy 8 ($Mg_{94}Zn_{4.2}Y_{1.8}$) contains 16% Zn and 44% Zn respectively. Besides W phase, very thin LPSO phases exist in the Mg matrix when the Zn to Gd ratios are 0.5 and 1. A similar morphology is also observed in $Mg_{96.5}Zn_1Gd_{2.5}$ [160]. It is likely that the thin LPSO phases form during cooling of the solid Mg matrix.

In the Mg-Zn-Y-Gd system, the secondary phases are quite similar to the Mg-Zn-Y ternary system rather than Mg-Zn-Gd when the Zn to Y+Gd ratio varies from 0.5-2.33. However, the structures of the LPSO phase are different. In alloy 1 ($Mg_{94}Zn_2Y_4$), only 18R type LPSO phase is observed. When Gd replaced half the Y, 14H forms (alloy 3). The structure of LPSO also changes with different Zn to Y+Gd ratios in the system. When Zn to Y ratio is 1 ($Mg_{94}Zn_3Y_3$), 14H is the main type of LPSO phase. This is indicated by the XRD results: 14H LPSO peak is much higher than that of 18R LPSO. When the Zn to Y+Gd ratio is still 1 and Gd is present, only the 14H LPSO peak is present in the XRD spectrum. No 18R peak is observed. This indicates that Gd stabilised the 14H LPSO while Y stabilises the 18R LPSO in the as-cast condition. 14H LPSO is more likely to form with a larger Zn to Y+Gd ratio.

The Y and Gd distributions in different phases have been calculated and are shown in Figure 6.21. No obvious difference in Y and Gd distribution has been observed in the phases. It is due to the Y and Gd have some similar properties in Mg alloys: 1) the atomic radii of Y and Gd are 1.77 and 1.80 Å, respectively, which are about 11% larger than that of Mg [31]; 2) the electronic configurations of Y and Gd in the ground state are $5d^16s^2$ and $4f^75d^16s^2$ respectively. Both show typical R^{3+} ionic species and contain 3 electrons in the (5d+6s) orbitals (trivalent state) for the metallic state [31]; 3) the solid solubility limits of Y and Gd in Mg are about the same with a value of 1.66 at.% at 372℃ [31]; 4) the diffusion coefficients of Y and Gd in solid Mg are similar, e.g. about 3.5×10^{-15} m^2/s at 470 ℃, which is about one order of magnitude lower than the diffusion coefficients of Al and Zn in Mg [161].

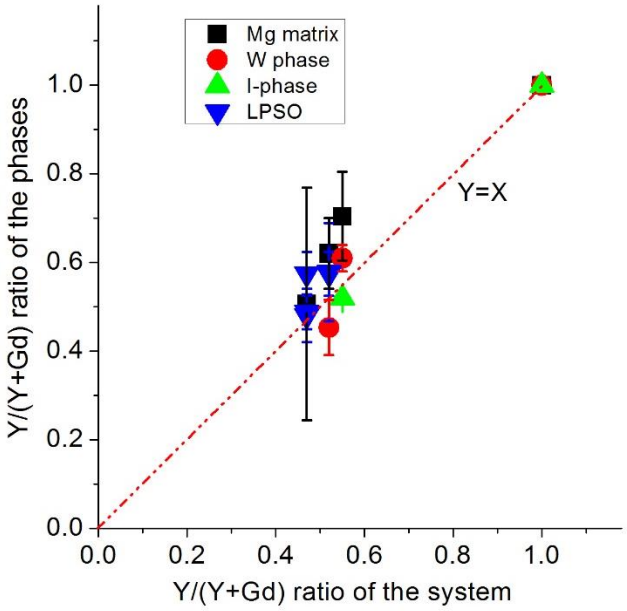

Figure 6.21 The Y/(Y+Gd) ratio measured in different phases versus the overall Y/(Y+Gd) ratios in the as-cast alloys.

6.6.5 The hardness

The hardness values of the as-cast alloys have been given in Table 6.5 and also shown in Figure 6.22 along with area fractions of second phase. The highest hardness of about 113 Hv is found in alloy 2, which contains about 21% of W phase. The lowest hardness of about 72 Hv is found in alloy 3 which contains 40% LPSO phase.

Alloys containing only W phase as main secondary phase have a large range of hardness values, e.g. from 75 Hv to 113 Hv. It is noticed that the hardness is related to the area fraction of W phase. The hardness decreased when the area fraction of the W phase decreased, except for alloys 8 and 9, when different amounts of Gd and Y are added. Alloys 8 and 9 have the same amount of alloying element and similar area fractions of W phases. The differences are that alloy 8 contains 1.8% of Gd while alloy 9 contains 0.8% of Y and 1% of Gd. The hardness of alloy 8 is higher than that of alloy 9.

The alloys which contains only LPSO as secondary phase, e.g. alloy 1 and alloy 3, have hardnesses of about 82 Hv and 72 Hv, although the area fractions are about 40 %.

The hardness of the alloys which contain mainly LPSO (about 30%) and about 5% W phase, e.g. alloys 4 and 6, are about 80 Hv. The hardness is quite similar to that of alloy 2, which is mainly due to the high area fraction of LPSO phase.

The different hardnesses of the alloys are mainly due to the strengthening effect of the secondary phases. W phase is an intermetallic compound, which generally have high hardness and brittleness. Due to the strengthening by the W phase, the hardness of the alloys is generally higher when higher area fractions of W phase are present. Compared to W phase, the LPSO

phase is softer. The LPSO phase is only a little harder than the Mg matrix [127]. So alloy 1 containing 41% LPSO phase has a lower hardness than alloy 2 containing 21% W phase.

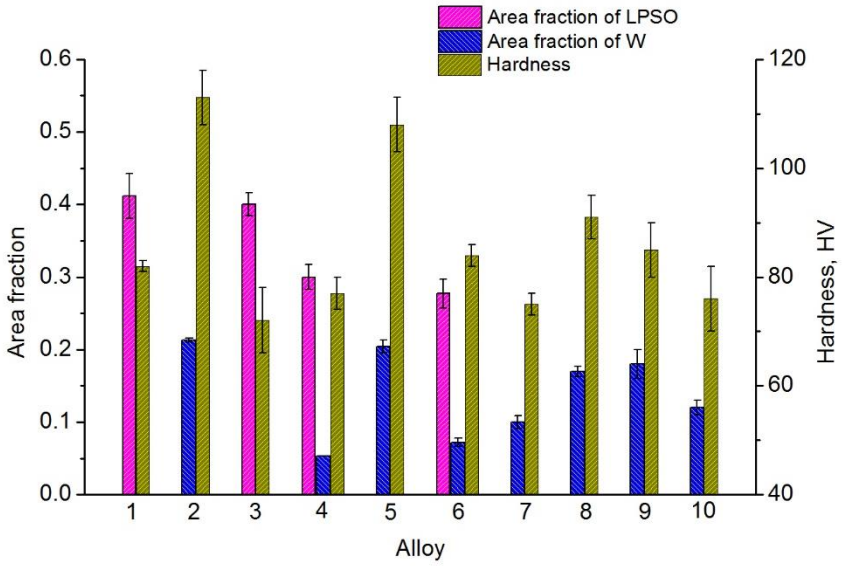

Figure 6.22 The relationship between area fraction of the secondary phases and hardness.

LPSO phase and W phase have different strengthening mechanisms in the alloy. W phase is generally harder than LPSO phase, but as the volume fraction increases, the strength and ductility must decrease. For example, Xu et al. [41] suggested that when the volume fraction of W phase exceeds 17% in as-cast Mg-Zn-Y-Zr alloys, the tensile strength and ductility dropped due to particle coarsening and stress concentration. As reviewed earlier, kinking of the LPSO phase is expected to increase both strength and ductility through grain refinement. So, alloys containing both LPSO and W phase, e.g. alloys 4 and 6, have the potential to be strong and ductile. But if alloys are to be used as components, varies of mechanical properties, e.g. yield strength and ductility, still need to be assessed in the further work.

6.7 Highlights

In this chapter, a systematic investigation of the secondary phases and their chemical compositions has been carried out on the as-cast Mg-Zn-(Y)-(Gd) alloys. The main highlights are summarised below.

1. Some results on the effect of the Zn/Y ratio on secondary phase formation in Mg-Zn-Y alloys have been reported. In addition to previous work, this study also considers the effect of different RE elements (Y or Gd) and the combination of two effects on the formation of secondary phase.

2. It has been discovered that the structure of the LPSO is related to the Zn to Y+Gd ratios and to the alloying element (ie Gd or Y).

3. With different chemical compositions, the lattice parameters of the phases vary, which is especially obvious in W phase. The relations between the lattice parameters and the alloying elements of W phase and Mg matrix have been established.

4. The results also show the hardnesses of the alloys and their relations to the secondary phases.

6.8 Conclusions

1. In the as-cast Mg-Zn-Y alloys (Alloy 1, 4, 7), the main secondary phase changes when different ratios of Zn/Y are applied: LPSO (Zn/Y ratio is 0.5) → LPSO+W (Zn/Y ratio is 1) → W (Zn/Y ratio is 2.33). The second phases in Mg-Zn-Y-Gd alloys (alloy 3, 6, 9, 10) are similar to

when only Y is present. In the Mg-Zn-Gd alloys (alloy 2, 5 and 8), W phase is the main secondary phase.

2. The structure of the LPSO phase changes with different Zn to Y+Gd ratios and different RE elements. In $Mg_{94}Zn_2Y_4$ alloy, only 18R type LPSO phase is observed. When Gd replaced half Y, 14H forms (alloy 3). When the Zn to Y ratio is 1 ($Mg_{94}Zn_3Y_3$), 14H type is the main LPSO phase. When the Zn to Y+Gd ratio is still 1 and Gd is present, only the 14H LPSO peak is present in the XRD results. No 18R peak is observed. This indicates that Gd stabilises 14H LPSO while Y stabilises 18R LPSO in the as-cast condition; 14H LPSO is more likely to form with a larger Zn to Y+Gd ratio.

3. The chemical compositions of the secondary phases and Mg matrix change with different concentrations of alloying elements. Thus the lattice parameters of the phases also change. In general, the lattice parameters of the Mg matrix and of the W phase increase when more Y and Gd but less Zn are present.

4. The hardness of the alloys is most affected by the presence of the secondary phases. The alloys with mainly LPSO phase (about 40%) have a hardness of about 80 HV. In the W containing alloys, a higher hardness is found when a higher area fraction of W phase is present. In general, alloys with W phase have a higher hardness than those with LPSO phase if there are similar area fractions of secondary phases.

7 Conclusions and suggestions for future work

7.1 Conclusions

Dislocation analysis of kinks in the LPSO phase and the LPSO/Mg structure (Chapter 4)

An as-cast $Mg_{94}Zn_2Y_4$ alloy containing LPSO and $Mg_{24}Y_5$ was compressed and ECAP processed separately. The deformed microstructure is investigated focusing on the dislocations in the kink boundaries of the LPSO phase and LPSO/Mg region. The following conclusions are drawn:

1. Deformation kinks have been observed after compressing at room temperature to 2%. The low angle kink boundaries in the LPSO phase are essentially dislocation walls, which are composed of <a> type (Burgers vector of $\frac{a}{3}\langle\bar{2}110\rangle$) basal dislocations. One example shows a dislocation wall caused crystal lattice rotation around the $[1\bar{5}40]$ zone axis; two dislocation line directions have been observed in this kink boundary. The misorientation angles calculated using dislocation spacings are consistent with those measured by TEM.

2. The TKD results shows that the kink boundaries in the LPSO/Mg region have rotation axes mainly distributed around the edge of a stereogram with 0001 at the centre, from $\langle 1\bar{2}10\rangle$ to $\langle 0\bar{1}10\rangle$. The rotation zone axes are not restricted to specific crystallographic zone axes: they can be positioned in the annular area, which is likely to lie in the (0001) plane. An [0001] rotational axis has also been observed.

3. Paired kink boundaries rotating in two opposite directions with a resulting total kink angle of about zero have been observed in the LPSO/Mg region; this may be explained by the generation of dipole-pair dislocations as proposed by Hess and Barrett. The double kinking, one pair of kink boundaries located inside another pair of kink boundaries (c.f. double twinning), has also been observed.

4. The dislocation morphology of the kink boundaries in LPSO/Mg is similar to that in the LPSO phase. However, non-basal slip in the Mg can accommodate strains comparable to those in the kinked area.

The effect of ECAP on the microstructure and mechanical properties of $Mg_{94}Zn_2Y_4$ alloy (Chapter 5):

5. Mg-Zn-Y alloys after ECAP developed a bimodal microstructure consisting of large deformed grains (Mg and LPSO) and sub-micron sized dynamically recrystallised (DRXed) grains. The DRXed Mg grains are mainly located in the original Mg grain boundaries and are caused by grain rotation. The DRXed grain boundaries are decorated with a large number of nano-sized $Mg_{24}Y_5$ precipitates, which limit the grain growth.

6. LPSO phase and LPSO/Mg structure kink to accommodate the strain, introducing many kink boundaries into the surrounding matrix. The kink boundaries in the LPSO/Mg regions are potential DRX nucleation sites for Mg grains. The DRXed Mg grains tend to form at kink boundaries with relatively high misorientation angles. Although high angle kink boundaries also

exist in the LPSO phase, DRX of the LPSO phase does not occur. This may be due to the high stacking fault energy and the low diffusion rates of Zn and Y in the LPSO phase.

7. The SPT strength of the $Mg_{94}Zn_2Y_4$ alloy increased significantly after ECAP. The bimodal structure exhibits asymmetrically shaped cracks along the ECAP shear direction and the perpendicular direction after SPT. The cracks start to form shortly after the linear elastic region during SPT under a biaxial tensile stress. The initial crack lies in the shear direction and DRXed grains are potential crack sources. This may be due to the strong fibre texture of the large grains inhibiting the dominant basal slip due to the low Schmid factors in the shear direction and perpendicular direction and leading to the deformation first of DRXed grains. These observations show that the bimodal structure exhibits better ductility when the tensile stress is applied along the shear direction than in the perpendicular direction. If ECAP is to be used to refine the microstructure of Mg-Zn-Y alloys and allow them to be employed as sheets it will be necessary to take into consideration the different deformation behaviour of the bimodal structure along different directions.

8. A fragmentation mechanism has been proposed for eutectic $Mg_{24}Y_5$ intermetallic particles during ECAP. Initially, cracks are formed which lead to fragmentation and reduce significantly the size of the $Mg_{24}Y_5$ particles; second, dynamic recrystallisation of these intermetallics occurs in the heavily deformed areas, e.g. near the crack. An agglomeration of DRXed $Mg_{24}Y_5$ grains gives rises to necking and thus to a dispersion of small $Mg_{24}Y_5$ particles. Meanwhile, the Mg matrix exhibits better formability than $Mg_{24}Y_5$, which makes it possible to separate the fragmented $Mg_{24}Y_5$ particles.

The effect of Gd additions on Mg-Zn-Y alloys (Chapter 6):

9. In the as-cast Mg-Zn-Y alloys (Alloy 1, 4, 7), the main secondary phase changes for different ratios of Zn/Y: LPSO (Zn/Y ratio is 0.5) → LPSO+W (Zn/Y ratio is 1) → W (Zn/Y ratio is 2.33). The secondary phases in the Mg-Zn-Y-Gd alloys (alloy 3, 6, 9, 10) are similar to when only Y is present. In the Mg-Zn-Gd alloys (alloy 2, 5 and 8), W phase is the main secondary phase.

10. The structure of the LPSO phase changes with different Zn to Y+Gd ratios and different RE elements. In $Mg_{94}Zn_2Y_4$ alloy, only 18R type LPSO phase is observed. When half Y are replaced by Gd, 14H forms (alloy 3). When the Zn to Y ratio is 1 ($Mg_{94}Zn_3Y_3$), 14H type is the main LPSO phase. When the Zn to Y+Gd ratio is still 1 and Gd is present, only the 14H LPSO peak is present in the XRD results. No 18R peak is observed. This indicates that Gd stabilises the 14H LPSO while Y stabilises the 18R LPSO in the as-cast condition; 14H LPSO is more likely to form with larger Zn to Y+Gd ratio.

11. The chemical compositions of the secondary phases and Mg matrix change with different amounts of alloying elements. The lattice parameters of the phases also change. In general, the lattice parameters of the Mg matrix and W phase increase when more Y and Gd and less Zn are present.

12. The hardness of the alloys is most affected by the presence of secondary phases. The alloys with mainly LPSO phase (about 40%) have a hardness of about 80 HV. In the W present alloys, a higher hardness is found when a higher area fraction of W phase is present. In general,

alloys with W phase have a higher hardness than those with LPSO phase for similar area fractions of secondary phases.

7.2 Suggestions for future work

1. From the current study, basal slip and kinking are responsible for the deformation of LPSO phase at room temperature and at 300 ℃. However, if deformed at higher temperature, evidence has shown that non-basal slip occurred. In the future, it is of interest to study non-basal slips and kinking of the LPSO phase at higher temperatures.

2. It is also interesting to study the effect of the ECAP parameters, including temperature, number of passes and different routes, on the microstructure and mechanical properties of the Mg-Zn-Y, ultimately to optimise the strength and ductility of the alloys.

8 Bibliography

1. J.Y. Lee, D.H. Kim, H.K. Lim, D.H. Kim, *Effects of Zn/Y ratio on microstructure and mechanical properties of Mg-Zn-Y alloys.* Materials Letters, 2005. **59**(29–30): p. 3801-3805.

2. Y. Kawamura, M. Yamasaki, *Formation and Mechanical Properties of $Mg_{97}Zn_1RE_2$ Alloys with Long-Period Stacking Ordered Structure.* Materials Transactions, 2007. **48**(11): p. 2986-2992.

3. E. Abe, Y. Kawamura, K. Hayashi, A. Inoue, *Long-period ordered structure in a high-strength nanocrystalline Mg-1 at% Zn-2 at% Y alloy studied by atomic-resolution Z-contrast STEM.* Acta Materialia, 2002. **50**(15): p. 3845-3857.

4. Y.M. Zhu, A.J. Morton, J.F. Nie, *The 18R and 14H long-period stacking ordered structures in Mg–Y–Zn alloys.* Acta Materialia, 2010. **58**(8): p. 2936-2947.

5. Y. Kawamura, K. Hayashi, A. Inoue, T. Masumoto, *Rapidly Solidified Powder Metallurgy $Mg_{97}Zn_1Y_2$ Alloys with Excellent Tensile Yield Strength above 600 MPa.* Materials Transactions, 2001. **42**: p. 1172-1176.

6. N. Li, *Automotive magnesium applications and life cycle environmental assessment.* 3rd International Conference on SF_6 and the environment, Scottsdale, 2004.

7. I. Ostrovsky, Y. Henn, *Present state and future of magesium application in aerospace industry.* International Conference "New Challenges in Aeronautics" ASTEC'07, 2007.

8. G.W. Groves, A. Kelly, *Independent slip systems in crystals.* Philosophical Magazine, 1963. **8**(89): p. 877-887.

9. G.I. Taylor, *Plastic strain in metals.* Journal of the Institute of Metals. 1938. **12**: p. 207-324.

10. P.G. Partridge, *The crystallography and deformation modes of hexagonal close-packed metals.* International Materials Reviews, 1967. **12**(1): p. 169-194.

11. W.J.McG. Tegart, *Independent slip systems and ductility of hexagonal polycrystals.* Philosophical Magazine, 1964. **9**(98): p. 339-341.

12. L. Jiang, J.J. Jonas, R.K. Mishra, A.A. Luo, A.K. Sachdev, S. Godet, *Twinning and texture development in two Mg alloys subjected to loading along three different strain paths.* Acta Materialia, 2007. **55**(11): p. 3899-3910.

13. Y.C. Lee, A.K. Dahle, D.H. StJohn, *The role of solute in grain refinement of magnesium.* Metallurgical and Materials Transactions A, 2000. **31**(11): p. 2895-2906.

14. R.T. Wood, *The Foundryman*, 1953.

15. D.H. StJohn, M. Qian, M.A. Easton, P. Cao, Z. Hildebrand, *Grain refinement of magnesium alloys.* Metallurgical and Materials Transactions A, 2005. **36**(7): p. 1669-1679.

16. Y. Wu, W. Han, S.X. Zhou, M.V. Lototsky, J.K. Solberg, V.A. Yartys, *Microstructure and hydrogenation behavior of ball-milled and melt-spun Mg–10Ni–2Mm alloys.* Journal of Alloys and Compounds, 2008. **466**(1–2): p. 176-181.

17. H.Q. Sun, Y.N. Shi, M.X. Zhang, K. Lu, *Plastic strain-induced grain refinement in the nanometer scale in a Mg alloy.* Acta Materialia, 2007. **55**(3): p. 975-982.

18. V.M. Skripnyuk, E. Rabkin, Y. Estrin, R. Lapovok, *The effect of ball milling and equal channel angular pressing on the hydrogen absorption/desorption properties of Mg–4.95 wt% Zn–0.71 wt% Zr (ZK60) alloy.* Acta Materialia, 2004. **52**(2): p. 405-414.

19. C.I. Chang, X.H. Du, J.C. Huang, *Achieving ultrafine grain size in Mg–Al–Zn alloy by friction stir processing.* Scripta Materialia, 2007. **57**(3): p. 209-212.

20. R.L. Fleisgher, *Solution hardening.* Acta Metallurgica, 1961. **9**(11): p. 996-1000.

21. R. Labusch, *A statistical theory of solid solution hardening.* Physica Status Solidi (B), 1970. **41**(2): p. 659-669.

22. L. Gao, R.S. Chen, E.H. Han, *Effects of rare-earth elements Gd and Y on the solid solution strengthening of Mg alloys.* Journal of Alloys and Compounds, 2009. **481**(1-2): p. 379-384.

23. J.F. Nie, *Precipitation and hardening in magnesium alloys.* Metallurgical and Materials Transactions a-Physical Metallurgy and Materials Science, 2012. **43A**(11): p. 3891-3939.

24. L.M. Brown, R. K. Ham, *Strengthening methods in crystals.* Elsevier, 1971.

25. F Czerwinski, *Magnesium alloys - design, processing and properties.* InTech, 2011.

26. B. Bhattacharya, M. Niewczas, *Work-hardening behaviour of Mg single crystals oriented for basal slip.* Philosophical Magazine, 2011. **91**(17): p. 2227-2247.

27. B.L. Mordike, T. Ebert, *Magnesium: Properties – applications – potential.* Materials Science and Engineering: A, 2001. **302**(1): p. 37-45.

28. S. Yoshimoto, M. Yamasaki, Y. Kawamura, *Microstructure and mechanical properties of extruded Mg-Zn-Y Alloys with 14H long period ordered structure.* Materials Transactions, 2006. **47**(4): p. 959-965.

29. T. Homma, N. Kunito, S. Kamado, *Fabrication of extraordinary high-strength magnesium alloy by hot extrusion.* Scripta Materialia, 2009. **61**(6): p. 644-647.

30. A. Singh, Y. Osawa, H. Somekawa, T. Mukai, *Ultra-fine grain size and isotropic very high strength by direct extrusion of chill-cast Mg-Zn-Y alloys containing quasicrystal phase.* Scripta Materialia, 2011. **64**(7): p. 661-664.

31. R. Ferro, A. Saccone, S. Delfino, *Magnesium alloys of the rare earth metals: systematics and properties.* Metallurgical Science and Technology, 1998. **16**(1): p. 25-44.

32. L.L. Rokhlin, *Magnesium Alloys Containing Rare Earth Metals: Structure and Properties.* 2003: p. 256.

33. K. Kishida, K. Nagai, A. Matsumoto, A. Yasuhara, H. Inui, *Crystal structures of highly-ordered long-period stacking-ordered phases with 18R, 14H and 10H-type stacking sequences in the Mg–Zn–Y system.* Acta Materialia, 2015. **99**: p. 228-239.

34. A.-P. Tsai, Y. Murakami, A. Niikura, *The Zn-Mg-Y phase diagram involving quasicrystals.* Philosophical Magazine A, 2000. **80**(5): p. 1043-1054.

35. A. Inaba, H. Takakura, A.P. Tsai, I.R. Fisher, P.C. Canfield, *Heat capacities of icosahedral and hexagonal phases of Zn-Mg-Y system.* Materials Science and Engineering A, 2000. **294**: p. 723-726.

36. J. Gröbner, A. Kozlov, X.Y. Fang, J. Geng, J.F. Nie, R. Schmid-Fetzer, *Phase equilibria and transformations in ternary Mg-rich Mg–Y–Zn alloys.* Acta Materialia, 2012. **60**(17): p. 5948-5962.

37. D.W. Deng, K.H. Kuo, Z.P. Luo, D.J. Miller, M.J. Kramer, K.W. Dennis, *Crystal structure of the hexagonal Zn_3MgY phase.* Journal of Alloys and Compounds, 2004. **373**(1–2): p. 156-160.

38. M.-X. Zhang, P.M. Kelly, *Morphology and crystallography of $Mg_{24}Y_5$ precipitate in Mg–Y alloy.* Scripta Materialia, 2003. **48**(4): p. 379-384.

39. Y.-P. Xie, Z.-Y. Wang, Z.F. Hou, *The phase stability and elastic properties of $MgZn_2$ and Mg_4Zn_7 in Mg–Zn alloys.* Scripta Materialia, 2013. **68**(7): p. 495-498.

40. J.F. Wang, P.F. Song, S. Gao, X.F. Huang, Z.Z. Shi, F.S. Pan, *Effects of Zn on the microstructure, mechanical properties, and damping capacity of Mg-Zn-Y-Zr alloys.* Materials Science and Engineering A, 2011. **528**(18): p. 5914-5920.

41. D.K. Xu, W.N. Tang, L. Liu, Y.B. Xu, E.H. Han, *Effect of W-phase on the mechanical properties of as-cast Mg–Zn–Y–Zr alloys.* Journal of Alloys and Compounds, 2008. **461**(1–2): p. 248-252.

42. A. Singh, M. Nakamura, M. Wantanabe, A. Kato, A.P. Tsai, *Quasicrystal strengthened Mg-Zn-Y alloys by extrusion.* Scripta Materialia, 2003. **49**(5): p. 417-422.

43. Y. Kawamura. *Materials Science and Technology on Synchronized LPSO Structure (Oral)*, International Symposium on Long-Period Stacking Ordered Structure and Its Related Materials 2014, *Japan, 2014*.

44. X.H. Shao, Z.Q. Yang, X.L. Ma, *Strengthening and toughening mechanisms in Mg-Zn-Y alloy with a long period stacking ordered structure.* Acta Materialia, 2010. **58**(14): p. 4760-4771.

45. J. Pons, V.A. Chernenko, R. Santamarta, E. Cesari, *Crystal structure of martensitic phases in Ni–Mn–Ga shape memory alloys.* Acta Materialia, 2000. **48**(12): p. 3027-3038.

46. M. van Sande, R. de Ridder, J. van Landuyt, S. Amelinckx, *A study by means of electron microscopy and electron diffraction of vacancy ordering in ternary alloys of the system AlCuNi.* Physica Status Solidi (a), 1978. **50**(2): p. 587-599.

47. K.H. Hwang;, W.S. Yang;, T.B. Wu;, C.M. Wan;, J.G. Byrne, *Long-period stacking-fault structure of the needle-like phase in a duplex Fe-Mn-Al-C alloy.* Acta Metallurgica et Materialia, 1991. **39**(5).

48. T. Nakano, A. Negishi, K. Hayashi, Y. Umakoshi, *Ordering process of Al_5Ti_3, h-Al_2Ti and r-Al_2Ti with f.c.c.-based long-period superstructures in rapidly solidified Al-rich TiAl alloys.* Acta Materialia, 1999. **47**(4): p. 1091-1104.

49. D. Broddin, G.V. Tendeloo, J.V. Landuyt, S. Amelinckx, R. Portier, M. Guymont, A. Loiseau, *Long-period superstructures in Cu3±xPd.* Philosophical Magazine A, 1986. **54**(3): p. 395-419.

50. E. Abe, A. Ono, T. Itoi, M. Yamasaki, Y. Kawamura, *Polytypes of long-period stacking structures synchronized with chemical order in a dilute Mg–Zn–Y alloy.* Philosophical Magazine Letters, 2011. **91**(10): p. 690-696.

51. S.-B. Mi, Q.-Q. Jin, *New polytypes of long-period stacking ordered structures in Mg-Co-Y alloys.* Scripta Materialia, 2013. **68**(8): p. 635-638.

52. M. Matsuda, S. Ii, Y. Kawamura, Y. Ikuhara, M. Nishida, *Variation of long-period stacking order structures in rapidly solidified $Mg_{97}Zn_1Y_2$ alloy.* Materials Science and Engineering: A, 2005. **393**(1–2): p. 269-274.

53. D. Egusa, E. Abe, *The structure of long period stacking/order Mg-Zn-RE phases with extended non-stoichiometry ranges.* Acta Materialia, 2012. **60**(1): p. 166-178.

54. M. Tane, H. Kimizuka, K. Hagihara, S. Suzuki, T. Mayama, T. Sekino, Y. Nagai, *Effects of stacking sequence and short-range ordering of solute atoms on elastic properties of Mg–Zn–Y alloys with long-period stacking ordered structures.* Acta Materialia, 2015. **96**(0): p. 170-188.

55. T. Horiuchi, A. Ono, K. Yoshioka, T. Watanabe, K. Ohkubo, S. Miura, T. Mohri, S. Tamura, *Liquid-solid equilibrium and intermediate phase formation during solidification in Mg-1.3 at%Zn-1.7 at%Y Alloy.* Materials Transactions, 2008. **49**(10): p. 2247-2253.

56. Y. Yamamoto, Y. Sakamoto, Y. Masaki, S.R. Nishitani, *First principles calculations of solute ordering in Mg-Zn-Y Alloys.* Materials Transactions, 2013. **54**(5): p. 656-660.

57. F.-S. Pan, S.-Q. Luo, A.-T. Tang, J. Peng, Y. Lu, *Influence of stacking fault energy on formation of long period stacking ordered structures in Mg–Zn–Y–Zr alloys.* Progress in Natural Science: Materials International, 2011. **21**(6): p. 485-490.

58. S. Iikubo, S. Hamamoto, H. Ohtani, *Thermodynamic analysis of the Mg-RE-Zn (RE = Y, La) ternary hcp phase using the cluster variation method.* Materials Transactions, 2013. **54**(5): p. 636-640.

59. H. Okuda, M. Yamasaki, Y. Kawamura, M. Tabuchi, H. Kimizuka, *Nanoclusters first: a hierarchical phase transformation in a novel Mg alloy.* Scientific Reports, 2015. **5**: p. 14186.

60. Y.M. Zhu, A.J. Morton, J.F. Nie, *Growth and transformation mechanisms of 18R and 14H in Mg–Y–Zn alloys.* Acta Materialia, 2012. **60**(19): p. 6562-6572.

61. T. Itoi, T. Seimiya, Y. Kawamura, M. Hirohashi, *Long period stacking structures observed in $Mg_{97}Zn_1Y_2$ alloy.* Scripta Materialia, 2004. **51**(2): p. 107-111.

62. T. Kiguchi, Y. Ninomiya, K. Shimmi, K. Sato, T.J. Konno, *Structural and compositional modulation in transformation of LPSO structure in $Mg_{97}Zn_1Y_2$ cast Alloys.* Materials Transactions, 2013. **54**(5): p. 668-674.

63. K. Hagihara, N. Yokotani, Y. Umakoshi, *Plastic deformation behavior of $Mg_{12}YZn$ with 18R long-period stacking ordered structure.* Intermetallics, 2010. **18**(2): p. 267-276.

64. A. Inoue, K. Kishida, H. Inui, K. Hagihara, *Compression of micro-pillars of a long period stacking ordered phase in the Mg-Zn-Y system.* MRS Online Proceedings Library, 2013. **1516**: p. 151-156.

65. S. Miura, S. Imagawa, T. Toyoda, K. Ohkubo, T. Mohri, *Effect of rare-earth elements Y and Dy on the deformation behavior of Mg alloy single crystals.* Materials Transactions, 2008. **49**(5): p. 952-956.

66. K. Hagihara, Y. Fukusumi, M. Yamasaki, T. Nakano, Y. Kawamura, *Non-basal slip systems operative in $Mg_{12}ZnY$ long-period stacking ordered (LPSO) phase with 18R and 14H structures.* Materials Transactions, 2013. **54**(5): p. 693-697.

67. M. Matsuda, S. Ii, Y. Kawamura, Y. Ikuhara, M. Nishida, *Interaction between long period stacking order phase and deformation twin in rapidly solidified $Mg_{97}Zn_1Y_2$ alloy.* Materials Science and Engineering: A, 2004. **386**(1–2): p. 447-452.

68. J.-K. Kim, S. Sandlöbes, D. Raabe, *On the room temperature deformation mechanisms of a Mg–Y–Zn alloy with long-period-stacking-ordered structures.* Acta Materialia, 2015. **82**: p. 414-423.

69. E. Orowan, *A type of plastic deformation new in metals.* Nature, 1942. **149**: p. 643-644.

70. M.W. Barsoum, A. Murugaiah, S.R. Kalidindi, T. Zhen, Y. Gogotsi, *Kink bands, nonlinear elasticity and nanoindentations in graphite.* Carbon, 2004. **42**(8–9): p. 1435-1445.

71. K. Jensen, W. Mickelson, A. Kis, A. Zettl, *Buckling and kinking force measurements on individual multiwalled carbon nanotubes.* Physical Review B, 2007. **76**(19): p. 195436.

72. J. Hess, C. Barrett, *Structure and nature of kink bands in zinc.* Transactions of the American Institute of Mining and Metallurgical Engineers, 1949. **185**(9): p. 599-606.

73. M. Paterson, L. Weiss, *Experimental folding in rocks.*Nature 1962. **195**: p. 1046-1048.

74. F. Frank, A. Stroh, *On the theory of kinking.* Proceedings of the Physical Society. Section B, 1952. **65**(10): p. 811.

75. K. Hagihara, M. Yamasaki, M. Honnami, H. Izuno, M. Tane, T. Nakano, Y. Kawamura, *Crystallographic nature of deformation bands shown in Zn and Mg-based long-period stacking ordered (LPSO) phase.* Philosophical Magazine, 2014. **95**(2): p. 132-157.

76. M. Yamasaki, K. Hagihara, S.-i. Inoue, J.P. Hadorn, Y. Kawamura, *Crystallographic classification of kink bands in an extruded Mg–Zn–Y alloy using intragranular misorientation axis analysis.* Acta Materialia, 2013. **61**(6): p. 2065-2076.

77. K. Hagihara, A. Kinoshita, Y. Sugino, M. Yamasaki, Y. Kawamura, H.Y. Yasuda, Y. Umakoshi, *Effect of long-period stacking ordered phase on mechanical properties of $Mg_{97}Zn_1Y_2$ extruded alloy.* Acta Materialia, 2010. **58**(19): p. 6282-6293.

78. M. Matsuda, S. Ando, M. Nishida, *Dislocation structure in rapidly solidified $Mg_{97}Zn_1Y_2$ alloy with long period stacking order phase.* Materials Transactions, 2005. **46**(2): p. 361-364.

79. A. Müller, G. Garcés, P. Pérez, P. Adeva, *Grain refinement of Mg–Zn–Y alloy reinforced by an icosahedral quasicrystalline phase by severe hot rolling.* Journal of Alloys and Compounds, 2007. **443**(1–2): p. L1-L5.

80. G. Garcés, A. Müller, E. Oñorbe, P. Pérez, P. Adeva, *Effect of hot forging on the microstructure and mechanical properties of Mg–Zn–Y alloy.* Journal of Materials Processing Technology, 2008. **206**(1–3): p. 99-105.

81. G. Garcés, M.A. Muñoz-Morris, D.G. Morris, P. Pérez, P. Adeva, *Optimization of strength by microstructural refinement of MgY_2Zn_1 alloy during extrusion and ECAP processing.* Materials Science and Engineering: A, 2014. **614**: p. 96-105.

82. M. Noda, K. Funami, Y. Kawamura, T. Mayama, *Thermal stability and mechanical properties of extruded Mg-Zn-Y Alloys with a long-period stacking order phase and plastic deformation*. New Features on Magnesium Alloys, INTECH, 2012.

83. Z. Horita, Y. Kawamura, Y. Miyahara, S. Yoshimoto. *Mechanical properties and microstructure of Mg-Zn-Y alloys processed by ECAE*. Materials Science Forum. 2006. **503-504**: p.769-774

84. Z.G. Su, R.G. Li, J. An, Y. Lu, *Effect of rolling temperature on the microstructures and mechanical properties of $Mg_{97}Zn_1Y_2$ magnesium alloy.* Journal of Materials Engineering and Performance, 2010. **19**(1): p. 70-76.

85. B.-S. Wang, S.-M. Xiong, Y.-B. Liu, *Tensile fracture of as-cast and hot rolled Mg-Zn-Y alloy with long-period stacking phase.* Transactions of Nonferrous Metals Society of China, 2010. **20, Supplement 2**(0): p. s488-s492.

86. M. Furukawa, Z. Horita, M. Nemoto, T.G. Langdon, *Review: Processing of metals by equal-channel angular pressing.* Journal of Materials Science, 2001. **36**(12): p. 2835-2843.

87. S.M. Razavi, D.C. Foley, I. Karaman, K.T. Hartwig, O. Duygulu, L.J. Kecskes, S.N. Mathaudhu, V.H. Hammond, *Effect of grain size on prismatic slip in Mg–3Al–1Zn alloy.* Scripta Materialia, 2012. **67**(5): p. 439-442.

88. R.B. Figueiredo, T.G. Langdon, *The development of superplastic ductilities and microstructural homogeneity in a magnesium ZK60 alloy processed by ECAP.* Materials Science and Engineering: A, 2006. **430**(1–2): p. 151-156.

89. J. Li, W. Xu, X. Wu, H. Ding, K. Xia, *Effects of grain size on compressive behaviour in ultrafine grained pure Mg processed by equal channel angular pressing at room temperature.* Materials Science and Engineering: A, 2011. **528**(18): p. 5993-5998.

90. M. Yamasaki, K. Hashimoto, K. Hagihara, Y. Kawamura, *Effect of multimodal microstructure evolution on mechanical properties of Mg-Zn-Y extruded alloy.* Acta Materialia, 2011. **59**(9): p. 3646-3658.

91. G. Garcés, D.G. Morris, M.A. Muñoz-Morris, P. Pérez, D. Tolnai, C. Mendis, A. Stark, H.K. Lim, S. Kim, N. Shell, P. Adeva, *Plasticity analysis by synchrotron radiation in a $Mg_{97}Y_2Zn_1$ alloy with bimodal grain structure and containing LPSO phase.* Acta Materialia, 2015. **94**: p. 78-86.

92. Y. Wang, M. Chen, F. Zhou, E. Ma, *High tensile ductility in a nanostructured metal.* Nature, 2002. **419**(6910): p. 912-915.

93. M.J.N.V. Prasad, S. Suwas, A.H. Chokshi, *Microstructural evolution and mechanical characteristics in nanocrystalline nickel with a bimodal grain-size distribution.* Materials Science and Engineering: A, 2009. **503**(1–2): p. 86-91.

94. D. Witkin, Z. Lee, R. Rodriguez, S. Nutt, E. Lavernia, *Al–Mg alloy engineered with bimodal grain size for high strength and increased ductility.* Scripta Materialia, 2003. **49**(4): p. 297-302.

95. B. Derby, M.F. Ashby, *On dynamic recrystallisation.* Scripta Metallurgica, 1987. **21**(6): p. 879-884.

96. R.D. Doherty, D.A. Hughes, F.J. Humphreys, J.J. Jonas, D.J. Jensen, M.E. Kassner, W.E. King, T.R. McNelley, H.J. McQueen, A.D. Rollett, *Current issues in recrystallization: a review.* Materials Science and Engineering: A, 1997. **238**(2): p. 219-274.

97. F.J. Humphreys, M. Hatherly, *Recrystallization and Related Annealing Phenomena*. Amsterdam ; Boston : Elsevier, 2004.

98. D.K. Sun, C.P. Chang, P.W. Kao, *Microstructural aspects of grain boundary bulge in a dynamically recrystallized Mg-Al-Zn Alloy.* Metallurgical and Materials Transactions A, 2010. **41**(7): p. 1864-1870.

99. D.G.J. Griffiths. *Understanding texture weakening in magnesium rare earth alloys*. Thesis, The Univeristy of Manchester, 2014.

100. O. Sitdikov, R. Kaibyshev, *Dynamic recrystallization in pure magnesium.* Materials Transactions, 2001. **42**(9): p. 1928-1937.

101. A. Galiyev, R. Kaibyshev, G. Gottstein, *Correlation of plastic deformation and dynamic recrystallization in magnesium alloy ZK60.* Acta Materialia, 2001. **49**(7): p. 1199-1207.

102. S.E. Ion, F.J. Humphreys, S.H. White, *Dynamic recrystallisation and the development of microstructure during the high temperature deformation of magnesium.* Acta Metallurgica, 1982. **30**(10): p. 1909-1919.

103. T. Al-Samman, G. Gottstein, *Dynamic recrystallization during high temperature deformation of magnesium.* Materials Science and Engineering: A, 2008. **490**(1–2): p. 411-420.

104. M.M. Myshlyaev, H.J. McQueen, A. Mwembela, E. Konopleva, *Twinning, dynamic recovery and recrystallization in hot worked Mg-Al-Zn alloy.* Materials Science and Engineering A, 2002. **337**(1-2): p. 121-133.

105. M.R. Barnett, M.D. Nave, C.J. Bettles, *Deformation microstructures and textures of some cold rolled Mg alloys.* Materials Science and Engineering A, 2004. **386**(1-2): p. 205-211.

106. S. Sandloebes, S. Zaefferer, I. Schestakow, S. Yi, R. Gonzalez-Martinez, *On the role of non-basal deformation mechanisms for the ductility of Mg and Mg-Y alloys.* Acta Materialia, 2011. **59**(2): p. 429-439.

107. M.R. Barnett, A. Sullivan, N. Stanford, N. Ross, A. Beer, *Texture selection mechanisms in uniaxially extruded magnesium alloys.* Scripta Materialia, 2010. **63**(7): p. 721-724.

108. N. Stanford, M.R. Barnett, *The origin of "rare earth" texture development in extruded Mg-based alloys and its effect on tensile ductility.* Materials Science and Engineering: A, 2008. **496**(1–2): p. 399-408.

109. F.J. Humphreys, *The nucleation of recrystallization at second phase particles in deformed aluminium.* Acta Metallurgica, 1977. **25**(11): p. 1323-1344.

110. L.B. Tong, X. Li, D.P. Zhang, L.R. Cheng, J. Meng, H.J. Zhang, *Dynamic recrystallization and texture evolution of Mg–Y–Zn alloy during hot extrusion process.* Materials Characterization, 2014. **92**: p. 77-83.

111. J.-M. Baik, J. Kameda, O. Buck, *Small punch test evaluation of intergranular embrittlement of an alloy steel.* Scripta Metallurgica, 1983. **17**(12): p. 1443-1447.

112. X. Mao, M. Saito, H. Takahashi, *Small punch test to predict ductile fracture toughness JIC and brittle fracture toughness KIC.* Scripta Metallurgica Et Materialia, 1991. **25**(11): p. 2481-2485.

113. J.S. Ha, E. Fleury, *Small punch tests to estimate the mechanical properties of steels for steam power plant: II. Fracture toughness.* International Journal of Pressure Vessels and Piping, 1998. **75**(9): p. 707-713.

114. R.Z. Valiev, T.G. Langdon, *Principles of equal-channel angular pressing as a processing tool for grain refinement.* Progress in Materials Science, 2006. **51**(7): p. 881-981.

115. E.M. Padezhnova, E.V. Mel'nik, R.A. Miliyevskiy, T.V. Dobatkina and V.V. Kinshibalo, *Investigation of the Mg-Zn-Y system.* Russian metallurgy (English translation), 1982. **4**: p. 185-188.

116. K.P. Rice, R.H. Geiss, R.R. Keller, *Transmission electron backscatter diffraction in the SEM specimen thickness effects (Poster). Frontiers of Characterization and Metrology for Nanoelectronics*, 2015.

117. R.R. Keller, R.H. Geiss, *Transmission EBSD from 10 nm domains in a scanning electron microscope.* Journal of Microscopy, 2012. **245**(3): p. 245-251.

118. P.W. Trimby, *Orientation mapping of nanostructured materials using transmission Kikuchi diffraction in the scanning electron microscope.* Ultramicroscopy, 2012. **120**: p. 16-24.

119. W.T. Read, *Dislocation in Crystals.* McGraw-Hill, 1953.

120. D. Egusa, M. Yamasaki, Y. Kawamura, E. Abe, *Micro-kinking of the long-period stacking/order (LPSO) phase in a hot-extruded $Mg_{97}Zn_1Y_2$ alloy.* Materials Transactions, 2013. **54**(5): p. 698-702.

121. J.-M. Baik, J. Kameda, O. Buck, *Development of small punch tests for ductile-brittle transition temperature measurement of temper embrittled Ni-Cr steels.* ASTM STP, 1986. **888**: p. 92-111.

122. J.S. Cheon, I.S. Kim, *Initial deformation during small punch testing.* Journal of testing and evaluation, 1996. **24**(4): p. 255-262.

123. I.J. Beyerlein, L.S. Toth, *Texture evolution in equal-channel angular extrusion.* Progress in Materials Science, 2009. **54**(4): p. 427-510.

124. J.A. del Valle, F. Carreño, O.A. Ruano, *Influence of texture and grain size on work hardening and ductility in magnesium-based alloys processed by ECAP and rolling.* Acta Materialia, 2006. **54**(16): p. 4247-4259.

125. Z. Li, J. Dong, X.Q. Zeng, C. Lu, W.J. Ding, *Influence of $Mg_{17}Al_{12}$ intermetallic compounds on the hot extruded microstructures and mechanical properties of Mg–9Al–1Zn alloy.* Materials Science and Engineering: A, 2007. **466**(1–2): p. 134-139.

126. M.H. Maghsoudi, A. Zarei-Hanzaki, H.R. Abedi, A. Shamsolhodaei, *The evolution of γ-$Mg_{17}Al_{12}$ intermetallic compound during accumulative back extrusion and subsequent ageing treatment.* Philosophical Magazine, 2015. **95**(31): p. 3497-3523.

127. E. Oñorbe, G. Garcés, P. Pérez, S. Cabezas, M. Klaus, C. Genzel, E. Frutos, P. Adeva, *The evolution of internal strain in Mg–Y–Zn alloys with a long period stacking ordered structure.* Scripta Materialia, 2011. **65**(8): p. 719-722.

128. T.-W. Fan, B.-Y. Tang, L.-M. Peng, W.-J. Ding, *First-principles study of long-period stacking ordered-like multi-stacking fault structures in pure magnesium.* Scripta Materialia, 2011. **64**(10): p. 942-945.

129. A. Datta, U.V. Waghmare, U. Ramamurty, *Structure and stacking faults in layered Mg-Zn-Y alloys: A first-principles study.* Acta Materialia, 2008. **56**(11): p. 2531-2539.

130. S.P. Bellier, R.D. Doherty, *The structure of deformed aluminium and its recrystallization—investigations with transmission Kossel diffraction.* Acta Metallurgica, 1977. **25**(5): p. 521-538.

131. F. Haessner, J. Schmidt, *Investigation of the recrystallization of low temperature deformed highly pure types of aluminium.* Acta Metallurgica Et Materialia, 1993. **41**(6): p. 1739-1749.

132. T. Furuhara, X. Gu, *Discussion on strain accommodation associated with formation of LPSO Structure.* Materials Transactions, 2013. **54**(5): p. 675-679.

133. J.-K. Kim, W.-S. Ko, S. Sandlöbes, M. Heidelmann, B. Grabowski, D. Raabe, *The role of metastable LPSO building block clusters in phase transformations of an Mg-Y-Zn alloy.* Acta Materialia, 2016. **112**: p. 171-183.

134. C. Zener quoted by C.S. Smith, *Introduction to grains, phases, and interfaces—an interpretation of microstructure.* Transactions of the Metallurgical Society of AIME, 1948. **175**.

135. T.S. Byun, E.H. Lee, J.D. Hunn, K. Farrell, L.K. Mansur, *Characterization of plastic deformation in a disk bend test.* Journal of Nuclear Materials, 2001. **294**(3): p. 256-266.

136. J. Ragani, P. Donnadieu, C. Tassin, J.J. Blandin, *High-temperature deformation of the γ-$Mg_{17}Al_{12}$ complex metallic alloy.* Scripta Materialia, 2011. **65**(3): p. 253-256.

137. S.F. Pugh, *XCII. Relations between the elastic moduli and the plastic properties of polycrystalline pure metals.* The London, Edinburgh, and Dublin Philosophical Magazine and Journal of Science, 1954. **45**(367): p. 823-843.

138. N. Wang, W.-Y. Yu, B.-Y. Tang, L.-M. Peng, W.-J. Ding, *Structural and mechanical properties of $Mg_{17}Al_{12}$ and $Mg_{24}Y_5$ from first-principles calculations.* Journal of Physics D: Applied Physics, 2008. **41**(19): p. 195408.

139. H.E. Friedrich, B.L. Mordike, *Magnesium technology: metallurgy, design data, automotive applications*: Springer Berlin Heidelberg, 2006.

140. H.N. Mathur, V. Maier-Kiener, S. Korte-Kerzel, *Deformation in the γ-$Mg_{17}Al_{12}$ phase at 25–278 C.* Acta Materialia, 2016. **113**: p. 221-229.

141. M. Haghshenas, V. Bhakhri, R. Oviasuyi, R.J. Klassen, *Effect of temperature and strain rate on the mechanisms of indentation deformation of magnesium.* MRS Communications, 2015. **5**(03): p. 513-518.

142. I. Baker, *Recovery, recrystallization and grain growth in ordered alloys.* Intermetallics, 2000. **8**(9–11): p. 1183-1196.

143. X. Gao, J.F. Nie, *Characterization of strengthening precipitate phases in a Mg–Zn alloy.* Scripta Materialia, 2007. **56**(8): p. 645-648.

144. A. Singh, A.P. Tsai, *On the cubic W phase and its relationship to the icosahedral phase in Mg-Zn-Y alloys.* Scripta Materialia, 2003. **49**(2): p. 143-148.

145. L. Vegard, *Die Konstitution der Mischkristalle und die Raumfüllung der Atome.* Zeitschrift für Physik, 1921. **5**(1): p. 17-26.

146. D. Hardie, R.N. Parkins, *Lattice spacing relationships in magnesium solid solutions.* Philosophical Magazine, 1959. **4**(43): p. 815-825.

147. F.H. Spedding, A.H. Daane, K.W. Herrmann, *The crystal structures and lattice parameters of high-purity scandium, yttrium and the rare earth metals.* Acta Crystallographica, 1956. **9**(7): p. 559-563.

148. V.P. Perminov, *Structural characteristics and crystal chemistry of binary magnides.* Soviet Powder Metallurgy and Metal Ceramics, 1967. **6**(5): p. 409-416.

149. S. Zhang, G.Y. Yuan, C. Lu, W.J. Ding, *The relationship between $(Mg,Zn)_3RE$ phase and 14H-LPSO phase in Mg-Gd-Y-Zn-Zr alloys solidified at different cooling rates.* Journal of Alloys and Compounds, 2011. **509**(8): p. 3515-3521.

150. G. Shao, V. Varsani, Y. Wang, M. Qian, Z. Fan, *On the solidification microstructure of Mg–30Zn–2.5Y metal–intermetallic alloy.* Intermetallics, 2006. **14**(6): p. 596-602.

151. S. Minamoto, T. Horiuchi, S. Miura, *Refinement of Thermodynamic Parameters of the $Mg_{24}Y_5$, W and H Phases in the Mg-Zn-Y System.* Materials Transactions, 2015. **56**(10): p. 1670-1674.

152. H.Y. Qi, G.X. Huang, H. Bo, G.L. Xu, L.B. Liu, Z.P. Jin, *Experimental investigation and thermodynamic assessment of the Mg–Zn–Gd system focused on Mg-rich corner*. Journal of Materials Science, 2012. **47**(3): p. 1319-1330.

153. Y. Liu, G. Yuan, C. Lu, W. Ding, *Stable icosahedral phase in Mg–Zn–Gd alloy.* Scripta Materialia, 2006. **55**(10): p. 919-922.

154. G. Shao, V. Varsani, Z. Fan, *Thermodynamic modelling of the Y–Zn and Mg–Zn–Y systems.* Calphad, 2006. **30**(3): p. 286-295.

155. G. Shao, *Erratum to: "Thermodynamic modelling of the Y–Zn and Mg–Zn–Y systems by G. Shao, V. Varsani and Z. Fan" [CALPHAD 30 (2006) 286–295]*. Calphad, 2007. **31**(2): p. 313.

156. J.F. Liu, Z.Q. Yang, H.Q. Ye, *Solid-state formation of icosahedral quasicrystals at $Zn_3Mg_3Y_2$/Mg interfaces in a Mg–Zn–Y alloy.* Journal of Alloys and Compounds, 2015. **650**: p. 65-69.

157. Z. Zhu, A.D. Pelton, *Thermodynamic modeling of the Y–Mg–Zn, Gd–Mg–Zn, Tb–Mg–Zn, Dy–Mg–Zn, Ho–Mg–Zn, Er–Mg–Zn, Tm–Mg–Zn and Lu–Mg-Zn systems.* Journal of Alloys and Compounds, 2015. **652**: p. 426-443.

158. Y. Kawamura, M. Yamasaki, *Formation and mechanical properties of $Mg_{97}Zn_1RE_2$ alloys with long-period stacking ordered structure.* Materials Transactions, 2007. **48**(11): p. 2986-2992.

159. M. Yamasaki, M. Sasaki, M. Nishijima, K. Hiraga, Y. Kawamura, *Formation of 14H long period stacking ordered structure and profuse stacking faults in Mg-Zn-Gd alloys during isothermal aging at high temperature.* Acta Materialia, 2007. **55**(20): p. 6798-6805.

160. Y.J. Wu, X.Q. Zeng, D.L. Lin, L.M. Peng, W.J. Ding, *The microstructure evolution with lamellar 14H-type LPSO structure in an $Mg_{96.5}Gd_{2.5}Zn_1$ alloy during solid solution heat treatment at 773 K.* Journal of Alloys and Compounds, 2009. **477**(1-2): p. 193-197.

161. S.K. Das, Y.-B. Kang, T. Ha, I.-H. Jung, *Thermodynamic modeling and diffusion kinetic experiments of binary Mg–Gd and Mg–Y systems.* Acta Materialia, 2014. **71**: p. 164-175.